Bridging PIV spatial and temporal resolution using governing equations and development of the coaxial volumetric velocimeter

Schneiders, Jan

DOI
10.4233/uuid:244b9699-0814-4bc9-aa48-07361989bd64

Publication date
2017

Document Version
Final published version

Citation (APA)
Schneiders, J. (2017). *Bridging PIV spatial and temporal resolution using governing equations and development of the coaxial volumetric velocimeter*. [Dissertation (TU Delft), Delft University of Technology]. TU Delft OPEN Publishing. https://doi.org/10.4233/uuid:244b9699-0814-4bc9-aa48-07361989bd64

Important note
To cite this publication, please use the final published version (if applicable).
Please check the document version above.

Bridging PIV spatial and temporal resolution using governing equations

and

Development of the coaxial volumetric velocimeter

(page intentionally left blank)

Bridging PIV spatial and temporal resolution using governing equations
and
Development of the coaxial volumetric velocimeter

Proefschrift

ter verkrijging van de graad van doctor
aan de Technische Universiteit Delft,
op gezag van de Rector Magnificus prof. ir. K.C.A.M. Luyben,
voorzitter van het College voor Promoties,
in het openbaar te verdedigen op donderdag 14 december 2017 om 15:00 uur

door

Jan Ferdinand Gerardus SCHNEIDERS

Ingenieur in de Luchtvaart en Ruimtevaart,
Technische Universiteit Delft, Nederland,
geboren te Leidschendam, Nederland.

Dit proefschrift is goedgekeurd door de *promotor*:
Prof. dr. F. Scarano

Samenstelling promotiecommissie

Rector Magnificus,	voorzitter
Prof. dr. F. Scarano,	Technische Universiteit Delft

Onafhankelijke leden

Prof. dr. ir. C. Poelma,	Technische Universiteit Delft
Prof. dr. rer. nat. habil. C.J. Kähler,	Universität der Bundeswehr München
Dr. B.S. Thurow,	Auburn University
Dr. rer. nat. A. Schröder,	Deutsches Zentrum für Luft- und Raumfahrt
Dr. B. Leclaire,	Office National d'Etudes et de Recherches Aérospatiales
Dr. B. Wieneke,	LaVision, Göttingen
Prof. dr. S. Hickel,	Technische Universiteit Delft, reservelid

This research has been conducted as part of the 'CFD for PIV' project funded by LaVision GmbH., Göttingen.

ISBN: 978-94-92516-97-8
An electronic version of this dissertation is available at
http://repository.tudelft.nl/

Summary

A series of techniques is proposed for volumetric air flow measurements that are based upon the principles of particle image velocimetry (PIV). The proposed techniques fall in two categories; part 1 of this dissertation considers measurement data processing using constitutive laws and part 2 focuses on development of a coaxial volumetric flow measurement system that uses helium filled soap bubbles (HFSB) as tracer particles.

In part 1, first a technique is proposed to measure instantaneous volumetric pressure using a low repetition rate tomographic PIV system. Instead of time-resolved measurement of the flow temporal evolution, which typically required for pressure-from-PIV procedures, the required temporal information is obtained by solution of the incompressible Navier-Stokes equations in vorticity-velocity formulation using the spatial information available from the instantaneous measurements.

The reverse is proposed for cases where temporal resolution is more abundant, but spatial resolution is limited. The vorticity transport equation is leveraged to couple temporal information with instantaneous velocity data in the proposed VIC+ framework, in an attempt to obtain a dense velocity field at high spatial resolution. The governing principle is that by using the flow governing equations, the data ensemble used for interpolation is increased beyond instantaneous velocity measurements only. The technique is demonstrated to allow for measurement of vorticity and dissipation in a real-world experiment, which would otherwise be underestimated by more than 40% using the established tomographic PIV approach.

The proposed VIC+ technique uses a data ensemble for dense velocity interpolation consisting of the instantaneous velocity and material derivative measurements obtained from Lagrangian particle tracking velocimetry. An extension of the VIC+ framework that uses a measurement time-segment instead of instantaneous data only is shown to potentially improve the measurement fidelity further, when a cost-effective three-dimensional implementation can be realized.

An uncertainty quantification technique is proposed for future developments of such dense interpolation techniques. It is shown that the results from Lagrangian particle tracking measurements can be directly used for uncertainty quantification of dense interpolations and no independent measurement data is required.

In part 2 of this dissertation, a technique is first proposed for large-scale volumetric pressure measurement. The method follows recent developments of large-scale measurements using HFSB tracer particles, in combination with Lagrangian particle tracking and ensemble bin-averaging. This allows for evaluation of accurate velocity statistics and in turn the time-averaged pressure field.

The dissertation concludes with the proposal of the coaxial volumetric velocimeter (CVV). The CVV brings imaging and illumination together in a compact box, viewing and illuminating a measurement volume from a single viewing direction. The theoretical background that is derived shows that measurements in air using the CVV are only possible using tracer particles that scatter significantly more light than traditional micron sized tracer particles. Here, HFSB tracer particles are used. Due to the small solid angle of the imaging system, tracer particles need to be imaged over an extended number of snapshots to increase particle positional accuracy, making use of particle trajectory regularization.

A prototype CVV has been realized, which is first used to confirm that the flow around a sphere is measured with acceptable correspondence to a potential flow solution. Second, in the case of the flow around a cyclist, the CVV is shown to allow for measurements near both concave and convex surfaces within one measurement volume. This allows for flow analysis using skin-friction lines. In addition, the compact nature of the CVV allows mounting on a robotic arm for time-averaged of a large and complex wind tunnel model. The full-scale measurement of the flow around Giro d'Italia cyclist Tom Dumoulin shown using the CVV is an example of the latter.

Samenvatting

In deze dissertatie worden nieuwe technieken worden voorgesteld voor volumetrische luchtstroom metingen, gebaseerd op de principes van particle image velocimetry (PIV). Het werk bestaat uit twee delen. Deel 1 onderzoekt en introduceert technieken voor dataverwerking op basis van constitutieve wetten. Deel 2 onderzoekt de mogelijkheden van en introduceert een coaxiaal volumetrisch luchtstroom meetsysteem.

In deel 1 wordt eerst een techniek voorgesteld om de instantane volumetrische druk te meten middels een tomografisch PIV systeem met lage meetfrequentie. Normaal gesproken zijn tijd-opgeloste meting van de temporele evolutie van de stroming nodig. In plaatst daarvan wordt hier de benodigde temporele informatie verkregen middels oplossing van de incompressibele Navier-Stokes vergelijkingen in vorticiteit-snelheid formulatie toegepast op de instantane metingen.

Het omgekeerde wordt voorgesteld voor gevallen waar temporele resolutie wel beschikbaar is, maar in plaats daarvan ruimtelijke resolutie gelimiteerd is. De vorticiteitsvergelijking wordt wederom gebruikt om temporele informatie met instantane snelheidsdata te koppelen middels het voorgestelde VIC+ framework, om zo een snelheidsveld met hoge ruimtelijke resolutie te verkrijgen. Het onderliggende principe is dat door middel van een model het data ensemble dat gebruikt wordt voor interpolatie vergroot kan worden tot meer dan alleen de instantane snelheidsmetingen. De techniek wordt gedemonstreerd in het geval van turbulente grenslaag metingen. Waar met tomographic PIV vorticiteit en dissipatie meer dan 40% onderschat zouden worden, worden met VIC+ resultaten binnen 5% van een numerieke referentie behaald.

De VIC+ techniek gebruikt een data ensemble voor interpolatie dat bestaat uit de instantane snelheid en de instantane materiaalafgeleide metingen die verkregen worden uit Lagrangian particle tracking (LPT). Een uitbreiding van het VIC+ framework maakt gebruik van een meting over een tijdsegment in plaats van instantane data alleen. Een twee-dimensionale analyse laat zien dat nauwkeurigheid potentieel verder

vergroot kan worden, wanneer een kosten-efficiënte driedimensionale implementatie gerealiseerd kan worden.

Tot slot van deel 1 wordt een methode voor kwantificatie van de meetonzekerheid van snelheidsinterpolatie resultaten wordt voorgesteld. Er wordt gedemonstreerd dat de resultaten van LPT metingen direct gebruikt kunnen worden voor onzekerheidskwantificatie zonder dat extra onafhankelijke data verreist is.

In deel 2 van deze dissertatie wordt eerst een techniek voorgesteld voor volumetrische druk metingen op grote schaal. De methode volgt de recente ontwikkeling van grote schaal metingen met behulp van met helium gevulde zeepbellen (HFSB) als tracers. Daarnaast wordt ensemble-LPT gebruikt voor evaluatie van nauwkeurige statistieken van de stroming, waaruit het gemiddelde drukveld wordt berekend.

De dissertatie sluit af met een onderzoek naar de coaxiale volumetrische velocimeter (CVV). De CVV brengt opname en belichting samen in een compacte box, waardoor een meting vanuit een enkele richting plaats kan vinden. Metingen in luchtstromen met de CVV zijn alleen mogelijk zijn als er gebruik gemaakt wordt van tracers die significant meer licht verstrooien dan traditionele deeltjes van micron-grootte. In het huidige werk worden daarom HFSB gebruikt. Door de kleine ruimtehoek van het opnamesysteem moeten tracer deeltjes gevolgd worden over meerdere snapshots om zo de nauwkeurigheid te vergroten, gebruik makend van regularisatie van het pad van een deeltje.

Een prototype CVV wordt eerst gebruikt om te bevestigen dat de stroming rondom een bal met acceptabele nauwkeurigheid gemeten kan worden in vergelijking met de potentiaalstromingsoplossing. Vervolgens, in het geval van de stroming rondom een fietser, wordt de CVV gebruikt om de stroming in de buurt van concave en convexe oppervlakken te meten. Dit maakt het mogelijk wrijvingslijnen te berekenen. Daarnaast maakt de compacte vorm en constante kalibratie van de CVV het mogelijk het systeem op een robotarm te monteren om zo de gemiddelde stroming rondom een groot en complex model te meten. De volledige schaal meting van de stroming rondom de Giro d'Italia winnende fietser Tom Dumoulin in deze dissertatie is daar een voorbeeld van.

Contents

PART 2

Prologue

Contents

Chapter 1
Introduction

This dissertation is a work within the field of experimental fluid dynamics. A field where wind tunnel models of for example cars, wind turbines, aircraft or even rockets are tested in wind tunnel facilities. It is a field where one gets his hands dirty in fluid dynamics laboratories. However, this is also a work that was only possible by bridging a gap between laboratory work, signal processing and computational fluid dynamics.

In an age where computer science flourishes one may question the relevance of wind tunnel experiments. A common response recognizes the need for experiments to validate computational models for previously unexplored aerodynamic configurations, such as plasma actuators that could allow more efficient aircraft take-off through. But surely, experiments cannot provide the full picture? Comparison of the first Google image search results for 'experimental fluid dynamics' (Fig. 1.1-left) and 'computational fluid dynamics' (CFD, Fig. 1.1-right) suggest experimental techniques allow only for coarse flow visualization using for example smoke, whereas CFD allows for quantitative inspection.

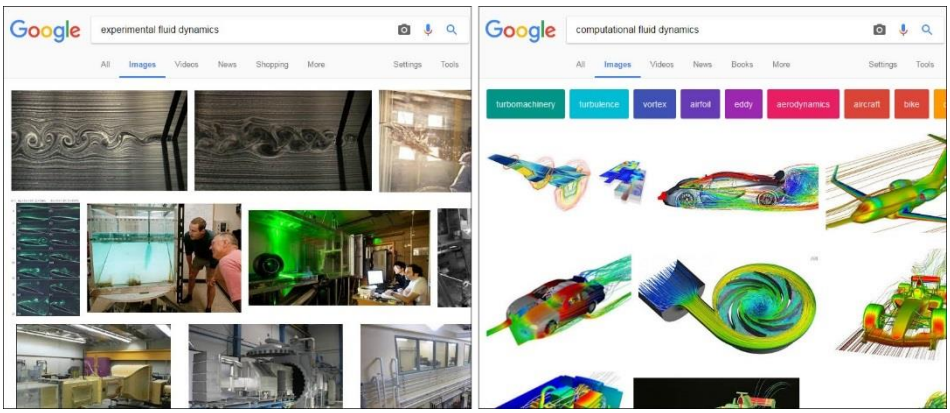

Fig. 1.1 Comparison of Google image search results (www.google.com, visited on 25 July 2017) for the search terms 'experimental fluid dynamics' (left) and 'computational fluid dynamics' (right).

However, moving beyond point-wise measurements and classical signal processing techniques, particle image velocimetry (PIV, Adrian 1991) currently a well-established technique for two-dimensional planar flow measurements. Recently derived techniques bring this a step further and allow for volumetric and even time-resolved flow measurements. The results from experiments and numerical simulations are starting to look more like each other.

The communities have now more than ever the opportunity to benefit from each other's frameworks and techniques. This has led to the increased focus on data-assimilation techniques for PIV measurement data in the past decade. The first part of this dissertation (Chapters 3 to 8) also tries to take this opportunity. It is attempted to overcome spatial and temporal resolution limitations of volumetric PIV measurements by use of flow governing equations. As will be explained by analogies in Chapters 3, it is envisaged that the use of governing equations allows measurement temporal resolution to be leveraged to increased spatial resolution dimension, and vice-versa.

The second part of this dissertation (Chapters 9 to 11) takes inspiration from the recent rise of large-scale PIV and Lagrangian particle tracking, to develop a compact volumetric flow measurement technique. Compact in the sense that imaging and illumination hardware is brought together along approximately one viewing axis, to simplify measurement setup complexity and alleviate requirements for optical access.

Both parts are introduced in more detail and with literature background later in this dissertation. The next chapter, first, provides the reader with the necessary background on the PIV measurement technique.

Chapter 2
Particle Image Velocimetry

This chapter summarizes the working principles of particle image velocimetry (PIV) and related flow measurement techniques, with a focus on volumetric techniques such as tomographic PIV and Lagrangian particle tracking. The working principles are considered first (Sec. 2.1), after which the established data processing procedures are summarized (Sec. 2.3).

2.1 PIV Working principles

All PIV techniques involve imaging of tracer particles that are seeded in a wind tunnel. When two or more images are taken consecutively at a small time-separation, the velocity of the particles can be derived. Already visual inspection of multiple consecutive images acquired in the seeded air flow past a truncated cylinder (Fig. 2.1-left) indicates for example the presence of a turbulent and separated flow region behind the cylinder. Subsequent processing of such images—details are given later in Sec. 2.3—allows for a quantitative inspection of the flow field and the vortical structures it contains (Fig. 2.1-right).

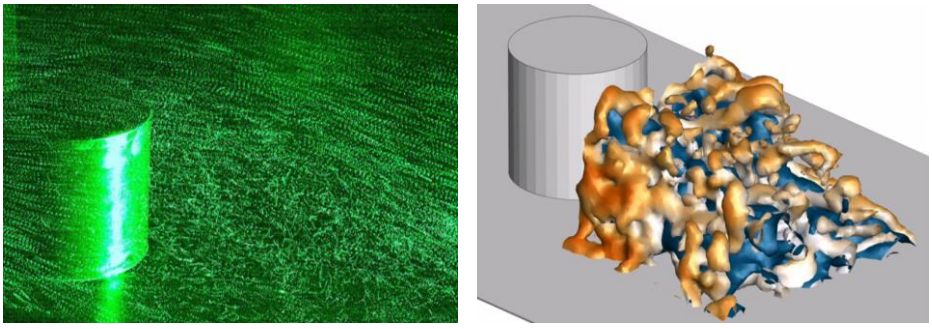

Fig. 2.1 The sum of six consecutive snapshots of the flow past a truncated surface mounted cylinder (left) and the corresponding flow field processed by VIC+ (right), visualized by isosurfaces of velocity and vorticity magnitude (right).

Analysis of the flow field based on tracer particle images is done under the assumption that the tracer particle velocity is a good measure for the local air flow speed. This is the case when the Stokes number of the tracer particles is small (Tropea et al. 2007), i.e. when the tracer particle response time, τ_p, is sufficiently smaller than the relevant flow time-scales that are to be measured, τ_f:

$$Stk = \frac{\tau_p}{\tau_f} < 0.1, \tag{2.1}$$

where the threshold of 0.1 for acceptable tracing fidelity is taken from Tropea et al. (2007). The response time of a tracer particle is derived in the same manuscript and equals:

$$\tau_p = \frac{d_p^2}{18}\frac{(\rho_p - \rho_f)}{\mu}, \tag{2.2}$$

where d_p and ρ_p are the tracer particle diameter and density, respectively, and ρ_f is the density of the fluid. Neutrally buoyant particles therefore make accurate tracers, but are relatively difficult to realize in air flows in wind tunnels (Scarano et al. 2015). Instead, heavier-than-air tracer particles with a diameter on the order of a micron, are typically employed in wind tunnel experiments.

To capture the instantaneous position of the micron sized tracer particles in the measurement domain as if they are frozen in time, exposure time is restricted. Laser illumination is typically both used and required because of the high achievable pulse energy over a short pulse duration: 200 mJ pulse energy at a 10 ns pulse width is no exception for dual-pulsed lasers, which is sufficient to capture the instantaneous tracer particle positions even in the supersonic flow regime (Westerweel et al. 2013). For standard PIV measurements, a double-pulsed laser is used in combination with imagers that capture two consecutive particle images in rapid succession. Whereas the laser pulse separation can be on the order of microseconds as noted above, allowing for instantaneous velocity measurements, the time-separation between particle image pairs

is typically on the order of tens of a seconds and velocity fields obtained are uncorrelated in time.

Classically, so-called planar PIV measurements of the two in-plane velocity components are taken in a thin measurement plane. In the past decade, volumetric PIV measurements by use of multiple cameras (Fig. 2.2) have reached a degree of maturity that they can be used for fluid dynamics investigations. The review article by Scarano (2013) shows such volumetric measurements are feasible in 'iPhone-sized' measurement volumes on the order of 20 cm^3.

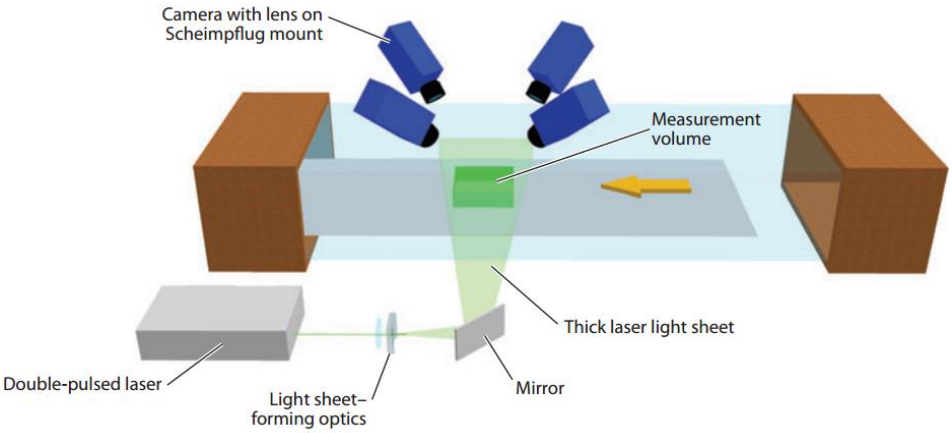

Fig. 2.2 Tomographic PIV measurement setup (figure reproduced from Westerweel et al. 2013).

The most successful volumetric PIV technique to date is likely tomographic PIV (Elsinga et al. 2006). A typical tomographic PIV measurement setup is illustrated in Fig. 2.2. Three or four cameras are arranged to view the laser-illuminated measurement volume from different angles. Scheimpflug mounts are typically used to tilt the image plane such that the full measurement volume can be focused at the smallest *f*-number; i.e. the largest aperture opening to achieve maximum particle image intensity.

The measurement volume depth achievable with tomographic PIV is typically significantly smaller than its other dimensions and therefore the volume can be regarded as a thick sheet. This is a consequence of the

particle image density approaching the limits for reliable volume reconstruction when the volume thickness is increased (Elsinga et al. 2006; Elsinga et al. 2011). For illustration, consider the turbulent boundary layer measurement setup sketched in Fig. 2.3. Three cameras are configured to look at the measurement volume (shaded in green). In the left figure, the laser is cut-off such that the measurement volume thickness is h and in the right figure the volume is cut-off at a height of $2h$. The bottom two figures show the corresponding particle images obtained by camera 2, where for both experiments the tracer particle seeding concentration is equal.

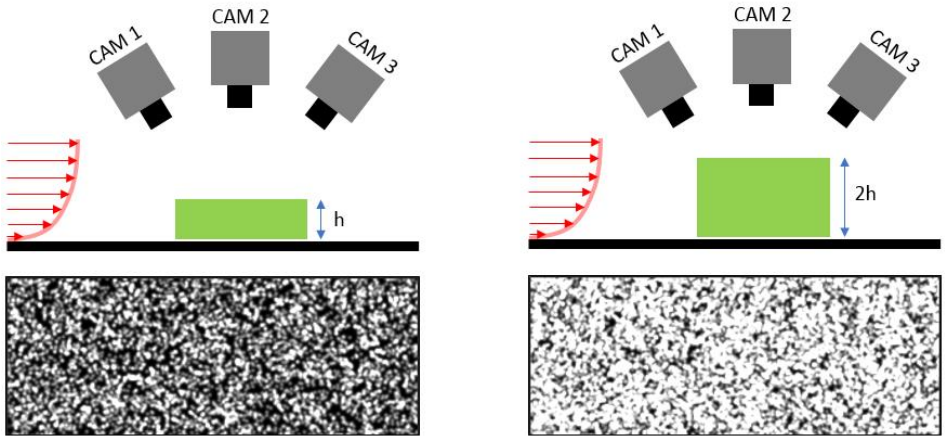

Fig. 2.3 Schematic illustration of the particle images obtained at a measurement volume thickness of h (left) and $2h$ (right) at the same seeding concentration.

The measurement volume depth is doubled in the right figure and consequently the particle image density is also doubled: there are two times as much particles per pixel in the right recording as in the left recording. Whereas in the left figure individual particles can still be recognized, the right figure has become almost fully saturated. A reliable volumetric reconstruction in such case is not possible anymore (e.g. Elsinga et al. 2006). In addition, opacity of the medium comes as an additional constraint on measurement volume size. This holds especially for measurements in water, where excessive seeding concentration leads to diffusion of the laser light and loss of image contrast (Michaelis et al.

2010; Scarano 2013). The remainder of this dissertation will treat in detail that such limitations on tracer particle seeding concentrations limits the achievable spatial resolution of the measurements.

2.2 Challenges

The above introduction to volumetric PIV measurements by tomographic PIV has touched upon several key challenges when using the technique: (i) the complex measurement system consists of multiple cameras and a separate laser all requiring mounting, optical access, alignment, focus and calibration; (ii) measurement volumes are relatively small; (iii) dual-pulse measurements yield uncorrelated instantaneous but non-time-resolved measurements; and (iv) the achievable spatial resolution is limited by tracer particle seeding concentration. The first two challenges are addressed in detail in part 2 of this dissertation, where a system simplification is proposed, integrating all components of the tomographic PIV measurement system in a single football-sized box while still allowing for volumetric measurements.

To address the third point, a temporally correlated measurement time-series can be obtained using a high-speed laser and high-speed cameras. According to a recent survey (Scarano, 2013), measurement rates achieved in time-resolved tomographic PIV experiments range from 2.7 kHz (airfoil trailing edge by Ghaemi and Scarano 2011; bluff body wake by de Kat and van Oudheusden 2012) to 5 kHz (turbulent boundary layer by Schröder et al. 2008; rod-airfoil interaction by Violato et al. 2011). More recent experiments in turbulent boundary layers have been conducted at a rate up to 10 kHz (Ghaemi et al. 2012; Pröbsting et al. 2013). These measurement rates are typically sufficient for measurements up to 20 m/s; the abovementioned experiments were conducted with airflow velocities in the range from 7 to 14 m/s. To date, time-resolved volumetric PIV experiments at flow velocities on the order of 100 m/s are to be deemed unrealistic, considering that they would require acquisition rates on the order of 100 kHz.

Even when restricted to relatively low-speed flows up to 20 m/s, high-speed systems come at significant costs: both monetary and in terms

of particle image quality. Laser pulse energy and sensor size both are significantly reduced for high-speed system in comparison to low repetition rate double-pulsed systems. This motivated development of a multi-pass light amplification system (Schröder et al. 2008; Ghaemi and Scarano 2010), but still the measurement volumes achieved using high-speed systems are very limited. Scarano et al. (2015) summarized the measurement volume and acquisition frequency of several salient tomographic PIV experiments in a figure, that is adapted in this work (Fig. 2.4-left). As can be seen, at 10 kHz the achievable measurement volume is size is just a couple of cubic centimeters. Note that one apparent outlier is visible in this figure showing both high measurement frequency and large measurement volume. This measurement was performed using helium-filled soap bubble (HFSB) tracer particles, which allow for significantly increased measurement volumes and will be treated in detail in part 2 of this dissertation.

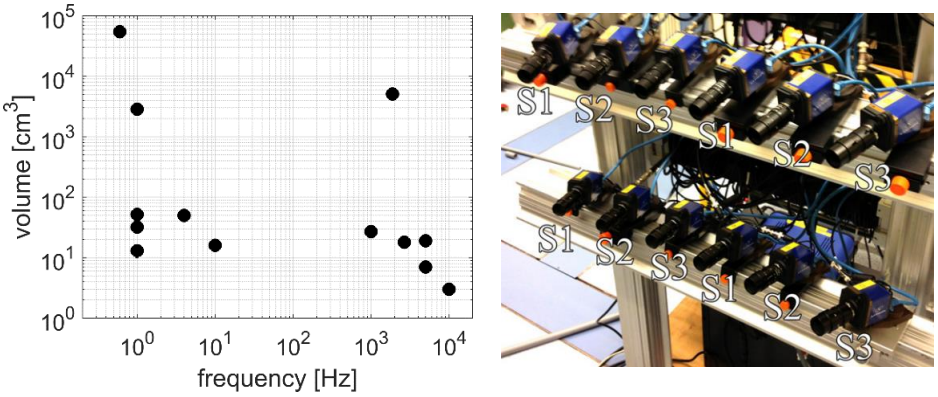

Fig. 2.4 Measurement volume versus acquisition frequency for salient tomographic PIV experiments (left; figure adapted from Scarano et al. 2015) and camera setup for a multi-pulse 12-camera tomographic PIV system (figure reproduced from Lynch and Scarano 2014).

Instead of performing a fully time-resolved experiment, multiple PIV systems have been combined to obtain volumetric measurements. Such a significant increase in system complexity is warranted in literature by the relevance of the instantaneous volumetric pressure field that can be

obtained from such measurements (Sec. 4.1), without suffering from the hardware and volume limitations of high-speed measurement systems.

The extension of dual-plane PIV (Kähler and Kompenhans, 2000) or dual-time PIV (Perret et al. 2006) to dual-tomographic PIV systems overcomes the trade-off between measurement volume and recording rate affecting the time-resolved approach, in that it makes use of two low repetition-rate lasers and CCD cameras. Such systems also allow investigating flows at higher velocity as one can arbitrarily reduce the time separation between the two velocity measurements, without the restriction set by the repetition rate of a single PIV system. A four-pulse tomographic PIV system has been described (Fig. 2.4-right; Lynch and Scarano, 2014) that can perform acceleration measurements in the compressible flow regime. The drawback is the complexity associated to 8 to 12 cameras that need to record images from a volume illuminated with two separate dual-pulse lasers.

In part 1 of this dissertation (Chapters 3 and 4), it is attempted to avoid the above increase in system complexity of time-resolved and multi-pulse measurements by leveraging the flow governing equations in combination with the measurement data obtained from standard low-repetition-rate volumetric PIV measurements.

Moving to the fourth challenge mentioned in the beginning of this section, also the achievable spatial resolution that remains a limiting factor for tomographic PIV and especially time-resolved tomographic PIV measurements. For example, recently published results of PIV measurements in a turbulent boundary layer by Pröbsting et al. (2013) indicate that the turbulent velocity fluctuations are being underestimated by approximately 20%. This is discussed in more detail in Sec. 2.3 and in Chapters 5 to 7 of this dissertation, where it is attempted to increase spatial resolution using again flow governing equations.

Before proceeding to the main body of this dissertation, however, this introductory chapter will conclude with an overview of the state-of-the-art particle image processing techniques that are used to obtain the

volumetric velocity field and derived quantities from the two-dimensional particle images.

2.3 From particle images to velocity

After recording, the two-dimensional particle images taken by the cameras need to be processed to obtain the desired volumetric velocity field measurements. Tomographic PIV is based on tomographic reconstruction of particle objects and subsequent cross-correlation (Sec. 2.3.1). Recently, literature has shown the potential benefits of discrete reconstruction techniques and individual Lagrangian particle tracking. These particle tracking techniques are discussed later in Sec. 2.3.2.

2.3.1 Cross-correlation based approaches

Planar PIV classically uses the cross-correlation operation to obtain velocity measurements from particle image pairs, as discussed in detail in, for example, the book by Raffel et al. (2007). The particle images are windowed and through cross-correlation of each so-called interrogation window a velocity vector field is found. The procedure is schematically illustrated in Fig. 2.5.

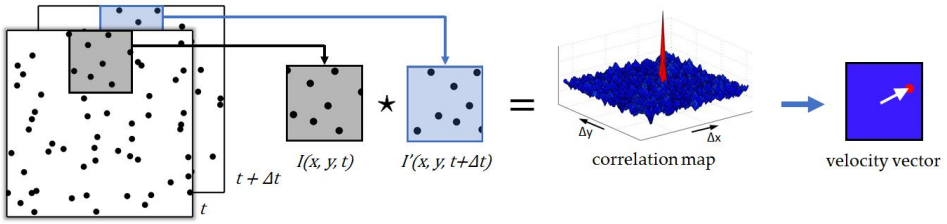

Fig. 2.5 Windowing and cross-correlation procedure illustrated for a planar PIV measurement. The cross-correlation peak is colored red in the correlation map.

In today's practice, one rarely performs cross-correlation using one pass only and iterative multigrid window-deformation (WIDIM, Scarano and Riethmuller 2000) has become a standard. The cross-correlation analysis is started with large interrogation windows, which are reduced to smaller volumes over multiple iterations. Each pass provides a predictor for window displacement and deformation in the next pass.

Inspired by planar PIV procedures, tomographic PIV (Elsinga et al. 2006) is based upon the same cross-correlation algorithm extended to 3D. The two-dimensional particle images are reconstructed into three-dimensional voxel-volumes by tomographic reconstruction. These are subsequently windowed into interrogation volumes and the velocity vector field is obtained through cross-correlation.

Considering that the true velocity field is on first approximation averaged inside an interrogation volume, the spatial resolution of tomographic PIV is dependent on the interrogation volume size. As a rule of thumb, the interrogation volume size should contain on average approximately five tracer particles for reliable cross-correlation (Scarano 2013). Consequently, the spatial resolution of tomographic PIV is directly related to the tracer particle seeding concentration. Maximum seeding concentration and thereby spatial resolution is typically dictated by the maximum particle image density in particles per pixel (ppp) that can be dealt with by particle triangulation or tomographic reconstruction in view of the ghost particles phenomenon (Elsinga et al. 2006; Lynch and Scarano 2015).

Elsinga et al. (2006) proposed the use of the multiplicative algebraic reconstruction technique (MART, Herman and Lent 1976) for particle volume reconstruction. With a four-camera system, the maximum particle image density, N_p, for MART reconstruction is approximately 0.05 ppp (Elsinga et al. 2006).

Recent literature shows significant efforts to increase reliability of tomographic PIV analysis at smaller interrogation volumes sizes and increased particle image density. The most salient of these works leverage the temporal information that is available from time-resolved tomographic PIV. Fluid trajectory correlation (FTC, Lynch and Scarano 2013) and ensemble-averaged cross-correlation (FTEE, Jeon et al. 2014) have demonstrated improved correlation by performing cross-correlation over an extended number of snapshots. Tomographic reconstructions using MART were also improved by leveraging the temporal information with motion tracking enhanced MART (MTE, Novara et al. 2010), where the velocity field obtained from cross-correlation is used to predict

particle locations for the tomographic reconstructions. The latter has been recently implemented in a cost-effective time marching approach instead of a time-sliding approach (sequential MTE, SMTE, Lynch and Scarano 2015). Still, for all the above techniques, spatial resolution remains limited by the interrogation volume size. The next section discusses Lagrangian particle tracking techniques that attempt to improve upon this by avoiding the interrogation volume based filtering operation. These techniques form the basis for the high-spatial resolution reconstruction approaches proposed in Chapters 5 to 7 of this dissertation.

2.3.2 Lagrangian particle tracking

Particle tracking velocimetry (PTV) techniques pair particles over two or more consecutive exposures (Fig. 2.6) to obtain velocity measurements at each tracer particle location. This could potentially offer a higher spatial resolution than tomographic PIV because the spatial filtering effect inherent to the cross-correlation analysis used for tomographic PIV is avoided.

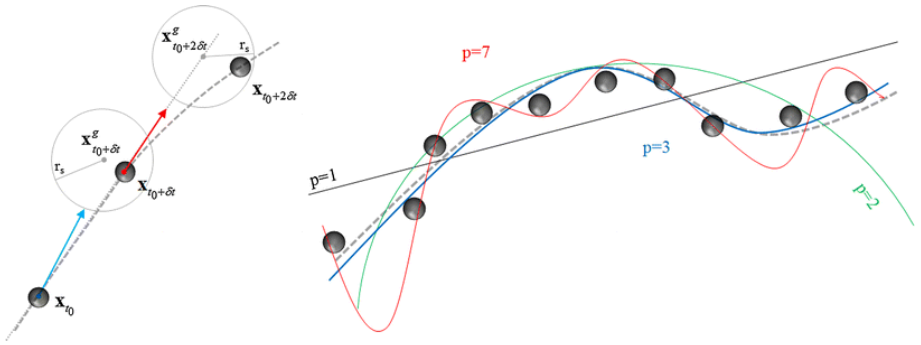

Fig. 2.6 Multi-step search algorithm (left) and particle position regularization by polynomial track fitting (right). Figure reproduced from Novara and Scarano (2013).

As particle tracking techniques do not benefit from the robustness of the statistical cross-correlation operation that operates on multiple particles, significant efforts can be found in literature to perform reliable particle pairing and tracking. Stitou and Riethmuller (2001) discussed further the possibility of super-resolution PIV, originally introduced by Keane et al.

(1995), by refining the PIV result using a PTV algorithm. Particle pairing in this case is done using a predictor obtained from PIV analysis. When time-resolved measurements are available, particles can be tracked over multiple exposures using tree-search algorithms as discussed by amongst others Malik et al. (1993) and Novara and Scarano (2013), where in case multiple particle trajectories are found within a search window, a criterion is applied that selects the most likely trajectory based on a minimum change in acceleration criterion.

Especially volumetric time-resolved measurements can allow tracks over an extended number of exposures, typically on the order of 10, to be build, because the problem of out-of-plane motion is avoided. The benefit of such long trajectories is twofold: the risk of incorrect particle pairing is reduced and the particle positions can be regularized by fitting of a function (e.g. polynomial, Fig. 2.6-right, Novara and Scarano 2013; spline, Schanz et al. 2016; amongst others).

For volumetric measurements, the original particle triangulation based 3D-PTV approach (Maas et al. 1993) poses, however, a strong limitation on the seeding concentration to allow reliable particle triangulation. Maas et al. (1993) reports a maximum particle image density of 0.005 ppp for a three-camera system. This limit value is raised when using tomographic reconstruction instead of triangulation, which as noted above can be done up to an image source density of approximately 0.025 ppp using a three-camera system (Elsinga et al. 2006). Individual particle positions are subsequently identified in the reconstructed voxel volumes using a peak finding algorithm, where sub-voxel accuracy of the particle centroid can be obtained using for example a commonly used 3-point Gaussian fit (Raffel et al. 2007).

A disadvantage of all techniques based on tomographic reconstruction is their computational costs. Especially when only discrete particle positions are desired, as is the case for particle tracking techniques, a significant reduction in computational cost is achieved by discrete reconstruction techniques such as the recently introduced iterative particle reconstruction triangulation method (IPR, Wieneke 2013). The IPR technique has been demonstrated to allow for reliable

particle reconstruction at similar levels as tomographic PIV. The technique is used by the Shake-the-Box (STB, Schanz et al. 2016) Lagrangian particle tracking technique, which has demonstrated accurate particle tracking at seeding concentrations on the order of those used for tomographic PIV, by leveraging temporal consistency of particle trajectories to obtain accurate predictions of the particle positions.

Inspired by the potential of STB and volumetric Lagrangian particle tracking techniques in general, a significant part of this dissertation (Chapters 5 to 8) focusses on techniques to grid and interpolate the scattered particle tracking measurements at potentially higher spatial resolution than what is possible by established interpolation techniques. This is of relevance, as many relevant derived quantities rely on accurate spatial velocity gradients. Indeed, despite all techniques mentioned in this chapter are often abbreviated as PIV or PTV methods, the word 'velocimetry,' certainly does not mean that only velocity data can be extracted from the measurements. A wide range of relevant derived quantities can be obtained, especially from volumetric and time-resolved measurements, as discussed in detail in the next chapter.

Part I
Measurement Data Augmentation using Governing Equations

Contents

Chapter 3
Bridging experiments, models and simulations

As already touched upon in the introduction, the past decade has seen increased interest and research into the direction of data assimilation techniques for PIV. This dissertation adds to this research in two ways: it is attempted to obtain temporal information from measurements by leveraging the available spatial resolution and vice-versa. This is explained conceptually by means of two analogies in Sec. 3.1 and Sec. 3.2, respectively. This introductory chapter concludes with a literature review of the already existing data assimilation techniques.

3.1 Leveraging spatial information using a model

The previous chapter has already introduced the difficulties of time-resolved volumetric flow measurements using tomographic PIV or similar experimental techniques. Measurement volumes are on the order of cubic centimeters and time-resolved measurements at flow speeds on the order of 100 m/s are well out of reach as they would require an unrealistic acquisition frequency on the order of 100 kHz. More realistic are volumetric measurements at lower measurements rates on the order of 1 to 5 kHz; clearly insufficient, one may say, as signal processing techniques will not be able to resolve temporal velocity fluctuations beyond the Nyquist frequency. However, established signal processing techniques do not leverage the available measurement data completely.

Consider, by analogy, an instantaneous measurement of a tennis ball that has been thrown up by a tennis player for his service. The measurement provides the balls location at time T_1 and its velocity, $v(T_1)$, as sketched in Fig. 3.1a. It doesn't require much imagination to understand the tennis ball will initially continue travelling up at approximately the speed $v(T_1)$. Such a linear extrapolation is sketched in Fig. 3.1b.

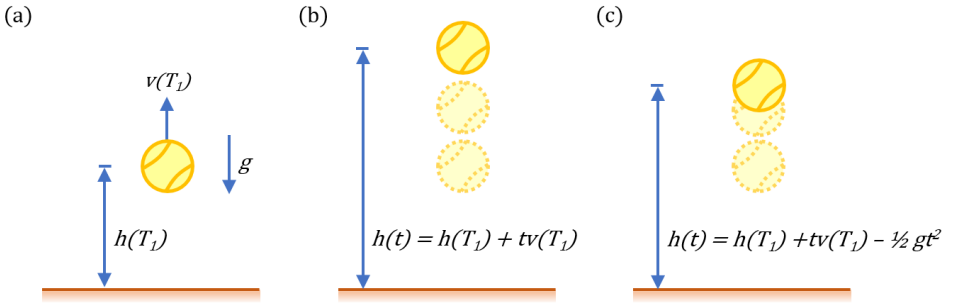

Fig. 3.1 Schematic illustration of extrapolation using constitutive laws. (a) measurement of a tennis ball thrown up in the air; (b) approximation of the path of the tennis ball for $t > T_1$ with a linear approximation and (c) a non-linear model. Figure adapted from Schneiders (2014).

A significantly improved estimation can in addition be made using secondary school physics. Knowledge of the earth's gravitational acceleration, g, allows formulation of a non-linear model of the tennis ball's trajectory (Fig. 3.1c). A model that will accurately predict the height of the tennis ball until the tennis player hits it with his racket.

The above analogy illustrates how a single instantaneous measurement can be animated by invoking constitutive laws. These laws combined with the available spatial—contextual—information can allow for the animation of frozen measurements. Also for air flows the constitutive laws are well known: the Navier-Stokes equations. Application of this concept to PIV measurements could allow for a significant increase in measurement temporal resolution. As will be discussed in sections 3.3 and 3.4, this has been attempted already by Scarano and Moore (2012) using linearized flow equations and current efforts attempt to extend this using a non-linear flow model.

3.2 Leveraging temporal information using a model

Consider the reverse of the previous section: what if instead of temporal resolution, spatial resolution is limited? In the previous chapter it was discussed how particle tracking techniques only provide measurement data at the scattered tracer particle locations and their concentration determines the achievable spatial resolution. Information in between

particles is to be derived by use of interpolation techniques. However, again, signal processing techniques such as linear, polynomial or spline interpolation do not fully leverage the measurement data that is available.

By an analogy it is illustrated how constitutive laws can be leveraged to increase the data ensemble that is used for the data interpretation. Imagine talking with a friend over the phone. The connection drops intermittently and only fractions of words are audible:

t___e_____o_____b_

On first inspection, the sentence above is sampled insufficiently to make sense of it. A common data processing technique for scattered data is linear interpolation. Using linear interpolation to find the missing letters gives the following:

tpli**e**gikmpr**t**qoljg**e**

Clearly, linear interpolation is not suitable in this case. However, one has more knowledge of the situation than just the letters. The phone conversation was in English, thus most likely the sequence is one of English words that follow English grammar. A fitting phrase could be:

to_**b**e_dev**o**ured_**b**y

However, with some effort one could find also other equally valid ones. The number of options can be reduced significantly however by considering more contextual information. Imagine that just before the telephone connection started dropping, the conversation considered famous quotes from the writer William Shakespeare. Knowing this, it becomes most probable that the phrase reads:

to_b**e**_or_n**o**t_to_**b**e

This example shows how by use of constitutive laws–language and grammar in this case–and by use of contextual information, an undersampled sequence of letters can be interpreted. The same can be attempted when dealing with sparse velocity measurements coming from

particle tracking procedures. The constitutive laws are available: mass conservation should hold for example (see Sec. 3.3; Zhong et al. 1991; Vedula and Adrian 2005; de Silva et al. 2013; Schiavazzi et al. 2014; Wang et al. 2016; amongst others). Contextual information is also available: the particle trajectories are temporally very well sampled. The momentum equation can potentially be used to couple the temporal and spatial information provided by the measurement. This coupling could make it possible to use an increased data ensemble for interpretation of the instantaneous velocity field, thereby potentially increasing spatial resolution. This is investigated in detail in Chapters 5 to 7 of this dissertation. The next section first reviews the salient existing data assimilation techniques.

3.3 Data assimilation for PIV

It is not the first time that it is proposed to apply models or constitutive laws to PIV measurement data. However, to-date none of these techniques are adopted in real-world environments for three-dimensional aerodynamic investigations. In fact, almost no application to volumetric measurement data is shown in literature. This can be explained on the one hand by the relative complexity and cost involved with realizing volumetric flow measurements, which makes that only a limited number of laboratories have access to such measurements, and on the other hand by computational cost involved with such so-called data assimilation approaches.

Nonetheless, pioneering data assimilation approaches can be found in literature. Not necessarily the most basic ones are techniques that do not consider a flow physics model provided by the Navier-Stokes equations, but rely on reduced order modelling using more general signal processing techniques. For example, the use of proper orthogonal decomposition (POD) is well adopted by the PIV community (see, amongst others, Patte-Rouland et al. 2001; Kostas et al. 2005; Gurka et al. 2006). A recent addition in the field of reduced order modelling for PIV measurements is the theory of compressed sensing (CS, Candes et al. 2006), which can allow reconstruction of highly undersampled

measurements when a sparse basis exists for the signal. Bai et al. (2015) have employed a reduced order modelling approach using compressive sensing for reconstruction of velocity time-series from PIV measurements performed at limited temporal resolution. Dalitz et al. (2017) also leveraged compressive sensing theory for their 'compressive motion sensing' framework that attempts tomographic reconstruction of time-varying volumes such as particle volumes.

Probably the first data assimilation techniques found in literature that directly employ part of the flow governing equations are divergence free filters (Zhong et al. 1991; Vedula and Adrian 2005; de Silva et al. 2013; Schiavazzi et al. 2014; Wang et al. 2016; amongst others). These impose the incompressibility constraint to improve fidelity of the velocity vector field. For example, a result from Schiavazzi et al. (2014) is reproduced here (Fig. 3.2). The left figure shows the unfiltered volumetric PIV measurement of the flow behind a swimming jellyfish, where the black isosurfaces are vortical structures identified by the $\lambda 2$ criterion. The right figure shows the filtered result, which still contains the largest flow structures but lacks the small features found in the original dataset.

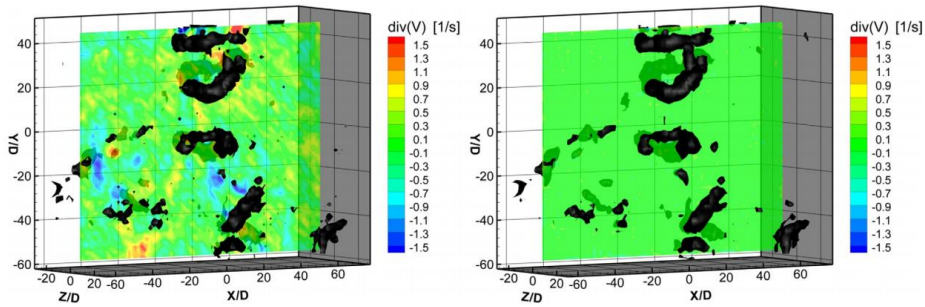

Fig. 3.2 Unfiltered (left) and solenoidal-filtered (right) volumetric PIV measurement of the flow behind a swimming jellyfish; the black isosurfaces are vortical structures identified by the $\lambda 2$ criterion. Figure reproduced from Schiavazzi et al. (2014).

Instead of the continuity equation, also the momentum equation has been solved for pressure using velocity fields measured by PIV as reviewed by van Oudheusden (2013). Considering this and the above paragraph, a logical next step would be to combine divergence free filters with

temporal information of the flow, making use of the momentum equation. The first attempts reported in literature consider a so-called measurement-integrated simulation where a body force is added to the momentum equation that is proportional to the difference between the simulated and measured velocity fields (Hayase and Hayashi 1997; Yamagata et al. 2008). More research into use of frameworks for coupled flow simulations has followed rapidly: Cuzol and Mémin (2005), Gronskis et al. (2013), Vlasenko et al. (2015), Yegavian et al. (2015) and Lemke and Sesterhenn (2016) have all proposed techniques for combination of numerical flow simulations with flow measurements. Sometimes these techniques are combined with further reduced order modelling. For example, Suzuki (2012) proposed a reduced-order Kalman filter technique combining PTV and DNS, and later a POD-based hybrid simulation (Suzuki, 2014). A result from the latter manuscript is reproduced here (Fig. 3.3). The figure shows a significantly more regularized flow field is obtained from the Kalman filtering approach coupled with a numerical simulation (left figure) than from the raw PTV measurements (right figure).

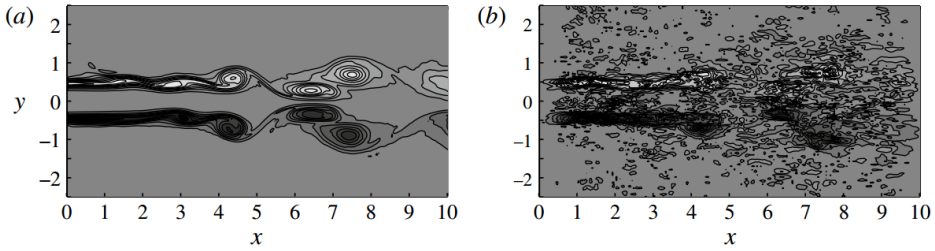

Fig. 3.3 Comparison of instantaneous vorticity contours corresponding obtained from optimal Kalman (left) and the raw PTV measurements (right, both figures reproduced from Suzuki 2014).

An advantage of the above frameworks is that they can naturally incorporate also local information from other measurement devices (e.g. surface pressure measurements) as alternative or in addition to PIV. Computational cost associated with the abovementioned variational or Kalman filter based techniques has however limited practical application to real-world experiments and no practical application to volumetric

measurements has been demonstrated. It is worth anticipating the work in part 1 of this dissertation here and note the FlowFit (Gesemann et al. 2016) and VIC+ (Schneiders and Scarano 2016) techniques, that are more computationally feasible exceptions because they operate on instantaneous measurement data only.

Less computationally expensive data assimilation approaches solve directly and non-iteratively the flow governing equations using the PIV data as initial or boundary conditions. For example, the use of CFD simulations to fill gaps in the measurement domain has been discussed by Sciacchitano et al. (2012). To alleviate measurement rate requirements which limit current pressure-from-PIV setups, Scarano and Moore (2012) proposed to leverage directly the spatial information available by the measurement to increase temporal resolution (time-supersampling) using a linearized model. The work is based on Taylor's hypothesis of frozen turbulence, and advects spatial velocity fluctuations to produce intermediate velocity estimates in between the measured samples. It was found to allow for reconstruction of velocity fluctuations in a turbulent wake flow, even when the velocity field was sampled at a fraction of the Nyquist frequency (Fig. 3.4).

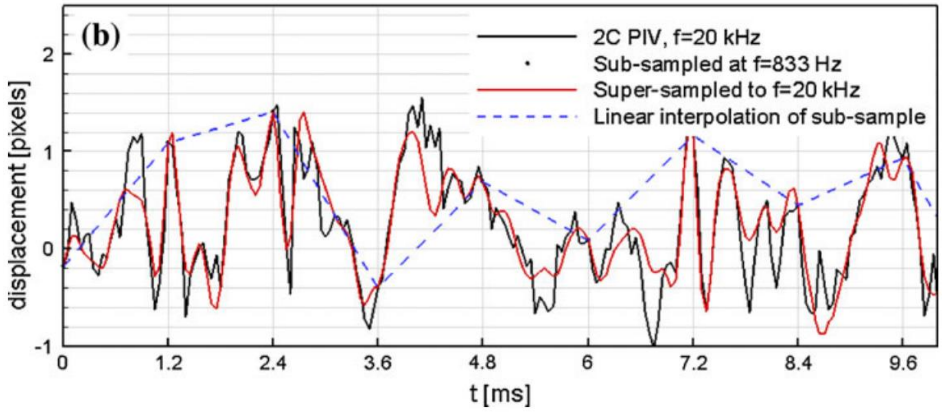

Fig. 3.4 Time history of the vertical velocity component in pixels displacement as obtained by the advection model (red line) from data sampled at 833 Hz, in comparison to the reference signal at 20 kHz (black line). Figure reproduced from Scarano and Moore (2011).

The relatively low computational cost of the linearized advection model has allowed for demonstration of the method on real-world tomographic PIV data. For example, Beresh et al. (2016) obtained reliable velocity spectra up to 150 kHz by supersampling pulse-burst planar PIV measurements taken at 25 kHz in a cylinder-wake flow at 175 m/s. A similar Taylor's hypothesis based approach was later used by de Kat and Ganapathisubramini (2012) and Laskari et al. (2016) for PIV-based pressure measurement (see Sec. 4.1), who discussed the importance of estimating the local convection velocity.

To avoid local convection velocity estimation, the time-supersampling concept was generalized to broader flow regimes (separated flows, vortex-dominated regimes) by Schneiders et al. (2014), who introduced the use of the vortex-in-cell (VIC) technique for tomographic PIV measurements in incompressible flows; analogous to the non-linear extrapolation in Sec. 3.1. The measured samples of the velocity field are used both as initial and final conditions for a numerical simulation of the vorticity transport equation, which is solved within the measurement domain. The study returned an accurate time-reconstruction, demonstrating that the sampling rate requirements could be significantly reduced with such a procedure.

The following chapters of this dissertation build upon the latter work to further alleviate measurement hardware requirements for pressure-from-PIV (Chapter 4) and increased measurement fidelity (Chapters 5 to 7). The method, however, deserves a more thorough introduction, which is presented in the next section.

3.4 Vortex-in-cell simulation for PIV measurements

The vortex-in-cell (VIC) technique was originally introduced by Christiansen (1973) for pure numerical simulations and can be classified as a 'vortex method' as reviewed in Leonard (1980; 1985) and Anderson and Greengard (1985). Vortex methods are a class of CFD methods that solve the Navier-Stokes equations in vorticity-velocity equations using a particle discretization, promising stable simulation when using relatively coarse grids and large computational time-steps compared to alternative

numerical techniques. These benefits have been recognized also outside of the field of computational fluid dynamics and have been leveraged in data assimilation frameworks in for example the field of optical flow and computer vision (Cuzol and Memin 2005; Heitz et al. 2010; amongst others). Recently, the VIC technique was adapted by Schneiders et al. (2014) for time-supersampling of PIV measurements.

The VIC-based time-supersampling technique performs time-marching simulations in between consecutive velocity measurements, as illustrated in Fig. 3.5-top. Both forward and backward simulations are performed taking the PIV measurements as initial conditions. The results of these simulations are then averaged (Fig. 3.5-bottom) to provide an estimate of the temporal velocity fluctuations in between consecutive measurements.

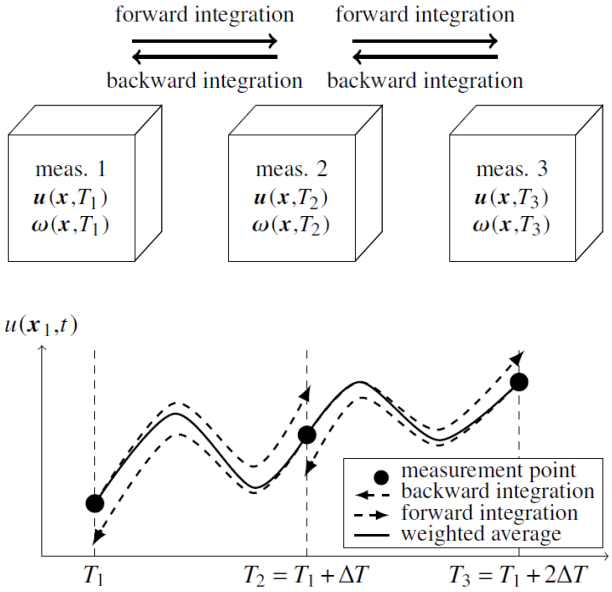

Fig. 3.5 The time-supersampling principle, increasing time series resolution by combined forward–backward integration between snapshots (left). The right diagram illustrates the velocity temporal evolution at a point and its time-supersampling reconstruction. Figure reproduced from Schneiders et al. (2014).

As mentioned above, VIC employs the Navier-Stokes equations in vorticity-velocity formulation:

(3.1) $\boldsymbol{\omega} = \nabla \times \boldsymbol{u}$,

(3.2) $\nabla^2 \boldsymbol{u} = -\nabla \times \boldsymbol{\omega}$,

(3.3) $\frac{\partial \boldsymbol{\omega}}{\partial t} + (\boldsymbol{u} \cdot \nabla)\boldsymbol{\omega} = (\boldsymbol{\omega} \cdot \nabla)\boldsymbol{u} + \nu \Delta \boldsymbol{\omega}$,

where it is assumed that the flow is incompressible,

(3.4) $\nabla \cdot \boldsymbol{u} = 0$,

and $\boldsymbol{u}$ and $\boldsymbol{\omega}$ are the velocity and vorticity vectors, respectively. Note that the solution of the above equations is only possible when volumetric data is available, hence restricting the application of VIC time-supersampling to volumetric PIV measurements. The VIC framework employs a particle-based discretization of the vorticity field, which simplifies the time-marching scheme to the sequential solution of two ordinary differential equations governing the vortex particle advection and vortex particle strength, respectively:

(3.5) $\frac{\partial \boldsymbol{x}_i}{\partial t} = \boldsymbol{u}(\boldsymbol{x}_i, t)$,

(3.6) $\frac{\partial \boldsymbol{\omega}_i}{\partial t} = [\boldsymbol{\omega}(\boldsymbol{x}_i, t) \cdot \nabla]\boldsymbol{u}(\boldsymbol{x}_i, t)$,

where $\boldsymbol{x}_i$ is the location of the vortex particle and $\boldsymbol{\omega}_i$ is its strength.

For illustration, the result of time-supersampling a jet flow (Fig. 3.6-left) is recalled from Schneiders et al. (2014). The vortex shedding in the jet flow, originally measured by Violato and Scarano (2011), occurs at approximately 30 Hz. The velocity temporal evolution at a point in the shear layer is given in Fig. 3.6-right. Reference measurements are sampled at 1000 Hz. From sub-sampled measurements at 22 Hz (circled dots), the velocity fluctuations cannot be reconstructed by linear interpolation. Also in this flow case, the assumption of frozen turbulence does not hold and

a linear advection model (dashed line) is unable to reconstruct the fluctuations. The non-linear time-supersampling procedure using VIC (red line), however, can reconstruct the velocity fluctuations. This shows that by leveraging spatial information, using VIC the velocity fluctuations can be reconstructed even if they are sampled well below the vortex shedding and Nyquist frequencies.

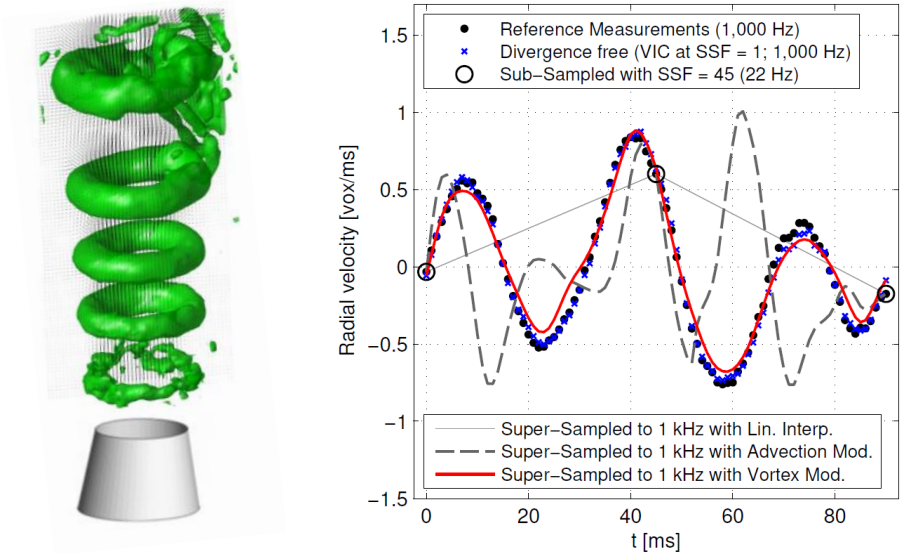

Fig. 3.6 Instantaneous velocity field with vortices visualized by the Q-Criterion (left, measurement by Violato and Scarano 2011). Reconstructed time histories of the radial velocity components in a point in the shear layer at (x/D, y/D, z/D) = (−1/3, 5/2, 0), using point-wise linear interpolation, the advection model and the proposed vortex method (right, figure reproduced from Schneiders et al. 2014).

In the next chapter, the time-supersampling principle is applied to extract pressure fields from instantaneous velocity measurements, to completely alleviate the requirement for time-resolved measurements. Also, inspiration is taken from the time-supersampling procedure to increase fidelity of time-resolved measurements. One way to accomplish this is to simulate multiple independent measurements at one time-instant, which can be averaged to reduce measurement noise (Fig. 3.7). This idea of 'simulating repeated measurements' was investigated briefly by the author and presented in Schneiders et al. (2015). In the present

dissertation, however, focus is on increasing spatial resolution of Lagrangian particle tracking measurements, where the use of constitutive laws promises to allow for increases in measurement fidelity (Chapters 5 to 7).

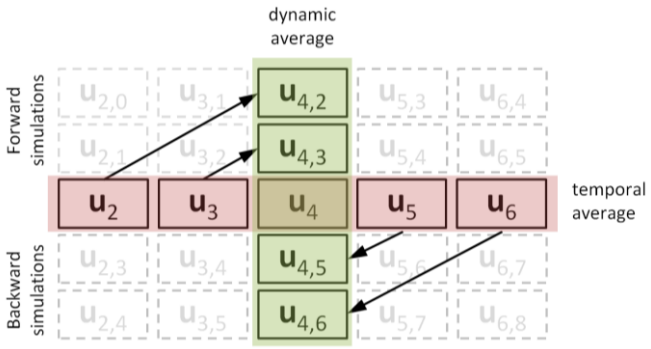

Fig. 3.7 Schematic comparison of conventional and dynamic average filter. Measured sequence of velocity fields (snapshots number 2-6, in red) and repeated measurements obtained with VIC simultaneous to snapshot 4 (green column). Figure reproduced from Schneiders et al. (2015).

Chapter 4
Instantaneous pressure from velocity snapshots

This work has been published in Schneiders et al. (2016) Exp. Fluids 57:53

The measurement of unsteady pressure fluctuations is particularly relevant in the fields of aero-elasticity and aero-acoustics, since it provides with information for estimation of the unsteady loads and noise sources. Today, pressure-from-PIV techniques (Sec. 4.1) provide an alternative to the complex instrumentation of a wind tunnel model with pressure transducers for pressure measurement, but require relatively expensive time-resolved tomographic PIV measurements. Alleviating the requirement for time-resolved data, in this chapter a technique is introduced for pressure measurement from standard low repetition-rate tomographic PIV measurements.

4.1 Pressure-from-PIV

In only a decade, techniques that determine the fluid flow pressure based on PIV measurements have come to a degree of maturity that justifies their application in practical problems. These developments have been surveyed in a recent review article by van Oudheusden (2013). The appealing aspect of the approach is that it avoids the requirement of instrumentation of wind-tunnel models using pressure transducers. Pressure sensitive paint (PSP, Bitter et al. 2012) offers similar advantages being less intrusive, however, its use in the low-speed regime is hampered by the low sensitivity of PSP.

The established time-resolved pressure-from-PIV procedure solves the incompressible Poisson equation for pressure,

$$\nabla^2 p = -\rho \nabla \cdot \frac{D\boldsymbol{u}}{Dt}, \tag{4.1}$$

by approximating D$\boldsymbol{u}$/Dt from time-resolved tomographic PIV measurements. Possible extensions to compressible flows are reviewed in van Oudheusden (2013), but the discussion here is limited to incompressible and isothermal flows. Von Neumann type boundary conditions on the pressure gradient are provided by the momentum equation, and typically at least at one point a Dirichlet type boundary condition on pressure is prescribed as detailed in Section 4.4.

Starting from the work of Liu and Katz (2006), who used a dual-PIV system to measure velocity and its material derivative and subsequently applied the momentum equation for pressure evaluation, all following studies dealing with instantaneous pressure from PIV have made use of either time-resolved measurements or followed the dual-PIV approach to experimentally determine the velocity material derivative.

It has been shown that an accurate determination of the velocity material derivative in turbulent flows requires full three-dimensional evaluation of the velocity and acceleration field, which is currently possible by high-speed tomographic PIV experiments (Ghaemi et al. 2012). Due to uncorrelated random errors in consecutive PIV snapshots, recent studies have employed a Lagrangian pseudo-tracking approach to obtain the velocity material derivative from a series of consecutive time-resolved velocity measurements. For example, Liu and Katz (2013) employed five consecutive velocity fields and Novara and Scarano (2013) applied a PTV technique to eleven consecutive camera images. Other studies have focused on noise reduction of the PIV velocity measurements using for example a POD-based filtering approach (Charonko et al. 2010) to increase accuracy of the pressure determined from the time-resolved PIV measurements.

4.2 Pressure evaluation from a single PIV snapshot

As discussed in the introductory chapters, data assimilation techniques can provide an alternative to time-resolved pressure-from-PIV approaches. The tennis-ball analogy in Sec. 3.1 has illustrated how spatial information can be leveraged in combination with constitutive laws to obtain temporal information. The objective of the present work moves the

attention to the use of VIC (Sec. 3.4) on a single velocity field snapshot to estimate the instantaneous pressure field in flows where the pressure fluctuations are dominated by vortical structures in the flow. The single-snapshot pressure evaluation using VIC follows a time-marching approach, whereby a single time-step starting from the instantaneous tomographic PIV velocity measurements is needed to approximate the velocity material derivative and subsequently, the instantaneous pressure. As a result, a significant simplification of the measurement systems is potentially obtained, with respect to dual systems for the evaluation of pressure-from-PIV.

For single-snapshot pressure evaluation, the present study also employs eq. (4.1). However, D$\boldsymbol{u}$/Dt is approximated from the single velocity measurement $\boldsymbol{u}_m(\boldsymbol{x}, t_0)$ using VIC, as detailed later in Sec. 4.3. Once D$\boldsymbol{u}$/Dt is calculated, the Poisson equation is solved following an established time-resolved pressure-from-PIV procedure. The right-hand side of the equation is computed using second order central differences in the interior domain and first order single-sided differences on the domain boundaries. The Laplace operator is discretized using second order central differences and following e.g. Ebbers and Farneback (2009) ghost points at the external side of the domain boundary are eliminated through the von Neumann boundary condition (Section 4.4).

4.3 Approximation of D*u*/Dt from single velocity snapshot

From a tomographic-PIV velocity measurement $\boldsymbol{u}_m(\boldsymbol{x}, t_0)$ in a domain Ω with boundary $\partial\Omega$, vorticity is approximated on the measurement grid,

$$\boldsymbol{\omega}_h = \boldsymbol{\nabla} \times \boldsymbol{u}_m, \tag{4.2}$$

where the subscript h indicates a quantity that is computed by finite differences. Following the VIC procedure outlined in Schneiders et al. (2014), the divergence free approximation of the measured velocity field is calculated by solution of,

$$\boldsymbol{\nabla^2 u}_h = -\boldsymbol{\nabla} \times \boldsymbol{\omega}_h, \quad \boldsymbol{u}_h|_{\partial\Omega} = \boldsymbol{u}_m. \tag{4.3}$$

Although imposing the divergence-free condition has been demonstrated as an effective tool for noise reduction of 3D data (e.g. by de Silva et al. 2013 and Schiavazzi et al. 2014), in the present study, the divergence-free approximation is an inherent step of the procedure, and is not meant for preconditioning or noise reduction of the measured velocity field. In the interior domain, typically $\boldsymbol{u}_h \neq \boldsymbol{u}_m$, which is mostly ascribed to measurement errors. Recent studies have proposed to estimate the measurement error with the difference between a divergence free flow field and $\boldsymbol{u}_m$ (Atkinson et al. 2011; Lynch and Scarano 2014; Sciacchitano and Lynch 2015, among others).

The temporal derivative of vorticity can subsequently be calculated by a finite-difference discretization of the inviscid vorticity transport equation,

$$\left.\frac{\partial \boldsymbol{\omega}}{\partial t}\right|_{h,Eul} = (\boldsymbol{\omega}_h \cdot \boldsymbol{\nabla})\boldsymbol{u}_h - (\boldsymbol{u}_h \cdot \boldsymbol{\nabla})\boldsymbol{\omega}_h \tag{4.4}$$

The subscript *Eul* stands here for Eulerian, as later an alternative discretization (using VIC) will be introduced. Approximation of $\partial\boldsymbol{\omega}/\partial t$ using (4.4) allows for approximation of the temporal velocity derivative by solution of

$$\boldsymbol{\nabla}^2 \left.\frac{\partial \boldsymbol{u}}{\partial t}\right|_h = -\boldsymbol{\nabla} \times \left.\frac{\partial \boldsymbol{\omega}}{\partial t}\right|_h \qquad \left.\frac{\partial \boldsymbol{u}}{\partial t}\right|_h = f_{du} \text{ on } \partial\Omega \tag{4.5}$$

with Dirichlet boundary conditions f_{du} as discussed in Section 4.4. The velocity material derivative is subsequently approximated by,

$$\left.\frac{D\boldsymbol{u}}{Dt}\right|_h = \left.\frac{\partial \boldsymbol{u}}{\partial t}\right|_h + (\boldsymbol{u}_h \cdot \boldsymbol{\nabla})\boldsymbol{u}_h. \tag{4.6}$$

Solution of (4.4) requires approximation of the gradient of vorticity. The VIC approach avoids this by employing a vortex particle discretization, as discussed in Schneiders et al. (2014). The VIC time-supersampling procedure detailed in the latter paper yields $\boldsymbol{\omega}_h(\boldsymbol{x}, t_0 + \Delta t)$ directly from a single forward-time integration in the interior domain. Using single-sided

finite differences the temporal vorticity derivative is subsequently approximated,

$$(4.7)\quad \left.\frac{\partial \boldsymbol{\omega}}{\partial t}\right|_{h,VIC} = \frac{\boldsymbol{\omega}_h(\boldsymbol{x},t_0+\Delta t) - \boldsymbol{\omega}_h(\boldsymbol{x},t_0)}{\Delta t}$$

The integration time-step is chosen on the order of the PIV pulse time separation; sufficiently small to avoid truncation errors, but large enough to avoid rounding errors. Still, on the two grid points adjacent to each volume boundary, the VIC procedure requires boundary values (Schneiders et al. 2014), which are here taken from (4.4),

$$(4.8)\quad \left.\frac{\partial \boldsymbol{\omega}}{\partial t}\right|_{h} = \begin{cases} \left.\frac{\partial \boldsymbol{\omega}}{\partial t}\right|_{h,VIC} & 2 < i < L,\ 2 < j < M,\ \text{and } 2 < k < N \\ \left.\frac{\partial \boldsymbol{\omega}}{\partial t}\right|_{h,Eul} & \text{otherwise} \end{cases}$$

where $i \in \{1,..,L\}$, $j \in \{1,..,M\}$ and $k \in \{1,..,N\}$ are the grid points indices in the computational volume. In the experimental assessment (Sec. 4.6) it is witnessed that when (4.8) is employed instead of (4.4) in the full domain, this improves the pressure computation, reflected by the slight increase in correlation coefficient.

4.3.1 Range of application and limitations

The proposed technique can only use the information available from a single velocity measurement to approximate the velocity temporal derivative and subsequently pressure. The limitations of the technique become apparent upon splitting of equation (4.5) into a non-homogeneous Poisson equation with homogeneous boundary conditions, and a homogeneous Poisson equation with non-homogeneous boundary conditions,

$$(4.9)\quad \frac{\partial \boldsymbol{u}}{\partial t} = \left.\frac{\partial \boldsymbol{u}}{\partial t}\right|_A + \left.\frac{\partial \boldsymbol{u}}{\partial t}\right|_B$$

$$(4.10)\quad \boldsymbol{\nabla}^2 \left.\frac{\partial \boldsymbol{u}}{\partial t}\right|_A = -\boldsymbol{\nabla}_h \times \frac{\partial \boldsymbol{\omega}}{\partial t}, \qquad \left.\frac{\partial \boldsymbol{u}}{\partial t}\right|_A = 0 \ \text{ on } \partial\Omega,$$

$$(4.11)\quad \boldsymbol{\nabla}^2 \left.\frac{\partial \boldsymbol{u}}{\partial t}\right|_B = 0, \qquad \left.\frac{\partial \boldsymbol{u}}{\partial t}\right|_B = f_{du} \ \text{ on } \partial\Omega$$

Equation (4.10) can be solved directly from the temporal vorticity derivative approximated by (4.5) from a single tomographic PIV velocity snapshot. However, equation (4.11) cannot be readily solved in the absence of knowledge about the boundary conditions on the temporal velocity derivative, which is not measured by the PIV system. When boundary conditions on (4.11) cannot be approximated, the pressure field can only be determined up to the pressure induced by the irrotational acceleration field following from equation (4.11). To illustrate this, consider the extreme case where pressure is determined solely by this component. Take for example the flow in a cylinder, which is uniformly accelerated by a piston: a uniform pressure gradient is associated to the acceleration caused by the piston motion. As a result, the absolute value of the pressure cannot be determined unless, for this example, the piston path is known, or in general, when the fluid flow acceleration at the domain boundary can be estimated. For many relevant applications in the turbulent flow regime the instantaneous value of $\partial \boldsymbol{u}/\partial t$ is dominated by the contribution from equation (4.10). Such cases include turbulent boundary layers, flow over stationary airfoils, wakes and jets. In addition to the above considerations, in Sec. 4.4 three types of boundary conditions are proposed to approximate boundary conditions for equation (4.11) for a wider variety of cases.

4.4 Treatment of boundary conditions

For the present problem, the treatment of boundary conditions (BC) needs to be considered at two stages in the procedure: first for the Poisson equation for pressure (4.1); second for the solution of the Poisson equation for the velocity temporal derivative (4.5).

4.4.1 Pressure boundary conditions

Mixed BCs on pressure are generally employed in PIV-based pressure determination methods, with a Dirichlet BC f_p on $\partial\Omega_1$ and Neumann BC g_p on $\partial\Omega_2$. The Dirichlet boundary condition f_p may be obtained from additional experimental data, using pressure probes or surface pressure transducers. Alternatively, a more practiced approach is including in the

measurement domain regions where the flow is known to be irrotational and possibly steady. In that case, pressure-velocity models as simple as the Bernoulli equation or isentropic relations may be employed (see e.g. Kurtulus et al. 2007; Ragni et al. 2009; de Kat and van Oudheusden 2012). The use of such a model for pressure yields a Dirichlet BC f_p along an extended region $\partial\Omega_1$ of one or more volume boundaries.

Neumann boundary conditions g_p on the pressure gradient are provided by the momentum equation,

$$\nabla p = -\rho \frac{D\boldsymbol{u}}{Dt} + \mu \nabla^2 \boldsymbol{u}. \tag{4.12}$$

Note that for pressure evaluation the viscous terms are typically neglected (van Oudheusden, 2013). Ghaemi et al. (2012) have directly evaluated the viscous terms from a PIV measurement in a turbulent boundary layer and showed that in a turbulent boundary layer these terms are typically two orders of magnitude smaller than the other terms in the momentum equation. It may be remarked that the viscous terms are only neglected for the computation of the instantaneous pressure. The measured velocity field inherently incorporates the physical effects of viscosity.

4.4.2 Velocity acceleration boundary conditions

Boundary conditions for (4.5) are not measured by the single-snapshot PIV experiment or readily provided by the system of equations, in contrast to the Neumann type BC for pressure. When the measurement volume boundary involves a free stream or steady flow, $\partial \boldsymbol{u}/\partial t = 0$ can be imposed there. Similarly, at a wall the no-slip BC also implies $\partial \boldsymbol{u}/\partial t = 0$. However, where the volume boundaries involve unsteady flow regions, a model for the unsteady boundary conditions is required depending on the flow case under consideration, as discussed in detail in Section 4.4.2. These models approximate the temporal velocity derivative on the domain boundary to account for boundary effects. In the interior domain the VIC model approximates the temporal velocity derivative by simulation of the vorticity captured in the measurement volume. Three types of approximations for Dirichlet boundary conditions will be

considered in the present study; in the experimental assessment, the sensitivity of the solution to the different approximations is assessed.

1. Convection boundary conditions of the form:

$$\frac{\partial \boldsymbol{u}}{\partial t} = -(\boldsymbol{u}_c \cdot \nabla)\boldsymbol{u},$$

which are expected to be accurate when the assumption of "frozen turbulence" holds on the boundary region and small velocity fluctuations are convected by a larger mean convection $\boldsymbol{u}_c$ velocity (Taylor's hypothesis). The problem of determining the correct value of the convective velocity has been addressed over the past decades (e.g. Wills 1964; Krogstad et al. 1998; de Kat and Ganapathisubramani 2013). For conciseness however, in the experimental assessment (Section 4.6) the local instantaneous flow velocity is used as an estimate for the convection velocity. It should be remarked that similar models have also been used for boundary conditions for pure numerical simulations (e.g. Orlanski 1976) and the model has recently been employed by Gronskis et al. (2013), who attempted to combine direct numerical simulation with PIV measurements.

2. Padding boundary conditions: when the vorticity outside of the measurement volume is small compared to the vorticity contained within the measurement volume, the measurement volume may be padded with an extension region of zero vorticity and a homogeneous boundary condition on the acceleration is prescribed on the enlarged domain, which allows the temporal velocity derivative on the measurement domain volume to become non-zero. This procedure is illustrated in more detail in Section 4.5 using a numerical example. It should be remarked that this boundary condition type is also used in pure numerical simulations using the vortex-in-cell technique (e.g. Cottet and Poncet 2003).

3. Homogeneous boundary conditions: when $\partial \boldsymbol{u}/\partial t \approx 0$ on the volume boundaries, the homogeneous boundary condition $\partial \boldsymbol{u}/\partial t = 0$ is a trivial approximation. Additionally, this boundary condition is considered in the present investigation to assess sensitivity of the result when a homogeneous boundary condition is prescribed.

These three boundary condition types will all be considered in the experimental assessment (Section 4.6) using independent microphone measurement data to establish the sensitivity of the solution to a change in boundary conditions. In the next section, the use of the padding type of boundary condition will be illustrated for the numerical test case of an advecting Gaussian vortex.

4.5 Numerical illustration

Consider a two-dimensional Gaussian vortex being advected at a constant velocity u_c and positioned in the center of a simulated measurement domain at time t_0 (Fig. 4.1a).

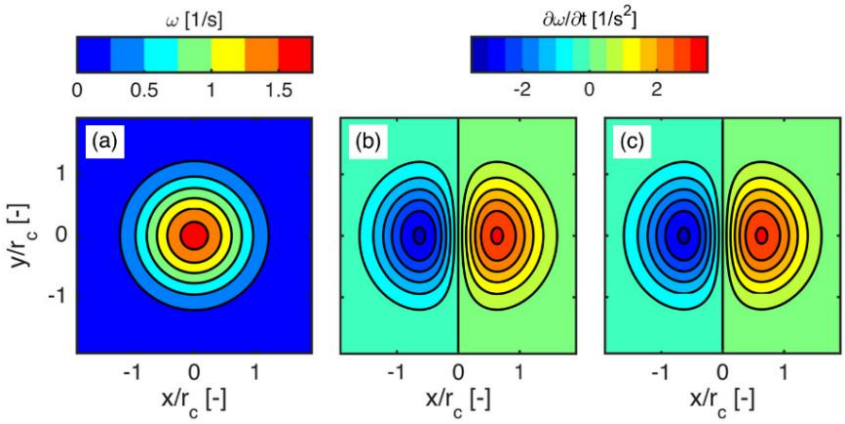

Fig. 4.1 Vorticity field in the simulated measurement domain (a), exact temporal vorticity derivative (b) and the temporal derivative of vorticity calculated by VIC from the single velocity measurement (c)

This case has been used previously for assessment of time-resolved PIV pressure evaluation procedures by amongst others de Kat and van Oudheusden (2012) and Lynch and Scarano (2014). The tangential velocity field induced by the Gaussian vortex blob is given by,

$$(4.13)\quad V_\theta = \frac{\Gamma}{2\pi r}\left(1 - e^{-\frac{r^2}{c_\theta}}\right),$$

where Γ is the circulation and $c_\theta = r_c^2/\gamma$. Choosing $\gamma = 1.256$, the tangential velocity peaks at the core radius r_c. A positive uniform velocity u_c is added to the velocity field. For this illustrative case, $r_c/L = 0.25$ and $u_c L/\Gamma = 2$, with L being the width of the square measurement domain. The analytical expression for the exact pressure field centered on the vortex core is given by

$$(4.14)\quad p = -\frac{1}{2}\rho V_\theta^2 - \frac{\rho\Gamma^2}{4\pi^2 c_\theta}\left(Ei\left(\frac{r^2}{c_\theta}\right) - Ei\left(\frac{2r^2}{c_\theta}\right)\right)$$

with Ei(x) the exponential integral function. For reference, the exact $\partial \boldsymbol{u}/\partial t$ and pressure fields are plotted in respectively Fig. 4.2a and Fig. 4.2e.

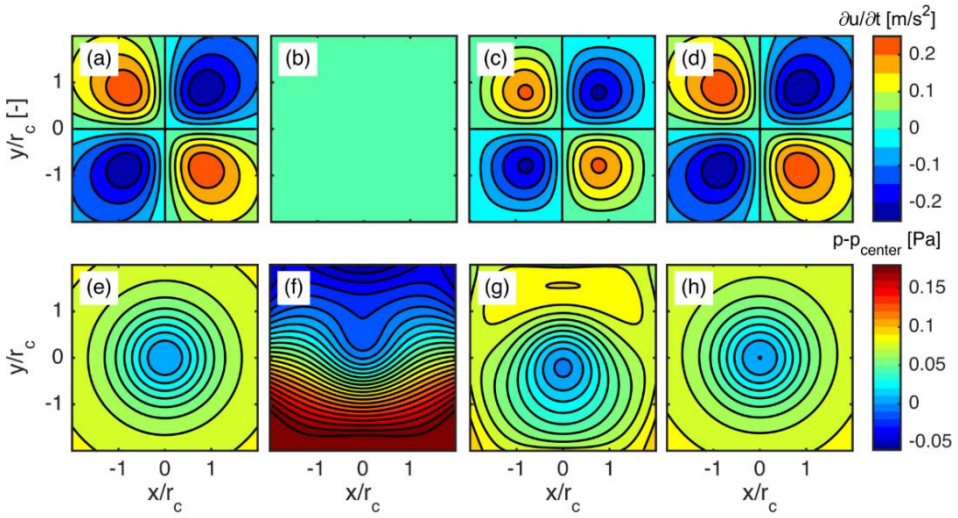

Fig. 4.2 Temporal derivative of streamwise velocity (top) and pressure (bottom); (a, e): exact, (b, f): assuming $\partial u/\partial t = 0$ (c, g): single-snapshot VIC without boundary padding and (d, h): with boundary padding.

It should be remarked that the pressure fields given in this section are unique up to a constant and to allow for comparison to the exact pressure they are fixed to zero in the domain center.

Consider now a simulated single-snapshot measurement of the exact instantaneous velocity field in a measurement domain equal to the region plotted in Fig. 4.1a ($-2 < x/r_c < 2$, $-2 < y/r_c < 2$). When pressure is calculated directly from this velocity field, neglecting the $\partial \boldsymbol{u}/\partial t$ term using the steady Poisson equation with Neumann boundary conditions, this leads to an unsatisfactory result as can be seen directly by comparison of Fig. 4.2e (exact pressure) and Fig. 4.2f (approximated pressure neglecting $\partial \boldsymbol{u}/\partial t$).

The proposed single-snapshot method aims to improve upon this by approximating $\partial \boldsymbol{u}/\partial t$. The temporal vorticity derivative estimated with the VIC method is given in Fig. 4.1c. The temporal derivative of vorticity is positive to the right of the vortex blob and negative to its left, according to the motion of the vortex blob to the right. The temporal velocity derivative is subsequently calculated by solution of Poisson equation (6). Fig. 4.2a shows in this test case that $\partial \boldsymbol{u}/\partial t$ on the measurement domain boundary is non-zero. Prescribing $\partial \boldsymbol{u}/\partial t = 0$ on the boundaries for solution of (6) forces the temporal velocity derivative to zero near the domain boundaries (Fig. 4.2c). Nevertheless, an improved approximation of the exact pressure field is obtained in comparison to neglecting $\partial \boldsymbol{u}/\partial t$ entirely, as can be seen upon comparison of Fig. 4.2f and Fig. 4.2g.

To obtain a further improvement of the approximated pressure field, note that vorticity outside of the simulated measurement domain is practically zero (Fig. 4.1a). This can be exploited for solution of (4.5), by using padding type boundary conditions (Section 4.4.2). The approximated temporal derivative of vorticity calculated is padded with zeros around the domain, enlarging the computational domain (Fig. 4.3, left figure). The size of the padded region should account for the length scale of flow fluctuations, and is in the present case chosen equal to the size of the vortex in the measurement domain ($2r_c$). Hence the domain is extended on all sides by $2r_c$. Prescribing the value of the temporal derivative to zero on the extended computational boundary for solution

of (4.5) allows the temporal derivative to attain nonzero values in the actual measurement domain (Fig. 4.3, right figure). The results show that a more accurate approximation of the exact temporal derivative can be obtained with this approach (Fig. 4.2d). Also, the pressure field evaluated from a single velocity snapshot with VIC and boundary padding is reasonably accurate (Fig. 4.2h) and improves further upon the result without zero-padding (Fig. 4.2g).

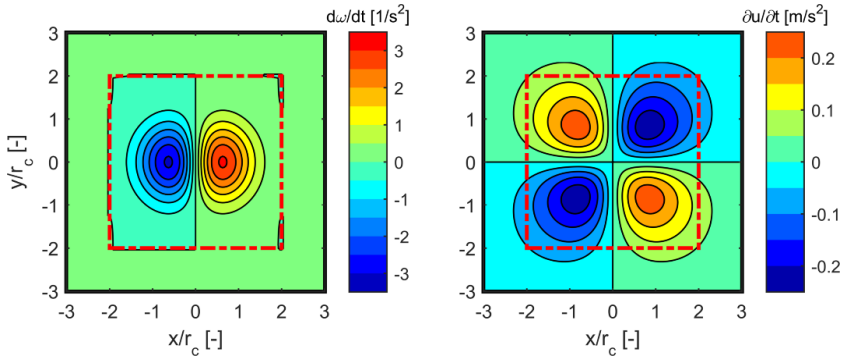

Fig. 4.3 Domain padding applied to the temporal vorticity derivative computed by VIC (left) and the corresponding $\partial \boldsymbol{u}/\partial t$ computed with homogeneous BC (right); the measurement domain is given by the dashed red line.

The padding boundary condition and the other two boundary conditions proposed in Section 4.4.2 are evaluated in a more realistic case in the next section, where the procedure is applied to a real tomographic PIV experiment in a turbulent boundary layer and validated against independent microphone pressure fluctuation measurements.

4.6 Experimental Assessment

The problem of the flat-plate boundary layer is considered for the experimental assessment, which has been studied in recent studies employing time-resolved tomographic PIV for pressure determination (Ghaemi and Scarano 2011; Schröder et al. 2011; Pröbsting et al. 2013; Ghaemi and Scarano 2013, amongst others). These studies follow two decades of literature on turbulent boundary layer flows as reviewed in Marusic et al. (2010). Because of the inherent unsteady nature of the turbulent flow structures in the boundary layer, pressure evaluation from

tomographic PIV in such flows has only been demonstrated using a time-resolved (repetition rate ~ 10kHz) measurement setup.

The turbulent boundary layer tomographic PIV measurements of Pröbsting et al. (2013) are employed for the assessment. In this study, the pressure from time-resolved PIV was compared to a surface-mounted pressure transducer. The two independent measurements yielded a maximum cross-correlation coefficient of 0.6. This value repeats that obtained earlier by Ghaemi et al. (2012) under a more favorable measurement configuration. In the present validation of the single-snapshot method, the procedure follows the above studies, using the cross-correlation coefficient as a metric of measurement accuracy.

The experiment considers a turbulent boundary layer on a flat plate at a free stream velocity of 10 m/s, corresponding to a Reynolds number based on the local boundary-layer thickness ($\delta = 9.4$ mm) of $Re_\delta = 6{,}240$. The measurement setup is schematically illustrated in Fig. 4.4. The tomographic PIV measurements are performed at 10 kHz with four LaVision *HighSpeedStar* CMOS cameras equipped with Nikon *Micro-Nikkor* 105 mm prime lenses and a Quantronix *Darwin Duo* Nd:YLF laser.

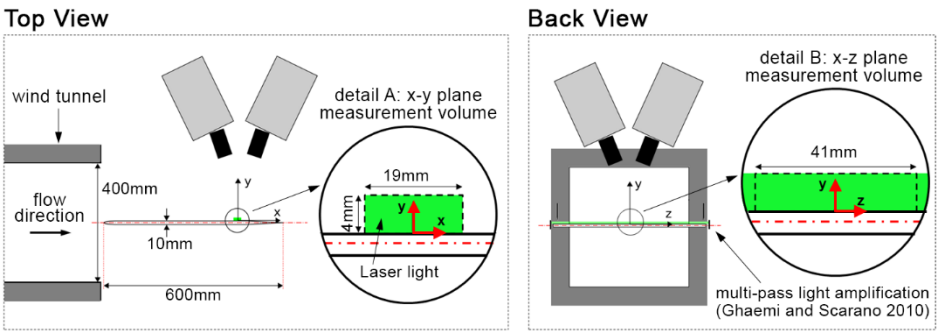

Fig. 4.4 Schematic of the tomographic PIV experiment (schematics not to scale); top view (left) and back view (right); the measurement volume is indicated by the black dashed line in details A and B.

A multi-pass light amplification system is installed, following the indications of Ghaemi and Scarano (2010) to increase the illumination intensity. Knife-edges are employed to obtain a top-hat intensity profile and avoid attenuation of laser intensity near volume boundaries. To

obtain the vector field, the sequence of objects is analyzed with a volume deformation iterative multigrid technique and boundary vectors are cropped to avoid loss-of-correlation effects. The surface pressure fluctuations are measured simultaneously with the PIV measurements at a single location within the measurement volume using a Sonion 8010T condenser microphone. Further salient details of the experiment are given in Tab. 4.1 and
Tab. **4.2**. For a more complete discussion the reader is referred to Pröbsting et al. (2013). In the next section, first the benchmark time-resolved pressure evaluation procedure is outlined. Subsequently, in Sec. 4.6.2 results of the experimental assessment are discussed.

Tab. 4.1 Measurement conditions

Free stream velocity	V_∞	10 m/s
Reynolds number	Re_δ	6,240
	Re_θ	723
	Re_τ	436
Shape factor	H	1.45
Boundary layer thickness	δ	9.4 mm
Displacement thickness	δ^*	1.5 mm
Momentum thickness	θ	1.1 mm
Wall shear velocity	u_τ	0.52 m/s

Tab. 4.2 Tomographic PIV configuration

Reconstructed volume	$L_x \times L_y \times L_z = 19 \times 4 \times 41$ mm^3
Magnification	0.45
Interrogation volume size	$l_x \times l_y \times l_z = 32 \times 16 \times 32$ vox
Overlap	75%
Vector spacing	$\Delta x = \Delta z = 0.33$ mm, $\Delta y = 0.16$ mm
Acquisition frequency	10 kHz
Number of samples	1,500

4.6.1 Benchmark time-resolved pressure evaluation

The time-resolved pressure evaluation procedure is chosen equal to the procedure used originally by Pröbsting et al. (2013), allowing for direct comparison of the results. The latter paper employed the following stencil for approximation of the velocity material derivative,

$$(4.15)\quad \left.\frac{D\boldsymbol{u}}{Dt}\right|_{\mathrm{TR-PIV}} = (\boldsymbol{\Delta t}^T\boldsymbol{\Delta t})^{-1}\boldsymbol{\Delta t}^T\boldsymbol{\Delta u},$$

where $\boldsymbol{\Delta t} = [\Delta t_{-j}, \ldots, \Delta t_j]^T$, with $\Delta t_j = t_j - t_0$ and similarly for $\boldsymbol{\Delta u}$, with $\Delta \boldsymbol{u}_i = \boldsymbol{u}(\boldsymbol{x}_p(t_i),t_i) - \boldsymbol{u}(\boldsymbol{x}_p(t_0),t_0)$, where,

$$(4.16)\quad \boldsymbol{x_p}(t_{\pm j}) = \pm\boldsymbol{u}\left(\boldsymbol{x_p}(t_{\pm(j-1)}), t_{\pm(j-1)}\right)\Delta t + \boldsymbol{x_p}(t_{\pm(j-1)}),$$

and $j = 1 \ldots M$. Pröbsting et al. (2013) found the $M = 4$ nine-snapshot stencil to be optimal for the present experimental dataset. The present work does not aim to improve the time-resolved pressure evaluation procedure, but proposes a pressure evaluation procedure for non-time-resolved PIV measurements and therefore the case of M = 4 is taken as reference and benchmark result. In addition, a smaller three-snapshot stencil (M = 1) will be considered for comparison, which is illustrative for dual-PIV cases where only three to four consecutive measurements are available instead of nine. For a more extensive discussion on time-resolved PIV pressure evaluation methods, the reader is referred to van Oudheusden (2013) and references therein.

It should be remarked that due to the Lagrangian nature of the material derivative evaluation, the procedure does not yield values near the in- and outflow boundaries as information from outside the measurement domain would be required in these regions. The extent of this region can be approximated by

$$(4.17)\quad L_{cr} \approx \frac{u_\infty M}{\Delta x},$$

and the measurement volume is cropped by this region, 12Δx, on both in- and outflow. In addition, a crop of 5Δx is applied on both sides in spanwise direction and of respectively 2Δy and 5Δy on respectively the

bottom and top surfaces of the volume. The extent of the domain crop is sketched also in Fig. 4.5.

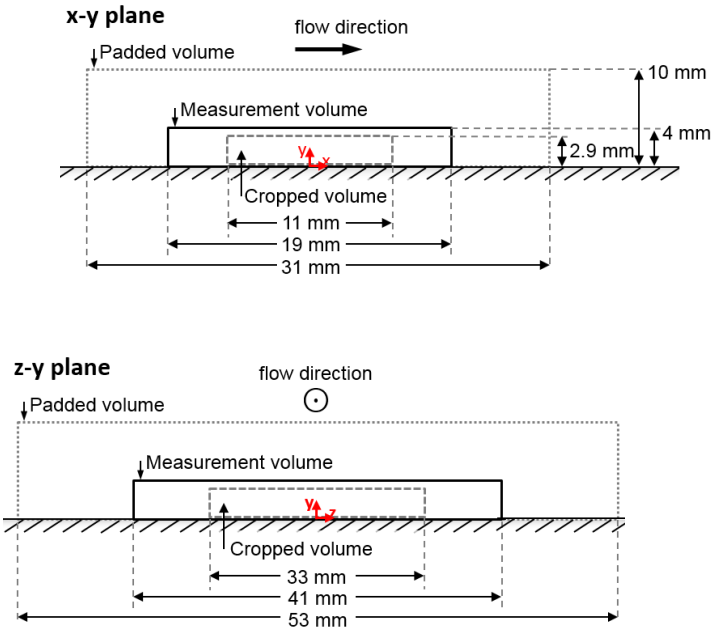

Fig. 4.5 Overview of the measurement, cropped and padded volumes (schematic not to scale).

For pressure evaluation in the cropped volume, mixed boundary conditions are employed for the Poisson equation for pressure. Neumann boundary conditions given by (4.12) are prescribed on all boundaries, except the top boundary ($y/\delta = 0.4$), where Dirichlet conditions are prescribed based on an extended version of the Bernoulli equation, corrected for an unsteady convective perturbation as proposed by de Kat and van Oudheusden (2012),

$$p'_{top} = -\frac{1}{2}\rho(\boldsymbol{u}' \cdot \boldsymbol{u}') = f_p. \quad (4.18)$$

4.6.2 Results

First the pressure from time-resolved PIV results are discussed to provide a benchmark for the proposed single-snapshot method (Section 4.2.1), after which the single-snapshot results (Section 4.2.2) are discussed.

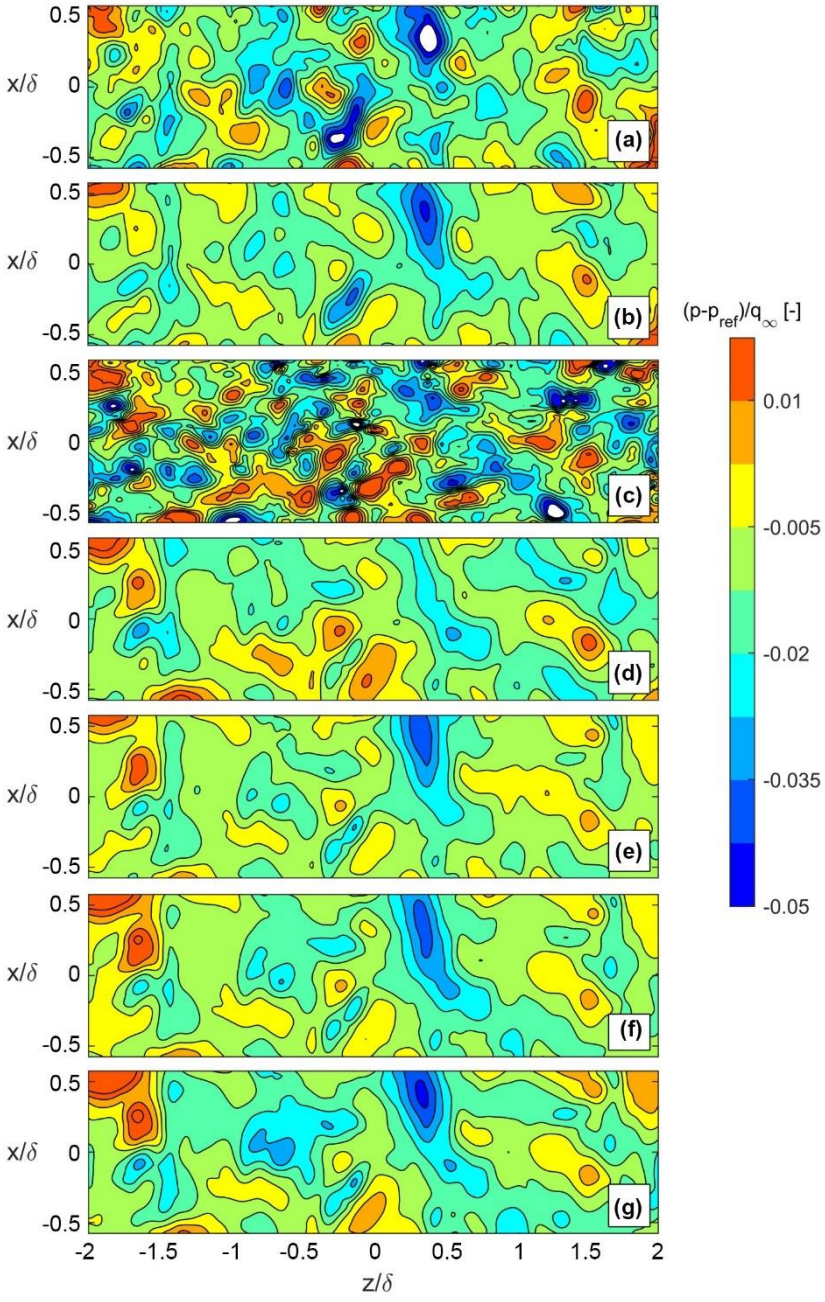

Fig. 4.6 Comparison of the instantaneous pressure field at t = 2.5 ms and y/δ = 0.2, calculated from, **a:** TR-PIV, M = 1, **b:** TR-PIV, M = 4, **c:** PIV, **d:** PIV+VIC and $\partial \boldsymbol{u}/\partial t$ = 0, **e-g:** PIV+VIC ($\partial \boldsymbol{u}/\partial t \neq 0$) with BC type 1-3.

Benchmark time-resolved results

A single instantaneous pressure field in the plane parallel to the wall at $y/\delta = 0.2$ evaluated using the time-resolved procedure with the three (M = 1) and nine (M = 4) snapshot stencil is plotted in respectively Fig. 4.6a and Fig. 4.6b. It is expected that the result with M = 1 is strongly affected by random errors in the velocity measurements, which can also be observed in Fig. 4.6a and b by comparison of the two results. In these figures the free stream pressure level p_{ref} has been subtracted from the fields.

For validation, the pressure fluctuations are compared to the simultaneous instantaneous microphone surface pressure measurements, where both the PIV and microphone results are band-pass filtered for 300 Hz < f < 3 kHz (analogous to Pröbsting et al, 2013). For computation of the cross-correlation coefficients, the microphone signal is sub-sampled after application of the band-pass filter to match the sampling frequency of the time-resolved tomographic PIV measurement.

Comparison to the microphone surface pressure measurement in the center of the measurement domain (Fig. 4.7, grey line) confirms low correlation to the reference microphone signal of the time-resolved pressure from PIV result using a small three-snapshot stencil (M = 1, blue line). The corresponding peak value of the correlation coefficient is only $R_{pp'} = 0.45$ (Tab. 4.3).

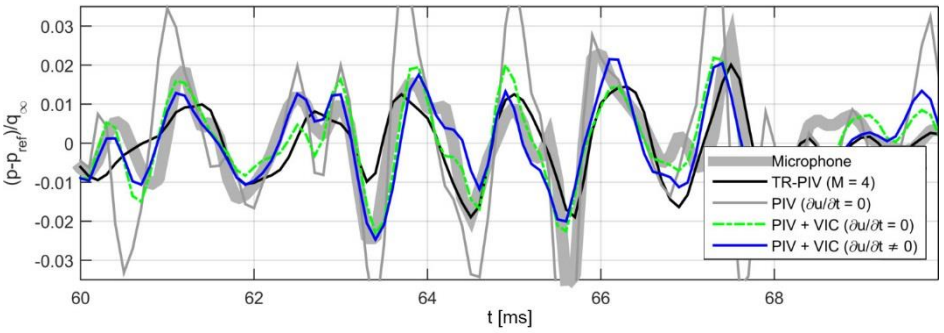

Fig. 4.7 Pressure fluctuation time-series obtained from TR-PIV, single-snapshot PIV and single-snapshot PIV+VIC (type 3 boundary conditions), in comparison to the reference microphone measurements at $x/\delta = z/\delta = 0$ (grey line, increased thickness for clarity); all results are band-pass filtered between 0.3-3 kHz.

This result is significantly improved when the larger stencil of M = 4 is considered. Similar to the results reported in Pröbsting et al. (2013), in the present study a correlation peak of $R_{pp',M4} = 0.65$ is found with this stencil.

Tab. 4.3 Correlation coefficient peak values and RMS pressure fluctuation levels obtained by the pressure-from-PIV techniques

Input	Case	Stencil size	D$\boldsymbol{u}$/Dt approximation	$R_{pp'}$	$\frac{p'_{rms}}{p'_{rms,ref}}$
TR-PIV	A	3 snapshots	Lagrangian, M=1	0.45	1.88
TR-PIV	B	9 snapshots	Lagrangian, M=4	0.65	1.00
PIV	C	1 snapshot	Eulerian, $\partial u/\partial t = 0$	0.45	2.55
PIV	D	1 snapshot	VIC, $\partial u/\partial t = 0$	0.62	1.31
PIV	E	1 snapshot	VIC, $\partial u/\partial t \neq 0$, BC = 1	0.59	0.88
PIV	F	1 snapshot	VIC, $\partial u/\partial t \neq 0$, BC = 2	0.59	0.95
PIV	G	1 snapshot	VIC, $\partial u/\partial t \neq 0$, BC = 3	0.61	1.11

Single-snapshot pressure results

First the single-snapshot pressure is calculated without the proposed procedure for approximation of $\partial\boldsymbol{u}/\partial t$. The flow regime is incompressible (Ma = 0.03) and the velocity field and $\partial\boldsymbol{u}/\partial t$ are expected to be divergence free. Consequently $\partial\boldsymbol{u}/\partial t$ drops out of the incompressible Poisson equation for pressure and hence it may be argued that it is not required for pressure evaluation. However, considering that (i) due to measurement errors velocity divergence is never exactly zero and (ii) $\partial\boldsymbol{u}/\partial t$ is needed for Neumann boundary conditions for the Poisson equation for pressure, this is not expected to give acceptable results. To assess this, the approach of entirely neglecting $\partial\boldsymbol{u}/\partial t$,

$$\left.\frac{D\boldsymbol{u}}{Dt}\right|_{\mathrm{PIV}} = (\boldsymbol{u}_m \cdot \nabla)\boldsymbol{u}_m, \tag{4.19}$$

is also included in the present study. This was attempted before by Imaichi and Ohmi (1983), who reported an increase in error levels and attributed these to neglecting the unsteady term. The present study also finds a low correlation coefficient peak of 0.46 and a significant overestimation of the peak pressure levels (Fig. 4.6c) in case $\partial\boldsymbol{u}/\partial t$ is

neglected and pressure is calculated directly using the material derivative approximated using (4.19).

The proposed PIV + VIC single-snapshot procedure is expected to improve upon this. The first part of the procedure regularizes the velocity field $\mathbf{u}_m$ through eqn. (4.3) to yield $\mathbf{u}_h$. The RMS difference between $\mathbf{u}_m$ and the $\mathbf{u}_h$ is 0.2 m/s at y/δ = 0.4, which is considered acceptable for a tomographic PIV experiment at a rather extreme measurement rate of 10 kHz. Still neglecting the unsteady term (i.e. setting $\partial \boldsymbol{u}/\partial t = 0$), this regularized field can be employed to approximate the velocity material derivative,

$$\left.\frac{D\boldsymbol{u}}{Dt}\right|_{\mathrm{VIC}\ \partial \mathrm{u}/\mathrm{dt}=0} = (\boldsymbol{u}_h \cdot \nabla)\boldsymbol{u}_h. \tag{4.20}$$

Solving pressure with this approximation of the material derivative on the full measurement volume results in a significantly improved correlation coefficient of 0.6. This approaches the correlation coefficient obtained by the benchmark time-resolved PIV result (Tab. 4.3). The instantaneous pressure field depicted in Fig. 4.7d also shows significant improvement over Fig. 4.6c. However, the RMS level of the pressure fluctuations, p'_{RMS}, is 31% larger than the benchmark result.

In the second step of the proposed procedure, $\partial \boldsymbol{u}/\partial t$ is approximated using VIC to allow for approximation of the full velocity material derivative from (4.6). The velocity material derivative is evaluated on the full domain using the VIC procedure outlined in Section 4.3. Subsequently, as it is expected that the approximation of $\partial \boldsymbol{u}/\partial t$ is less accurate close to the volume boundaries, for pressure evaluation the volume is cropped by the same amount as for the time-resolved procedure (Section 4.6.1). Three single-snapshot PIV + VIC cases are discussed, where for cases 1-3 respectively boundary conditions 1-3 (Section 4.4.2) are employed for the Poisson equation for $\partial \boldsymbol{u}/\partial t$ (eqn. 6) on all volume boundaries except at the wall, where the no-slip condition ($\partial \boldsymbol{u}/\partial t = 0$) is prescribed.

The instantaneous pressure fields approximated using the single-snapshot PIV + VIC procedure with boundary condition types 1 to 3 are

plotted in Fig. 4.6e-g respectively. All three approaches yield similar results, indicating a low sensitivity of the VIC procedure to variations in the $\partial\mathbf{u}/\partial t$ boundary condition approximation for the present flow case. In addition, minor improvement over the case where the unsteady term was neglected and $\mathbf{u}_h$ was used to solve the steady Poisson equation is visible (e.g. at $x/\delta \approx z/\delta \approx 0.5$ in Fig. 4.6). The correlation coefficient is however not improved further and remains around 0.6, in comparison to 0.65 for the time-resolved benchmark result (Tab. 4.3). On the other hand, the inclusion of the approximation of $\partial\boldsymbol{u}/\partial t$ allows for prediction of the RMS pressure fluctuations, with 10% difference with respect to the time-resolved result, whereas neglecting this term leads to 31% higher RMS pressure fluctuations (Tab. 4.3, last column). For completeness, it should be recalled that in section 4.3 it was anticipated that when $\partial\boldsymbol{\omega}/\partial t|_{h,Eul}$ is employed instead of $\partial\boldsymbol{\omega}/\partial t|_{h,VIC}$, a small reduction in quality of the pressure approximation is expected. This has been assessed for the present test case, and only a minor reduction in correlation coefficient was found; i.e. for case 3 boundary conditions, $R_{pp'}$ becomes 0.60 instead of 0.61.

To assess the correlation of the results in the frequency domain, the magnitude of the coherence of the time-resolved and single-snapshot results is calculated with respect to the microphone signal using Welch's overlapped segment averaging. The result is plotted in Fig. 4.8 (left figure) and shows that all results have the highest coherence at approximately 0.8-1 kHz and no coherence with the microphone signal for frequencies above 3 kHz, where it should be recalled that the results have been band-pass filtered between 300 Hz and 3 kHz. The time-resolved result with M = 4 shows the expected significant improvement in coherence with respect to M = 1, with a peak of 0.77 around 900Hz. Also, the single-snapshot result using VIC improves upon the M = 1 time-resolved result, showing similar coherence as the time-resolved result using the larger nine-snapshot stencil. The peak coherence around 800 Hz is approximately 10% smaller than the benchmark M = 4 time-resolved result, however at higher frequency the VIC result follows the trend of the benchmark result.

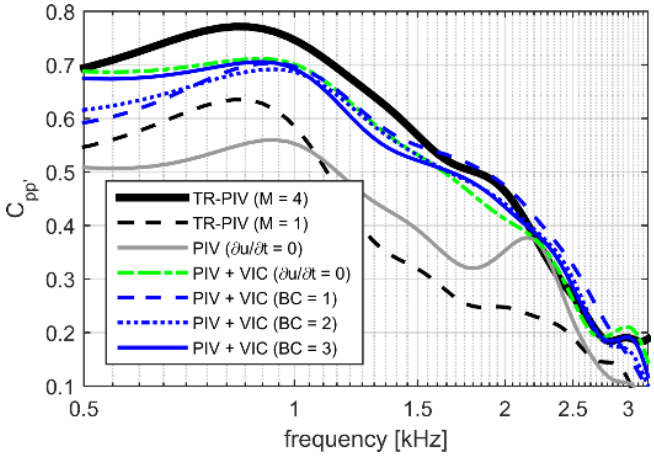

Fig. 4.8 Coherence of the cross spectrum of the PIV results with the microphone measurements.

The higher correlation achieved by the single-snapshot procedure in comparison to the M = 1 time-resolved procedure is especially relevant for dual-PIV systems (Liu and Katz 2006; Lynch and Scarano 2014), where the limited number of exposures does not allow to regularize the results using a large time-stencil. However, considering that the present study focuses on single-snapshot pressure evaluation, no further speculation is made here that the time-resolved result with M = 1 may be improved when a larger time-separation between the measurements is chosen to reduce the random error component, as discussed in studies by amongst others Jensen and Pedersen (2004) and Perret et al. (2006).

To assess the dependence of the method to measurement noise and spatial resolution, here an increase of measurement noise is simulated by adding normally distributed random errors to the velocity vectors and by sub-sampling the velocity fields. Subsequently the pressure is evaluated as discussed above and the correlation coefficient of the pressure time-series with respect to the microphone measurements is calculated. It is expected that the established time-resolved pressure-from-PIV procedure is less sensitive to these error sources, as multiple PIV velocity snapshots are available for pressure evaluation. Recent literature has shown that the use of multiple snapshots from time-resolved analysis is an effective

approach to reduce the effect of measurement errors (e.g. FTEE, Jeon et al. 2014; FTC, Lynch and Scarano 2013).

First, the effect of random noise is considered. Fig. 4.9-left shows the resulting correlation coefficients with respect to the microphone measurements varying the standard deviations of the numerically simulated random errors. The time-resolved procedure is practically insensitive to the random errors, which results from the use of nine consecutive snapshots for pressure evaluation through the Least-Squares procedure that effectively cancels out the effect of random errors. For the single-snapshot procedure, a gradual reduction of correlation coefficient is observed by increasing the measurement noise. It should be remarked type 3 boundary conditions have been used for the results plotted. For the other boundary condition types, the same behavior is observed. A correlation coefficient of approximately 0.5 is retrieved when the error is increased towards 1 m/s, which corresponds to the order of the turbulent velocity fluctuations close to the microphone location.

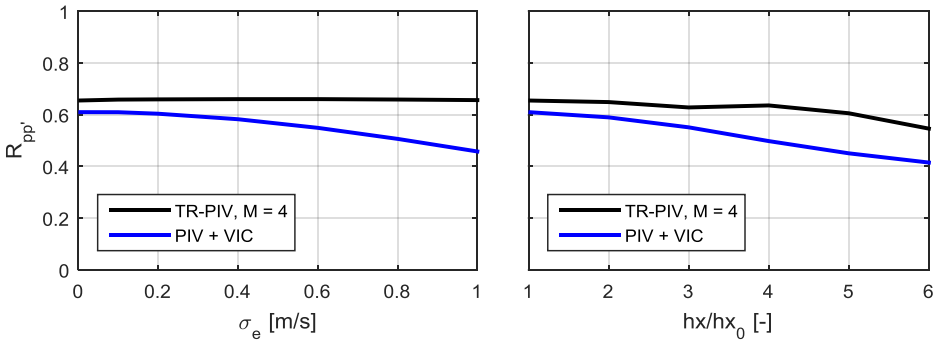

Fig. 4.9 Measurement sensitivity to measurement noise and spatial resolution. Cross-correlation coefficient with random errors (left) and grid point spacing (right).

The effect of spatial resolution is considered by evaluating the velocity vectors from a coarser grid. Figure 4-right shows the cross-correlation coefficient when the grid point spacing is increased from hx_0 in the original data to hx. Both, the time-resolved and the single-snapshot methods are sensitive to the spatial resolution. The time-resolved approach still exhibits a plateau up to a fourfold decrease of resolution

and a roll-off after that point. Instead the single-snapshot technique appears to be more sensitive to the decrease of resolution: a small plateau is observed up to a twofold decrease of resolution and then a more rapid decrease is observed.

4.7 Conclusions

A method is proposed to approximate the instantaneous flow pressure field from a single instantaneous tomographic PIV velocity snapshot using the vortex-in-cell (VIC) technique, and is applied to a flat-plate turbulent boundary layer. By solving the incompressible vorticity transport equation on the measurement volume, the spatial information available from the measurement is leveraged to approximate the temporal velocity derivative. Pressure is subsequently approximated by solution of the Poisson equation for pressure.

The experimental validation compared the correlation coefficient of instantaneous pressure obtained by both the single-snapshot procedure and a benchmark pressure from PIV procedure based on time-resolved data, with respect to simultaneous measurement with a surface pressure transducer. The results show that the instantaneous pressure field in a turbulent boundary layer can be evaluated from single-snapshot PIV, yielding very comparable results to those obtained with time-resolved measurement data acquired at 10 kHz and a stencil of nine consecutive measurements. When a smaller stencil of three consecutive measurements is employed for the time-resolved pressure evaluation, the single-snapshot VIC procedure even outperforms the time-resolved approach, giving a higher cross-correlation with the microphone signal.

The single-snapshot procedure requires a model for the flow acceleration to be used as boundary conditions on the flow governing equations and in the experimental assessment three such models were assessed: convective, padding and homogeneous boundary conditions, which under the present conditions all yielded similar instantaneous pressure fields. The experimental assessment considered a solid profile along one domain boundary. If the tomographic-PIV experiment experiences solid interfaces within the measurement volume, the Poisson

solver needs to be adapted accordingly to handle such non-rectangular computational domains.

In the experimental validation, the method yields results corresponding well to those obtained by time-resolved PIV with a nine-snapshot stencil. The advantage of the proposed single-snapshot PIV+VIC procedure is that it does not rely on the acquisition of time-resolved velocity data. Use of the method should be cautioned when the contributions to fluctuating pressure from outside the measurement volume are significant. In the turbulent boundary layer considered here, the proposed method demonstrates that PIV camera and laser hardware requirements can be alleviated, which is relevant for the investigation of high-speed flows where pressure-from-time-resolved-PIV becomes prohibitive.

Chapter 5
Dense velocity interpolation using VIC+

This work has been published in Schneiders and Scarano (2016) Exp. Fluids 57:139

Volumetric Lagrangian particle tracking has proven to be able to provide accurate particle velocity and acceleration measurements, making use of a measurement setup similar to time-resolved tomographic PIV and at comparable particle image densities. Chapter 2 has introduced the potential spatial resolution benefits of the particle tracking approach, but it was also discussed that even when using such particle tracking approaches the spatial resolution remains limited.

As outlined in Sec. 3.2 by use of an analogy, constitutive laws could potentially be coupled with the particle tracking measurements to increase instantaneous spatial resolution of the resulting flow field. This chapter introduces the VIC+ technique that reconstructs the instantaneous velocity field from sparse and scattered Lagrangian particle tracking measurements. It uses both the instantaneous particle velocity and acceleration, which are coupled using the vorticity transport equation. Thereby, the VIC+ technique uses an increased interpolation data ensemble in comparison to standard interpolation techniques, promising an increase in spatial resolution. Before the method is explained and assessed in detail, the next section provides first an overview of such established interpolation techniques.

5.1 Background

The velocity measured with particle tracking techniques is returned at scattered locations corresponding to the instantaneous particle positions. Although some data post-processing operations can be performed on scattered data (Neeteson and Rival 2015), it is common to transport the information onto a Cartesian uniform grid before performing more

general data post-processing and visualization operations. A straightforward approach is to apply tri-linear interpolation (Fig. 5.1, left) or to average the velocity vectors in an interrogation window analogously to PIV (Fig. 5.1, middle).

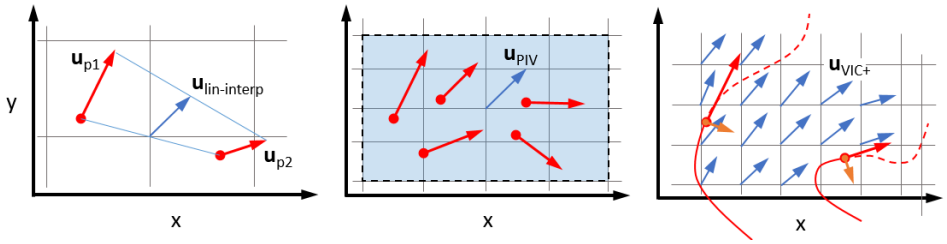

Fig. 5.1 Velocity reconstruction (blue vectors) from PTV measurements (red vectors). Linear interpolation between two PTV velocity measurements (left), PIV interrogation window (shaded blue) approach (middle) and VIC+ interpolation between two PTV particle trajectories (right, the orange vector is $D\boldsymbol{u}/Dt$). The grey lines indicate the reconstruction grid.

Tri-linear interpolation does guarantee continuity of the velocity field, but it yields a discontinuous (piecewise constant) distribution of the velocity gradient field, which prevents an accurate estimation of the vorticity field. Several interpolation methods have appeared in the literature that deal with the problem of reconstructing scattered PTV data onto a Cartesian grid with the constraint of smoothness. The adaptive Gaussian windowing technique (AGW, introduced by Agüí and Jiménez 1987) has been widely used and recently radial basis function regression (RBF, amongst others Casa and Krueger, 2013) have been proposed. The choice of a length-scale is necessary for both AGW and RBF. The length scale should be larger than the inter-particle distance such to suppress measurement noise, at the cost of low-pass filtering the result. Zhong et al. (1991) and Vedula and Adrian (2005) proposed to impose the velocity field to be divergence free (viz. incompressibility constraint). Furthermore, very recently Gesemann et al. (2016) presented the 'FlowFit' method. This method makes a B-splines reconstruction of the velocity field that minimizes a cost function, which can include, similar to the method proposed in this work, a weighted sum of differences between

measured particle velocity and acceleration, and other differences such as nonzero divergences of velocity. The weights are set based on the flow properties (e.g. incompressibility) and measurement quality (e.g. measurement uncertainty and seeding concentration). It should be remarked that techniques invoking the incompressibility constraint are applicable to volumetric measurements only, as from planar PIV no information on the out-of-plane components of the velocity gradient is available and the in-plane velocity field is rarely divergence free in applications involving turbulent flow fields.

These techniques have not yet dealt specifically with increasing spatial resolution of the instantaneous velocity measurements, in the cases where the spatial resolution is limited by tracer particle seeding concentration, as discussed in the first paragraph. As information in the spatial domain has proven to allow for an increase in temporal resolution, the reversed principle of *pouring time into space* potentially offers an increase in spatial resolution. In the present study, it is investigated whether next to the instantaneous velocity measured by time-resolved tomographic PTV, also the velocity material derivative can be used to increase spatial resolution of the reconstructed velocity field (Fig. 5.1-right). The velocity material derivative is obtained by tomographic PTV from the second temporal derivative of a particle trajectory. The spatial and temporal information is linked through the flow governing equations, i.e. Navier-Stokes. The relevant applications mentioned above consider flow cases at speeds well below Ma = 0.3 and thus the incompressible Navier-Stokes equations can be used. These however still include pressure, which is not measurable by PIV. The pressure term is avoided in the present study by using the vorticity transport equation and the vortex-in-cell framework, as applied earlier to tomographic PIV measurements by Schneiders et al. (2014) and Schneiders et al. (2016a).

5.2 The VIC+ method

Consider a Lagrangian particle tracking experiment. The particle trajectories are fitted with an appropriate function – e.g. a polynomial or spline. The analytical time-derivatives yield from each particle trajectory,

γ, at time-instant t_i and location $\boldsymbol{x}_\gamma(t_i)$ a measurement of velocity, $\boldsymbol{u}_m$, and a measurement of the velocity material derivative, $D\boldsymbol{u}_m/Dt$. This is the input for VIC+. Subsequently, VIC+ attempts to find the flow field that fits the measurement data best, while satisfying the incompressible continuity and vorticity transport equation. These governing equations of the flow field are introduced in Sec. 5.2.1. The actual VIC+ optimization procedure is subsequently discussed in Sec. 5.2.2.

5.2.1 Coupling in the velocity-vorticity formulation

Consider a computational grid with mesh spacing h. Vorticity, $\boldsymbol{\omega}_h$, is defined on the grid using radial basis functions. Details on selection of h and the radial basis function discretization are given in Sec. 5.2.3. Vorticity is related to velocity, $\boldsymbol{u}_h$, through a Poisson equation (Christiansen 1973; Schneiders et al. 2014):

$$\nabla^2 \boldsymbol{u}_h = -\nabla \times \boldsymbol{\omega}_h, \tag{5.1}$$

with boundary conditions on velocity. Second-order central differences are used for evaluation of all the spatial derivatives in the present work, except at the volume boundaries where first-order single-sided differences are used. The velocity material derivative, $D\boldsymbol{u}_h/Dt$, is defined on the grid by:

$$\frac{D\boldsymbol{u}_h}{Dt} = \frac{\partial \boldsymbol{u}_h}{\partial t} + (\boldsymbol{u}_h \cdot \nabla)\boldsymbol{u}_h. \tag{5.2}$$

The temporal velocity derivative in eq. (5.2) is calculated from the temporal vorticity derivative by solution of a Poisson equation (Schneiders et al. 2016),

$$\nabla^2 \frac{\partial \boldsymbol{u}_h}{\partial t} = -\nabla \times \frac{\partial \boldsymbol{\omega}_h}{\partial t} \tag{5.3}$$

with boundary conditions on the temporal velocity derivative. The temporal vorticity derivative in turn is calculated from the vorticity transport equation,

(5.4) $$\frac{\partial \boldsymbol{\omega}_h}{\partial t} = (\boldsymbol{\omega}_h \cdot \nabla)\boldsymbol{u}_h - (\boldsymbol{u}_h \cdot \nabla)\boldsymbol{\omega}_h.$$

5.2.2 Optimization procedure

The velocity and velocity material derivative fields can be calculated at a single time-instant from equations (5.1) and (5.2) if the radial basis coefficient weights for vorticity and boundary conditions on velocity and its temporal derivative are known on the computational grid. Depending on the flow case, one or more boundary conditions could be known *a-priori* from a no-slip condition or a free stream condition. The remaining vorticity values on the grid and boundary conditions are however unknown. Consider a vector, $\boldsymbol{\xi}$, that collects the unknown radial basis function weights for vorticity and boundary conditions on velocity and its temporal derivative,

(5.5) $$\boldsymbol{\xi} = \{\boldsymbol{\xi}_{\boldsymbol{\omega}}, \beta_1 \boldsymbol{\xi}_{BC,\boldsymbol{u}}, \beta_2 \boldsymbol{\xi}_{BC,\partial \boldsymbol{u}}\},$$

where coefficients β_1 and β_2 are scaling parameters (Sec. 5.2.3). The vector $\boldsymbol{\xi}$ contains the optimization variables for the VIC+ optimization procedure.

The goal of the VIC+ optimization procedure is to find the optimization variables, $\boldsymbol{\xi}$, that minimize a cost function, J, under the constraint that the motion equations in velocity-vorticity form (Sec. 5.2.1) are respected at a single measurement time-instant. The cost function is defined by eq. (5.6),

(5.6) $$J = J_{\boldsymbol{u}} + \alpha^2 J_{D\boldsymbol{u}},$$

where α is a weighting coefficient (Sec. 5.2.1), J_u is given by eq. (5.7) and J_{Du} by eq. (5.8),

(5.7) $$J_{\boldsymbol{u}} = \sum_p \left\| \boldsymbol{u}_h(\boldsymbol{x}_p) - \boldsymbol{u}_m(\boldsymbol{x}_p) \right\|^2,$$

(5.8) $$J_{D\boldsymbol{u}} = \sum_p \left\| \frac{D\boldsymbol{u}_h}{Dt}(\boldsymbol{x}_p) - \frac{D\boldsymbol{u}_m}{Dt}(\boldsymbol{x}_p) \right\|^2,$$

where $\boldsymbol{u}_h$ and $D\boldsymbol{u}_h/Dt$ are calculated from equations (5.1) and (5.2) and are evaluated at the particle locations, $\boldsymbol{x}_p$, by linear interpolation from the

computational grid. In summary, the cost function penalizes the difference between the PTV measurements and the velocity and material derivative at a single measurement time-instant calculated from the optimization variables. Because the cost function for the optimization only considers the instantaneous velocity and its material derivative, the optimization problem does not require time-integration of the vorticity transport equation.

The optimization problem is solved iteratively using the limited-memory Broyden–Fletcher–Goldfarb–Shanno method (L-BFGS, Liu and Nocedal 1989), which is a commonly used method for large-scale optimization problems. The L-BFGS method is a quasi-Newton method technique that approximates the standard BFGS method using a limited amount of memory. It approximates the typically dense Hessian matrix to reduce the cost of storing and manipulating it. For details on the Hessian approximation and the step size determination, the reader is referred to Liu and Nocedal (1989).

At each iteration, the method requires the gradient of the cost function with respect to the optimization variables, $\partial J/\partial \boldsymbol{\xi}$. This gradient could be approximated using finite differences, requiring N evaluations of the cost function, where N is the number of optimization variables. Following recent literature (Gronskis et al. 2013; Yang et al. 2015; Yegavian et al. 2015; Lemke and Sesterhenn 2016; amongst others), an alternative and more cost-efficient method to calculate the gradient is provided by the adjoint approach. This approach gives the exact gradient, but more importantly the computational cost of the adjoint approach is approximately equal to only one evaluation of the cost function.

Therefore, also within VIC+ the adjoint approach is used for evaluation of the gradient $\partial J/\partial \boldsymbol{\xi}$. The steps to calculate this gradient using the adjoint approach are given in Appendix A. It should be remarked that the adjoint procedure within VIC+ is relatively simple in comparison to the adjoint procedures in the abovementioned literature, because many calculation steps within VIC+ are linear operations and because the procedure does not involve time-integration. Only the state at a single time-instant needs to be kept in memory for evaluation of the adjoint

equations and therefore the method does not suffer from the typically large memory requirements for adjoint-based optimization techniques, which led to the proposal of for example a storage/recomputation strategy by Gronskis et al. (2013).

Appendix B contains a pseudo code of the VIC+ method and Fig. 5.2 schematically summarizes the method. The PTV measurements (lines 5-7 in the pseudo code; green box in Fig. 5.2) are used to obtain an initial estimate of the velocity field on the grid (line 10; grey box in Fig. 5.2), using for example the adaptive Gaussian windowing technique (AGW, Agüí and Jiménez 1987).

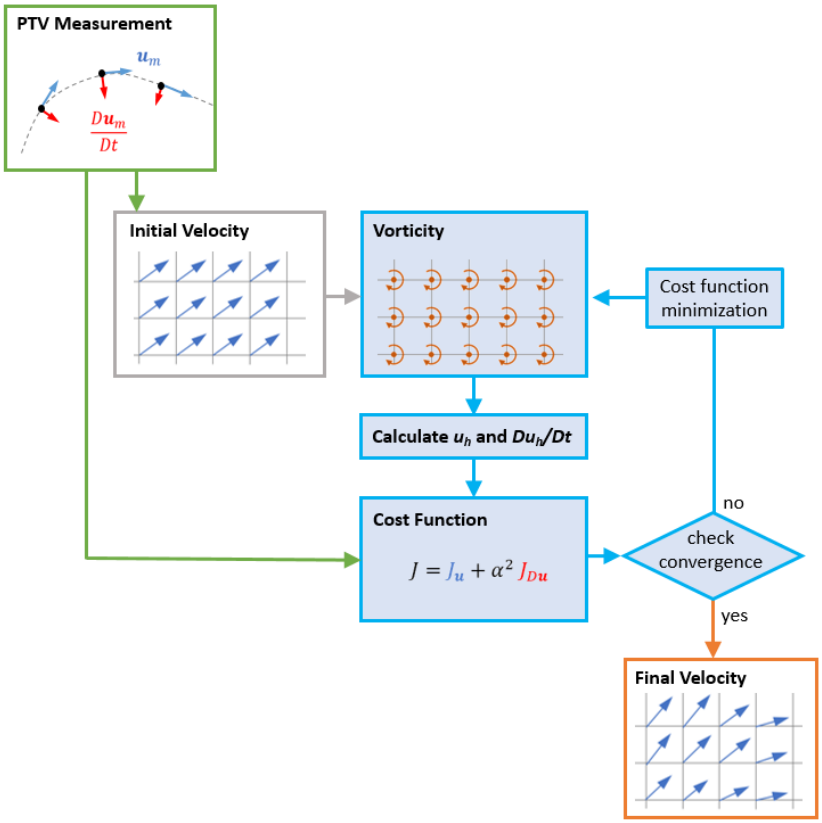

Fig. 5.2 VIC+ reconstruction framework. From the PTV input (left, green box) an initial velocity estimate is made (grey box), which is input into the VIC+ iterative procedure (blue loop) to find the optimization variables that yield a velocity and velocity material derivative of minimum discrepancy with the PTV measurements (orange box).

This initial condition provides the initial estimate of the degrees of freedom vector, $\boldsymbol{\xi}$ (lines 15-18). The optimization procedure is illustrated by the blue loop in Fig. 5.2 and spans lines 22-69 in the pseudo code. It starts by calculation of velocity and its material derivative on the computational grid from the optimization variables (lines 24-29) and subsequently the interpolation of these quantities to the tracer particle locations (lines 32-33). The cost function, eq. (5.6), is calculated at lines 36-38, after which the gradient of the cost function with respect to the degrees of freedom is calculated using the adjoint of the code (lines 41-53). The degrees of freedom are then updated using the step size and direction found by the L-BFGS algorithm (lines 59-61). When the system is converged (Sec. 5.2.3; lines 64-66 in the pseudo code) the optimization loop is stopped and the output velocity field is calculated (lines 72-73).

The procedure is christened as 'VIC+.' It is inspired by time-supersampling using VIC simulation (Schneiders et al. 2014) and the 'plus' symbol refers to the simultaneous use of the particle velocity and its time-derivative.

5.2.3 Problem closure

The VIC+ method introduces multiple parameters whose values need to be determined before performing the optimization. In recent literature on methods with similar weighting parameters, optimal setting is either left out for future research (e.g. Papadakis and Memin, 2008) or manually chosen on a case-by-case basis (Gronskis et al. 2013; Gregson et al. 2014; amongst others). In an optimization framework similar to VIC+, the 'FlowFit' method for interpolation of scattered data to an Eulerian grid (Gesemann et al. 2016) makes use of weighting parameters to penalize differences between the reconstruction and the velocity and material derivative measurements, and other differences such as nonzero curvature and divergence depending on the flow properties (e.g. incompressibility and measurement uncertainty). However, no direct relations are provided to obtain the values of these weights. To achieve a general treatment of experimental data and avoid case-dependent, or even user-dependent parameter selection by tuning, the present study

includes a fixed approach to closure for the mentioned parameters. These parameters are discussed separately in the sections below.

Mesh spacing and radial basis functions

The VIC+ method uses finite differences for evaluation of derivatives on the computational grid, requiring a grid-spacing that makes truncation errors negligible. The grid node spacing, h, is set based on the particle concentration, C, using eq. (5.9).

$$h = \frac{1}{4} C^{-1/3} \tag{5.9}$$

This equation implies that 64 grid nodes are employed per tracer particle. For tomographic PIV, the amount of grid nodes typically also exceeds the amount of tracer particles, as the window overlap factor is often set to 75% to avoid unnecessary truncation when evaluating spatial derivatives (Scarano and Poelma 2009, Togkoz et al. 2012). Also, considering an optimization technique similar to VIC+, the recent study of Schanz et al. (2016) reports that in the 'FlowFit' interpolation method typically 5 to 20 B-spline cells are chosen per tracer particle.

For the VIC+ method, at each grid node Gaussian radial basis functions, $\phi(r)$, are employed. The free parameter, σ, which defines the width of the Gaussian radial basis functions, is chosen slightly larger than the grid node spacing ($\sigma = 1.1h$) and the resulting radial basis functions are defined by eq. (5.10).

$$\phi(r) = e^{-\frac{r^2}{2\sigma^2}} = e^{-\frac{r^2}{2.4h^2}}. \tag{5.10}$$

Vorticity is calculated on the grid through eq. (5.11),

$$\boldsymbol{\omega}_h = \sum w_i \phi(\|\boldsymbol{x} - \boldsymbol{x}_i\|), \tag{5.11}$$

where w_i are the radial basis function weights. The boundary conditions of velocity and its temporal derivative are defined analogously. On average, 0.7 particles are present within a sphere with a radius of 2σ, that is centered around a grid node. Because each particle provides measurements of both velocity and material derivative, each radial basis

function includes on average 1.4 measurements (of three components) within such a sphere. In addition, the system is constrained by the motion equations in velocity-vorticity formulation (Sec. 5.2.1). As discussed in Sec. 5.2.2, the cost function of the non-linear system of equation is iteratively reduced using a gradient based quasi-Newton method (the L-BFGS method), where the optimization variables are the radial basis function weights for vorticity and the boundary conditions on velocity and the velocity temporal derivative.

Scaling of the optimization variables

The optimization variables ($\boldsymbol{\xi}_\omega$, $\boldsymbol{\xi}_{BC,u}$ and $\boldsymbol{\xi}_{BC,\partial u}$) have different units, requiring weighting or non-dimensionalization of the optimization variables. A non-dimensional vector with the optimization variables, $\boldsymbol{\xi}^*$, can be defined by non-dimensionalization of the optimization variables with their standard deviation,

$$\boldsymbol{\xi}^* = \{\frac{1}{\sigma_\omega}\boldsymbol{\xi}_\omega, \frac{1}{\sigma_{BC,u}}\boldsymbol{\xi}_{BC,u}, \frac{1}{\sigma_{BC,\partial u}}\boldsymbol{\xi}_{BC,\partial u}\}, \tag{5.12}$$

where σ_ω, $\sigma_{BC,u}$ and $\sigma_{BC,\partial u}$ are the standard deviation of $\boldsymbol{\xi}_\omega$, $\boldsymbol{\xi}_{BC,u}$ and $\boldsymbol{\xi}_{BC,\partial u}$ as defined by equations (5.13) to (5.15),

$$\sigma_\omega = \sqrt{\frac{1}{n_\omega}\sum\left(\boldsymbol{\xi}_{\boldsymbol{\omega}} - \bar{\boldsymbol{\xi}}_{\boldsymbol{\omega}}\right)^2}, \tag{5.13}$$

$$\sigma_{BC,u} = \sqrt{\frac{1}{n_{BC,u}}\sum\left(\boldsymbol{\xi}_{BC,u} - \bar{\boldsymbol{\xi}}_{BC,u}\right)^2}, \tag{5.14}$$

$$\sigma_{BC,\partial u} = \sqrt{\frac{1}{n_{BC,\partial u}}\sum\left(\boldsymbol{\xi}_{BC,\partial u} - \bar{\boldsymbol{\xi}}_{BC,\partial u}\right)^2}, \tag{5.15}$$

with n_ω the number of grids points on which vorticity is an optimization variable and $n_{BC,u}$ and $n_{BC,\partial u}$ the number of boundary points on which velocity and its temporal derivative are optimization variables.

Multiplication of $\boldsymbol{\xi}^*$ by σ_ω gives the vector of optimization variables, $\boldsymbol{\xi}$, used for VIC+,

(5.16) $$\boldsymbol{\xi} = \sigma_\omega \boldsymbol{\xi}^* = \left\{\boldsymbol{\xi}_\omega, \frac{\sigma_\omega}{\sigma_{BC,u}}\boldsymbol{\xi}_{BC,u}, \frac{\sigma_\omega}{\sigma_{BC,\partial u}}\boldsymbol{\xi}_{BC,\partial u}\right\} = \{\boldsymbol{\xi}_\omega, \beta_1\boldsymbol{\xi}_{BC,u}, \beta_2\boldsymbol{\xi}_{BC,\partial u}\},$$

where the weighting coefficients β_1 and β_2 are defined by equations (5.17) and (5.18).

(5.17) $$\beta_1 = \frac{\sigma_\omega}{\sigma_{BC,u}}$$

(5.18) $$\beta_2 = \frac{\sigma_\omega}{\sigma_{BC,\partial u}}$$

Weighting coefficient α

A non-dimensional cost function, J^*, can be defined by non-dimensionalization of J_u and J_{Du} by the variance of the PTV velocity and velocity material derivative measurements,

(5.19) $$J^* = \frac{1}{\sigma_u^2}J_u + \frac{1}{\sigma_{Du}^2}J_{Du},$$

where σ_u and σ_{Du} are the standard deviation of the PTV velocity and velocity material derivative measurements,

(5.20) $$\sigma_u = \sqrt{\frac{1}{n_{PTV}}\sum_{p=1}^{n_{PTV}}\left\|\boldsymbol{u}_p - \bar{\boldsymbol{u}}_p\right\|^2},$$

(5.21) $$\sigma_{Du} = \sqrt{\frac{1}{n_{PTV}}\sum_{p=1}^{n_{PTV}}\left\|\frac{D\boldsymbol{u}_p}{Dt} - \overline{\frac{D\boldsymbol{u}_p}{Dt}}\right\|^2},$$

with n_{PTV} the number of tracer particles (i.e. the number of PTV measurements). Multiplication of the non-dimensional cost function J^* by σ_u^2 gives the cost function used in the present study,

(5.22) $$J = \sigma_u^2 J^* = J_u + \frac{\sigma_u^2}{\sigma_{Du}^2}J_{Du} = J_u + \alpha^2 J_{Du},$$

where the weighting coefficient α is defined by,

(5.23) $$\alpha = \sigma_u/\sigma_{Du}.$$

Convergence criterion

A convergence criterion similar to, amongst others, Lemke and Sesterhenn (2016) is used, where an iterative procedure is stopped (converged) when the change in the cost function J becomes small. Here the convergence level is selected at 10^{-4} % of the initial value of J.

5.3 Spatial response of the VIC+ interpolation technique[1]

The spatial response of the proposed VIC+ interpolation technique is assessed following the approach by Scarano and Riethmuller (2000) and Schrijer and Scarano (2008). In these manuscripts, the modulation of PIV cross-correlation techniques using analytical sine and cosine flow fields with a predefined wavelength.

Because the VIC+ method leverages particle acceleration measurements for the dense interpolation of velocity to a grid, the present assessment considers a velocity field where the velocity material derivative is non-zero and non-homogeneous:

$$\boldsymbol{u} = \begin{cases} u = A \sin\frac{2\pi x}{\Lambda} \sin\frac{2\pi y}{\Lambda} \\ v = A \cos\frac{2\pi x}{\Lambda} \cos\frac{2\pi y}{\Lambda} \\ w = 0 \end{cases} \tag{5.24}$$

Tomographic PIV and PTV measurements are simulated in a volume of $L_x \times L_y \times L_z = 500 \times 500 \times 500$ voxels, with Gaussian-shaped tracer particles of 2 voxels diameter and a uniform peak intensity value. The tracer particle concentration is $C = 5 \cdot 10^{-5}$ particles per voxel (ppv) and the wavelength of the waves, Λ, is varied between 20 and 500 voxels. No particle reconstruction errors are simulated for the reconstructed volumes and the PTV measurements to assess the ideal response for both cases. The maximum tracer particle displacement is equal to $A = 2$ voxels.

For tomographic PIV analysis, a multi-pass volume deformation algorithm is used with 8 passes. After each pass, outliers are removed using universal outlier detection (Westerweel and Scarano 2005) and the

[1] The contents of this section are adapted from Schneiders et al. (2017)

vector field is smoothed using Gaussian smoothing with a 3 × 3 × 3 vector kernel. No smoothing is applied on the final pass. The interrogation volume (IV) size is chosen such that there are on average 5 particles present in a volume and 75% overlap is used. Five tracer particles are considered the minimum number for reliable cross-correlation peak detection. Therefore, the present interrogation volume size represents the best possible spatial resolution for tomographic PIV. This yields a volume size of 48 × 48 × 48 voxels and a vector spacing of 12 voxels.

For VIC+ analysis the grid spacing, h, is determined using eq. (5.9). This yields a vector spacing of 7 voxels. In addition to VIC+ and tomographic PIV, the data is also analyzed using VIC+ with no account for D$\boldsymbol{u}$/Dt. This is done to establish the contribution of the additional material derivative term in improving the velocity reconstruction. Because VIC+ without using D$\boldsymbol{u}$/Dt is essentially a divergence free interpolator, the corresponding results are labelled as 'Div Free.'

Similar to Scarano and Riethmuller (2000) and Schrijer and Scarano (2008), the amplitude modulation is calculated for the considered range of Λ. The amplitude modulation u/u_0 is defined as the ratio of peak streamwise velocity in the measurement volume in comparison to the reference provided by eq. (5.24). The peak velocity is evaluated from the tomographic PIV and VIC+ measurements grids through second order polynomial interpolation. Recent literature reports the spatial response of iterative cross-correlation with window deformation in the abovementioned flow case improves slightly upon the squared sinc function (Schrijer and Scarano 2008). This is confirmed in Fig. 5.3, which shows the amplitude modulation of cross-correlation (blue line) and the squared sinc function (black line) plotted against the normalized interrogation volume size $l^* = \mathrm{IV}/\Lambda$. The -3 dB cut-off wavelength for PIV equals $l_c^* = 0.53$ ($r_c^* = 0.17$) and for the sinc function $l_c^* = 0.44$ ($r_c^* = 0.14$), which corresponds well to the values reported by Schrijer and Scarano (2008). Because VIC+ does not use interrogation volumes, the normalized minimum inter-particle distance $r^* = \bar{r}/\Lambda$ is a more appropriate scaling for comparison of the results and is therefore used on the bottom horizontal axis.

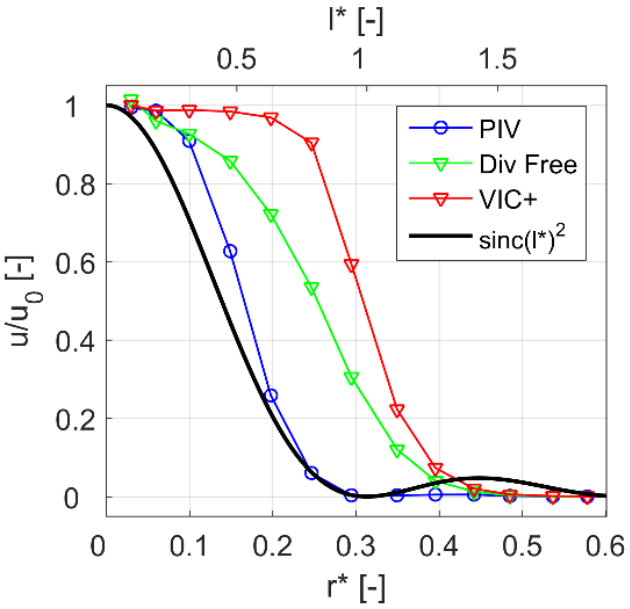

Fig. 5.3 Modulation flow fields by cross-correlation (blue line) and VIC+ (red line), as a function of wavelength. For comparison, also the squared sinc function is plotted (black line).

The VIC+ technique (red line) shows a practically flat response up to r^* = 0.2 and a -3 dB cut-off wavelength of r_c^* = 0.31, which is approximately twice the cut-off wavelength of PIV, as summarized in Tab. 5.1. Without inclusion of D***u***/D*t*, increased amplitude is found (green line in Fig. 5.3). The -3 dB cut-off wavelength at r_c^* = 0.25 consequently is also lower than VIC+ is used with D***u***/D*t* penalization.

Tab. 5.1 Normalized window size l^* and normalized inter-particle distance r^* at the -3 dB cut-off point for the squared sinc function, PIV cross-correlation analysis and VIC+.

	sinc²	PIV	DF	VIC+
l_c^*	0.44	0.53	0.81	0.98
r_c^*	0.14	0.17	0.25	0.31

For illustration of the results, Fig. 14 shows the streamwise velocity component at the center z-plane for a normalized average minimum

inter-particle separation of $r^* = 0.2$. The reference flow field (top-left figure) shows the expected pattern of sine waves resulting from eq. (5.24). Using cross-correlation analysis yields a significantly modulated flow field. As expected from the above results, a divergence free interpolation (bottom-left) and VIC+ (bottom-right) improve upon this result and part the sine-wave lattice visible. Note that the fidelity appears locally higher in part of the domain, which is ascribed to the randomly distributed instantaneous tracer particle distribution being locally denser.

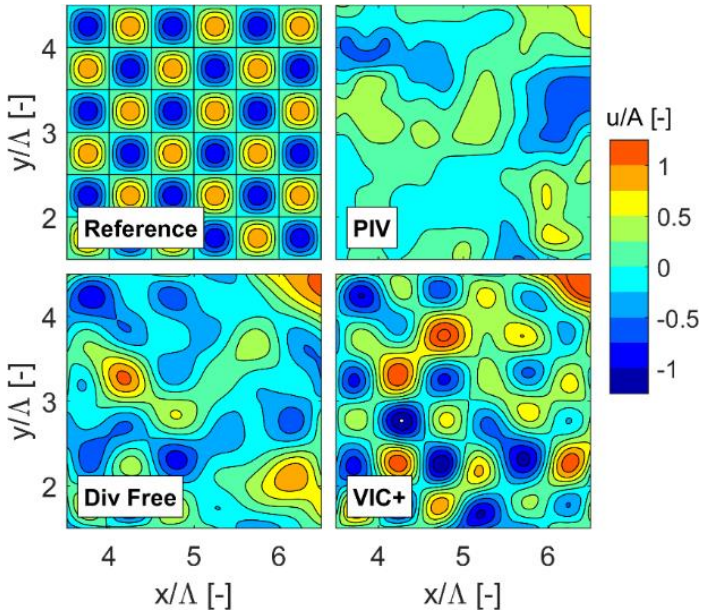

Fig. 5.4 Streamwise velocity contour plot at the center z-plane at a normalized particle separation of $r^* = 0.2$.

It should be remarked that the VIC+ results are expected to depend upon the grid spacing, because coarser grid spacing corresponds to less degrees of freedom for the optimization to reconstruct the flow field and introduces truncation effects in the finite differences calculations. To investigate this, the study is repeated for a range of grid spacings. The resulting amplitude modulation is plotted in Fig. 5.5 for a range of wavelengths ($r^* = \bar{r}/\Lambda$, vertical axis), each processed over a range of grid spacings ($h^* = h/\bar{r}$, horizontal axis). For comparison, the grid spacing given by the criterion of eq. (5.9) equals $h^* = 0.5$.

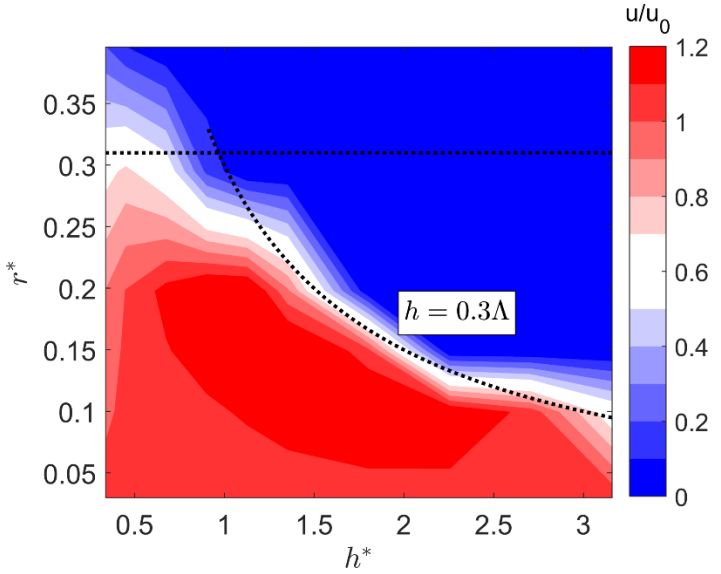

Fig. 5.5 Contour plot of amplitude modulation for a range of grid spacing (horizontal axis) and wavelengths (vertical axis).

The results show that $u/u_0 < 0.5$ when grid spacing is coarser than approximately one third of the wavelength to be reconstructed. Moreover, when $r^* > 0.31$, the seeding concentration has become so small that refining the grid spacing does not significantly improve the result.

5.4 Simulated turbulent boundary layer

The proposed method is now assessed in the more practical case of a turbulent boundary layer.

5.4.1 Test case and data processing

The assessment considers the time-resolved tomographic PIV experiment of a flat-plate turbulent boundary layer ($u_\infty = 10$ m/s, $\delta_{99} = 9.4$ mm), simulated from a direct numerical simulation (DNS) by Bernardini and Pirozzoli (2011). The Reynolds number based on boundary layer thickness is $Re_\delta = 8185$. This numerical simulation was used previously for assessment of tomographic PIV processing techniques by Pröbsting et al. (2013) and Lynch and Scarano (2015). The salient boundary layer parameters are summarized in Tab. 5.2.

Tab. 5.2 Boundary layer parameters for the numerical assessment

Free stream velocity	u_∞	10 m/s
Displacement thickness	δ	9.4 mm
Momentum thickness	θ / δ	0.12
Shape factor	H	1.50
Reynolds number	Re_δ (Re_θ)	8185 (1000)

The configuration of the simulated experiment is chosen similar to the existing real-world time-resolved PIV experiment by Pröbsting et al. (2013), whose data are also used in the present study for assessment. The simulated measurement volume has streamwise length $L_x/\delta_{99} = 2.1$ and spanwise length $L_z/\delta_{99} = 4$ corresponding to the real-world experiment and the wall-normal length is chosen to capture the full turbulent boundary layer height ($L_y/\delta_{99} = 1.1$). The procedure to generate the simulated experiment is chosen similar to the approach used by Novara and Scarano (2013). Tracer particles are randomly and uniformly distributed in space. Their motion is obtained by integrating the velocity over time using a fourth-order Runge-Kutta method. With the same voxel/mm ratio of 0.042 as for the existing experiment by Pröbsting et al. (2013), intensity volumes of 470 × 250 × 890 voxels are generated. A reconstructed particle diameter of 2 voxels is assumed and the exact particle positions in the objects are purposely corrupted with normally distributed random noise with a standard deviation of 0.2 voxels to model a remaining registration error (Novara and Scarano 2013).

Objects are generated with a time separation of 0.1 ms, corresponding to a measurement rate $f_{acq} = 10$ kHz, which is equal to the existing real-world experiment by Pröbsting et al. (2013). The free-stream particle displacement at this acquisition frequency is 20 vox. Similar to Novara and Scarano (2013), the approach followed here solely simulates the motion of particle tracers and tomographic imaging is not included in the simulation. Therefore, also the artefacts of tomographic reconstruction such as ghost particles (Elsinga et al. 2006) are not reproduced. This approach allows a study of the effect of tracer particle concentration on the potential velocity reconstruction quality, separately

from that of the tomographic reconstruction quality. A range of seeding concentrations from C = 50 particles/δ_{99}^3 to C = 2000 particles/δ_{99}^3 is considered. Extracts from the projected intensity volumes at the seeding concentrations considered are shown in Fig. 5.6. For the lowest particle concentrations (C = 50 and 200 particles/δ_{99}^3) the particle image density is below N_I = 0.005 ppp, which is a typical level for 3D-PTV. At C = 2000 particles/δ_{99}^3 the particle image density equals N_I = 0.045 ppp, corresponding to an optimal working condition for tomographic reconstruction (Elsinga et al. 2006) and advanced triangulation methods such as iterative particle reconstruction (IPR, Wieneke 2013).

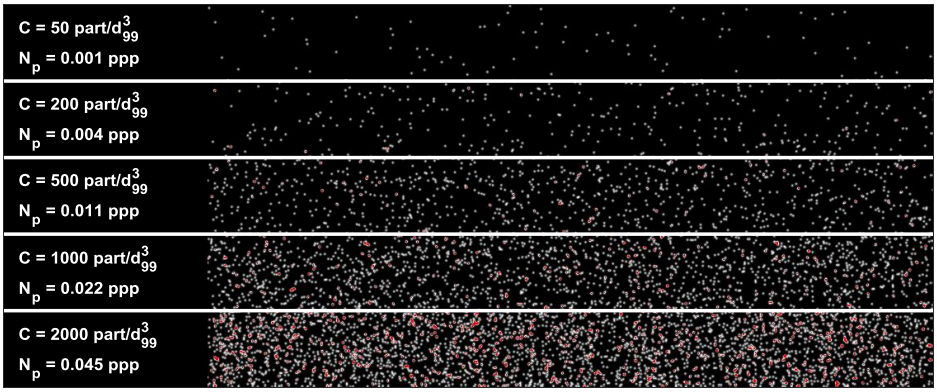

Fig. 5.6 Projected volumes of the test cases at different particle concentration. The seeding density, C, for each strip is indicated in particles/δ_{99}^3 and the particle image density, N_I, in particles per pixel (ppp). The colormap is clipped at $I = 2{\cdot}10^5$ for clarity and larger values of intensity are colored red.

The objects are processed using the proposed technique, VIC+, and for comparison also using PIV (spatial cross-correlation), linear interpolation, adaptive Gaussian windowing (AGW, Agüí and Jimenéz 1987) and VIC with no account of $D\boldsymbol{u}/Dt$. For tomographic PIV analysis, an iterative cross-correlation technique with multigrid and window-deformation (Scarano and Riethmuller 2000) is used with four iterations and an interrogation volume size such that 10 particles are included in the measurement box. A window overlap of 75% is used. Following Pröbsting et al. (2013), the aspect ratio of the interrogation volumes is chosen as

$2 \times 1 \times 2$, with the smallest dimension along the wall-normal to account for the velocity gradient in the boundary layer. After each iteration, the vector fields are subject to universal outlier detection to remove spurious vectors (Westerweel and Scarano 2005). For the intermediate iterations, the vector fields were filtered using a second order polynomial filter. No filter was applied to the final PIV velocity fields.

The other techniques require input from PTV analysis. To this extent, 7-snapshot tracks are built, through which a 2nd order polynomial is fitted to regularize the particle positions (Novara and Scarano 2013). The analytical time-derivatives of the particle tracks yield the velocity and velocity material derivative measurements at the time-centered position of each track. For both VIC without $D\boldsymbol{u}/Dt$ and VIC+, the no-slip condition is prescribed at the wall. On the other boundaries, the time-averaged velocity is prescribed, which can be obtained from cross-correlation analysis or more efficiently from time-averaging of the result of linear interpolation of the PTV results to a regular grid. To prevent this boundary condition from affecting the instantaneous velocity, the computational volume is padded by 30% at all boundaries, except into the wall. This is similar to the padding procedure used in Schneiders et al. (2016a). The padded domain is not considered for further data analysis. For VIC+, the VIC without $D\boldsymbol{u}/Dt$ result is used as initial condition, for which in turn the AGW result is used as initial condition. Furthermore, the weighting coefficient α is calculated using eq. (17), which gives a value of $4 \cdot 10^{-4}$ for α. In the present study, computational time was not considered as a limiting factor. However, in future studies a potential improvement of the initialization approach can be envisaged. Inspired by SMTE (Lynch and Scarano 2015), starting from the second time-step in a series the VIC+ method could potentially be initialized efficiently using the result from the previous time-instant advected forward in time over the time corresponding to the laser pulse separation.

5.4.2 Assessment of the results

First, the results are inspected by visual comparison of the high and low speed streaks and the vortical structures in the turbulent boundary layer.

An instantaneous snapshot of the reference flow field from DNS is shown in Fig. 5.7. The figure shows isosurfaces of low- and high-speed streaks. The expected streamwise elongated low- and high-speed streaks in the turbulent boundary are visible from the blue and yellow isosurfaces.

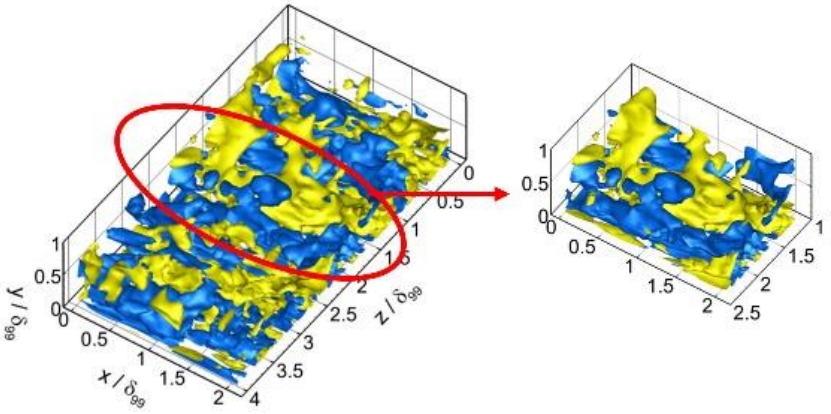

Fig. 5.7 Instantaneous reference flow field visualized by isosurfaces of streamwise velocity fluctuations (u'/u_∞ = -/+0.07, blue/yellow).

The sub-volume indicated in Fig. 5.7 is selected for visual comparison of the different reconstruction techniques. In Fig. 5.8 the corresponding velocity fluctuations are shown as obtained by PIV (a), linear interpolation (b), AGW (c), VIC without D***u***/D*t* (d) and VIC+ (e). From left to right the results of three seeding concentration cases are shown: 200 particles/δ_{99}^3 (left), 500 particles/δ_{99}^3 (middle) and 1000 particles/δ_{99}^3 (right). The PIV analysis (Fig. 5.8a) is found to reconstruct the low- and high-speed streaks only at the highest seeding concentration that is considered (right figure). The particle tracking based linear interpolation (Fig. 5.8b) and AGW (Fig. 5.8c) techniques do not suffer from window-based filtering of the cross-correlation analysis and show the streaks already at the lowest seeding concentration. The VIC-based techniques (Fig. 5.8d-e) show similar results, but with somewhat increased coherence in the lowest seeding density case.

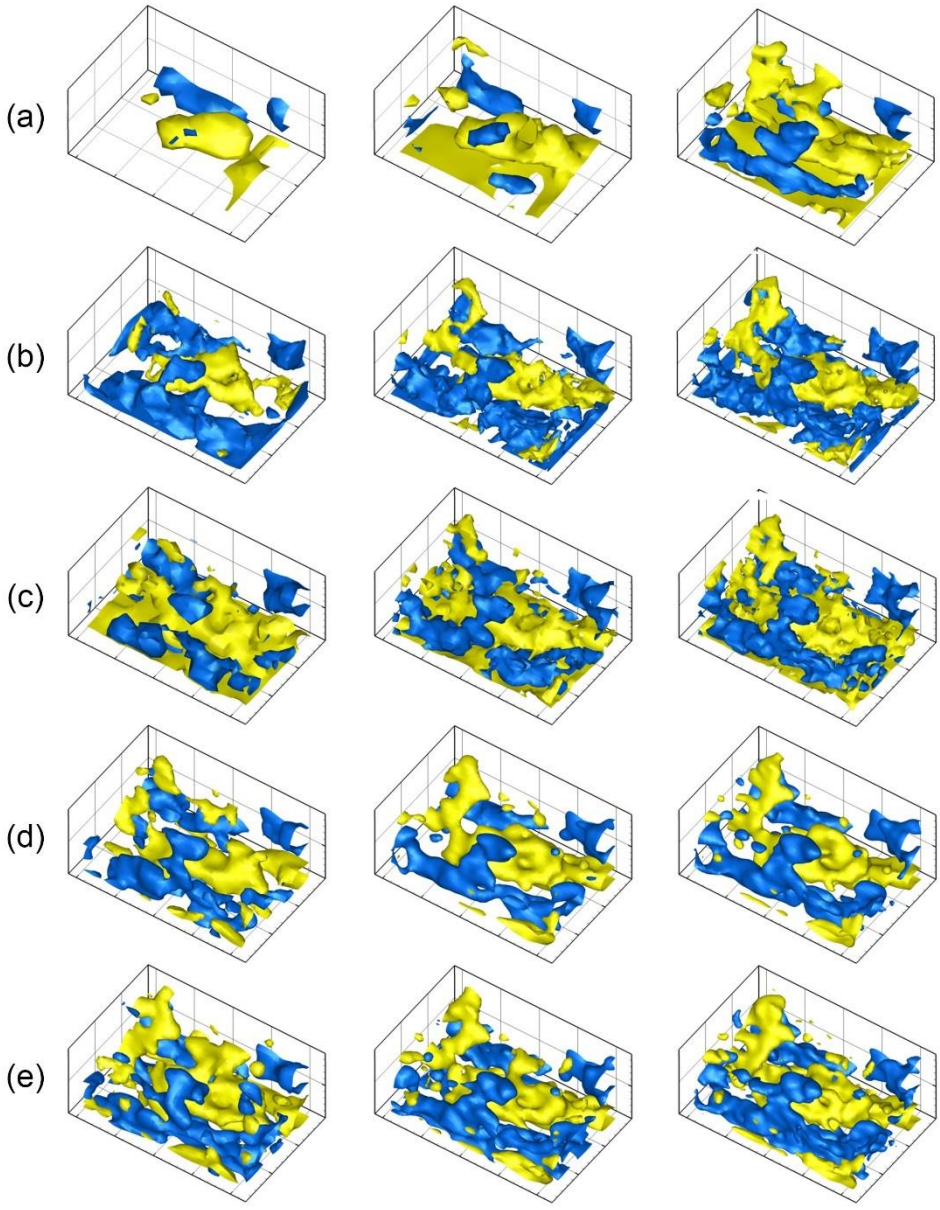

Fig. 5.8 Flow field reconstructions by PIV (a), linear interpolation (b), AGW (c), VIC without Du/Dt (d) and VIC+ (e), visualized by isosurfaces of $u'/u_\infty = -0.07$ (blue) and $u'/u_\infty = +0.07$ (yellow). From left to right the results at particle seeding concentrations of 200, 500 and 1000 particles/δ_{99}^3 are given.

The vorticity field is compared similarly to the above comparison of the low- and high-speed streaks. Because vorticity depends on instantaneous velocity gradients, a more expressed difference between the methods is expected. In Fig. 5.9 the instantaneous reference flow field is visualized by isosurfaces of u'/u_∞ = -0.07 (blue) and vorticity magnitude ($|\boldsymbol{\omega}|$ = 2500 1/s, red). Again, a sub-volume is selected for visual comparison of the results. The selected sub-volume (right figure) contains a pair of hairpin vortices on top of a low-speed streak.

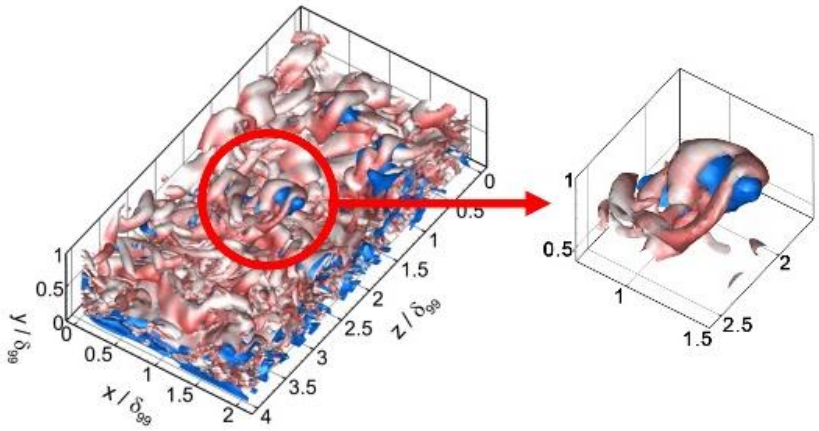

Fig. 5.9 Instantaneous reference flow field obtained from DNS, visualized by isosurfaces of u'/u_∞ = -0.07 (blue) and vorticity magnitude ($|\boldsymbol{\omega}|$ = 2500 1/s, red).

In Fig. 5.10 the corresponding results are shown as obtained from PIV (a), linear interpolation (b), AGW (c), VIC without D$\boldsymbol{u}$/Dt (d) and VIC+ (e). Again, from left to right the results of three seeding concentration cases are shown: 200 particles/δ_{99}^3 (left), 500 particles/δ_{99}^3 (middle) and 1000 particles/δ_{99}^3 (right).

In the PIV result, the hairpin vortex pair is combined to a single structure at the highest seeding density considered, and not visible at lower seeding densities. The linear interpolation result marginally shows two separated vortical structures at the highest seeding density, where the AGW result shows increased spatial coherence introduced by the weighting function.

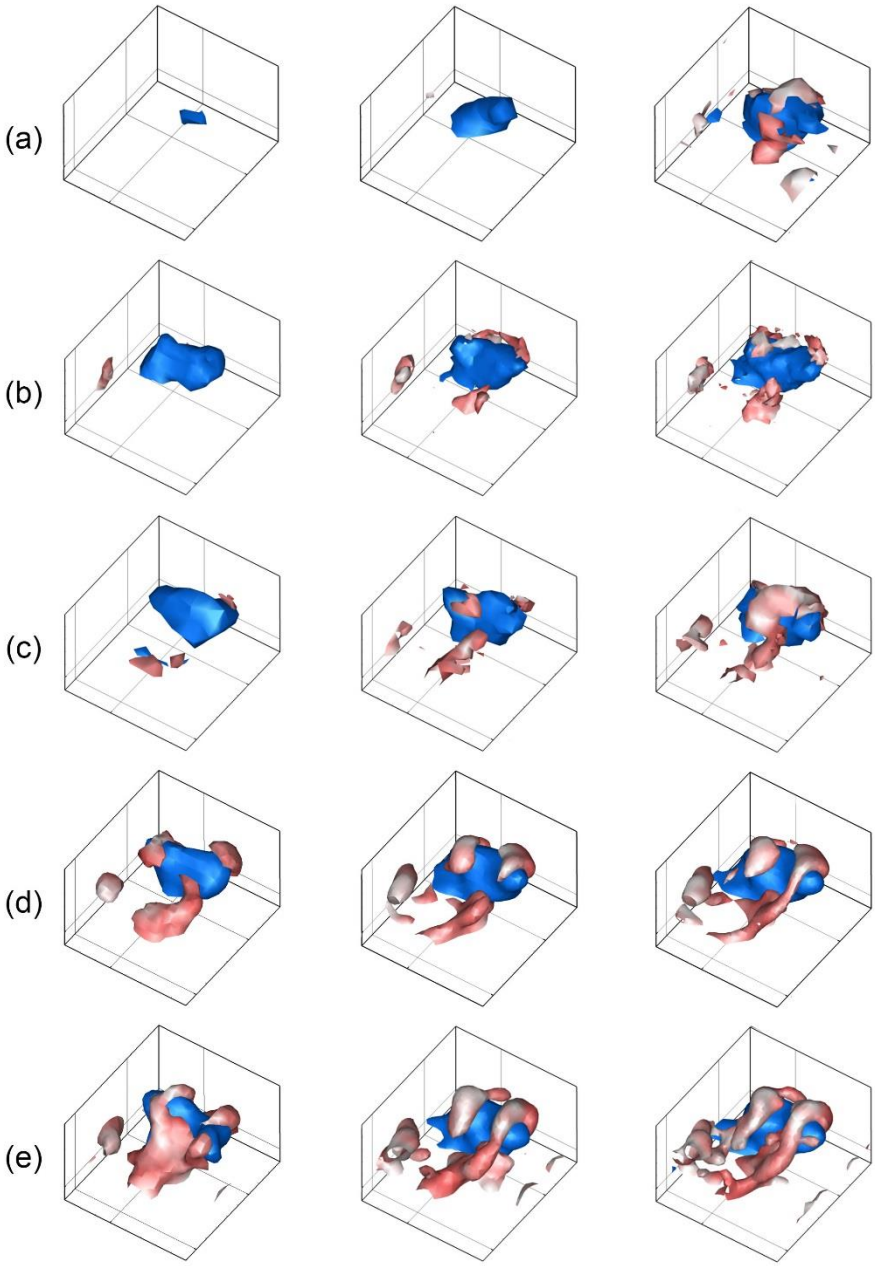

Fig. 5.10 Flow field reconstructions by PIV (a), linear interpolation (b), AGW (c), VIC without Du/Dt (d) and VIC+ (e), visualized by isosurfaces of $u'/u_\infty = -0.07$ (blue) vorticity magnitude ($|\boldsymbol{\omega}| = 2500$ 1/s, red). From left to right the results at particle seeding concentrations of 200, 500 and 1000 particles/δ_{99}^3 are given.

Due to the choice of basis for the VIC reconstructions, both VIC with and without $D\boldsymbol{u}/Dt$ are expected to reconstruct a smoother vorticity field than the reconstructions resulting from linear interpolation and AGW. Indeed, smoothness and coherence of the hairpin vortices is found to be improved with the VIC methods in Fig. 5.10. For VIC without $D\boldsymbol{u}/Dt$, the pair of hairpin vortices can be clearly identified at the highest concentration of 1000 particles/δ_{99}^3. When the $D\boldsymbol{u}/Dt$ term is used for the reconstruction with VIC+, visually similar fidelity is obtained at half the seeding concentration (500 particles/δ_{99}^3).

In the introduction, it was noted that in recent volumetric particle velocimetry experiments a damping of the turbulent velocity fluctuations is found. To illustrate how the application of the velocity reconstruction techniques impacts estimation of the turbulent velocity fluctuations, velocity statistics are plotted in Fig. 5.11 for the range of seeding concentrations considered. From left to right, Fig. 5.11 shows: u'_{rms}, v'_{rms}, and $(u'v')_{rms}$. From top to bottom the seeding concentration increases from 50 particles/δ_{99}^3 to 1000 particles/δ_{99}^3. The statistics were obtained using 100 snapshots (measurement duration of 10 ms) and the data ensemble along x and z directions was also used for averaging.

The time-averaged streamwise velocity profile is not plotted in the figure, because all techniques are able to capture this already at the lowest seeding concentration the mean streamwise velocity profile. Only the PIV and AGW techniques suffer from an overestimation of the time-averaged streamwise velocity close to the wall because of the interrogation volumes and Gaussian windows not being able to capture the strong velocity gradient near the wall (see e.g. Kähler et al. 2012).

As expected from the qualitative comparisons above, the differences between PIV and PTV based techniques are more pronounced in the u'_{rms} statistics. Differences between the PTV based techniques remain small however for $u'_{rms,}$ as these fluctuations are associated with low and high-speed streaks occurring as rather elongated structures, which correspond to relatively small wavenumbers.

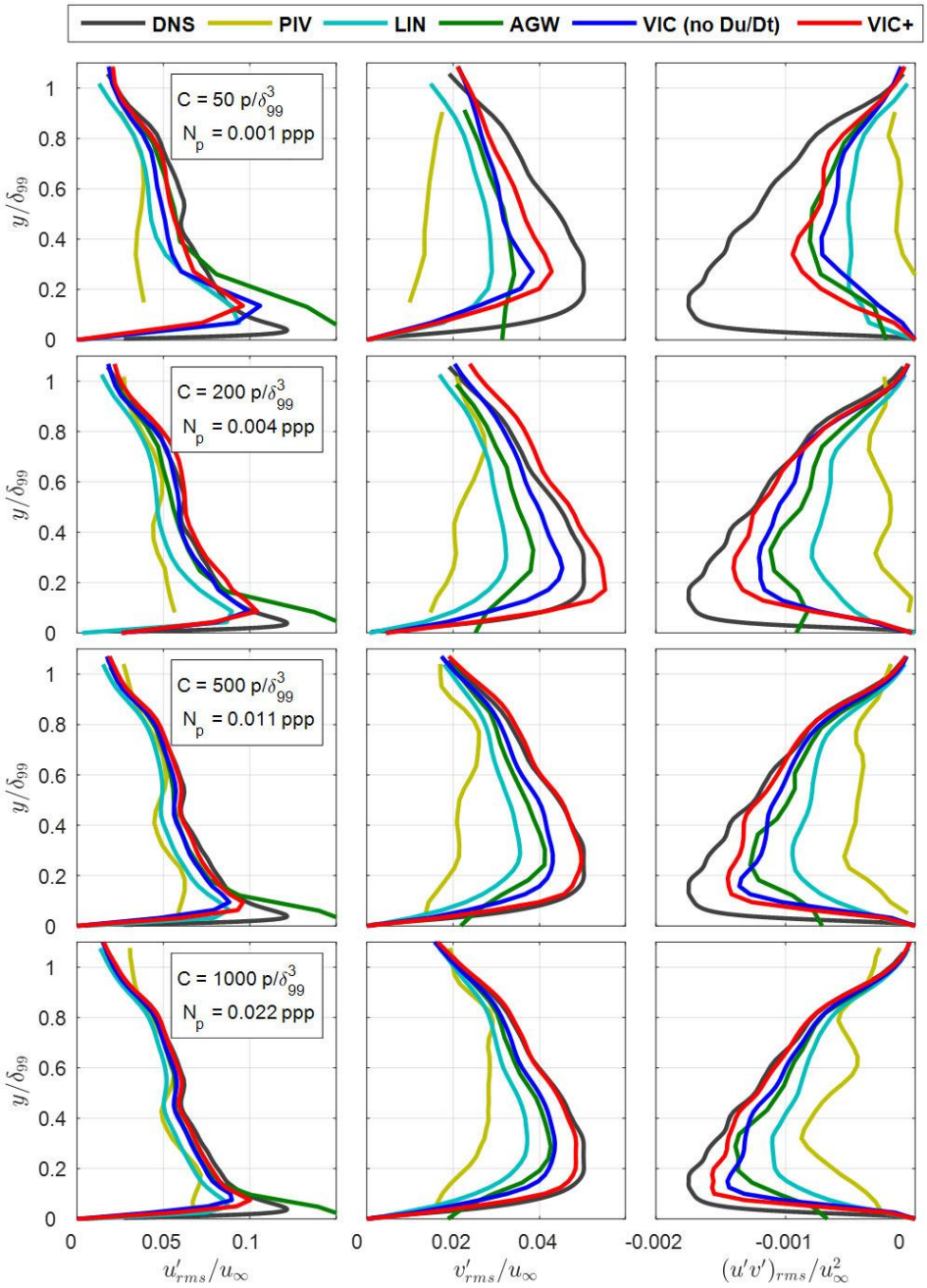

Fig. 5.11 Turbulence statistics calculated from the different velocity field reconstructions; from top to bottom the tracer particle concentration, *C*, equals C = 50, 200, 500 and 1000 particles/δ_{99}^3.

In contrast, the wall-normal velocity fluctuations corresponding to smaller flow structures such as hairpins and hairpin packets (e.g. Adrian et al. 2000) are expected to be poorly captured at low concentration of tracers, as their wavenumbers are filtered by the different reconstruction techniques. At 1000 particles/δ_{99}^3, the PIV result yields most significant damping at y/δ_{99} = 0.3 (~ 45% damping). Linear interpolation reduces this to 35%. The adaptive Gaussian windowing technique performs similar to VIC without the aid of $D\boldsymbol{u}/Dt$ with 15% damping. When the material derivative is used for the reconstruction with VIC+, damping of v'_{rms} and w'_{rms} is 5%. A similar trend is found at the highest seeding density case of 2000 particles/δ_{99}^3. The latter results are not given in the present dissertation for clarity of the visualizations, but can be found in in the published manuscript by Schneiders and Scarano (2016).

The VIC+ result remains within 5% at y/δ_{99} = 0.3, also when the particle seeding concentration is reduced by an order of magnitude to 200 particles/δ_{99}^3. At this seeding concentration, the differences between VIC+, VIC without the use of D**u**/Dt (10% damping) and AGW (20% damping) are more pronounced, as expected also from the study of the hairpin vortex reconstruction above.

The cross term $(u'v')_{\mathrm{rms}}$ requires most tracer particles for correct reconstruction, as indicated by the more significant damping at especially the low seeding concentration cases. The trend of the results remains, however, and, as also indicated by the isosurfaces of instantaneous u' and vorticity in Fig. 5.8 and Fig. 5.10, at each seeding concentration case PIV yields significantly damped statistics and VIC+ the most accurate reconstruction.

5.5 Pressure measurement using VIC+[2]

The Poisson equation for pressure, eq. (4.1), can be solved after application of VIC+, as the method provides the required velocity and material derivative fields. The author participated in a comparative assessment of pressure reconstruction techniques that was performed

[2] The contents of this section are adapted from van Gent et al. (2017).

within the European 'NIOPLEX' framework (van Gent et al. 2017). In addition to VIC+, four pressure reconstruction techniques for Lagrangian particle tracking measurements were considered: two implementations of FlowFit (Gesemann et al. 2016), Voronoi-based pressure evaluation (Neeteson et al. 2016), iterative least-square pseudo-tracking (van Gent et al. 2017). The test case of a simulated experiment in an axisymmetric base flow at Mach 0.7 (Fig. 5.12) is considered. The original zonal detached eddy simulation (ZDES) serves as ground truth for the pressure assessment.

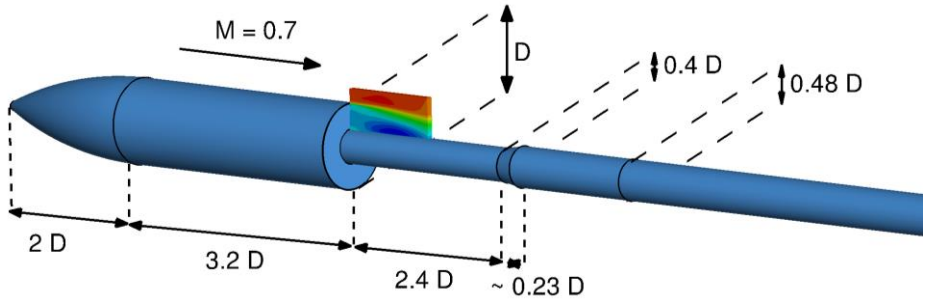

Fig. 5.12 The contoured volume indicates the measurement volume with respect to the axisymmetric base (the diameter D = 50 mm, figure reproduced from van Gent et al. 2017).

Full details of the test case setup and the results are given in van Gent et al. (2017). To demonstrate the potential of VIC+ for pressure evaluation, the salient results are reproduced here. In Fig. 5.13 (left column) the instantaneous pressure fields obtained by the pressure reconstruction techniques are given. The top figure shows the reference pressure field obtained by the ZDES simulation. The right figure shows the rms errors when considering all z-planes of the measurement volume. The lower errors obtained by VIC+ in comparison to the other state-of-the-art pressure measurement techniques indicate the potential of the technique also for pressure measurement.

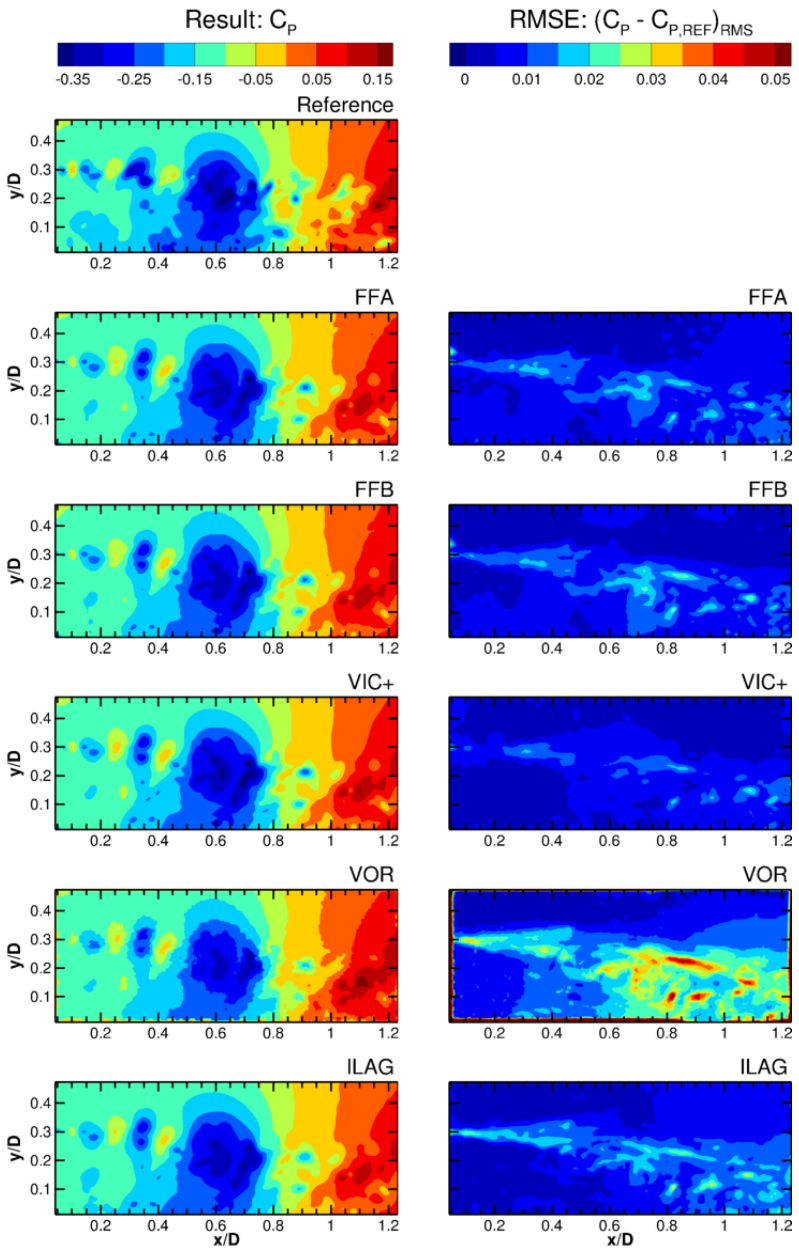

Fig. 5.13 Results obtained by van Gent et al. (2017), comparing a range of LPT-based pressure field reconstruction techniques applied to time-resolved input data. A typical result (left) from the time-resolved pressure reconstruction techniques considered in the assessment and their rms error levels (right). Figure reproduced from van Gent et al. (2017).

5.6 Conclusions

The VIC+ method is proposed for reconstruction of instantaneous velocity from time-resolved volumetric PTV measurements, by leveraging the temporal information available by the measurements in form of the velocity material derivative. This is christened as pouring time into space.

The numerical assessment considers first quantification of the spatial response of VIC+ with a sine-wave lattice analysis and the case of a simulated experiment in a direct numerical simulation of a turbulent boundary layer. The sine-wave lattice assessment results indicate a twofold increase of spatial resolution of VIC+ with respect to cross-correlation interrogation. A divergence free reconstruction (i.e. VIC+ without using the Du/Dt term) yields only a 50% increase of spatial resolution.

In the second numerical assessment considering turbulent boundary layer measurements, VIC+ is found to reconstruct turbulent velocity fluctuations at a fraction of the seeding concentration required for tomographic PIV. Coherent hairpin vortices could be identified by VIC+ at a concentration of 500 particles/δ_{99}^3, whereas for tomographic PIV, a concentration beyond 2000 particles/δ993 is required. When VIC is employed without the use of the velocity material derivative, a concentration beyond 1000 particles/δ_{99}^3 is needed.

An additional numerical assessment of a pressure field obtained by VIC+ was performed within the 'NIOPLEX' framework. The comparative assessment from this framework showed that in comparison to other state-of-the-art LPT-based pressure measurement techniques, the lowest errors are obtained by VIC+.

All the above assessments were performed on synthetic datasets. In the next chapter the VIC+ technique is applied to an experimental dataset for a real-world validation.

Chapter 6
Measuring vorticity and dissipation using VIC+

This work has been published in Schneiders et al. (2017) Exp. Fluids 58:27

Following the introduction of VIC+ and its numerical assessment in the previous chapter, here the technique is applied to a real-world experiment. Existing time-resolved tomographic PIV measurements by Jodai and Elsinga (2016) in a turbulent boundary layer significantly underestimated vorticity and turbulence dissipation. Following the promising numerical assessment now it is attempted to measure these quantities by use of VIC+.

6.1 Vorticity and dissipation measurement

Following two decades of experimental and numerical work in wall-bounded turbulent flows, as reviewed in Marusic et al. (2010), todays experiments by tomographic particle image velocimetry (PIV) have allowed for unprecedented volumetric and time-resolved measurement of such flows (Schröder et al. 2008, 2011; Elsinga et al. 2010, 2012). As however already touched upon earlier in this dissertation, recent studies have stumbled upon the spatial resolution limitations of tomographic PIV for measurements in a turbulent flow (Atkinson et al. 2011; Kähler et al. 2012b; Lynch et al. 2014).

Velocity fluctuations are typically dominated by large-scale events, which can be resolved even with a relatively coarse spatial resolution. On the other hand, the components of the velocity gradient tensor, which govern vorticity and energy dissipation, act at smaller scale and thus require a higher spatial resolution. For the turbulent dissipation, a vector spacing of 2 Kolmogorov length scales is recommended (Tokgoz et al. 2012). This point is illustrated in Fig. 6.1 for a turbulent boundary layer,

where the velocity fluctuations measured by time-resolved tomographic PIV agree with direct numerical simulation (DNS) data to within 5%.

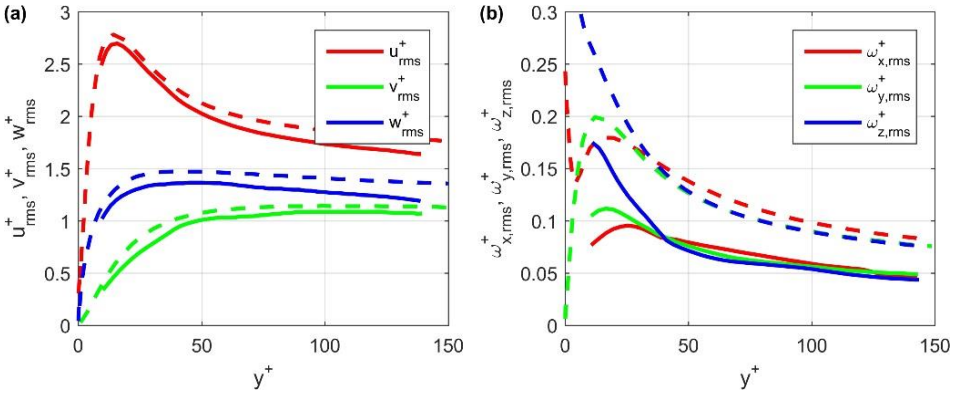

Fig. 6.1 Wall normal profiles of the rms of the fluctuating velocity (a) and vorticity (b) components. Time-resolved tomographic PIV measurement of Jodai & Elsinga (2016) (solid lines) and DNS data of Schlatter & Örlü (2010) (dashed lines) are presented. The x, y and z coordinates correspond to streamwise, wall-normal and spanwise directions, respectively.

The root mean square (rms) vorticity profiles, instead, are systematically underestimated to approximately half the value predicted by DNS. The spatial resolution in these measurements thus captures the velocity fluctuations accurately, but at the same time under-resolves the (peak) vorticity fluctuations.

For velocity statistics, high spatial resolution can be achieved by ensemble particle tracking velocimetry (ensemble PTV) approaches as proposed by Kähler et al. (2012b) and refined for volumetric experiments by Agüera et al. (2016). This approach evaluates velocity statistics in small interrogation volumes from the full PTV velocity measurement time series. For evaluation of statistics that are dependent on instantaneous spatial velocity gradients (e.g. vorticity, strain rate, turbulent dissipation), the ensemble PTV approach cannot be used and one needs to use techniques that are based on the evaluation of instantaneous gradients from PTV measurements.

In the present work, the VIC+ technique is applied to an actual experiment in a turbulent boundary layer, to assess the accuracy of the

velocity gradients, vorticity and dissipation. For the present analysis, the existing experimental data of Jodai and Elsinga (2016) is used. These authors have performed time-resolved tomographic PIV measurements to obtain a detailed characterization of the turbulent motions in a turbulent boundary layer. The experiments are conducted in the same conditions as the DNS study of Schlatter & Örlü (2010). The comparison showed good agreement with the reference in terms of velocity statistics (Fig. 6.1a). Instead, vorticity fluctuations are systematically underestimated (Fig. 6.1b), which is ascribed to the limited spatial resolution of the measurement. In the present work, the VIC+ technique is applied to these measurements with the aim of assessing the potential benefits when evaluating properties dominated by small-scale motions, such as vorticity and dissipation.

6.2 Experimental Setup

The time-resolved tomographic PIV turbulent boundary layer experiment was performed in a water channel at the TU Delft. A full description of the experiment is given by Jodai and Elsinga (2016). Relevant details related to the boundary layer properties and measurement setup are repeated here for completeness. The Reynolds number based on the momentum thickness, Re_θ, and the friction velocity, Re_τ, were 2038 and 782 respectively. The free-stream velocity, U_∞, was 0.253 m/s, while the boundary layer thickness, δ_{99}, was 69.9 mm.

Since the paper focusses on the near wall region and small-scale quantities, the relevant turbulent scales for comparison are the so-called wall-units, which are summarized in Tab. 6.1. Here ν is the kinematic viscosity and u_τ is the friction velocity. Normalization by these wall-units is indicated by the superscript +.

Tab. 6.1 Turbulent boundary layer scales used for normalization.

u_τ	0.0107 m/s
ν/u_τ	0.0901 mm
ν/u_τ^2	8.42 ms

The measurement volume spanned 60 mm and 55 mm in the streamwise (x) and spanwise (z) direction respectively, while it covered 13 mm in the wall-normal (y) direction starting at the wall ($y = 0$). The tracer particles were illumined by a high-speed laser, and their images were recorded by four cameras. The recording rate equaled 1279 Hz, resulting in approximately 3.3 pixels maximum particle displacement between frames. In total three time-series of 3140 images were recorded, corresponding to 7.37 s of observation time. The present temporal resolution causes subsequent time samples to be highly correlated. Correlated samples, however, do not contribute to statistical convergence. For reason of computational efficiency, the data is analyzed in bursts for tomographic PTV processing with VIC+. Each burst is a short sequence of 24 ms on which particle tracking analysis is performed. This analysis yields for each burst the velocity and acceleration of the tracer particles, allowing VIC+ analysis to obtain the instantaneous velocity fields. The time separation between bursts is chosen at 0.2 s, corresponding to 0.7 large-scale turnover times (δ_{99}/U_∞). The flow properties are homogeneous along the span and are considered homogeneous along the streamwise direction over the length of the measurement domain. The data ensemble along both directions is considered for the statistical evaluation of the turbulent properties. For further details of the experimental setup the reader is referred to Jodai and Elsinga (2016).

6.3 Data Processing Methods

The recorded images were originally processed using tomographic PIV as outlined in Sec. 6.3.1. In the present work, the data is evaluated using VIC+ and the processing steps are outlined in Sec. 6.3.2. For both tomographic PIV and VIC+ processing, the same set of recorded images is used.

6.3.1 Tomographic PIV

Tomographic PIV processing was performed by Jodai and Elsinga (2016) and salient aspects are recalled in this section. The intensity volumes were reconstructed using the MART algorithm (Elsinga et al. 2006) and the

average intensity profile of the reconstruction in wall-normal direction as calculated from the reconstructed objects is reported in Fig. 6.2a, which is used to obtain the wall location in the reconstructed volumes. The intensity profile shows at $y^+ = 0$ a sharp intensity increase. Towards the end of the illuminated volume, a more gradual reduction in intensity is found up to $y^+ \approx 150$, after which the intensity decreases to the noise level. The sharp change in intensity at $y^+ = 0$ indicates the wall location, which is obtained at an accuracy on the order of the particle image diameter in the reconstructed volumes, which equals 3 voxels (1.4 wall units).

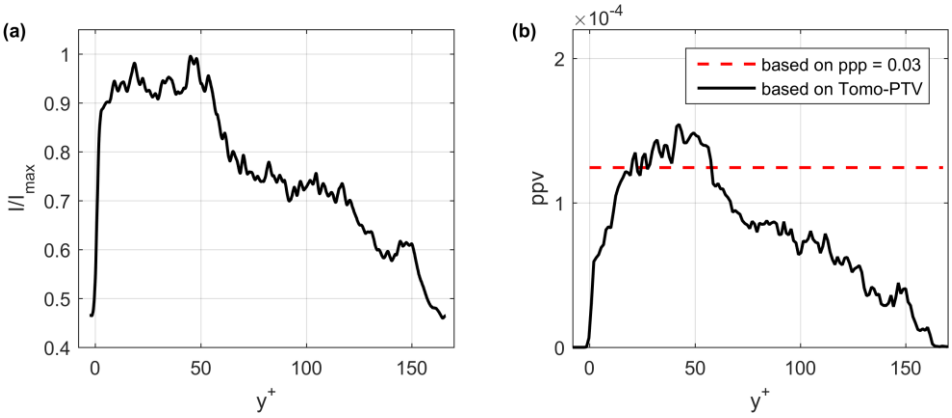

Fig. 6.2 Wall normal profiles of reconstructed light intensity by MART (a) and density of detected particle tracks (b).

The particle displacement field was obtained from the sequence of reconstructed volumes using direct cross-correlation. Object pairs were taken with a time separation of 4.6 ms (factor six sub-sampling) yielding a maximum particle displacement of 19.8 voxels, which enhances the dynamic velocity range. The first reconstructed volume was thus cross-correlated with the 7th volume in the time sequence, the 2nd with the 8th volume and so on. The resulting temporal oversampling of the velocity field was used later to further suppress measurement noise. The final size of the interrogation volume was 32 × 32 × 32 voxels (1.37 × 1.37 × 1.37 mm^3) and neighboring interrogation volumes overlap by 75%. The resulting vector spacing in each direction was 0.34 mm (approx. 3.8 wall units). The region near the wall ($y^+ < 40$) was also processed using a final correlation

window of 64 × 16 × 32 voxels at 75% overlap to improve the spatial resolution along the wall-normal direction. The universal outlier detection method was used to remove spurious vectors (Westerweel and Scarano 2005). To suppress measurement noise, the velocity fields were spatiotemporally filtered using a second-order polynomial regression over a period of 14.1 ms ($1.7\,\nu/u_\tau^2$) and in a cubic filter volume of 2.05^3 mm^3, which corresponds to 23^3 wall units. In the near-wall region, the filter volume was 4.10 mm × 1.02 mm × 2.05 mm (46 × 12 × 23 wall units) due to the different interrogation volume used. The coefficients of the polynomial regression were also used to determine the local value of the velocity gradients.

6.3.2 Tomographic PTV with VIC+

The VIC+ method interpolates scattered PTV measurements towards a Cartesian grid. For details of the method the reader is referred to Chapter 5 of this work. Specific details of the present tomographic PTV and VIC+ processing steps are given in the remainder of this section.

Particle trajectories are obtained using the same tomographic PTV algorithm as reported in Schneiders and Scarano (2016). This algorithm uses the volumetric intensity distribution as obtained with sequential motion tracking enhanced MART (SMTE, Lynch and Scarano 2015). The reconstruction is applied to the measurement time-series sub-sampled by a factor two, yielding a maximum particle displacement of 6.6 voxels. Particle locations are identified with sub-voxel accuracy using a 3-point Gaussian fit along each coordinate direction. A particle-tracking algorithm based on Malik et al. (1993) is used to find particle tracks and the minimum acceleration criterion is used in case multiple particles are identified within a search box. The tomographic PIV results (Sec. 3.1) are used as predictor for the tracking algorithm. The discrete positions of a particle in motion are then used to produce a least-squares 3rd order polynomial fit estimating the trajectory over 15 exposures. The result yields the fitted particle position at each time instant. Its time derivative yields the velocity and in turn the Lagrangian acceleration (viz. velocity material derivative). Fig. 6.2b shows the profile of identified particles per

voxel (ppv) along wall-normal direction following from the PTV algorithm (black line). The water tunnel was seeded homogeneously and therefore a uniform track density is expected at an estimated level of 0.0013 particles per voxel (ppv, dashed red line), based on an estimate of 0.03 particles per pixel (ppp) from the recorded images. For $y^+ > 60$ a lower number of particles is observed, which is associated with lower laser light intensity reducing particle detectability. The estimated ppv based on the particle image density, therefore, represents a volume average concentration of detected particles. The actual seeding concentration can be higher, and will be closer to the peak ppv in figure 2b.

After particle tracking, the iterative VIC+ procedure is started with the results obtained from tomographic PTV. The no-slip condition is prescribed at the wall. The VIC+ method discretizes the vorticity field using Gaussian radial basis functions. The base function spacing, h, for VIC+ is calculated using eq. (5.9). Following this criterion, the spacing of the base functions is set to 0.25 mm, corresponding to 2.8 wall units, for $y^+ < 60$. Further away from the wall less tracks are identified and hence a coarser base function spacing of 0.5 mm (5.6 wall units) is used. The computational grid is evaluated at a factor two oversampling resulting in a vector spacing of 0.125 mm (1.4 wall units) in the near-wall region and 0.25 mm (2.8 wall units) for $y^+ > 60$. All gradients are obtained using second order finite differences on the computational grid.

6.4 Results and discussion

The validity of the velocity reconstructions is first examined by analysis of the velocity statistics (Sec. 6.4.1). Subsequently, the instantaneous flow organization is studied (Sec. 6.4.2) and the statistics of vorticity fluctuations are considered (Sec. 6.4.3). The discussion concludes with the estimation of the dissipation rate (Sec. 6.4.4).

6.4.1 Velocity statistics

The velocity statistics are compared to the results by Schlatter & Örlü (2010) from a DNS simulation at $Re_\theta = 2000$, which is close to the Reynolds number in the experiment ($Re_\theta = 2038$). The performance of tomographic PIV using the cubic and elongated interrogation volumes for the

measurement of the velocity statistics in this experiment is already discussed in Jodai and Elsinga (2016). They are recalled here for comparison to the results from VIC+. The mean velocity profile along wall-normal direction is plotted in Fig. 6.3. The blue and yellow lines show the results obtained by tomographic PIV with respectively the cubic and elongated interrogation volumes. The red line shows the VIC+ result. For reference, the black line shows the DNS results. For $10 < y^+ < 140$, all methods agree well with each other, indicating that the time averaged velocity profile is captured by all approaches and that the experiments agree with the DNS data.

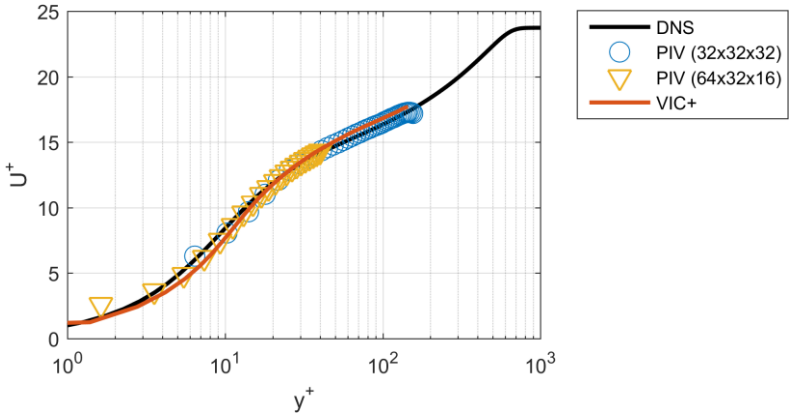

Fig. 6.3 Time-averaged velocity profiles returned by tomographic PIV with cubic and elongated correlation volumes and with VIC+, in comparison to the DNS result by Schlatter & Örlü (2010).

The PIV result with cubic interrogation volumes of 32 × 32× 32 voxels shows its first vector at 16 voxels, corresponding to 7.6 wall units. With elongated correlation volumes, the first vector that results from interrogation windows not overlapping with the wall is located at 8 voxels (3.8 wall units) from the wall. Vectors below this wall-normal distance result from interrogation volumes overlapping with the wall and overestimate the mean velocity. The result of VIC+ is in good correspondence to the PIV results for $y^+ > 3$. Closer to the wall it follows the DNS reference profile and because the no-slip condition is prescribed at the wall for VIC+ the velocity goes exactly to zero at the wall.

The profiles of rms velocity fluctuations are given in Fig. 6.4a-c, for the streamwise, wall-normal and spanwise components of velocity respectively. The PIV results with both cubic and elongated interrogation windows are largely equivalent, with the exception that the near wall peak at y^+ = 15 in the streamwise velocity fluctuations (Fig. 6.4a) is captured slightly better by tomographic PIV with the elongated volumes.

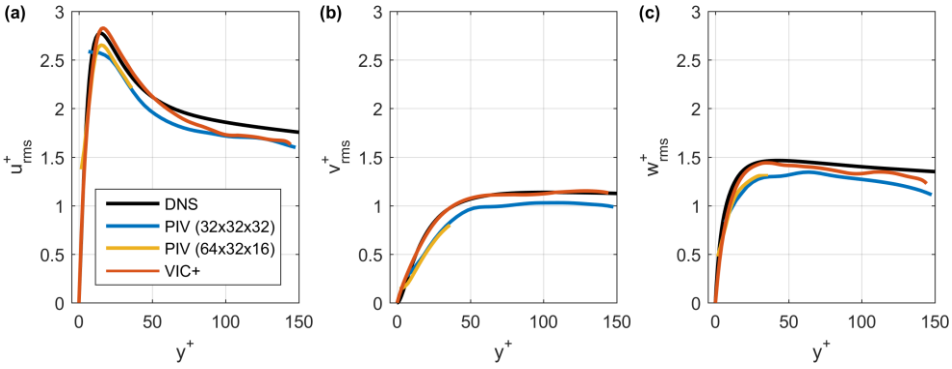

Fig. 6.4 Wall-normal profiles of rms velocity fluctuations returned by tomographic PIV with cubic and elongated correlation volumes and with VIC+, in comparison to the DNS result by Schlatter & Örlü (2010). Streamwise (a), wall-normal (b) and spanwise (c) velocity components.

The VIC+ estimate of the streamwise velocity fluctuations (Fig. 6.4a) follows closely the PIV results, which match well with the DNS result for $y^+ < 50$. Instead, the streamwise fluctuations depart from the DNS data for $y^+ > 50$ with approximately 10% lower values. The latter can be related to the slightly favorable pressure gradient in the water channel facility and the uncertainty in determining u_τ (Jodai and Elsinga 2016). For the wall-normal and spanwise velocity fluctuations (Fig. 6.4b and c, respectively), tomographic PIV shows slightly lower values than the DNS result along the full y-range, but remains within 10% between y^+ = 50 and 140. The VIC+ analysis follows more closely the DNS (within 5%) for the wall-normal (Fig. 6.4b) and spanwise (Fig. 6.4c) components. This behavior already indicates a potential improvement in rendering turbulent fluctuations with the VIC+ analysis.

Because divergence of velocity is expected to be zero in an incompressible flow, recent studies have used the level of velocity

divergence to assess the measurement accuracy of the velocity gradient (de Silva et al. 2013; Jodai and Elsinga 2016; amongst others). The velocity divergence consists of three components,

$$\nabla \cdot \boldsymbol{u} = \frac{\partial u}{\partial x} + \frac{\partial v}{\partial y} + \frac{\partial w}{\partial z}. \tag{6.1}$$

The joint probability density function of $-\partial u/\partial x$ and $(\partial v/\partial y + \partial w/\partial z)$ is plotted in Fig. 6.5. Points away from the diagonal correspond to non-zero divergence.

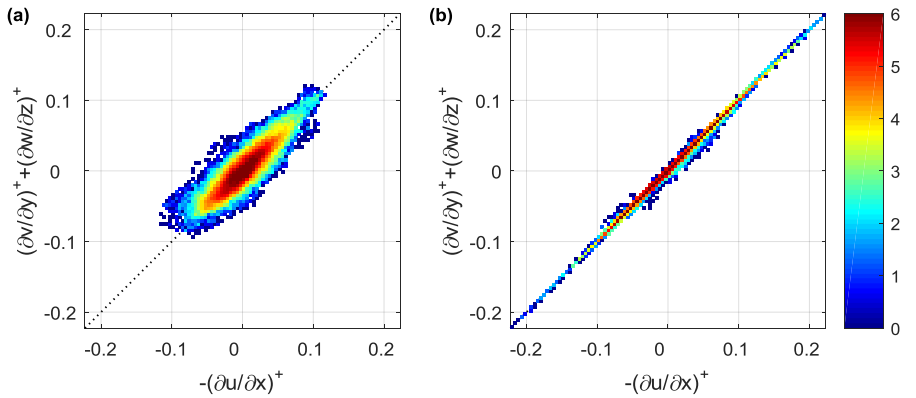

Fig. 6.5 Joint pdf of $-\partial u/\partial x$ and $(\partial v/\partial y + \partial w/\partial z)$ evaluated between y+ = 40 and 60. The contours are plotted in log-scale. Tomographic PIV (left) and VIC+ (right).

The comparison of the results obtained from tomographic PIV (a) and VIC+ (b) indicates a significantly lower divergence error for VIC+. The calculation of the cross-correlation coefficient between the two components plotted in Fig. 6.5, $-\partial u/\partial x$ and $(\partial v/\partial y + \partial w/\partial z)$, is a commonly used technique to assess the measurement quality (Tsinober et al. 1992; Casey et al. 2013; Ganapathisubramani et al. 2007; amongst others). For the present tomographic PIV result, this cross-correlation coefficient equals 0.88 (Jodai and Elsinga 2016) and for the VIC+ result it is 0.9994. Additionally, the rms divergence error is evaluated as the rms value of the velocity divergence between $y^+ = 40$ and $y^+ = 60$. It equals 0.013 u_τ^2/ν for PIV and 0.002 u_τ^2/ν for VIC+. This confirms that the latter yields, to a large extent, a divergence-free result.

6.4.2 Instantaneous flow organization

The pattern of coherent structures in the measurement volume at a single time instant is visualized in Fig. 6.6. Isosurfaces of vorticity magnitude ($|\boldsymbol{\omega}^+| = 0.3$, red, shaded by wall-normal distance for clarity) are representative of vortex filaments mostly exhibiting arc, cane and hairpin shapes. The streamwise velocity (blue, $\boldsymbol{u}^+ = 14$) highlights the organization of alternating elongated regions with momentum excess and defect.

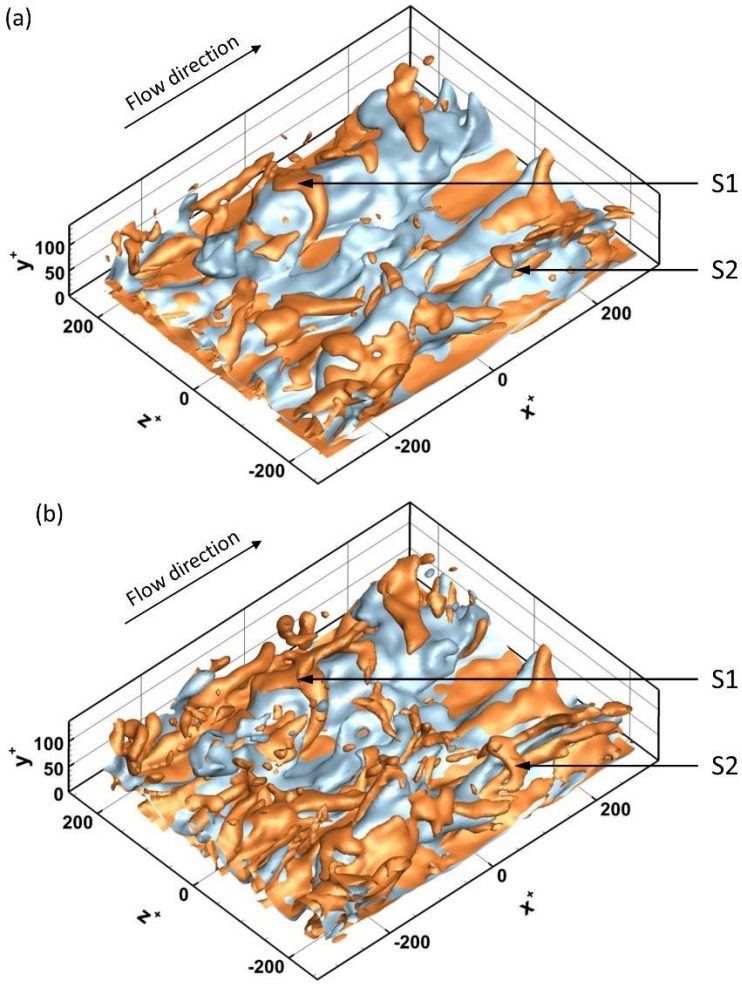

Fig. 6.6 Instantaneous flow organization in the measurement volume visualized by isosurfaces of vorticity magnitude ($|\boldsymbol{\omega}^+| = 0.3$, orange) and streamwise velocity ($\boldsymbol{u}^+ = 14$, blue). Tomographic PIV (a) and VIC+ (b).

From visual inspection of the two data sets, a richer pattern of vortical structures is retrieved with the VIC+ reconstruction. Two hairpin vortices, S1 and S2, are indicated by arrows in Fig. 6.6. The largest of the two, S1, is visible in both the tomographic PIV and VIC+ reconstructions. On the other hand, at the selected vorticity level, S2 is clearly visible only within the VIC+ reconstruction. Also, two tongue-like appendices (Zhou et al. 1999) are revealed attached to the hairpin structure. The vortex structures S1 and S2 are inspected in more detail in the paragraphs below.

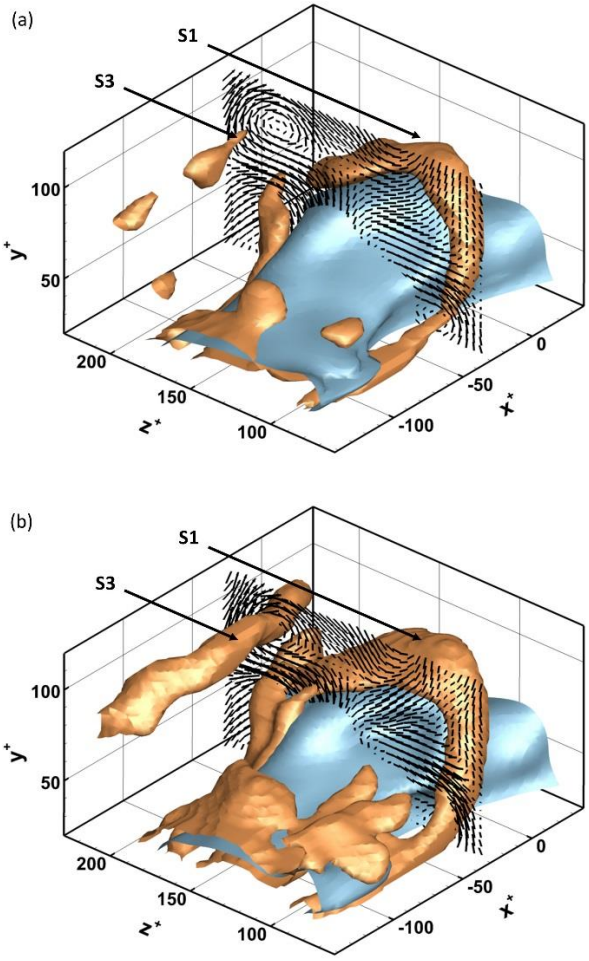

Fig. 6.7 Cut-out of hairpin structure S1, with the instantaneous in-plane velocity at x^+ = -35. Isosurfaces show vorticity magnitude ($|\boldsymbol{\omega}^+| = 0.35$, orange) and streamwise velocity ($\boldsymbol{u}^+ = 12$, blue). Tomographic PIV (a) and VIC+ (b).

Fig. 6.7 illustrates the detailed view of the hairpin structure S1, as reconstructed by tomographic PIV (a) and VIC+ (b). The in-plane velocity vectors are plotted in the plane x^+ = -35. Visual comparison shows no significant difference between the velocity vectors. Despite that streamwise vortex S3 is only marginally visible by the isosurface visualization in the PIV reconstruction, the velocity field does reveal the presence of the streamwise vortex. This indicates that the structure is present in both PIV and VIC+ results, but its associated vorticity magnitude is higher in the VIC+ result.

The question whether the PIV results are essentially like those produced by VIC+ except for a scaling factor in vorticity is addressed by analyzing the vorticity topology at several set-values of the isosurface. Fig. 6.8a-c illustrates the vorticity magnitude isosurface of the results obtained by tomographic PIV for a value ranging from 0.17 to 0.3 u_τ^2/ν.

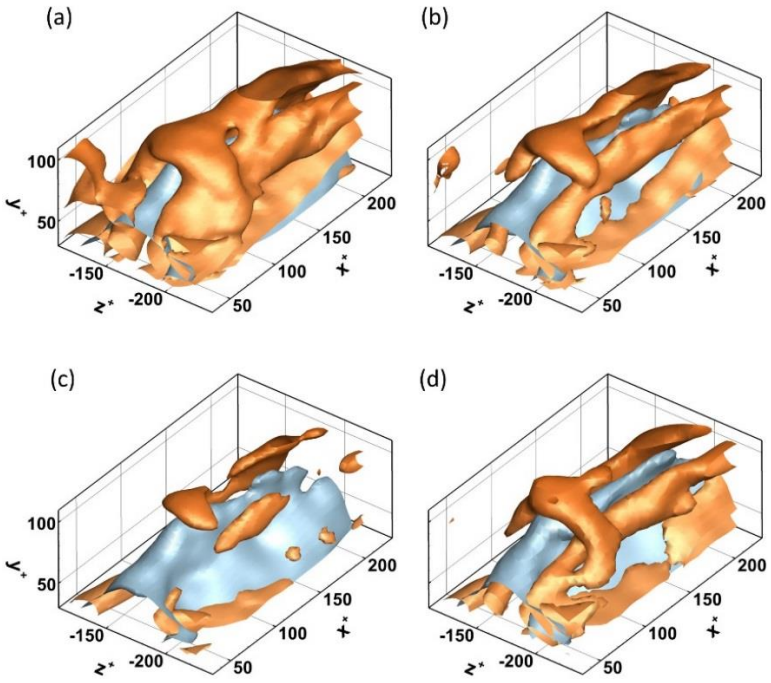

Fig. 6.8 Cut-out of hairpin structure S2. Isosurfaces of vorticity magnitude (orange) and streamwise velocity ($\boldsymbol{u}^+ = 14$, blue). Figures a-c show tomographic PIV with respectively isosurfaces of vorticity magnitude at $|\boldsymbol{\omega}^+|$ = 0.17, 0.23 and 0.3. Figure d shows the VIC+ result with $|\boldsymbol{\omega}^+|$ = 0.3.

For the highest value, details of the vorticity pattern are revealed in the VIC+ data but appear significantly degraded in the PIV results. The same details become somehow more visible in the PIV result when a lower value for the isosurface is chosen. This difference in vorticity magnitude suggests the effective spatial resolution is higher with VIC+ as compared to the tomographic PIV result. The likeness in vortex structure shape is quantified by the cross-correlation coefficient between the PIV and VIC+ vorticity distributions. Specifically, we consider the streamwise vorticity component in the wall parallel plane at $y^+ = 100$. This yields a cross-correlation coefficient of 0.83, which indicates that the vorticity distribution is very similar between the methods apart from a scaling constant. It supports the earlier conclusion obtained from vorticity visualizations.

The instantaneous flow organization is also studied by comparison of the Q-criterion (Hunt et al. 1988). Movies are added as supplementary material with Schneiders et al. (2017), showing the temporal evolution of the vortices visualized by the Q-criterion at three isosurface threshold levels; $Q^+ = 3.5 \cdot 10^{-3}$ (movie 1), $Q^+ = 7 \cdot 10^{-3}$ (movie 2) and $Q^+ = 14 \cdot 10^{-3}$ (movie 3). An extract of the instantaneous flow organization at time $t = 374$ ms is given in Fig. 6.9. The top row shows the results from tomographic PIV analysis and the bottom row shows the VIC+ result. From left to right the results are plotted at the abovementioned thresholds of Q. At each isosurface level of Q, the VIC+ result shows a richer pattern of vortical structures in comparison to tomographic PIV, which is consistent with the earlier observations made upon inspection of the isosurfaces of intense vorticity.

Because the Q-criterion is calculated from squared velocity gradients, similarly to the dissipation rate (Sec. 6.4.4), it is more sensitive to spatial resolution as compared to vorticity, which linearly depends on velocity gradients. Therefore, Q is expected to show more pronounced differences between tomographic PIV and VIC+. The vortical structure indicated by the black arrow, for example, is visible in the VIC+ result at the highest level of Q (Fig. 6.9 bottom-right), but is not reconstructed by tomographic PIV at the lowest level of Q (Fig. 6.9 top-left).

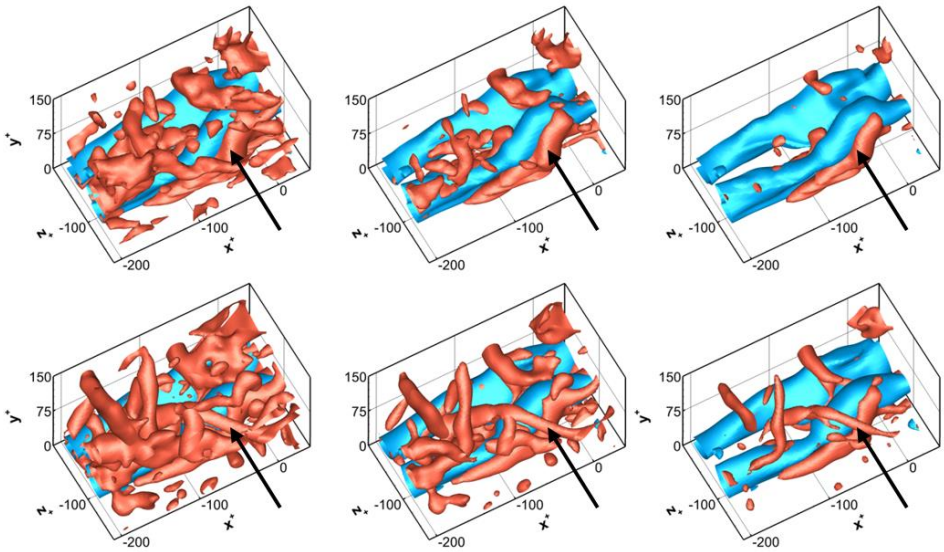

Fig. 6.9 Extract of the instantaneous flow organization at t = 374 ms visualized by isosurfaces of $u'^+ = -2.3$ (blue) and from left to right $Q^+ = 3.5 \cdot 10^{-3}$, $7 \cdot 10^{-3}$, and $14 \cdot 10^{-3}$ (red isosurfaces). The top row shows the results obtained by tomographic PIV and the bottom row the result of VIC+.

6.4.3 Vorticity statistics

The analysis in the previous sections suggests that the VIC+ data evaluation returns increased vorticity magnitude within the vortices and therefore has the potential to restore the original amplitude of vorticity fluctuations. In this section, the differences in vorticity magnitude are quantified using the rms vorticity fluctuations, which are presented in Fig. 6.10. The blue and yellow lines show the results obtained by tomographic PIV with respectively cubic and elongated interrogation volumes. The red lines are for VIC+, while the black lines show the DNS result (Schlatter & Örlü 2010) for reference. The rms vorticity fluctuations by tomographic PIV are approximately 40% lower than the reference DNS level for $y+ > 30$. This applies to all vorticity components. In the near-wall region ($y+ < 30$), a further reduction is observed with the cubic interrogation volumes, in comparison to the elongated volumes. Furthermore, the cubic interrogation *volumes* do not capture the peak in the rms wall-normal vorticity at $y+ = 15$. For comparison, a 35% reduction in rms vorticity is expected for the present PIV interrogation window size

according to Saikrishnan et al. (2006), who assessed the effect of spatial filtering. The reduced vorticity fluctuations by tomographic PIV in the current experiment can therefore be largely ascribed to the effects of spatial filtering of the velocity field.

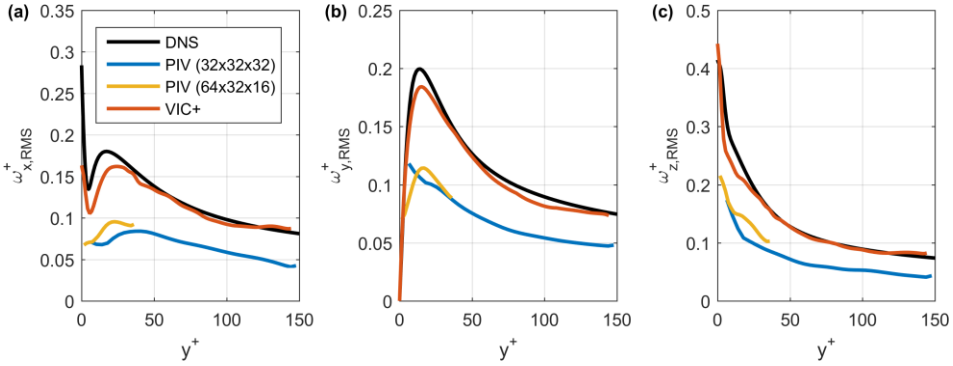

Fig. 6.10 Wall-normal profiles of rms vorticity returned by tomographic PIV with cubic and elongated correlation volumes and with VIC+, in comparison to the DNS result by Schlatter & Örlü (2010). Streamwise (a), wall-normal (b) and spanwise (c) rms vorticity fluctuations.

The red lines in Fig. 6.10 show the VIC+ result. For all three components of vorticity an increase in the level of rms fluctuations can be observed in comparison to tomographic PIV, which is consistent with the visualizations shown in Sect. 4.2. The vorticity fluctuations in all directions (Fig. 6.10) are found within 10% of the reference from DNS for $y^+ > 20$. In the near-wall region ($y^+ < 20$), on the other hand, there is a larger deviation with the DNS even with the VIC+ method, which is attributed to difficulties in resolving the strong velocity gradient in this region near the wall ($y+ < 25$) at a reduced density of identified particle tracks (c.f. Fig. 6.2). The wall-normal vorticity fluctuations (Fig. 6.10b), however, approach zero at the wall, and remain approximately within 10% from the DNS reference along the full profile. The data in Saikrishnan et al. (2006) shows that approximately 90% of the vorticity rms is captured at a spatial resolution of around 10 to 12 wall-units. Based on this, the effective spatial resolution of VIC+ in the present experiment is estimated at < 12 wall-units in all directions.

To assess the size of the coherent fine-scale eddies in the flow, the autocorrelation of the streamwise vorticity component is computed and plotted in Fig. 6.11 for two wall-normal locations. Streamwise vorticity is associated with the streamwise vortices in the near wall region. Based on the -3 dB cut-off point ($R_{\omega,\omega} = 0.5$), the PIV results yield a vortex core size of approximately 16 wall units in spanwise direction. The core size appears insensitive to the wall-normal distance, which is consistent with the constant interrogation window size and the slowly varying vortex radius in turbulent boundary layers (Herpin et al. 2013). Inspecting Fig. 6.11, the VIC+ result shows a smaller vortex core size of 11 wall units. As shown in the Appendix, approximately a factor two smaller cutoff wavelength is expected for VIC+ in comparison to tomographic PIV. The present improvement in vortex core size is less, which suggests that the vortex size returned by VIC+ is determined by the actual vortices in the flow and is not limited by the spatial resolution. This, moreover, is consistent with the rms vorticity fluctuation being nearly resolved by VIC+ (to within 10% of the DNS).

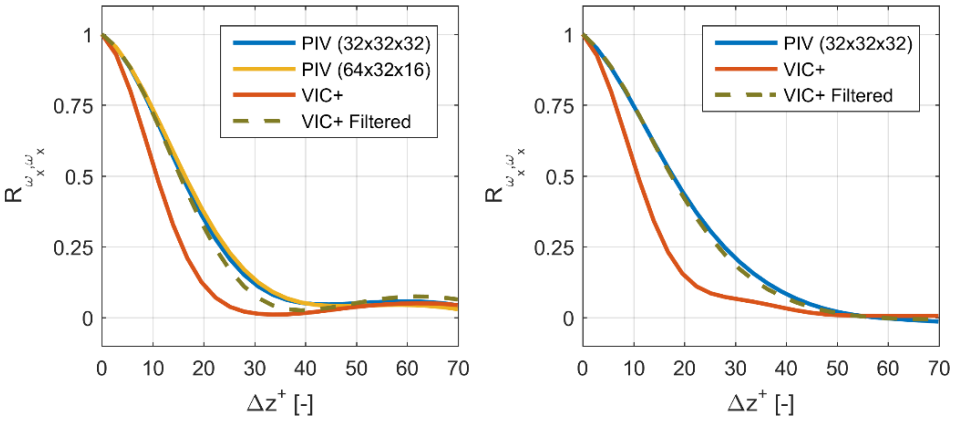

Fig. 6.11 Normalized autocorrelation peak values of x-vorticity at $y+ = 25$ (left) and $y+ = 100$ (right).

For a channel flow at comparable Reynolds number ($Re_\tau = 800$), Tanahashi et al. (2004) report that the diameter of the coherent fine-scale eddies at these near-wall locations is approximately 8 to 9 times the Kolmogorov length scale, where the Kolmogorov length is estimated at 2.5 wall units

(Stanislas et al. 2008). This corresponds to a typical radius of the vortical structures of 10 to 11 wall units, which matches the result obtained by VIC+. It is a further indication that the vortices are resolved. Based on the autocorrelations and the expected coherent fine-scale eddy size, the spatial resolution of the VIC+ method in the present experiment is conservatively estimated to be better than 11 wall units. This compares well to the abovementioned estimated spatial resolution based on the damping of the rms vorticity statistics.

As a consistency check, the VIC+ velocity fields are filtered using a filter approximating the tomographic PIV processing chain used in Jodai and Elsinga (2016). The cross-correlation procedure is approximated using a moving average filter with a 15 wall units volume size, corresponding to the interrogation volume size. Subsequent polynomial filtering is using a 23 wall units moving average filter applied to the velocity gradient. After filtering the autocorrelation of the streamwise vorticity is evaluated, which is included in Fig. 6.11 (dashed line). The results closely resemble the PIV result. It again suggests the VIC+ results approximate the actual flow and that the differences with respect to the tomographic PIV can be understood by the effect of its spatial filter. Moreover, the cross-correlation coefficient between the streamwise vorticity distribution obtained by the filtered VIC+ and PIV is 0.96 at y^+ = 100, which also shows that the filtered VIC+ is nearly identical to the tomographic PIV result.

6.4.4 Dissipation rate

Compared to vorticity, the dissipation rate estimation is even more sensitive to spatial resolution, because it depends on velocity gradients raised to the power two. The underestimation of the dissipation rate by tomographic PIV is a problem recognized in recent literature (Tokgoz et al. 2012) and sub-grid scale modelling approaches have been proposed to improve the estimation of the dissipation rate from PIV (Sheng et al. 2000; Bertens et al. 2015). Following the results in the previous section, an improved dissipation rate estimate is expected with VIC+, in comparison to tomographic PIV. To assess this conjecture, the wall-normal profile of

the turbulent kinetic energy dissipation rate is plotted in Fig. 6.12. The blue and yellow lines show the results obtained by tomographic PIV with respectively cubic and elongated interrogation volumes. The red line shows the VIC+ result. For comparison, the DNS reference is plotted in black.

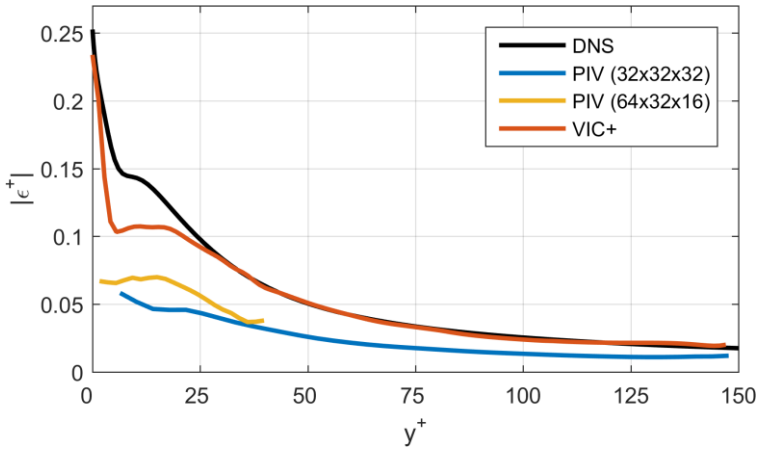

Fig. 6.12 Wall-normal profiles of kinetic energy dissipation rate returned by tomographic PIV with cubic and elongated correlation volumes and with VIC+, in comparison to the DNS result by Schlatter & Örlü (2010).

For the range $40 < y^+ < 140$ the tomographic PIV result with cubic interrogation volumes underestimates the dissipation rate by 50%. For $y+ < 40$, the result of PIV with elongated interrogation volumes follows more accurately the trend of the DNS reference, but the result remains damped by 50% until $y+ = 15$. Closer to the wall the dissipation predicted by PIV remains constant and the near-wall peak value is not captured. The strong damping of the dissipation confirms the difficulties encountered in the abovementioned literature when estimating dissipation from PIV measurements. The VIC+ method yields, on the other hand, a result within 5% of the reference for $y^+ > 25$, with no need to introduce further sub-grid scale models. Closer to the wall, the damping increases and becomes 20% at $y+ = 15$. Moreover, the VIC+ result shows a peak dissipation value at the wall within 8% of the reference value.

6.5 Practical aspects and computational cost

The present section discusses some practical aspects and computational costs of the VIC+ technique in comparison to tomographic PIV. Contrary to tomographic PIV, which can be used for low repetition rate dual-pulse measurements, the VIC+ technique can be applied only when time-resolved Lagrangian particle tracking measurements (e.g. tomographic PTV or Shake-the-Box) are available. The latter are required to provide measurements of both instantaneous tracer particle velocity and its material derivative. When only flow statistics are desired, as in the present work, the requirement for time-resolved measurements can lead to a large measurement dataset and consequentially a large computational burden. The latter was alleviated in the present study by processing short bursts, each separated by approximately a large-scale turnover time (δ_{99}/u_∞) to obtain the statistics. To further reduce storage requirements, the measurement data can also be acquired in bursts to allow for time-resolved particle tracking. With this processing, the computer memory requirements for tomographic PIV and VIC+ are found to be on the same order of magnitude, but the computation time for VIC+ is approximately an order of magnitude longer than for tomographic PIV.

When a full time-series is to be processed for inspection of the flow temporal evolution, however, the computation time required for the iterative VIC+ procedure can be reduced to the level of tomographic PIV cross-correlation. This is done by starting the VIC+ procedure at each time-instant with an estimate of the velocity field based the result from the previous time-instant. The estimated can, for instance, be obtained from a short time advancement of the flow using VIC (Schneiders et al. 2014). This is analogous to the sliding implementation of motion tracking enhanced MART (MTE, Novara et al. 2010) by sequential MTE (SMTE, Lynch and Scarano 2015). The supplementary material provided with Schneiders et al. (2017) shows movies of the Q-Criterion of 1173 ms of flow obtained using this procedure.

6.6 Conclusions

The VIC+ method was applied to an actual turbulent boundary layer experiment at Re_θ = 2038, and was demonstrated to resolve the rms vorticity fluctuations to within 10% of a reference from DNS. In comparison, tomographic PIV analysis yielded approximately 40% damping of the vorticity fluctuations. The VIC+ flow fields comply with the continuity equation and they are consistent with the measured velocity and acceleration of the tracer particles. Additionally, the present vorticity and dissipation statistics match an existing DNS reference to within 5% for $y^+ > 25$, which suggests the VIC+ flow fields are well resolved and accurate. In comparison, dissipation statistics are damped by 50% by tomographic PIV. The novel aspect is that the dissipation statistics are obtained from the measurement without relying on isotropy assumptions or correction factors. The effective spatial resolution of VIC+ in the present experiment was conservatively estimated at 11 wall-units. Isosurface visualizations of instantaneous velocity and vorticity showed increased coherence in the vortical structures at higher isosurface levels. Tomographic PIV, however, revealed similar vortical structures at lower vorticity magnitude. The study demonstrates that the VIC+ method can be applied effectively to actual tomographic PIV and volumetric particle tracking measurements for increased reconstruction quality of vorticity and dissipation. The study is supported by quantification of the spatial response of VIC+ with a sine-wave lattice analysis. The results indicate a twofold increase of spatial resolution with respect to cross-correlation interrogation.

Chapter 7
Full trajectory data assimilation

This work has been presented in
Schneiders, Singh & Scarano (2016) 18th Lisbon Symposium. Lisbon. Portugal

The VIC+ method has in the previous chapters been demonstrated to allow for accurate flow reconstruction from Lagrangian particle tracking experiments, at a fraction of the seeding concentrations required for similar accuracy with tomographic PIV. The method uses a measurement data ensemble of both instantaneous velocity and its material derivative. In the present chapter, it is proposed to increase this measurement data ensemble and use particle tracking measurements over a finite time-interval.

7.1 Working principle

Recent advances in the field of Lagrangian particle tracking algorithms, in particular Shake-the-Box (Schanz et al. 2016), have allowed for measurement of long particle trajectories spanning over more than 10 snapshots in densely seeded flows (comparable to tomographic PIV). It is proposed to extend the VIC+ framework such that it uses the full scattered and sparse velocity time histories available from such Lagrangian particle trajectory measurements.

The original VIC+ method avoids time-integration by only considering instantaneous measurement data. When the data ensemble considers measurements at multiple time-instants, these need to be coupled in by a time-marching procedure.

The proposed method considers an initial condition that is optimized iteratively to minimize the difference between the velocity obtained from VIC time-marching over a finite time-segment and the PTV

velocity measurements in that time-segment (illustrated in Fig. 7.1). This generalization of VIC+ is called 'VIC++' in the present work.

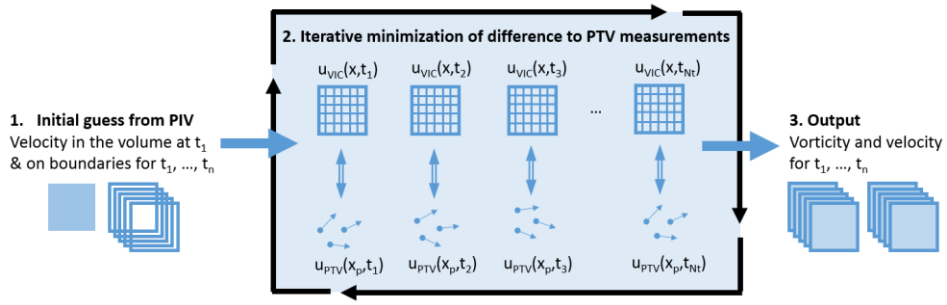

Fig. 7.1 Flowchart of the proposed velocity reconstruction technique

The method relies on the availability of particle trajectories. This requires time-resolved measurements where particles can be observed moving on long tracks (> 10 snapshots) before exiting the measurement domain. The particle trajectories can be obtained from voxel-based approach (e.g. tomographic PTV) or directly from iterative particle reconstruction (IPR, Wieneke 2014; Shake-the-Box, Schanz et al. 2016).

The matrix containing the locations of all particles at each time-instant is $\overline{\overline{\boldsymbol{X}}}_{\boldsymbol{PTV}}$ of a particle trajectory with length N_t. The corresponding particle velocities are collected in the matrix $\overline{\overline{\boldsymbol{V}}}_{\boldsymbol{PTV}}$. The VIC time-integration starting from an initial condition calculates at each measurement time-instant the velocities $\overline{\overline{\boldsymbol{V}}}_{\boldsymbol{VIC}}$ at the particle locations $\overline{\overline{\boldsymbol{X}}}_{\boldsymbol{PTV}}$. Note the integration time-step dt is typically smaller than the measurement time-interval and determined according to the criteria defined in Schneiders et al. (2014). The computational domain is chosen equal to the measurement volume and linear interpolation is used to obtain $\overline{\overline{\boldsymbol{V}}}_{\boldsymbol{VIC}}$ at $\overline{\overline{\boldsymbol{X}}}_{\boldsymbol{PTV}}$ from the computational grid.

A non-linear optimization problem is defined in which the degrees of freedom (i.e. initial and boundary conditions) are iteratively adjusted to minimize the difference between $\overline{\overline{\boldsymbol{V}}}_{\boldsymbol{VIC}}$ and $\overline{\overline{\boldsymbol{V}}}_{\boldsymbol{PTV}}$ (see Fig. 7.1, middle). This difference is quantified in the cost function, J, for the optimization procedure,

(7.1) $J = \sum\left[\overline{\overline{\boldsymbol{V}}}_{\boldsymbol{PTV}} - \overline{\overline{\boldsymbol{V}}}_{\boldsymbol{VIC}}\right]^2.$

A gradient based optimization technique is used (L-BFGS, Liu and Nocedal, 1989) to find the degrees of freedom minimizing the cost function. The degrees of freedom for the optimization are collected in a vector $\boldsymbol{\xi}$. For the gradient based optimization, at each iteration it is necessary to calculate the gradients $dJ/d\boldsymbol{\xi}$. Using finite-differencing, this would come at the cost of the number of degrees of freedom (~ nx×ny×nz) times the number of time-integrations *per iteration.* To avoid this, similar to VIC+ the gradient is calculated efficiently by the numerical adjoint of the VIC code. An efficient implementation of the adjoint was recently written by Azijli (2016). To recall, in short, the adjoint is a mathematical 'trick' to evaluate the gradient $dJ/d\boldsymbol{\xi}$ at the CPU cost of a single time-integration only, but at the cost of increased memory usage. The latter memory usage remains however very limited due to the relatively short time-integrations that are performed along particle trajectories of typically 5-20 snapshots. The iterative procedure is stopped when the cost function J is on the order of the measurement error in the PTV velocity measurements.

Because of the computational cost associated with the extension of VIC+ to include a time-marching procedure, the focus of the present work is on a concept demonstration on the analytical case of a two-dimensional vortex, to investigate the potential of the method. This is done in the next section.

7.2 Numerical assessment

Consider a two-dimensional Gaussian vortex positioned in the center of a simulated measurement plane. The case of such a vortex blob has been used previously for assessment of time-resolved PIV techniques by amongst others de Kat and van Oudheusden (2012), Lynch and Scarano (2014) and Schneiders et al. (2016b). The tangential velocity field induced by the Gaussian vortex blob is given by,

(7.2) $V_\theta = \frac{\Gamma}{2\pi r}\left(1 - e^{-\frac{r^2}{c_\theta}}\right),$

where Γ is the circulation and $c_\theta = r_c^2/\gamma$. Choosing $\gamma = 1.256$, the tangential velocity peaks at the core radius r_c. For the present assessment, $\Gamma/V_p L = 1.75$, where V_p is the peak velocity at the core radius r_c. For illustration, in Fig. 7.2a the resulting analytical vector field is shown. In Fig. 7.2b and c the u-component of velocity and vorticity are shown, respectively.

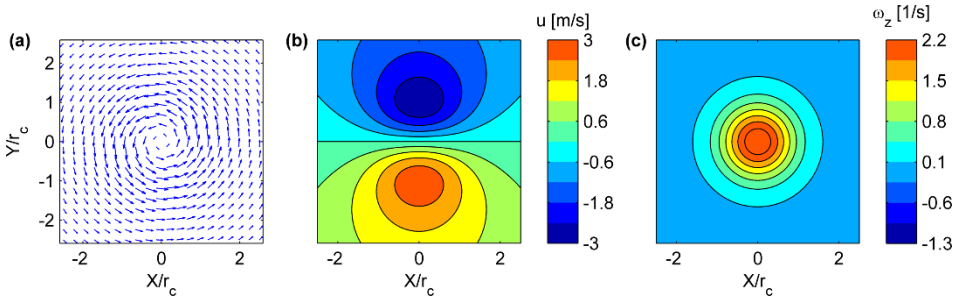

Fig. 7.2 Reference vector field (a), contours of u velocity (b) and vorticity (c).

The measurement plane is chosen to be a square with sides of $2.5r_c$. Simulated PTV measurements are made by seeding a computational plane uniformly with particles. The particles are integrated over time with the RK4 method, where the instantaneous velocity is provided by the analytical flow field given by (2). Scattered velocity measurements are taken from the analytical flow field at the particle locations at a time-separation of $\Delta t = 0.2$. The total measurement duration is taken to be $N_t =$ 40-snapshots. As discussed in the introduction, established techniques to interpolate velocity at t_i from the scattered particle positions onto a dense grid use only the instantaneous velocity measurements t_i. In the present study, trilinear interpolation and adaptive Gaussian windowing (AGW, Agüí and Jimenez 1987) are taken as examples of such techniques. The proposed vortex-in-cell technique can also be applied to a single velocity measurement, which results in a divergence free interpolation of the scattered velocity measurements. For all methods, velocity is interpolated to a regular grid with 20 x 20 vectors. For the vortex-in-cell methods, homogeneous padding type boundary conditions (Schneiders et al. 2016a) are employed.

The results are first assessed by comparison of contour plots of instantaneous velocity. The instantaneous analytical u-component of velocity is shown in Fig. 7.3a. A seeding concentration at which $N_p = 10$ tracer particles are present within at the measurement plane is considered. The result of tri-linear interpolation of the scattered velocity measurements to a regular grid is shown in Fig. 7.3b.

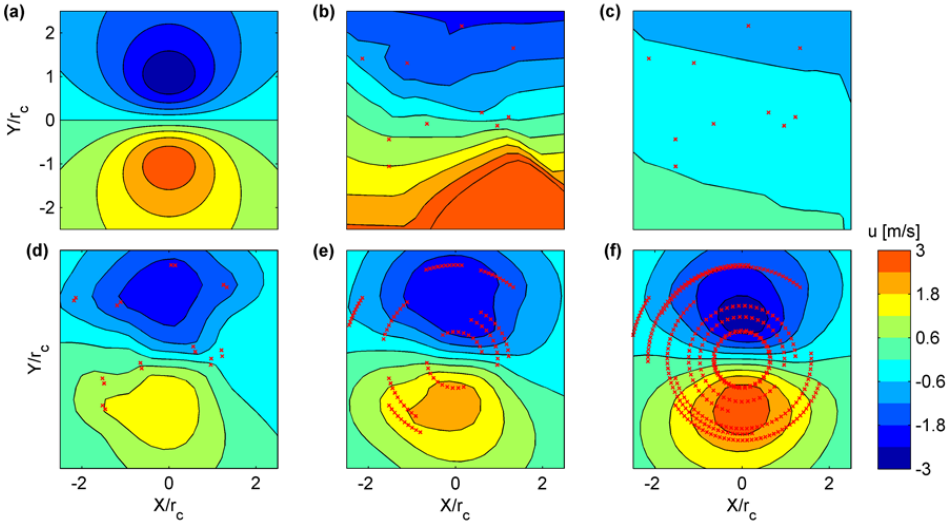

Fig. 7.3 Contours of the x-component of velocity. Reference flow field (a), linear interpolation (b), AGW (c) and the proposed method with $N_t = 2$, 10 and 40 (d-f, respectively)

The instantaneous particle locations are visualized by the red crosses in the figure. The linear interpolation result returns exactly the velocity measurement at the particle locations. In between the measurements, on the other hand, the result is affected by the limited tracer particle concentration and the two concentrated extrema in the velocity field (Fig. 7.3a) are not found by the linear interpolation (Fig. 7.3b). The adaptive Gaussian windowing technique returns the weighted averaged velocity field at each grid node, and therefore a filtered result is expected in comparison to the linear interpolation. This is confirmed by the AGW result in Fig. 7.3c, which is similar to the result of the linear interpolation (Fig. 7.3b), but shows a reduced velocity gradient.

The proposed vortex-in-cell technique can be employed for an instantaneous reconstruction using only one or N_t = 2 velocity measurement, to yield essentially a divergence free reconstruction of the flow. Because this imposes a physics-based restriction on the flow reconstruction, improved accuracy of the velocity reconstruction in between particles is expected. This is confirmed by the result in Fig. 4d, which shows the vortex-in-cell reconstruction using just two velocity time instants (N_t = 2). The result shows the two discrete extrema of u in the reconstruction. When more measurement time-instants are used for the instantaneous velocity reconstruction, a further regularization of the velocity is expected. Fig. 7.4e and f show the results using N_t = 10 and 40 measurement time-instants, respectively. The red crosses show the particle trajectories over the respective time-durations used for velocity reconstruction. When 40 time-instants are employed, the resulting velocity field is practically symmetric and shows the same contour levels as the reference solution (Fig. 7.3a). The towards the edges of the domain, the velocity decreases, which is expected as no particles are present in this region.

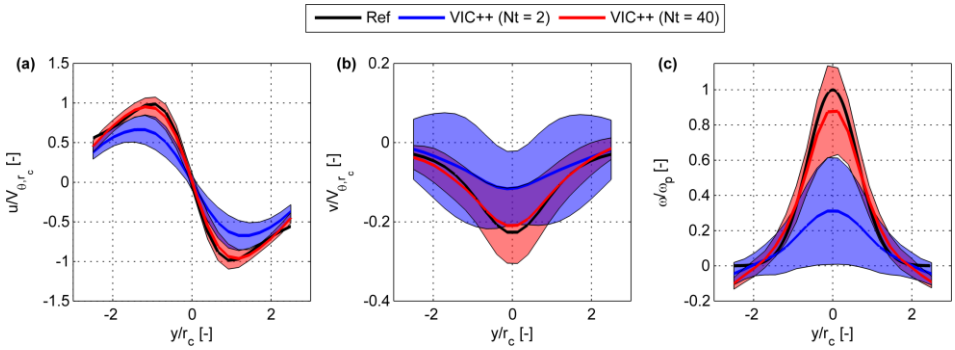

Fig. 7.4 Average center-line profiles of the velocity components u (a) and v (b) and vorticity (c), calculated from 50 random initializations of the tracer particles.

The results plotted in Fig. 7.3 depend on the particle locations, in particular for the methods that use only a limited number of time-instants for velocity interpolation. To inspect more closely the differences between short (N_t = 2) and long (N_t = 40) track lengths used for velocity

reconstruction, Fig. 7.4a and b show the average profiles along the center line of the measurement plane is given for the u and v components of velocity. The profiles are averaged from multiple random initializations of the particle locations. On average, 10 tracer particles were present in the measurement plane. The analytical profiles are plotted in black. The results for N_t = 2 and 40 are shown in blue and red, respectively. The shaded area represents the standard deviation from the mean results, which represents the variation in the reconstruction quality depending on the particle locations. As expected from the results in Fig. 7.3, when a longer trajectory is used for reconstruction, the peak velocities are approximated more accurately – at the same seeding concentration.

The improved estimation of the peak velocities when more time-instants are used for reconstruction is expected to yield a more accurate estimation of the peak vorticity levels. The vorticity contour plots are presented in Fig. 7.5. The figures follow the layout of the velocity contour plots (Fig. 7.3) discussed above, and again the particles trajectories used for reconstruction are plotted by the red crosses.

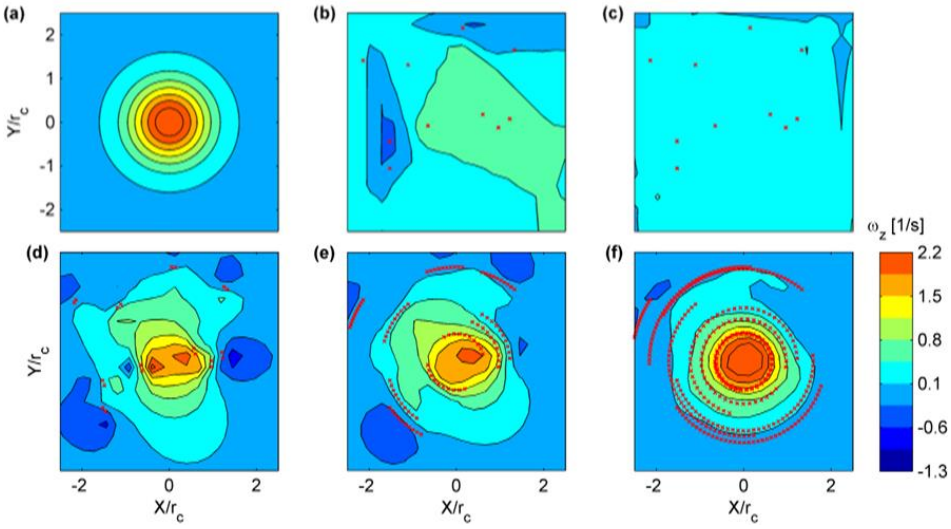

Fig. 7.5 Contours of vorticity. Reference flow field (a), linear interpolation (b), AGW (c) and the proposed method with Nt = 2, 10 and 40 (d-f, respectively).

As can be expected from the filtered results obtained by the linear interpolation and adaptive Gaussian windowing techniques (Fig. 7.3b

and c, respectively), the vortex blob is not identified by the contours plotted (Fig. 7.5b and c). The situation is much improved when the divergence free condition is enforced for the reconstruction (Fig. 7.5d). The shape of the vortex is however affected by the instantaneous particle locations and two peaks are visible in the reconstruction. When more time-instants are used (N_t = 10, Fig. 7.5e), the result is further regularized and practically circular for N_t = 40 (Fig. 7.5f). The statistically averaged profiles for vorticity are plotted in Fig. 7.4c, which confirms that with N_t = 40, the peak vorticity value is better resolved than when essentially only a divergence free reconstruction is made with N_t = 2. It should be remarked that the slight negative vorticity towards the domain boundaries follows from the fixed homogenous velocity boundary conditions used for this assessment.

For a more quantitative comparison of the results, the rms error level of velocity with respect to the analytical solution is evaluated in the domain center (x, y = $-r_c/2$ to $r_c/2$) and plotted in Fig. 7.6, which shows the rms error variation with seeding concentration, for the different interpolation techniques considered. The error is normalized by the peak velocity value.

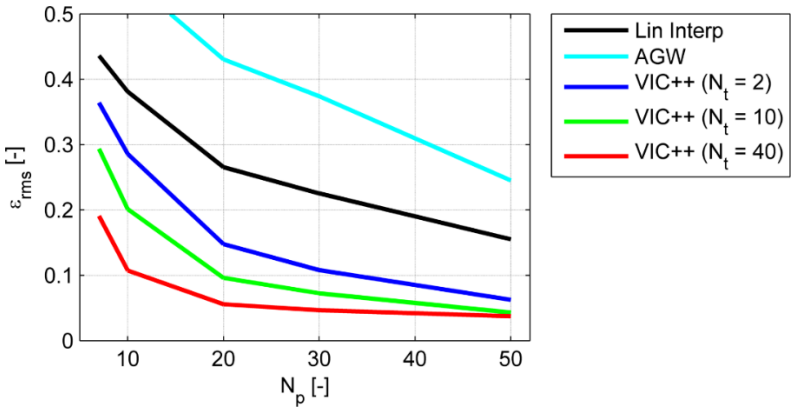

Fig. 7.6 Velocity rms error variation with number of particles and reconstruction technique.

When the number of particles used for the interpolation increases, the rms error decreases. More noteworthy, for all seeding concentrations, the error decreases when a longer time-series is used for the VIC++ reconstruction. The flattening of the $N_t = 40$ result for large Np is ascribed to the finite and relatively coarse grid size used for the reconstruction. This shows the potential of the novel technique to improve velocity accuracy in cases where time-resolved measurements are available.

7.3 Conclusions

The novel concept of using full particle trajectory measurements with vortex-in-cell simulations to allow for a dense interpolation of velocity in the measurement region is outlined and demonstrated on the numerical case of vortex blob. For all seeding concentrations considered, the use of longer particle trajectories yields a more accurate reconstruction of the velocity field. The study demonstrates the potential of assimilation of long Lagrangian particle trajectory measurements (e.g. from tomographic PTV or "Shake-the-Box") with vortex-in-cell simulations for increased accuracy of velocity and vorticity measurements.

Chapter 8
Uncertainty quantification by track benchmarking

This work has been published in
Schneiders and Sciacchitano (2017) Meas. Sci. Technol. 28:065302

The development Lagrangian particle tracking techniques have led to the introduction of new interpolation techniques for evaluation of velocity on a regular grid. Some of those techniques discussed extensively in the previous chapters, such as FlowFit (Schanz et al. 2016) and VIC+ (Schneiders and Scarano 2016), leverage constraints based on the flow governing equations, which allow for example for dense interpolation based on an increased measurement data ensemble containing both velocity and its material derivative. Because these techniques do not rely on cross-correlation and are consistent with (part of) the flow governing equations, uncertainty quantification techniques for planar PIV and tomographic PIV cannot be used. Therefore, in this chapter an uncertainty quantification technique for velocity fields obtained from dense interpolation of particle tracking measurements is introduced.

8.1 Background

A wide range of techniques to quantify uncertainty of planar PIV measurements have been and are being proposed (see for instance Kähler et al. 2012b; Timmins et al. 2012; Charonko and Vlachos 2013; Sciacchitano et al. 2013; Wilson and Smith 2013; Neal et al. 2015; Sciacchitano et al. 2015; Wieneke 2015; Xue et al. 2015; Scharnowski and Kähler 2016). Similarly, also uncertainty quantification techniques for tomographic PIV is an active research field (e.g. non-zero divergence check, Scarano and Poelma, 2009, Atkinson et al. 2011). As noted above, however, to-date these

techniques are not suitable for example for VIC+ or FlowFit, motivating the development of a new technique.

The manuscript by Agüí and Jiménez (1987), proposing the adaptive Gaussian windowing (AGW) technique for interpolation of scattered PTV data onto a regular grid, includes a dedicated uncertainty quantification approach that has received little attention within the PIV community. The method performs multiple velocity interpolations to a grid at a single measurement time-instant. For each interpolation, a different set of particle velocity measurement is used. Each set has the same size as the full set of particle velocity measurements at the considered time-instant, but is randomly drawn with repetition. The resulting velocity fields on the grid are subsequently compared to the full measurement dataset to estimate the measurement uncertainty. Stüer and Blaser (2000) use a similar method, but instead of randomly drawing measurements with repetition for each interpolation, they perform N_v local velocity interpolations in small volumes of N_v particles, where for each interpolation one measurement is left out. The left-out measurement is subsequently used as reference velocity for estimating the interpolation error. Both techniques described above are classified as cross-validation techniques (Efron 1979) and in particular as bootstrapping and jackknifing techniques (Benedict and Gould, 1996), respectively. The techniques use multiple velocity interpolations to a grid per time-instant, where the jackknifing technique uses as many dense interpolations as particles. Considering that the number of particles can easily be on the order of 10^4 in three-dimensional measurement volumes (see e.g. the experiment of a jet flow in the present work), the above approaches would yield excessive computational cost especially for recent relatively complex adjoint-based dense interpolation techniques involving the Navier-Stokes equations that require significant computational cost to obtain velocity fields (see e.g. Schneiders et al. 2016).

Recent literature on techniques that perform dense velocity interpolation using the Navier-Stokes equations has not used the abovementioned or similar cross-validation technique for uncertainty quantification. In absence of a general uncertainty quantification

technique for velocity interpolations for PTV data, the assessment of the measurement quality remains largely qualitative or based on the statistical evaluation of quantities known from a direct numerical simulation (DNS). The ideas proposed by the abovementioned cross-validation techniques, however, allow for formulation of a cost-effective uncertainty quantification technique. In the present work, the authors propose a generalized technique for a-posteriori uncertainty quantification of Lagrangian particle tracking measurements interpolated onto a grid. The proposed technique, called the *track benchmarking method* (TBM), estimates the uncertainty of the velocity at each grid point. The method distinguishes between bias and random uncertainty, where it should be noted that only measurement bias introduced by the velocity interpolation technique is estimated. Such bias occurs due to for example limited seeding concentration or incorrect positioning of a wall boundary condition. Conversely, the approach does not estimate a bias due to unresolved length scales in the scattered particle tracking measurements, i.e. spatial modulation along tracks. The technique is assessed by means of a simulated experiment, where the ground-truth velocity field is known (Sec. 8.3). In addition, the application to a circular jet flow in water is shown to demonstrate the practical use of the technique in cases where a ground-truth or reference velocity is not available (Sec. 8.4). In both sections, the recently introduced VIC+ technique is used for velocity interpolation, which uses the vorticity transport equation for consistent velocity interpolation. This provides a practical application for the method and in the experimental validation the measurement uncertainty of VIC+

8.2 Track benchmarking method (TBM)

The track benchmarking method quantifies the uncertainty of dense velocity interpolations from scattered PTV measurements onto a grid. In the present work, the *bias uncertainty* and *random uncertainty* are defined as the TBM estimate of the mean bias error and error standard deviation, respectively, in the velocity interpolation.

The underlying hypothesis of the TBM approach is that the PTV velocity measurements have locally higher accuracy than the velocity interpolation onto a grid point. This is motived by comparison of the expected order of magnitude of the PTV measurement accuracy and the interpolation errors. The particle position error is typically a fraction of the particle image size, d_p. The instantaneous particle velocity is evaluated from the temporal derivative of a continuous function (e.g. polynomial, B-Spline) that is fitted through a particle trajectory of typically five to twenty snapshots. This reduces the measurement error proportional to approximately $N^{3/2}$, where N is the track length. Care is to be taken that errors are not increased by filtering of high frequencies that are caused by the flow, as discussed in amongst others Novara and Scarano (2013) and Schanz et al. (2016). Therefore, the accuracy of particle tracking measurements at the scattered particle locations is expected to be a fraction of $d_p/N^{3/2}$. Conversely, interpolation errors in the gridded velocity field scale with the local flow velocity and occur for wavelengths that are smaller than those that can be resolved by the measurement. At a certain particle image density and corresponding seeding concentration, C, the latter is typically on the order of $O(C^{-1/3})$. In addition, an interpolation technique may introduce errors that are not present in the particle tracking measurements, such as noise amplification or a bias following prescription of a boundary or an incompressibility assumption. The TBM technique is designed for uncertainty quantification in such cases, where errors introduced by a dense velocity interpolation technique dominate the error in the particle tracking measurements.

The proposed uncertainty quantification method takes as input the PTV measurement data, which is split into two separate datasets as indicated in the flow chart of Fig. 8.1. A set of *reconstruction tracks* is considered that typically contains 95% of the particle track measurements, randomly selected from the full measurement dataset. The remaining particle track measurements (typically 5% of the total) constitutes the *benchmark tracks* dataset.

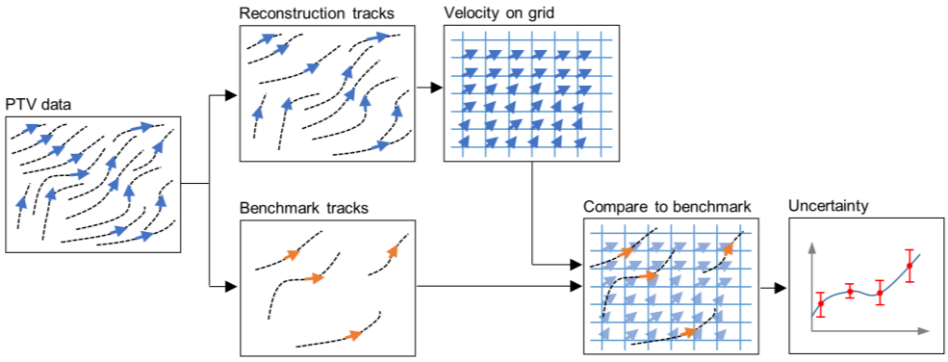

Fig. 8.1 Flowchart of the track benchmarking method (TBM).

Using the reconstruction set, the dense velocity interpolation to a grid is performed. The benchmark track dataset is not used for the velocity interpolation. The benchmark measurements of velocity, $\boldsymbol{u}_b$, are considered independent velocity measurements for uncertainty estimation. The local and instantaneous discrepancy between the gridded velocity field, $\boldsymbol{u}_h$, and the benchmark results is calculated at each data point, $\boldsymbol{x}_{b,i}$, and time, t_j, in the benchmark set using:

$$\boldsymbol{\varepsilon}(\boldsymbol{x}_{b,i}, t_j) = \boldsymbol{u}_h(\boldsymbol{x}_{b,i}, t_j) - \boldsymbol{u}_b(\boldsymbol{x}_{b,i}, t_j), \tag{8.1}$$

where $i = [1 \ldots N_b]$ with N_b the number of measurements in the benchmark track dataset. Notice that the gridded velocity $\boldsymbol{u}_h$ needs to be evaluated at the location $\boldsymbol{x}_{b,i}$ of the benchmark measurements, which corresponds to scattered instantaneous particle positions. For techniques that yield an analytical representation of the velocity field (e.g. FlowFit yields a B-Splines field), $\boldsymbol{u}_h$ can be evaluated analytically at $\boldsymbol{x}_{b,i}$. When the velocity is available only at discrete grid points, interpolation is used to evaluate $\boldsymbol{u}_h$ at the particle location. Such interpolation does not introduce significant additional errors because the grid point spacing is typically much smaller than the average inter-particle distance (e.g. 64 times oversampling with VIC+, Schneiders and Scarano 2016). In the present work, cubic spline interpolation is used.

The bias and random uncertainty in the measurement is subsequently obtained by evaluating the mean and standard deviation of $\boldsymbol{\varepsilon}(\boldsymbol{x}_{b,i}, t_j)$ over the measurement time-series in small interrogation bins,

analogous to the ensemble 3D PTV approach for evaluation of statistics from a PTV measurement time-series (Agüera et al. 2016). The resulting uncertainty of the measurement time-series are called $\boldsymbol{\epsilon}_{TBM,b}(\boldsymbol{x})$ and $\boldsymbol{\epsilon}_{TBM,\sigma}(\boldsymbol{x})$ for the bias and random uncertainty, respectively. Hence, at a location $\boldsymbol{x}_i = (x_i, y_i, z_i)$ and a bin size $2W$, the following equations are used to obtain the uncertainty from all N_i benchmark track results within the bin $\|\boldsymbol{x} - \boldsymbol{x}_i\|_\infty < W$ equals:

$$\boldsymbol{\epsilon}_{TBM,b}(\boldsymbol{x}_i) = \frac{1}{N_i}\sum_{j=1}^{N_i} \boldsymbol{\varepsilon}_j, \tag{8.2}$$

$$\boldsymbol{\epsilon}_{TBM,\sigma}(\boldsymbol{x}_i) = \left[\frac{1}{N_i - 1}\sum_{j=1}^{N_i}\left(\boldsymbol{\varepsilon}_j - \boldsymbol{\epsilon}_{TBM,b}(\boldsymbol{x}_i)\right)^2\right]^{1/2}. \tag{8.3}$$

Note that the bias uncertainty only includes an estimate of a bias introduced by the velocity interpolation technique. The TBM approach does not estimate a bias present in the PTV measurement data. The procedure is summarized by the flow-chart in Fig. 8.1.

The bin size is typically chosen on the order of the interrogation volume size for PIV or on the order of the mesh spacing used for the dense velocity interpolation technique. The uncertainty of the TBM results is estimated by general uncertainty estimation of the mean and standard deviation (Benedict and Gould 1996),

$$\boldsymbol{U}_b = \frac{\boldsymbol{\epsilon}_\sigma}{\sqrt{N}} \tag{8.4}$$

$$\boldsymbol{U}_\sigma = \frac{\boldsymbol{\epsilon}_\sigma}{\sqrt{2(N-1)}} \tag{8.5}$$

where $\boldsymbol{U}_b$ and $\boldsymbol{U}_\sigma$ are the uncertainty of the TBM bias and random uncertainty, respectively, and N is the number of benchmark tracks in the data ensemble.

At the cost of increased computational cost, the TBM approach can also be used for uncertainty quantification in instantaneous velocity field. Instead of evaluating the mean and standard deviation over the full measurement ensemble, they are evaluated at a single time-instant from the benchmark track results obtained from twenty reconstructions at the

single time-instant. For each of these reconstructions, a unique and randomly selected 5% of benchmark tracks is used to increase the benchmark track data ensemble for uncertainty quantification. The interrogation bin size is chosen to contain 9 benchmark tracks to obtain local random uncertainty estimates at an accuracy of 25% by eq. (8.5).

The above procedures rely on the assumption that the scattered PTV measurements have higher accuracy than the velocity on the measurement grid, as motivated above. Any error in benchmark track measurements that is not compensated for by the fitting algorithm yields an overestimation of the measurement uncertainty. This can be understood by considering a hypothetical perfect gridded velocity field of a uniform flow. In this case, the TBM approach gives the random error of the PTV velocity measurements, and not that of the hypothetically exact interpolated values. To avoid such overestimation, a *corrected* TBM (cTBM) random uncertainty is obtained by subtracting the root mean squared (rms) error in the PTV measurements,

$$\epsilon_{cTBM,\sigma} = \sqrt{\epsilon_{TBM,\sigma}^2 - \epsilon_{u,PTV}^2}, \tag{8.6}$$

where $\epsilon_{u,PTV}$ is the rms error in the PTV velocity measurements and $\epsilon_{TBM,\sigma}$ is the random uncertainty obtained by TBM. The former is related to the rms particle position error, $\epsilon_{x,PTV}$, by eq. (8.7),

$$\epsilon_{u,PTV}^2 = \alpha \Delta t^{-2} \epsilon_{x,PTV}^2, \tag{8.7}$$

where Δt is the pulse time separation and α is the propagation coefficient depending on the type of particle position regularization that was used. In the case a polynomial fit is used to regularize the particle positions, the coefficient α can be obtained using standard uncertainty propagation techniques applied to the polynomial (i.e. Savitzky-Golay) filter coefficients given in Gorry (1990). It should be remarked that here again it is assumed that random errors are dominant over truncation errors due to low-pass filtering of the particle tracks. The coefficient α is given in Tab. 8.1 for a range of polynomial fit kernel sizes and orders. The particle position error, $\epsilon_{x,PTV}$, that is required for solution of eq. (8.7) is typically

not known and depends on the reconstruction technique that is used (e.g. MART, Elsinga et al. 2006; IPR, Wieneke 2013 among others) and the peak finding algorithm (e.g. 3-point Gaussian, Willert and Gharib 1997). In absence of additional information, $\boldsymbol{\epsilon}_{x,PTV}$ can be approximated by the root mean squared value of the difference between the measured and fitted particle positions,

$$\boldsymbol{\epsilon}_{x,PTV} = \sqrt{\frac{1}{N}\sum_{i=1}^{N}\left(\boldsymbol{x}_{fitted} - \boldsymbol{x}_{measured}\right)^2}. \tag{8.8}$$

Tab. 8.1 Coefficients, α, for propagation of the unfitted rms particle position error to the rms displacement error calculated from a polynomial fit for a range of kernel sizes.

kernel	1st and 2nd order	3rd and 4th order
3	$5.0000 \cdot 10^{-1}$	-
5	$1.0000 \cdot 10^{-1}$	$9.0278 \cdot 10^{-1}$
7	$3.5714 \cdot 10^{-2}$	$2.6257 \cdot 10^{-1}$
9	$1.6667 \cdot 10^{-2}$	$1.1434 \cdot 10^{-1}$
11	$9.0909 \cdot 10^{-3}$	$6.0379 \cdot 10^{-2}$
13	$5.4945 \cdot 10^{-3}$	$3.5846 \cdot 10^{-2}$
15	$3.5714 \cdot 10^{-3}$	$2.3046 \cdot 10^{-2}$
17	$2.4510 \cdot 10^{-3}$	$1.5702 \cdot 10^{-2}$
19	$1.7544 \cdot 10^{-3}$	$1.1183 \cdot 10^{-2}$
21	$1.2987 \cdot 10^{-3}$	$8.2485 \cdot 10^{-3}$
23	$9.8814 \cdot 10^{-4}$	$6.2591 \cdot 10^{-3}$
25	$7.6923 \cdot 10^{-4}$	$4.8624 \cdot 10^{-3}$

8.3 Numerical assessment

The numerical assessment considers simulated volumetric particle tracking experiments in a turbulent boundary layer (u_∞ = 10 m/s, Re_δ = 8185) from the DNS dataset of Bernardini and Pirozzoli (2011). This dataset has been used prior to this work by Pröbsting et al. (2013), Lynch and Scarano (2015) and Schneiders and Scarano (2016) for assessment of novel PIV and PTV techniques. Tomographic measurements are obtained following a similar approach as in Lynch and Scarano (2015). Tracer

particles are homogeneously seeded in the measurement volume and their motion is obtained using a fourth-order Runge-Kutta time-marching approach. A 4-camera tomographic configuration is chosen where the cameras are positioned at 30° normal to the wall along both directions. Time-resolved measurements are simulated at an acquisition frequency of 10 kHz. Two-dimensional particle images are obtained using the pinhole camera model by Tsai (1987). The resulting particle size is approximately 3 voxels. Triangulation of the particles and particle tracking is performed using Shake-the-Box (Schanz et al. 2016). Velocity measurements are obtained by fitting a cubic polynomial through the particle trajectories over a track length of 9 snapshots. Further details of the experiment are listed in Tab. 8.2.

Tab. 8.2 Simulated experiment parameters

Free stream velocity	u_∞	10 m/s
Boundary layer thickness	δ_{99}	9.4 mm
Reynolds number	Re_δ	8185
Measurement volume	$L_x \times L_y \times L_z$	$20 \times 10 \times 37$ mm^3
		$470 \times 250 \times 890$ voxels
Acquisition frequency	f_a	10 000 Hz
Seeding concentration	C	2 000 particles/δ_{99}^3

In addition, instead of using the STB result, a simulated measurement is considered where the particle positional error is accurately controlled by considering ground-truth particle tracks with particle positions that are purposely corrupted by Gaussian noise with a 0.2 voxels standard deviation to simulate a typical random error. Both short 2-snapshot particle tracks and longer 9-snapshot time-resolved particle tracks are considered. In the time-resolved case, the particle positions are regularized by fitting of cubic polynomial through each particle track. This is expected to improve both the velocity interpolation and the uncertainty quantification in comparison to the double-pulse case, due to reduced random errors in particle position and velocity (Novara and Scarano 2013). It should be remarked that for the double-pulse case, the TBM approach bears similarity to the image matching technique by

Sciacchitano et al. (2013) for planar PIV measurements, which considers the particle disparity vectors within PIV interrogation windows for uncertainty estimation.

For evaluation of velocity onto a dense regular grid, the VIC+ technique (Schneiders and Scarano 2016) is used. This method obtains a velocity field consistent with the vorticity transport equation by using particle tracking measurements of both instantaneous particle velocity and acceleration. In the double-pulse case, where no particle acceleration measurements are available, divergence free interpolation by VIC is used. For implementation details for both interpolation techniques, the reader is referred to Schneiders and Scarano (2016).

The flow organization obtained at a single-time instant in the measurement time-series is visualized in Fig. 8.2 by isosurfaces of vorticity magnitude (grey) and low- and high-speed streaks (blue and red). The left figure shows the result from the double-pulse experiment and the right figure the time-resolved result. Upon visual inspection, the double-pulse result seems affected by a significant random noise component in comparison to the time-resolved result.

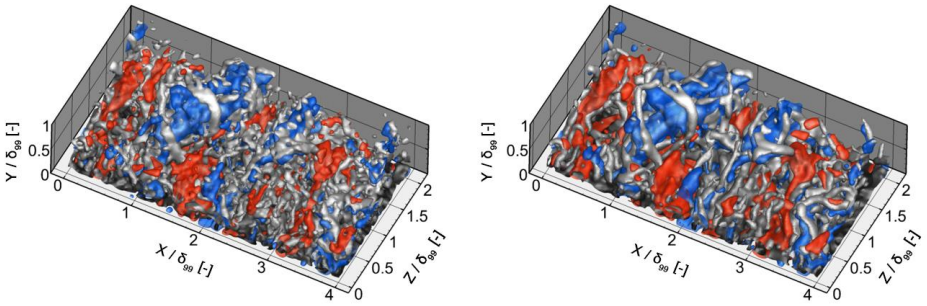

Fig. 8.2 Instantaneous flow organization in the turbulent boundary layer, visualized by isosurfaces of vorticity magnitude (grey, $|\omega| = 2000$ Hz) and low speed (blue, $u'/u_\infty = -0.05$) and high-speed streaks (red, $u'/u_\infty = +0.05$). Double-pulse VIC (*left*) and time-resolved VIC+ (*right*). Axes normalized by δ_{99}.

A typical assessment for the quality of the velocity measurement relies upon the evaluation of the velocity divergence (c.f. Scarano and Poelma 2009; Jodai and Elsinga 2016), which is expected to be zero in an

incompressible flow. However, both results of the VIC-based methods yield a divergence free flow field, because they require the resulting velocity field to satisfy the continuity equation, as validated in Schneiders et al. (2017). Hence, uncertainty quantification approaches based on non-zero divergence cannot be used. The uncertainty however can be readily calculated using TBM. The statistical uncertainty in the full measurement time-series is discussed first in Sec. 8.3.1. Subsequently, instantaneous uncertainty quantification is discussed in Sec. 8.3.2.

8.3.1 Statistical uncertainty quantification

A sequence of 100 images is considered for the analysis and the TBM bias and random uncertainty are calculated using 5% benchmark tracks from the 100 time-instants. For increased convergence, the results are averaged in the spanwise and streamwise directions. The averaging bin size in wall-normal direction is set equal to the vector spacing of 2.3 voxels resulting in 600 benchmark tracks per bin. Following eq. (8.4) and (8.5) this sample size is expected to yield bias and random uncertainty estimates with 4% and 3% accuracy, respectively. The accuracy of the TBM result is assessed via comparison of the uncertainty with the true error, which is obtained as the difference between reconstructed and ground-truth velocity. In this numerical assessment, the true error is available from the instantaneous DNS results.

The wall-normal uncertainty profiles are plotted in Fig. 8.3. The top figure shows the results for the $N_t = 2$ case and the bottom figures the $N_t = 9$ case. The black lines give the ground-truth bias (dashed line) and random error (solid line) calculated from comparison to the DNS reference. Near the wall, a negative bias (i.e. underestimation of velocity) is found for both the $N_t = 2$ and $N_t = 9$ cases in the streamwise velocity component (left figures). This is ascribed to the no-slip condition forcing the velocity to zero at the wall, and the lack of spatial resolution to resolve accurate the strong near-wall gradients resulting in a systematic underestimation of the velocity.

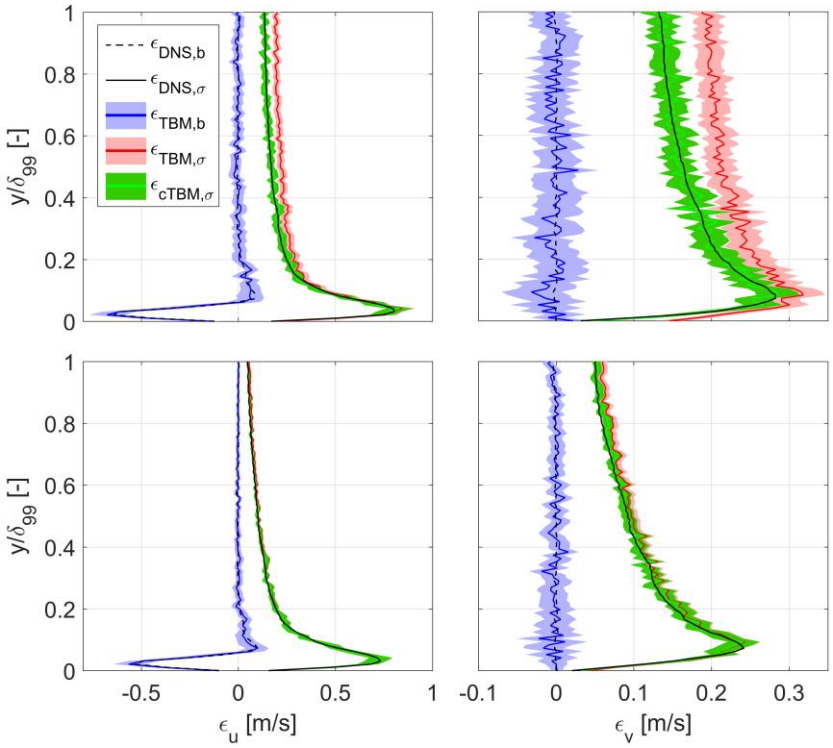

Fig. 8.3 Wall-normal profiles of the uncertainty on velocity in the case of double-pulse PTV (*top figures*) and time-resolved PTV (*bottom figures*). Streamwise (*left*) and wall-normal (*right*) velocity components. The shaded areas indicate the ±3U uncertainty in the TBM results.

The bias uncertainty obtained by TBM is also plotted in blue in Fig. 8.3 and given by the blue line. The shaded areas indicate the ±3U_b uncertainty in the TBM results. The negative near-wall bias in the streamwise velocity is indicated by TBM within 5% of the reference error obtained from DNS in both N_t = 2 and N_t = 9 cases, which corresponds well to the estimated uncertainty of the TBM bias uncertainty of 4%.

The random uncertainty in the streamwise velocity component (left figures) and the wall-normal velocity component (right figures) are highest near the wall, which is ascribed to the smaller velocity scales present in this region that are truncated by the velocity interpolation. Note that at the wall the random error goes to zero because the no-slip condition is enforced. The TBM uncertainty (red lines) also shows this

trend for both the double-pulse and time-resolved case. Closer inspection of the double-pulse case (top figures) shows an overestimation of the actual error by the TBM technique. As discussed in Sec. 8.2, this overestimation is ascribed to measurement errors in particle position. In this numerical assessment, the positional error equals $\boldsymbol{\epsilon}_{x,PTV} = 0.2$ voxels. Because in the double-pulse case the displacement is calculated using first order finite differences, the error on the displacement equals $\boldsymbol{\epsilon}_{u,PTV} = \boldsymbol{\epsilon}_{x,PTV}\sqrt{2} = 0.2\sqrt{2}$ voxels. Subsequently the corrected uncertainty is calculated using eq. (8.6) and also plotted in Fig. 8.3-top (green lines). It yields good agreement with the ground-truth error, which confirms that the overestimation by the TBM method in the double-pulse case is largely due to particle positional errors in PTV measurement. It should be remarked that in practical cases for double-pulse PTV measurements, the error $\boldsymbol{\epsilon}_{x,PTV}$ is not readily available and cannot be approximated using eq. (8.8). An estimate of the positional error of 0.2 voxels could be used based on assessments using synthetic data (Wieneke 2013). Alternatively, in case the measurement region contains a region with known flow speeds (e.g. free-stream), this region can be used to obtain the rms velocity errors in the particle tracking measurements. In the present experiment, the free-stream is not captured, but the standard deviation of streamwise velocity at $y/\delta_{99} = 1$ equals 0.31 voxels and provides an upper bound to the actual particle velocity measurement error of 0.28 voxels.

In the time-resolved case (Fig. 8.3-bottom), the error of the VIC+ interpolation to the dense grid is lower than in the double-pulse case. The possibility to fit a smooth function through the particle positions effectively reduces the positional error on the particles, reducing random errors in the measurements and increasing measurement accuracy. This also benefits the uncertainty obtained by TBM, as the difference between the corrected and standard TBM result reduces with increasing particle tracking accuracy and the TBM uncertainty approaches closely the actual error level. This is confirmed in Fig. 8.3-bottom, where the TBM uncertainty (red lines) captures the peak error level in the wall-normal velocity component to within 3%. The particle positional error is estimated from eq. (8.8) in the time-resolved case, which yields a value of

0.17 voxels. Using eq. (6) and $\alpha = 0.114$, corresponding to the current track length of 9 snapshots and third order polynomial fitting, the rms error on particle displacement is estimated at 0.06 voxels. In comparison, the particle displacement error level calculated with respect to the ground-truth equals 0.07 voxels. This corresponds to the result obtained with eq. (8.6) when the actual rms particle position error is used instead of the estimate obtained from eq. (8.8). The blue lines in Fig. 8.3-bottom show the cTBM result using the approximated correction. Because the particle displacement error levels for time-resolved PTV measurements are relatively small in comparison to the error level of the dense velocity interpolation, that is an order of a magnitude larger, the corrected TBM result is in close correspondence to both the ground truth error level and the TBM result.

Benchmark track percentage

The results discussed above were evaluated using a benchmark set of 5% of the tracks; the remaining 95% of the tracks were used for velocity interpolation on the grid. When a larger benchmark set size is used, it is expected that both the errors in the velocity interpolation and the TBM uncertainty increase, because less tracks remain available for the dense velocity interpolation.

This is confirmed in Fig. 8.4, which shows the TBM bias and random uncertainty estimates and the actual ground-truth errors at $y/\delta_{99} = 0.2$ for a range of benchmark set sizes. For conciseness, only the results in the time-resolved case are shown. The left and right figures show the uncertainty in the u and v components of velocity, respectively. Note that the uncertainty in u is found larger than the error in v, which is expected considering that the fluctuations u' are larger than v' at this boundary layer height. The TBM estimate recovers this difference and follows the reference error level for all benchmark set sizes. Therefore, typically one would choose a small percentage of benchmark tracks ($\leq 5\%$) to keep the actual interpolation error low.

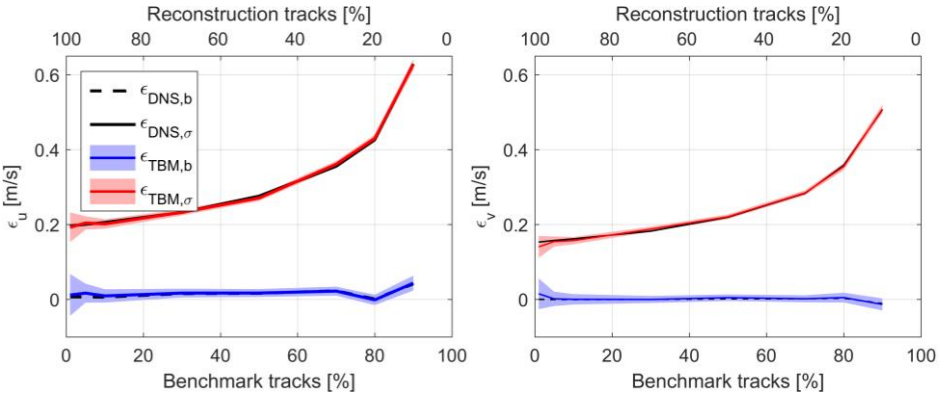

Fig. 8.4 The interpolation error (*black lines*) and TBM uncertainty (*red lines*) for a range of benchmark track set sizes. Streamwise (*left*) and wall-normal velocity (*right*) components. The shaded area indicates the ±3U uncertainty band of the TBM estimates.

For smaller benchmark track sizes, the uncertainty in the TBM result is expected to increase as less benchmark tracks are available for uncertainty quantification. This is also confirmed in Fig. 8.4, where the uncertainty in the TBM results is indicated by the shaded uncertainty band. At a benchmark set size of 5% the interpolation error is less than 1% larger than the error in the case the full dataset is used for the interpolation.

Particle image density

Using particle tracks obtained from Shake-the-Box analysis at a range of seeding concentrations, the behavior of TBM is studied at a range of particle image density, N_p (typically given in particles per pixel, ppp). At the lower end of particle image density (N_p < 0.05 ppp), relatively high error levels in the velocity field are expected due to a large inter-particle distance and corresponding low spatial resolution of the measurement. Note that the benchmark tracks do not suffer from this and remain accurate. Therefore, the TBM approach is expected to correctly show relatively high uncertainty in the velocity fields in the lower seeding density range. This is confirmed in Fig. 8.5, which shows the random (solid black line) and bias (dashed black line) uncertainty for a particle image density from 0.005 ppp to 0.150 ppp, in comparison to the bias (blue line) and random uncertainty (red line) obtained by TBM. A

reduction of random errors is visible when increasing the particle image density up to N_p = 0.1, which is correctly indicated by the TBM approach. The shaded areas indicate the ±3U uncertainty bands, calculated using eq. (8.4) and (8.5) for the bias and random uncertainty, respectively. These uncertainty bands reduce up to N_p = 0.1 due to the increased number of benchmark tracks at higher seeding concentration.

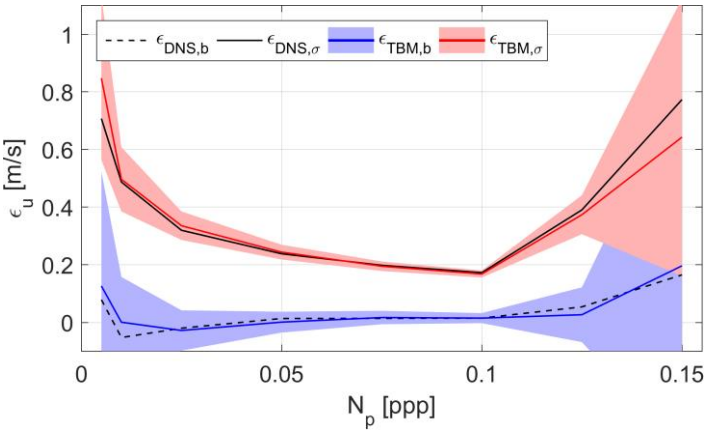

Fig. 8.5 The uncertainty obtained by TBM at y/δ_{99} = 0.2 at a range of particle image densities. The shaded band indicates the ±3U uncertainty in the TBM results calculated from eq. (4) and (5).

At high seeding concentration and particle image density, measurement accuracy suffers from overlapping particle images and incorrect particle pairing, as studied in detail by Kähler et al. (2012b) and in particular by Cierpka et al. (2013) for multi-frame particle tracking techniques. In the present case, an increase in error levels is visible for N_p > 0.1. The benchmark tracks suffer from similar measurement uncertainty, which reduces accuracy of the TBM uncertainty estimate as discussed in Sec. 8.2. However, as shown in Fig. 8.5, still the TBM approach indicates the error increase that follows when no reliable particle triangulation and tracking is possible at excessive particle source density.

8.3.2 Instantaneous uncertainty quantification

To obtain the uncertainty of velocity in an instantaneous snapshot, 20 interpolations to a grid are done at a single time-instant, each time using

a unique 5% of benchmark tracks. The instantaneous uncertainty is subsequently quantified by evaluating the mean and standard deviation in interrogation volumes sized such that they contain typically 9 benchmark tracks. This is done to obtain a local and instantaneous random uncertainty by TBM, with an uncertainty of 25% by eq. (8.5).

The streamwise velocity distribution along the spanwise direction is plotted in Fig. 8.6 in the measurement volume center at y/δ_{99} = 0.2. The top figure shows the VIC+ result (red line) at N_p = 0.025 ppp and the bottom figure the result at N_p = 0.075 ppp. The black line shows the reference velocity from DNS. As expected from the results in the previous section, the VIC+ result at the higher particle source density follows more closely the DNS reference. In particular, in contrast to the case of N_p = 0.075 ppp, the minimum velocity at z = -8.5 mm is not captured at the lower seeding concentration.

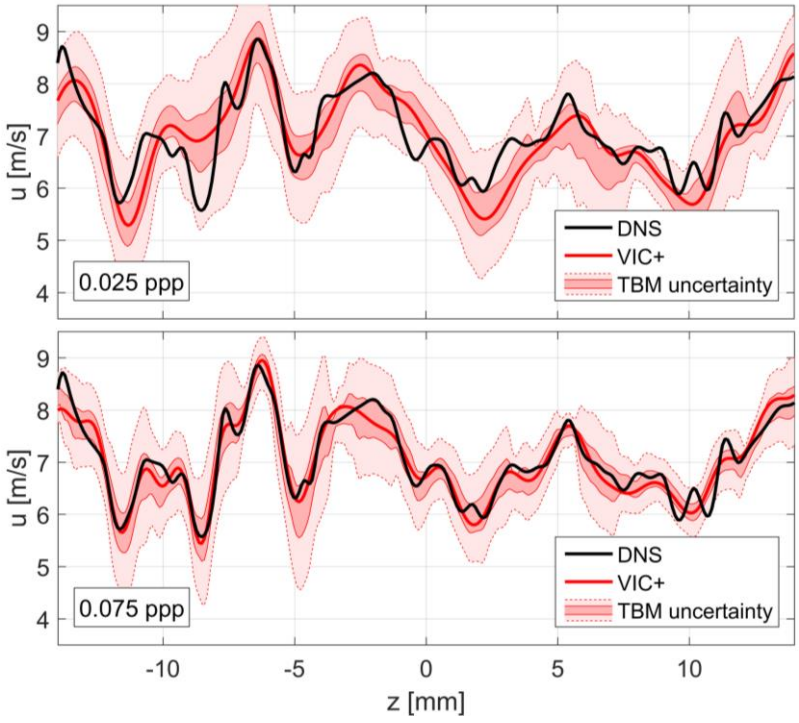

Fig. 8.6 Instantaneous velocity distribution along span at x/δ_{99} = 0 and at y/δ_{99} = 0.2. The TBM uncertainty estimate of the VIC+ result (red line) is given by the dark ($\pm\epsilon_{TBM,\sigma}$) and light ($\pm 3\epsilon_{TBM,\sigma}$) shaded bands.

The dark red shaded band indicates $\pm\epsilon_{TBM,\sigma}$ around the VIC+ result corrected by the bias obtained from TBM. The light red shaded band indicates $\pm 3\epsilon_{TBM,\sigma}$. The latter $\pm 3\epsilon_{TBM,\sigma}$ band encompasses the reference result obtained from DNS in both cases, indicating its use as an instantaneous uncertainty estimate. Moreover, the relatively large error at z = -8.5 mm in the N_p = 0.025 ppp case is indicated by a large uncertainty. In comparison, a smaller error and TBM uncertainty is found in the N_p = 0.075 ppp case.

To quantify the accuracy of the uncertainty obtained by use of the TBM approach, it is calculated how often the true error is larger than $\pm\epsilon_{TBM,\sigma}$ around the velocity field corrected with the TBM bias uncertainty. When errors are Gaussian distributed, this should occur theoretically in 68% of the data points. Such a procedure for assessment of the uncertainties was previously adopted by Timmins et al. (2012), Sciacchitano et al. (2013) and Charonko and Vlachos (2013). The results in the present study are in close correspondence to the expected value, and a coverage of 68% and 67% is obtained in the N_p = 0.025 and N_p = 0.075 cases, respectively.

8.4 Application to a circular jet experiment

The time-resolved tomographic PIV measurement of a circular jet in water is considered. The experiment is discussed in detail in Violato and Scarano (2011). Details of the original tomographic PIV measurements are recalled in Tab. 8.3. This experiment has been used in a range of recent literature for both flow physics investigations and method validation. A jet experiment with a similar measurement setup has been used by Schanz et al. (2016) to show the benefit of STB plus FlowFit data processing in comparison to tomographic PIV. In the absence of a ground-truth, the comparisons in the abovementioned paper are mostly based on qualitative inspection of vortical structures and assessment of temporal coherence. In the present section, a similar comparison between tomographic PIV and a new particle tracking based approach is made, but TBM is used to quantify the uncertainty of both methods uncertainty

quantification to demonstrate its relevance in cases where the ground-truth velocity is unknown.

Tab. 8.3 Parameters for the jet flow case by Violato and Scarano (2011).

Jet exit velocity	u_{jet} = 0.5 m/s
Jet exit diameter	D = 10 mm
Seeding	Polyamide particles, 56 μm diameter
Illumination	Quantronix *Darwin-Duo*
	Nd-YLF laser (2 × 25 mJ @ 1 kHz)
Recording devices	4 × LaVision HighSpeedStar 6 CMOS
Imaging	f = 105 mm Nikon objectives
Repetition rate	1000 Hz
Measurement field	(cylindrical) 30 mm (d) × 50 mm (h)

The original measurement data was re-processed using tomographic PTV in Schneiders and Scarano (2016). The same PTV results are used here. An example of the reconstructed particle trajectories is given in Fig. 8.7, where the particle positions over ten subsequent snapshots are plotted. The particles are colored by velocity magnitude (top) and streamwise acceleration (bottom) and their size is scaled by velocity magnitude in both figures for clarity. As discussed in Schanz et al. (2016), ring vortices in the flow accelerate particles when drawing them in and decelerate them upon ejection, resulting in the alternating high and low acceleration pattern in Fig. 8.7-bottom.

The results are subsequently processed using VIC+ to obtain velocity on a regular grid. The grid spacing is 0.4 mm, calculated from the relationship between grid spacing and seeding concentration for VIC+ in Schneiders and Scarano (2016). An overlap of 50% is used for the VIC+ radial basis functions. In comparison, for the tomographic PIV analysis interrogation volumes of 40 × 40 × 40 voxels were used with 75% overlap (Violato and Scarano 2011), resulting in a vector spacing of 0.5 mm. An example of the instantaneous flow organization is shown in Fig. 8.8 as evaluated by tomographic PIV (top) and VIC+ (bottom).

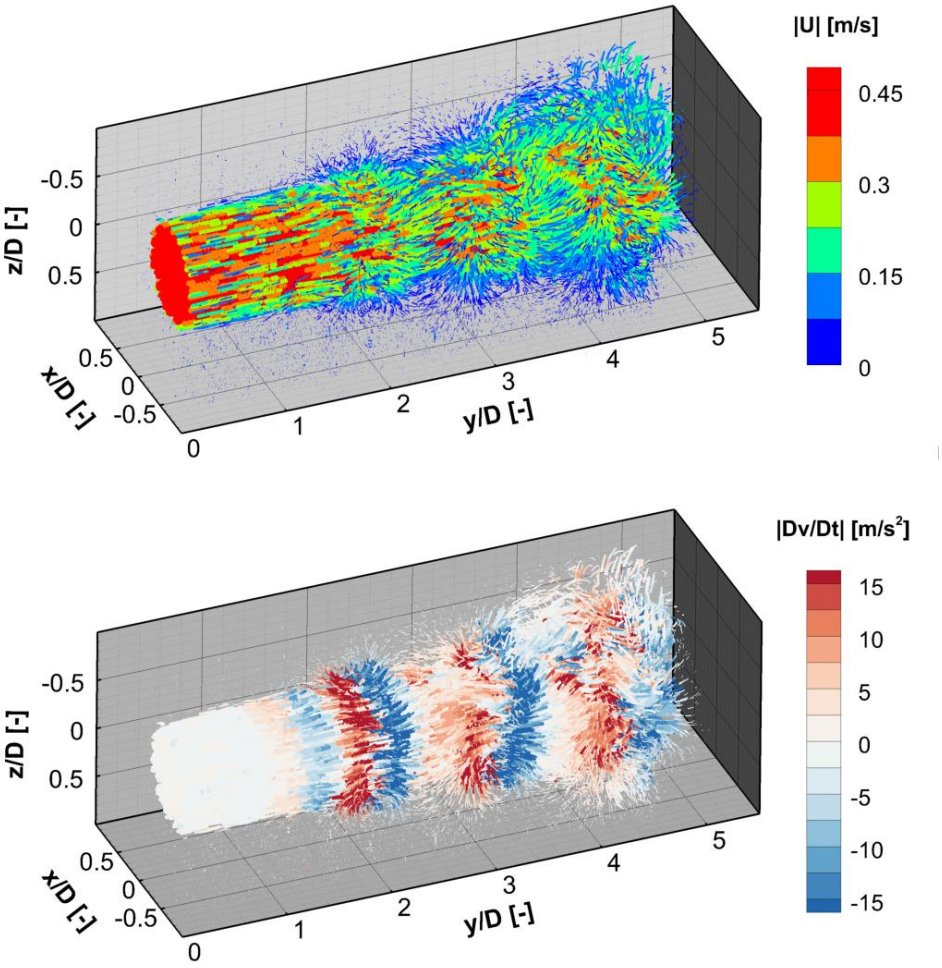

Fig. 8.7 Instantaneous particle positions over ten subsequent snapshots. The particles are scaled by velocity magnitude in both figures and colored by velocity magnitude (*top*) and streamwise acceleration (*bottom*).

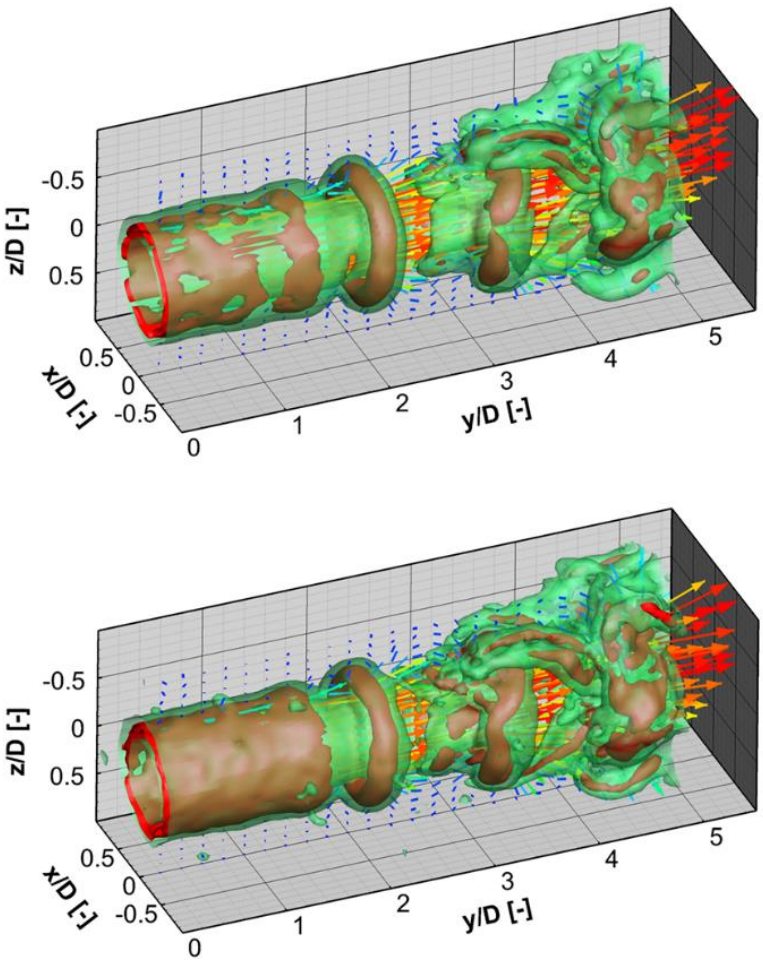

Fig. 8.8 Instantaneous flow organization visualized by isosurfaces of vorticity magnitude ($|\omega|$ = 50 Hz, red, and $|\omega|$ = 250 Hz, green) and instantaneous velocity vectors (sub-sampled to a 2mm vector spacing and colored by velocity magnitude for clarity). Tomographic PIV (*top*) and VIC+ (*bottom*).

A first qualitative comparison shows in both results the typical jet flow organization with vortex rings visualized by the isosurfaces of vorticity magnitude. However, similar to the improvement observed when using FlowFit (Schanz et al. 2016), the VIC+ result exhibits a more coherent representation of the flow field, as visible for example in the shear layer which is represented evenly by VIC+, whereas the tomographic PIV result shows less coherent patches of high vorticity magnitude. Such a visual comparison remains however subjective and therefore in Sec. 8.4.1 the statistical uncertainty in the results is quantified by TBM and in Sec. 8.4.2 the instantaneous uncertainty is quantified.

8.4.1 Statistical uncertainty quantification

To quantify the measurement quality of the two results in absence of a ground-truth, the uncertainty is calculated using TBM for both results. For uncertainty quantification by TBM, the VIC+ results are obtained from a reduced dataset of tracks (95%) to leave 5% benchmark tracks. Application of TBM to the tomographic PIV measurements is done by comparing the benchmark tracks to the gridded PIV velocity fields, without leaving any particles out in the tomographic reconstructions. Note that therefore when TBM is to be used for tomographic PIV in this way, it doubles processing of the measurement data, using in addition to tomographic PIV also particle tracking.

It is expected that the bias uncertainty is small in most of the measurement domain, except in the laminar shear layer region where insufficient spatial resolution can result in a consistent under- and overestimations of axial velocity as discussed in Kähler et al. (2012a). Despite the use of advanced iterative window deformation cross-correlation for tomographic PIV, the spatial resolution remains limited by seeding concentration. Also for the particle tracking based VIC+ approach resolution is limited by seeding concentration, but reduced errors are expected based upon existing literature comparing correlation and particle tracking approaches (amongst others Kähler et al. 2012a, Novara and Scarano 2013; Schanz et al. 2016; Schneiders and Scarano 2016). Consequently, relatively large uncertainty is expected in the shear layer

at the jet exit, where the shear layer is strongest. A reduction in uncertainty is expected downstream of the jet exit due to a reduction in the velocity gradients in the shear layer following mixing of the jet with the surrounding flow.

This is confirmed in Fig. 8.9, which shows the bias uncertainty as percentage of the jet exit velocity for the radial (left) and axial (right) velocity components. The top figures show the result from tomographic PIV and the bottom figures show the VIC+ result. A positive bias corresponding to an overestimation of velocity is found to the outer side of the shear layer near the jet exit and a negative bias corresponding to an underestimation of velocity is found in the inner side of the shear layer. Moreover, a velocity overshoot is found on both sides, as also observed in Kähler et al. (2012a).

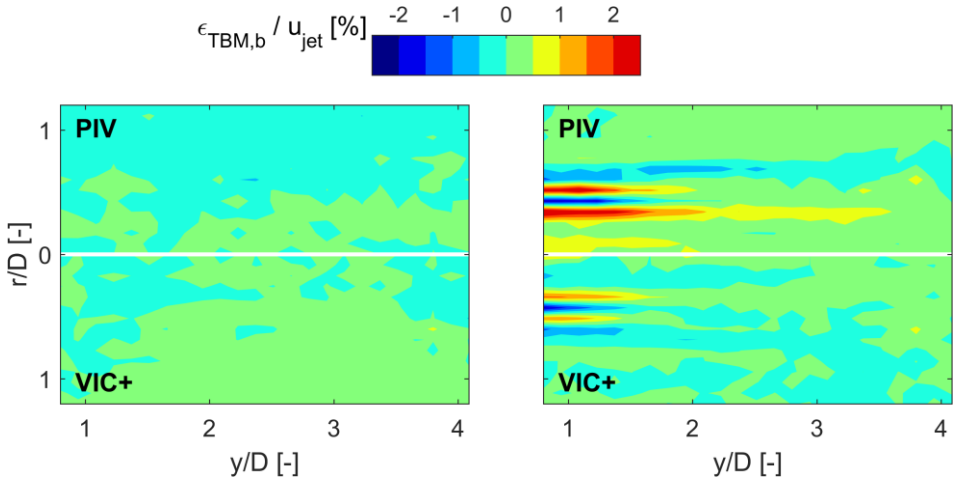

Fig. 8.9 The bias uncertainty for the radial (*left*) and axial (*right*) velocity components as percentage of the jet exit velocity. Tomographic PIV (*top*) and VIC+ (*bottom*).

The random uncertainty map is expected to similarly show relatively large uncertainty in the axial velocity component in the strong shear layer near the jet exit. Note that this is the statistical uncertainty evaluated on the full measurement time-series. Considering that due to vortex shedding the flow state locally can vary, the instantaneous uncertainty as evaluated in Sec. 8.3.2 can differ from the statistical uncertainty.

Uncertainty in the radial velocity component is expected to become visible in the error maps further downstream of the jet exit in the region of vortex shedding. This is confirmed by Fig. 8.10, which gives the random uncertainty obtained by TBM for the radial (left) and axial (right) velocity components. Note that the correction to TBM for random errors in the particle tracking measurements calculated from eq. (8.6) to eq. (8.8) is on the order of 10^{-4} and is therefore negligible in comparison to the estimated uncertainty.

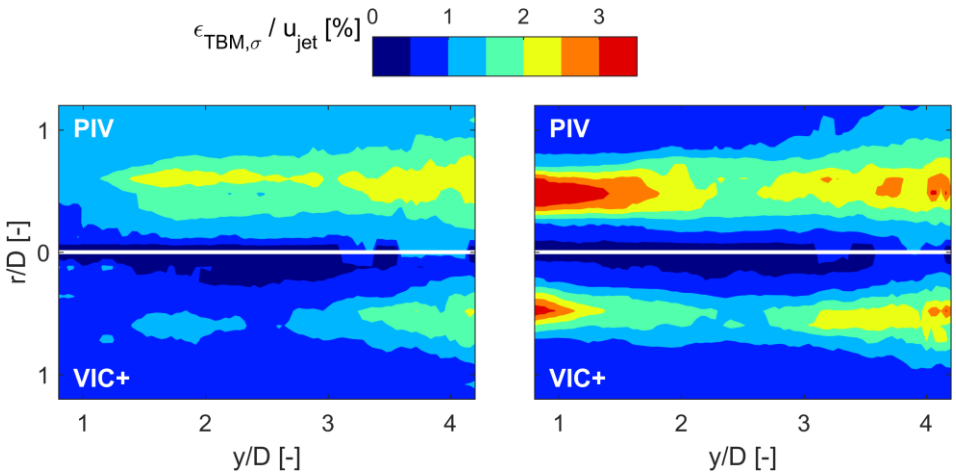

Fig. 8.10 The random uncertainty for the radial (*left*) and axial (*right*) velocity components as percentage of the jet exit velocity. Tomographic PIV (*top*) and VIC+ (*bottom*).

Comparison of the shed vortex around $y/D = 2$ in the tomographic PIV and VIC+ results in Fig. 8.8 shows little difference, indicating that the large-scale vortex ring is well resolved by both methods. However, further downstream, in the region of vortex-pairing ($y/D \sim 3$), the occurrence of smaller scale structures (c.f. Fig. 8.8) is expected result in increased uncertainty, as confirmed by the increase in random uncertainty for $y/D > 3$ in Fig. 8.10. Outside of the shear layer region, uncertainty is found to be below 2% of the jet exit velocity. The latter value corresponds to the uncertainty estimate obtained by Violato and Scarano (2011) based on the analysis of the residual of a polynomial regression through the dataset.

In the present experiment, measurement errors are largely due to velocity gradients. Fig. 8.11 shows the uncertainty of absolute velocity calculated using the TBM approach as a function of the vorticity magnitude. Vorticity is associated with velocity gradients, which as discussed above require sufficient spatial resolution to be resolved and therefore for increased levels of vorticity also increased uncertainty is expected. Indeed, this trend is noticed in the random uncertainty (solid lines) for both tomo-PIV and PTV-VIC+ in Fig. 8.11. In addition, a peak value in bias uncertainty is found for relatively low vorticity levels in both results, which is associated with the under- and overshoot of velocity just out- and inside of the shear layer, where vorticity is relatively small, as noted above in relation to Fig. 8.9.

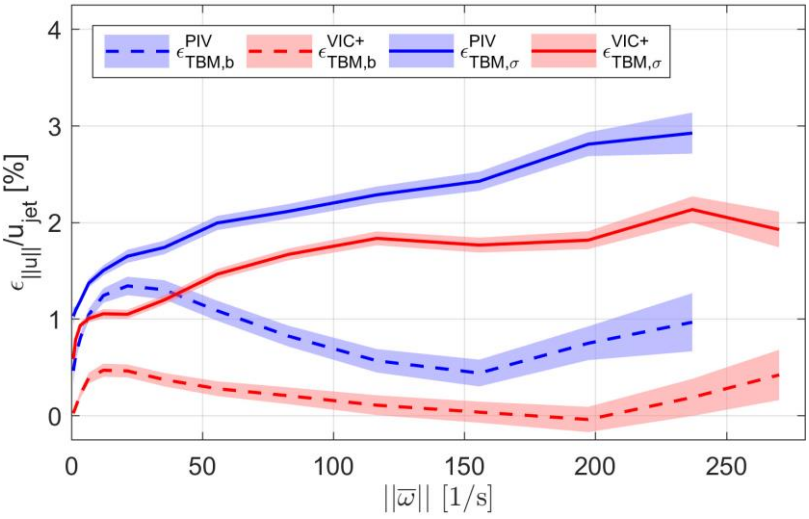

Fig. 8.11 The uncertainty variation with vorticity magnitude. The shaded color bands indicate the ±3U uncertainty band of the values.

8.4.2 Instantaneous uncertainty quantification

The instantaneous uncertainty is obtained similarly to the procedure used in Sec. 8.3.2. Fig. 8.12 shows the velocity profiles obtained by PIV (blue line) and VIC+ (red line) at y/D = 3 and z/D = 0. The shaded color bands indicate the $\pm 3\epsilon_{TBM,\sigma}$ band around the velocity corrected by the bias $\epsilon_{TBM,b}$. The u (radial, left) and v (axial, right) velocity components are plotted. The figures show a relatively close correspondence between PIV and

VIC+. Inspection of the u velocity component (left figure) shows that the discrepancies between PIV and VIC+ between x/D = -0.5 and 0 are largely within the uncertainty estimated using TBM. On the other hand, the fluctuation around x/D = 0.4 is found to be significant, as indicated by the relatively smaller uncertainty obtained by VIC+.

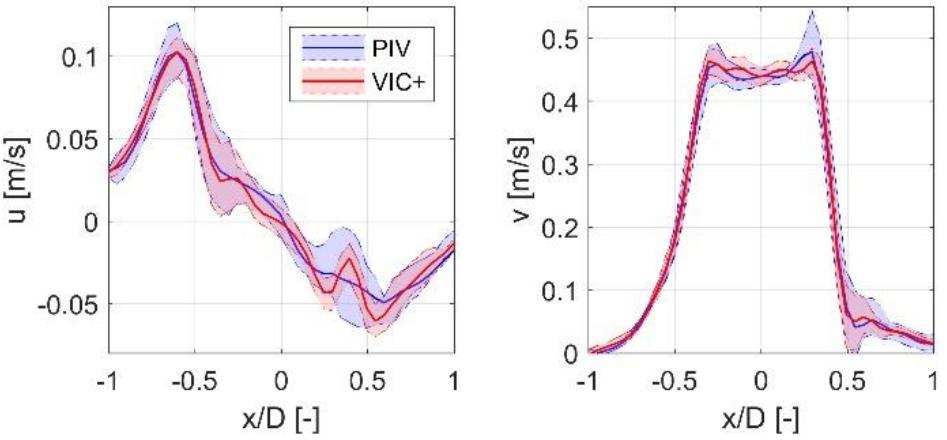

Fig. 8.12 The instantaneous u (radial, left) and v (axial, right) velocity obtained by PIV (blue line) and VIC+ (red line) at y/D = 3 and z/D = 0. Shaded color bands indicate $\pm 3\epsilon_{TBM,\sigma}$ around the velocity corrected by $\epsilon_{TBM,b}$.

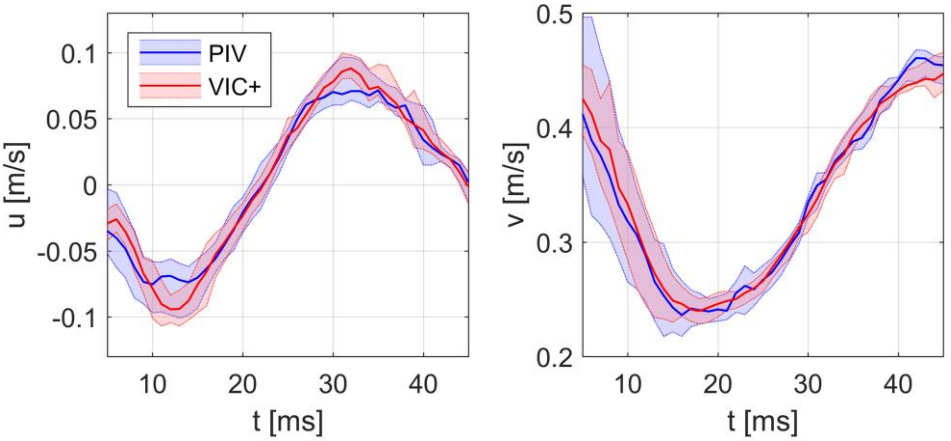

Fig. 8.13 Temporal evolution of the u (radial, left) and v (axial, right) velocity obtained by PIV (blue line) and VIC+ (red line) at the point (x/D = 0.4, y/D = 3, z/D = 0). Shaded color bands indicate $\pm 3\epsilon_{TBM,\sigma}$ around the velocity corrected by $\epsilon_{TBM,b}$.

The velocity time-history in the point ($x/D = 0.4$, $y/D = 3$, $z/D = 0$) is plotted in Fig. 8.13. The $\pm 3\epsilon_{TBM,\sigma}$ around the velocity corrected by $\epsilon_{TBM,b}$ is again indicated by the shaded uncertainty bands for both the tomographic PIV and the VIC+ results. The uncertainty indicates the large-scale velocity fluctuation is significantly larger than the uncertainty for both PIV and VIC+. Moreover, the uncertainty bands indicate that as expected the VIC+ approach resolves better the peak values as seen in the u component of velocity at $t = 10$ ms and $t = 30$ ms. However, the smaller scale fluctuations visible in the w component of velocity are within the uncertainty of the measurement.

8.5 Conclusions

The Track Benchmarking Method (TBM) is proposed for the uncertainty quantification of scattered Lagrangian particle tracking measurements mapped onto a regular grid. The method provides a quantitative and direct measurement of the quality of dense velocity interpolations, which is also relevant for comparison of processing algorithms and parameter tuning for advanced interpolation methods. The method makes use of 5% of the measured particle trajectories as a benchmark to evaluate the accuracy of the velocity interpolation as obtained from the remaining 95% trajectories. The numerical assessment shows excellent agreement between the statistical uncertainty obtained from TBM and the actual error statistics evaluated from knowledge of the ground-truth velocity. In the case of double-frame measurements, the uncertainty overestimates the actual measurement errors as the PTV velocity measurements are affected by a random error component in the particle positions. A correction is proposed and assessed to compensate for this overestimation. In addition, application of TBM for uncertainty quantification of instantaneous measurements is demonstrated. In the experimental assessment, a jet flow measurement is processed both by tomographic PIV and VIC+. The TBM approach provides a quantitative evaluation of the measurement uncertainty and highlights the regions of high uncertainty by means of an uncertainty map. The TBM approach enables quantifying the error reduction achieved by PTV and advanced

interpolation algorithms with respect to correlation-based tomographic PIV. This demonstrates the use of TBM for measurement uncertainty quantification and comparison of different processing techniques.

Part 2
Large-Scale Volumetric Flow Measurements

Contents

Chapter 9
Large-Scale Volumetric Pressure Measurement

This work has been published in Schneiders et al. (2016) Exp. Fluids 57:164

This chapter is the first of part 2 of this dissertation, where focus moves away from data assimilation and towards further development of the tomographic PIV measurement technique itself. In this chapter, a first step is made by leveraging recent developments in the large-scale PIV using helium-filled soap bubble (HFSB) tracer particles for large-scale volumetric pressure measurements.

9.1 Large-scale wind tunnel measurements using HFSB

All studies involving pressure-from-PIV measurements in air have dealt with a fairly limited size of the measurement volume of a few cubic centimeters. This is mostly due to the low intensity of the light scattered by micron-size tracers for tomographic PIV, even when a multi-pass light amplification system is employed (Ghaemi and Scarano 2010). For example, despite use of this system by Ghaemi and Scarano (2013) for pressure extraction from time-resolved tomographic PIV, only a 1.6 × 0.6 × 2.4 cm^3 measurement volume was achieved in a turbulent boundary layer at 10 m/s. The advantage of tomographic PIV with such small measurement volumes is the relatively good spatial resolution that it offers. However, very few time-resolved tomographic PIV experiments, mainly in water, are reported in literature where both the region of interest (typically rotational) and an irrotational region are included in the measurement volume (e.g. Jeon et al. 2016). As a result, boundary conditions for the pressure-Poisson equation may need to be imposed in rotational or turbulent regions (e.g. Pröbsting et al. 2013). Applying reliable boundary conditions is of importance for the accuracy of the solution (van Oudheusden 2013), which limits the applicability of today's

pressure-from-PIV techniques to large-scale and industry-relevant wind-tunnel experiments.

Recent advances of tomographic PIV using Helium-filled soap bubbles (HFSB) as tracers have shown that the measurement volume can be significantly increased for velocity measurements in air (Kühn et al. 2011). The HFSB have a diameter of approximately 300 microns, which is two orders of magnitude larger than conventional tracer particles used for air flow measurements. Consequently, they scatter on the order of 10^4 to 10^5 more light, allowing for significantly increased measurement volumes without requiring more powerful illumination systems.

Because the HFSB are neutrally buoyant, their characteristic response time is relatively small and estimated in the range of 10 μs by Scarano et al. (2015). Therefore, the application of HFSB in wind tunnels for aerodynamic investigations is possible (Scarano et al. 2015), but remains hampered by the limited seeding concentration due to limitations on tracer particle generation (Caridi et al. 2016). The limited tracer particle seeding concentration motivates the use of particle tracking techniques for processing of the time-resolved and volumetric data, as recent studies (e.g. Schanz et al. 2016; Schneiders and Scarano 2016) have shown increased spatial resolution in such cases. The spatial resolution of the instantaneous velocity fields becomes on the order of the inter-particle distance. Furthermore, velocity statistics of the flow field are obtained by ensemble averaging the PTV results and hence spatial resolution of the statistics can be increased by increasing the observation time at constant seeding concentration (Kähler et al. 2012b).

9.2 Surface mounted cylinder experiment

In the present study, an experiment is realized where the time averaged pressure and root mean squared (rms) pressure fluctuations are characterized. The instantaneous pressure distribution as well as its frequency spectra are extracted and compared with reference measurements obtained with surface pressure transducers. The flow past a truncated cylinder installed on a flat plate, is considered, which exhibits pressure fluctuations due to both wall bounded turbulence as well as

large scale unsteady separation. This configuration was considered in a variety of studies, reviewed in Sumner (2013), and is relevant for applications within the field of aerodynamics (e.g. car side mirror or aircraft landing gear), which involve issues related to flow induced vibration and aero-acoustics noise. The measurement of the instantaneous surface pressure in this flow case was proven to be a challenge, with recent studies employing wind tunnel models equipped with up to 179 simultaneously operated pressure taps (Dobriloff and Nitsche 2009).

The experiment is conducted in a low-speed wind tunnel with 40 × 40 cm^2 cross section. A cylinder of 10 cm diameter, D, and equal height, h, is installed on a flat plate (Fig. 9.1). Measurements are conducted at a Reynolds number based on the cylinder diameter of $Re_D = 3.5 \times 10^4$ (free stream velocity of 5 m/s).

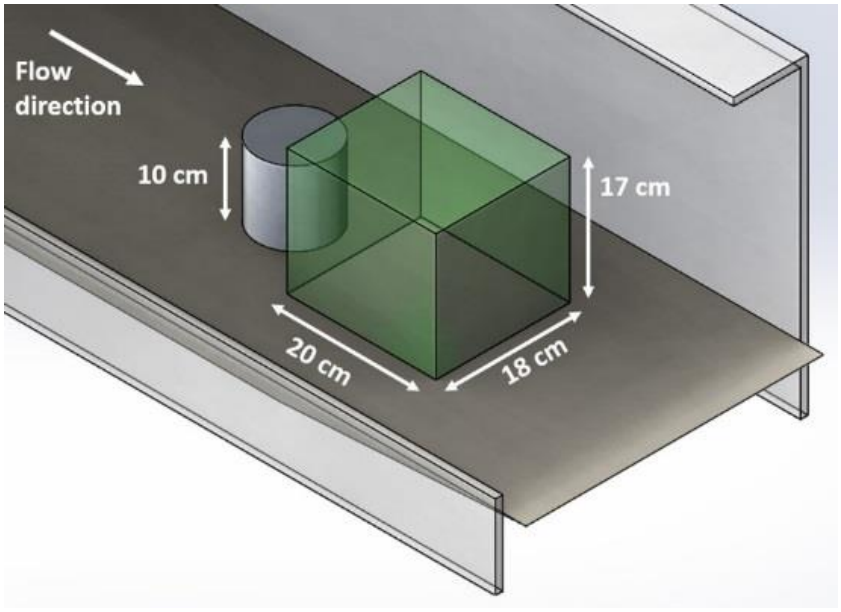

Fig. 9.1 Schematic of the setup in the test section, with measurement volume shaded in green and channel cut-out for clarity.

A tripping device past the leading edge of the ground plate forces laminar to turbulent transition. A tripping element was placed 10 cm downstream of the leading edge and 50 cm upstream of the cylinder. The boundary layer thickness, δ_{99}, at the cylinder mounting location (with the cylinder

removed) is 1.5 cm. Literature shows that the local relative boundary thickness to the cylinder height (δ_{99}/h = 0.15) and the aspect ratio of the cylinder (h/D = 1) play an important role in the wake development. The boundary layer in the current experiment is classified as a thin boundary layer (Bourgeois et al. 2011; Sumner et al. 2013, and references therein). For details regarding the wake development the reader is referred to the abovementioned literature. The near-wake of the cylinder is captured within a measurement volume of 20 × 17 × 18 cm^3 (6 L). In comparison, for measurements over a truncated cylinder with a diameter of 6 cm and a height of 13 cm, Hain et al. (2008) focused on the flow region on the top of the cylinder with a volume of 8 × 8 × 1 cm^3 (0.06 L) in a water tunnel with a low-repetition rate tomographic PIV system. In Fig. 9.1, the measurement volume (shaded green) is shown with respect to the test section. The test section channel is cut-out in the figure to illustrate the cylinder and the measurement volume. Achieving this measurement domain was only possible using HFSB as tracers, with a diameter of approximately 300 μm and in the neutrally buoyant regime. Scarano et al. (2015) report a relaxation time τ_{HFSB} for the HFSB tracer particles of below 50 μs. With a typical vorticity magnitude peak value of ω_p = 1000 Hz measured in the present experiment, the turnover time of the vortices is approximated at $1/\omega_p$ = 1 ms. Using this time scale, the Stokes number of the tracers is $Stk = \tau_{HFSB}/\tau_{flow} \leq 0.05$, which is below the threshold of 0.1 reported by Tropea et al. (2007) for accurate tracking fidelity. In addition, with a typical Lagrangian acceleration, a, of 300 m/s^2 in the present flow (evaluated from the particle tracking results), the slip velocity is on the order of $u_{slip} \approx \tau \times a$ = 15 mm/s, which is 0.3% of the free-stream velocity.

Three sequences of 2000 single-frame images are acquired at 2 kHz to obtain a time-resolved measurement. An example of a recorded particle image by one of the cameras is given in Fig. 9.2. Gaussian smoothing with a 3 × 3 pixel kernel was applied to the image for clarity of the visualization. In the supplementary material attached to this paper, a movie of a sequence of particle images is given. The particle density was approximately 0.7 bubbles per cm^3 and the resulting particle image source density equals 0.008 particles per pixel (ppp).

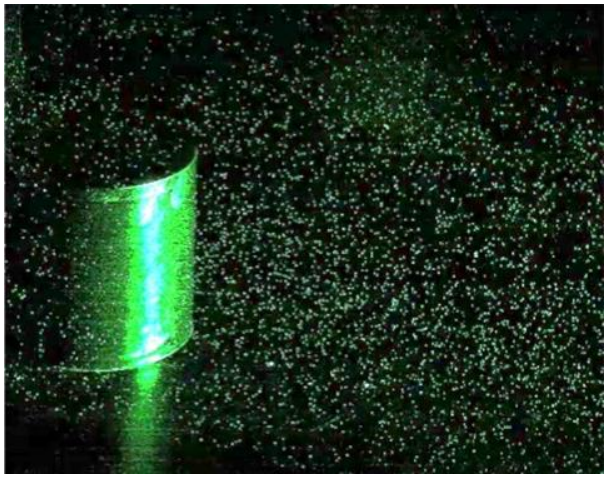

Fig. 9.2 Example of one of the instantaneous image captured.

The recorded images were pre-processed using a time-minimum subtraction filter and subsequently Gaussian smoothing with a 3 × 3 pixel kernel. The particle images are reconstructed using 6 iterations of the FastMART algorithm in the LaVision Davis 8.2 software package. The SNR of the reconstruction, calculated from the averaged z-intensity, profile is in the order of 100, significantly larger than values for tomographic PIV experiments (2 to 5) due to the low seeding concentration and large amount of light scattered by the HFSB. Further details of the measurement setup are given in Tab. 9.1.

Tab. 9.1 Tomographic measurement setup.

Measurement volume	20 × 17 × 18 cm3 (6 L)
Seeding	Helium filled soap bubbles (HFSB)
	300 μm diameter
Illumination	Quantronix Darwin-Duo Nd:YLF Laser
	Pulse energy 2 × 25 mJ at 1 kHz
Recording devices	4 × Photron FastCAM SA1
	CMOS, 1024 × 1024 px, 12-bit, 20 μm px size
Imaging	f = 105 mm Nikon objectives (aperture f/16)
Acquisition frequency	2000 Hz (single-frame mode)
Number of frames recorded	3 × 2000

Particles are identified in the reconstructed objects by peak-finding of peak intensity values in a 5 × 5 × 5 vox (1.3 × 1.3 × 1.3 mm^3) neighborhood. Approximately 10^{-5} particles per voxel (ppv) are present. Sub-voxel accuracy of particle location is obtained by fitting of a 3D Gaussian through the peak intensity distribution. The identified particles have a typical radius (standard deviation of the Gaussian peak fit) of $\sigma_x = \sigma_y = 0.4$ vox and $\sigma_z = 0.6$ vox. The elongation of the particles in depth direction is expected for tomographic reconstructions (Elsinga et al. 2006) and positional error on the particle position can potentially be reduced using novel reconstruction techniques (e.g. iterative particle reconstruction, IPR, Wieneke 2013) and particle tracking algorithms (e.g. 'Shake-the-Box', Schanz et al. 2016). A particle-tracking algorithm based on Malik et al. (1993) is used to build the trajectory of individual particles. A five-snapshot track length is employed, through which a third order polynomial is fitted. The time-derivative of each polynomial yields velocity at the particle locations. A visualization of the instantaneous particle trajectories is given in Fig. 9.4, where the tracks are colored by velocity magnitude.

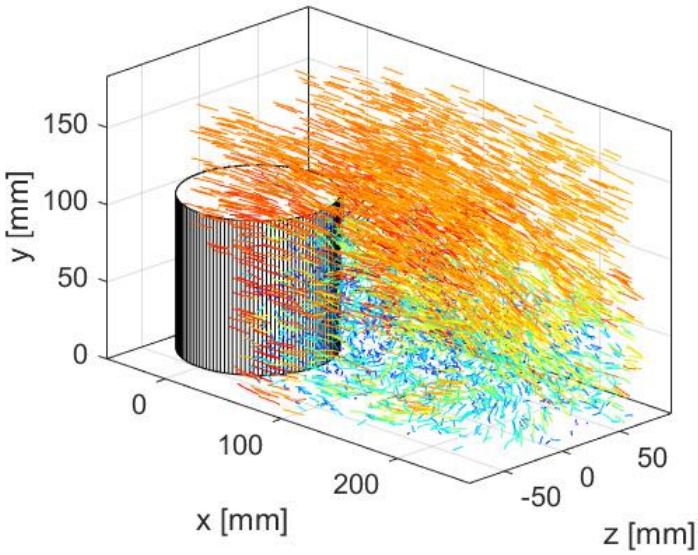

Fig. 9.3 Visualization of particle tracks (color coded by velocity magnitude).

Low speed particles (blue) are visible in the wake region and high-speed particles (red) in the outer flow. Velocity is subsequently calculated on a computational grid (200 × 170 × 180 mm^3) by the adaptive Gaussian windowing (AGW, Agüí and Jiménez 1987) technique. The standard deviation of the Gaussians was set to the average inter-particle distance of 6 mm and 75% overlap was used. The AGW interpolator acts as a Gaussian weighted sliding average filter. The recent study by Schneiders and Scarano (2016) shows that a better recovery of the magnitude of the turbulent velocity fluctuations can be obtained using more advanced and computationally expensive interpolators that incorporate constraints from flow physics (e.g. 'VIC+' Schneiders and Scarano 2016; 'FlowFit' Gesemann et al. 2016). However, the AGW technique was chosen in the present study for its computational efficiency and established position in the community. It should be remarked that with more advanced techniques potentially lower modulation of the velocity fields and pressure gradient fields could be obtained, thus enhancing the spatial resolution of the instantaneous pressure fields shown later in this chapter.

9.3 Pressure evaluation

Instantaneous pressure, p, is calculated by solving the Poisson equation for pressure (see e.g. van Oudheusden 2013),

$$\nabla^2 p = \nabla \cdot \left(-\rho \frac{D\boldsymbol{u}}{Dt} + \mu \nabla^2 \boldsymbol{u}\right), \tag{9.1}$$

with von Neumann (pressure gradient) boundary conditions from the momentum equation on all volume boundaries except the top side, where a Dirichlet boundary condition calculated from the Bernoulli equation is specified. It is verified that the flow at the upper boundary of the measurement is irrotational by visualizing the vorticity distribution. The velocity material derivative is evaluated using the Lagrangian technique by Pröbsting et al. (2013).

Time-averaged pressure, $\bar{p}$, is evaluated using the Reynolds averaged approach outlined in van Oudheusden (2013),

$$\nabla^2 \bar{p} = -\rho \nabla \cdot (\overline{\boldsymbol{u}} \cdot \nabla)\overline{\boldsymbol{u}} - \rho \nabla \cdot \nabla \cdot (\overline{\boldsymbol{u}'\boldsymbol{u}'}). \tag{9.2}$$

The instantaneous velocity fields are limited in spatial resolution by the tracer particle concentration. To obtain the time-averaged velocity field and the turbulence statistics at a higher spatial resolution, all instantaneous and scattered velocity vectors found from the PTV procedure are ensemble averaged in Gaussian interrogation windows with standard deviation σ = 5 mm. An overlap of the Gaussian windows of 75% overlap is used. The resulting time-averaged flow field shows two counter-rotating tip vortices emerging from the truncated cylinder (Fig. 9.4). This vortex pair is expected in the time-averaged field (Sumner 2013), but it should be remarked that literature (Hain et al. 2008; Bourgeois et al. 2011; amongst others) shows that the instantaneous velocity fields do not show one single vortex pair but a more complex flow field.

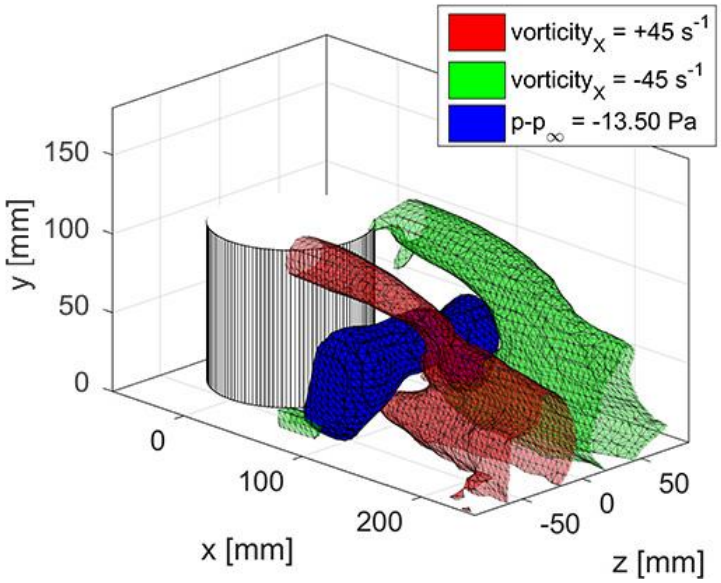

Fig. 9.4 Isosurfaces of time-averaged streamwise vorticity and pressure in the separated region.

The simultaneous measurement of the surface pressure fluctuations with surface pressure transducers provides a ground truth to estimate the accuracy of the proposed measurements. The instantaneous and time-averaged measurements are taken using respectively a LinearX M51 microphone and a Mensor (type 2101). The installation of the

microphones is sketched in Fig. 9.5. Both transducers are mounted under a 0.4 mm diameter pinhole. The acquisition frequency of the microphones is set to 10 kHz and the calibration-corrected frequency response is ±1dB in the range 10 Hz to 40 kHz. The length of the microphones (10.8 cm) indicates potential difficulty when instrumenting wind-tunnel models, which shows again the relevance of pressure-from-PIV approaches. The synchronization between microphone and tomographic PIV measurements is obtained recording the laser trigger signal on an additional channel of the data acquisition system. For the time-averaged pressure measurements, the Mensor signal is recorded at 10 Hz for a duration of 2 minutes.

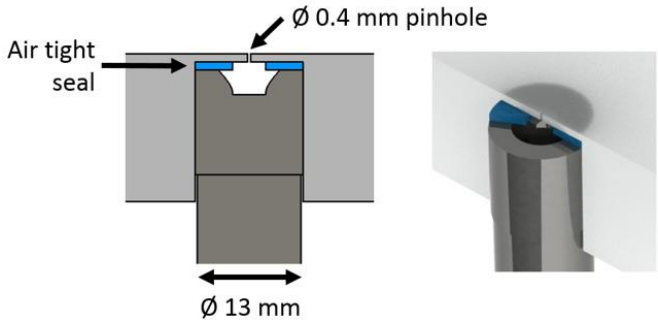

Fig. 9.5 Schematic of the microphone installation for reference measurements of instantaneous pressure. The isometric view (right) is cut-out in the figure.

The surface pressure is mapped on an array of 263 measurement positions obtained with pressure transducers. These measurements are obtained by moving the cylinder relative to 20 sensors arranged on a grid with steps of 17 mm and 13.5 mm in streamwise and spanwise directions, respectively. The measurement encompasses the stagnation region ahead of the cylinder area and the wake (Fig. 9.6-top). The results illustrate the expected pressure increase near the stagnation point and a lower pressure region in the cylinder wake. Two pressure minima are found in the wake of the cylinder, which are attributed to the presence of an arch-vortex in the time-averaged flow field (Pattenden et al. 2005). The results obtained from the tomographic experiment are shown in Fig. 9.6-bottom.

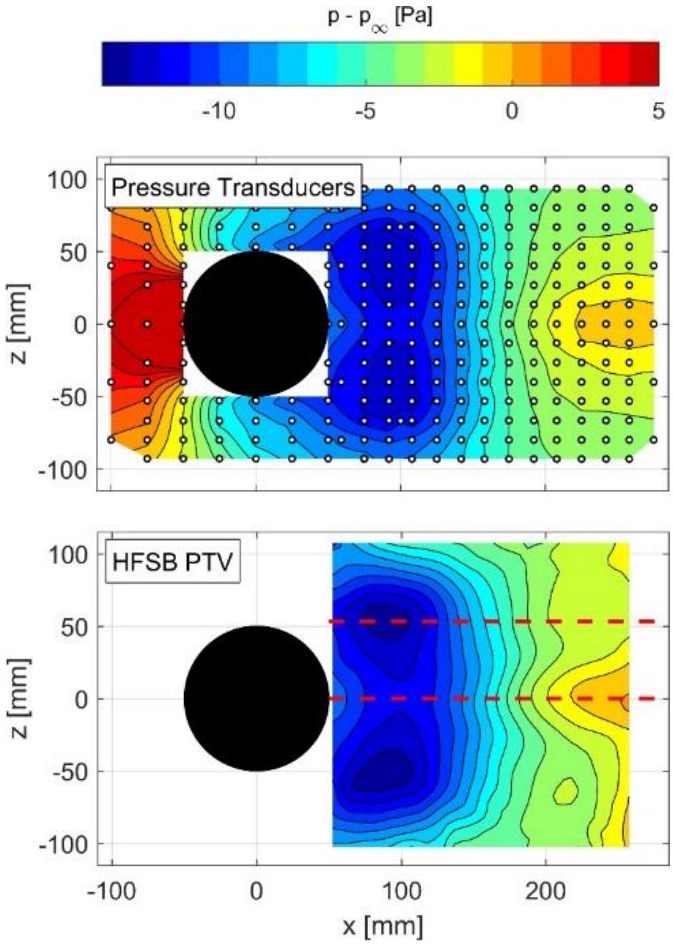

Fig. 9.6 Time-averaged surface pressure; surface pressure transducer measurements (left) and tomographic PTV with HFSB tracers (right). The dashed red lines correspond to the profiles plotted in Fig. 5. Colorbar values above $p - p_\infty = 5$ Pa are saturated and shown in dark red for clarity.

The measurements cover the wake region and the spatial distribution of pressure follows closely the distribution obtained with the surface pressure transducers and reproduces both the two pressure minima as well as the maximum after reattachment. The pressure reconstruction by large-scale tomographic PTV in addition provides pressure in the full measurement volume. In Fig. 9.4 an arch-shaped low-pressure region

(blue isosurface) is visible in the near-wake, which is consistent with the two minima in the surface pressure observed above.

A quantitative comparison is made extracting two streamwise profiles. The mean surface pressure is shown in Fig. 9.7 along the centerline z = 0 mm (top) and along the line at z = 53.3 mm (bottom). The position of these lines is indicated in Fig. 9.6-right (dashed red lines). The minimum pressure ($p - p_\infty$ = -12 Pa) is reached at approximately x = 100 mm. On both profiles, a good agreement is found between the two measurements, with a discrepancy in the order of 0.5 Pa.

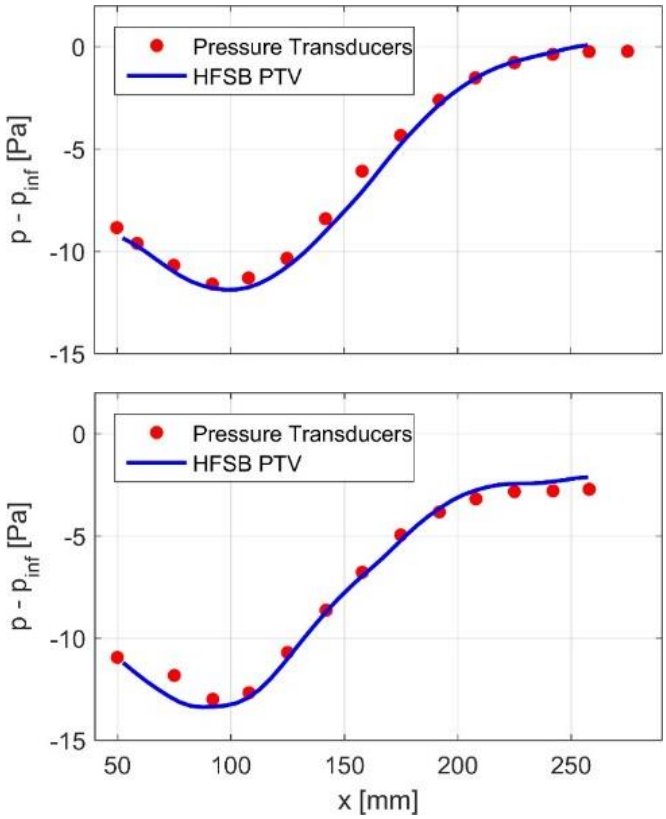

Fig. 9.7 Time-averaged surface pressure along z = 0 mm (top) and z = 53.3 mm (bottom). The cylinder is centered at x = 0 mm as shown in Fig. 4.

The measurement and assessment of instantaneous pressure fluctuations by tomographic PIV has shown to pose a formidable challenge within a number of experiments (de Kat and van Oudheusden 2012; Ghaemi and Scarano 2013; Pröbsting et al. 2013). The rms fluctuations of the surface pressure estimated with tomographic PTV is compared here to the results obtained with the surface-mounted microphone. Two profiles along z are illustrated in Fig. 9.8. Two peaks of pressure fluctuations correspond to the shear layer locations. Comparing the profiles at x = 100 mm and x = 150 mm, the amplitude of the rms fluctuations decreases and the distribution becomes flatter moving downstream. The comparison of tomographic PTV results and that obtained with the microphone show that the former slightly overestimates by about 0.5 Pa the rms fluctuations in minimum region at the symmetry plane. Some discrepancy is also observed at the edge of the domain (marked by the dashed black line).

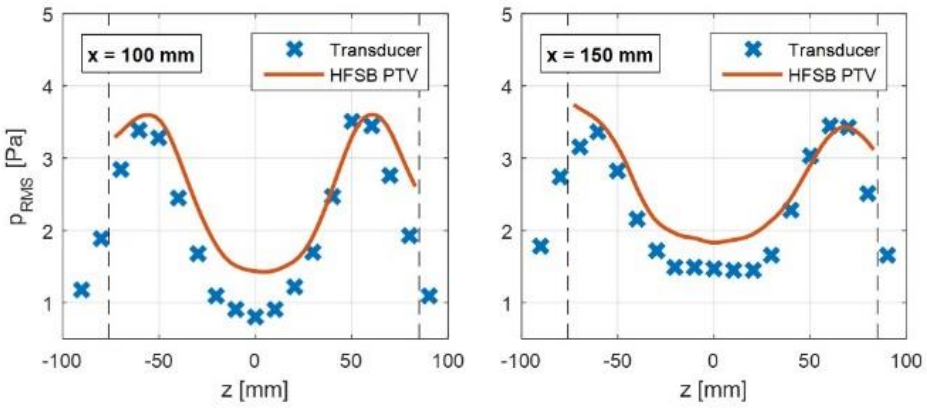

Fig. 9.8 Root mean squared surface pressure fluctuations at x = 100 mm (left) and x = 150 mm (right).

A relevant aspect of unsteady pressure measurements relates to the frequency content of the fluctuations. In this respect, tomographic PTV offers the potential of a field measurement that can be further analyzed in modes using proper orthogonal decomposition (POD) or dynamic mode decomposition (DMD). The time-resolved measurement of the surface

pressure at a point is used to evaluate its power spectral density (Fig. 9.9). The spectrum is calculated using Welch's method using 0.25 s Hamming windows. No signal processing has been applied to the signals, other than the anti-alias filter within the pressure transducer acquisition system which has negligible effects because of the relatively high acquisition frequency.

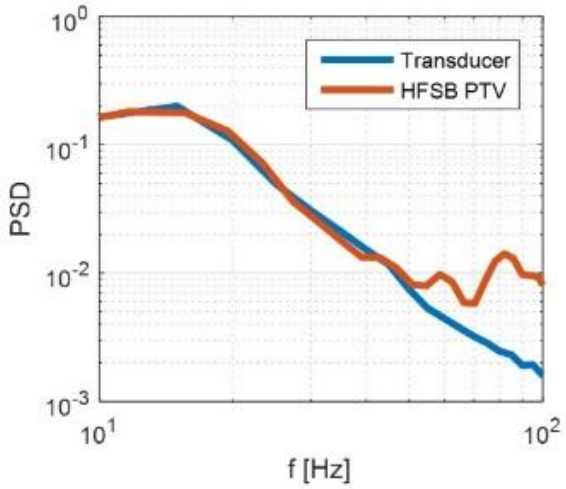

Fig. 9.9 Power spectral density of surface pressure fluctuations at x = 100 mm and z = 30 mm.

A broad peak is seen around 15 Hz and the spectrum obtained with tomographic PTV follows that measured by the microphone with good agreement up to 50 Hz. For higher frequencies, the measurement error seems to dominate the PTV result, which "peels off" the reference data and remains approximately constant. The errors in the present measurement are considered to be dominated by the low seeding concentration and consequently too limited spatial resolution to resolve small scale structures and fluctuations. When the signals are band-pass filtered between 10-100 Hz, the cross-correlation peak between the microphone and tomographic PTV results is approximately 0.6. This value corresponds to that reported in other studies that evaluate pressure-from-PIV (de Kat and van Oudheusden 2012; Ghaemi and Scarano 2013; Pröbsting et al. 2013).

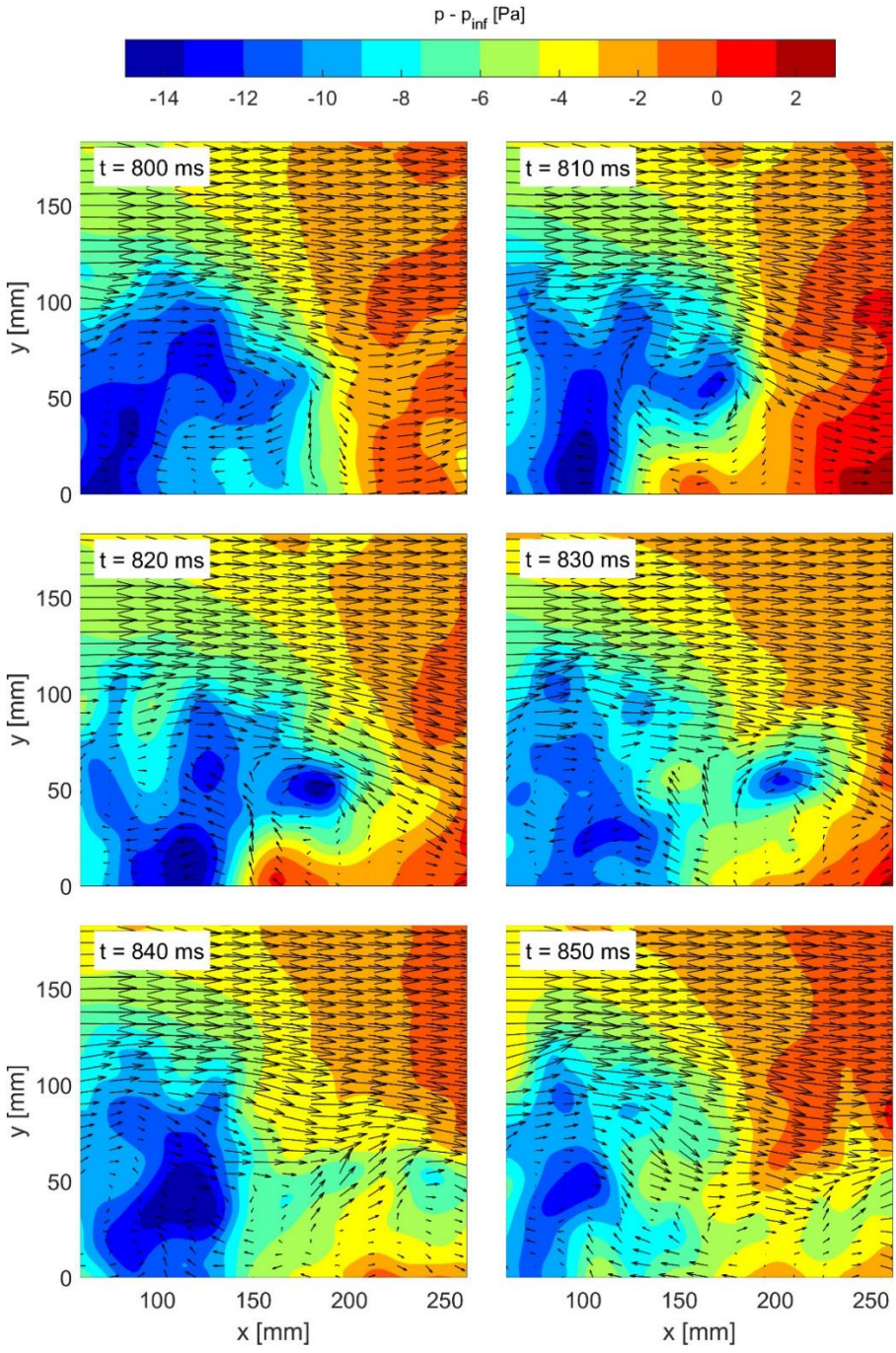

Fig. 9.10 Time-series of instantaneous pressure in the plane z = 50 mm. The in-plane velocity vectors are sub-sampled for clarity.

Finally, the instantaneous pressure visualization in the flow field and at the solid surface offers the opportunity to correlate the pressure fluctuations to the activity of large scale coherent structures in the flow. A short sample of a sequence is shown in Fig. 9.10, where the pressure spatio-temporal evolution in a plane (z = 50 mm) is displayed along with the velocity field that visualizes vortex shedding. The supplementary material added to Schneiders et al. (2016b) shows a video animation of the pressure spatiotemporal evolution. As mentioned above, the time-resolved flow field does not simplify to two counter rotating tip-vortices shown in the time-averaged flow field. For detailed understanding of the flow field in the near wake, the reader is referred to Bourgeois et al. (2011) and the references within the reviewer paper by Sumner (2013).

9.4 Conclusion

In conclusion, the present study shows the use of large scale tomographic PTV with HFSB tracers for the evaluation of the time-averaged and instantaneous volumetric pressure distribution. The measurement domain is more than two orders of magnitude larger than that obtained with tomographic PIV using conventional tracers. Despite the relatively low concentration of the tracers, the tomographic PTV approach reconstructs the velocity and pressure fields, yielding a highly accurate mean pressure distribution and rms fluctuations with reasonable accuracy. The HFSB tracer particles have demonstrated their use for measurement of pressure in a large measurement volume of 6 liters, in the case of the flow past a surface mounted truncated cylinder.

Chapter 10
Coaxial Volumetric Velocimetry

This work has been presented in
Schneiders et al. (2017) 12th International Symposium on PIV, Busan, South Korea

Just over a decade since its introduction, tomographic PIV (Elsinga et al. 2006) has become the benchmark technique for volumetric wind tunnel measurements. The technique employs a measurement setup similar to planar PIV and uses a laser to illuminate a relatively thin measurement volume. The tomographic imaging system features multiple cameras that subtend a finite solid angle of at least 60 degrees. The viewing axis is oriented approximately perpendicular to the illumination direction. A typical tomographic PIV system is illustrated in Fig. 10.1.

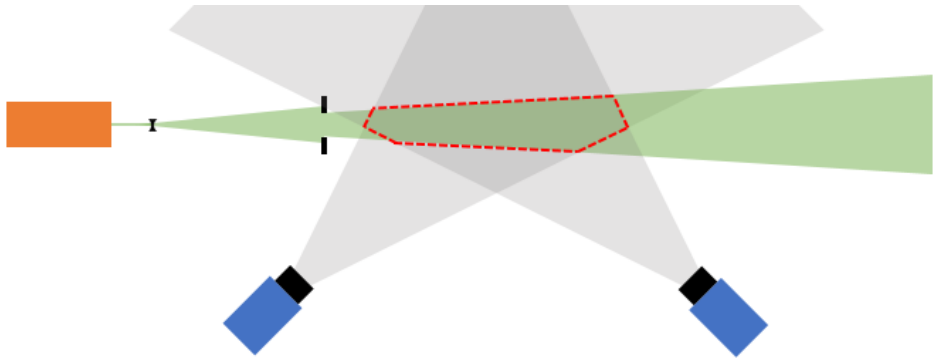

Fig. 10.1 Measurement setup for tomographic PIV, showing the cameras (blue), field of view (grey) and laser illumination (green). Measurement volume contoured by the dashed red line.

The tomographic PIV setup relies upon the available optical access, a stable structure to support the multiple cameras and extensive pre- and post-calibration to achieve an accurate mapping function between the object space and the images. The availability of small cameras has so far

not allowed a compact measurement system, considering the requirements for the system angular aperture on the order of 60 degrees (Scarano 2013). This limits the versatile application of tomographic PIV, in particular when complex shapes (i.e. non-convex shapes or multiple objects) are investigated for instance during wind tunnel experiments.

Near wall measurements and the evaluation of the near-surface flow topology by planar and tomographic PIV has remained largely limited to straight surfaces or concave with curvature along a single direction (e.g. airfoils). A relevant example is given by Depardon et al. (2005), who performed a series of near-wall PIV measurements aligned with the straight faces of a square cylinder. This yielded the arrangement of time-averaged skin-friction lines. When dealing with fully three-dimensional curved surfaces, however, the application of PIV is limited by the optical access requirements, or requires a facility and model that permit refractive index matching (e.g. Talapatra and Katz 2012; Johnson et al. 2017).

Multiple efforts have been devoted in other directions to reduce system size and optical access requirements. In-line holographic PIV (Meng et al. 2004, amongst others) achieves a measurement system where the imaging and illumination systems are positioned along one axis, where typically laser illumination is used from the opposite side of the camera. With the same technique the 3D velocity field over complex rough walls was inspected in a facility that permits refractive index matching (Talapatra and Katz 2012).

In addition, systems that reduce the requirement for imaging optical access have made use of the plenoptic concept (Fahringer et al. 2015), astigmatic aberrations (Hain and Kähler 2006) or defocusing (Willert and Gharib 1992). Mainly for application in liquid flows, volumetric velocimetry using a compact three-sensor system was recently achieved by the V3V system (Pothos et al. 2009). This system obtains particle depth measurements from the size of particle triangle patterns resulting from superposition of three camera images, following the defocusing concept (Pereira et al. 2000). Despite the variety of working

principles, the above systems are typically operated with illumination and imaging along approximately perpendicular directions.

A coaxial measurement configuration would bring imaging and illumination along the same direction. Such a configuration can be realized by introducing two main modifications to the tomographic PIV measurement setup: 1) reduction of the tomographic aperture β by an order of magnitude; 2) coaxial arrangement between the illumination and imaging directions. As a result, the imaging system comprises a number of compact cameras that are positioned at small relative distance (Fig. 10.2). The laser light, transmitted by an optical fiber, is emitted from the probe in between the cameras and expanded along a cone to match their field of view at a prescribed distance. The resulting coaxial volumetric velocimeter (CVV) can be integrated in a single module in a way similar to that of Laser Doppler anemometry operating in back-scatter mode (Durst et al. 1976).

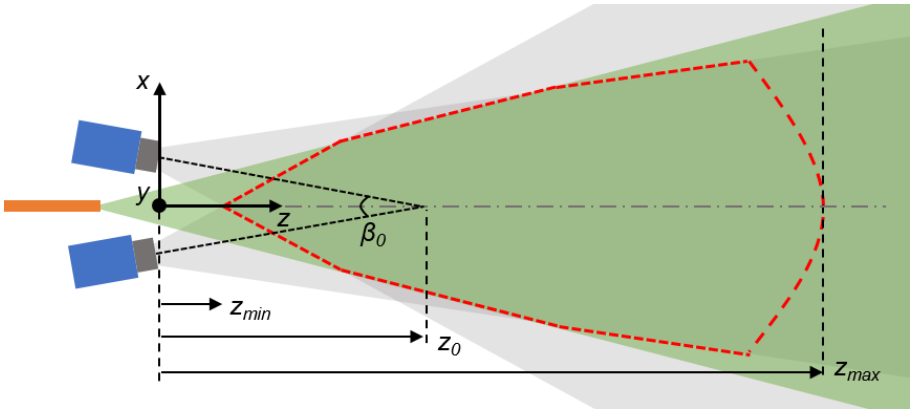

Fig. 10.2 Measurement setup for a coaxial velocimeter (CVV), showing the cameras (blue), field of view (grey) and laser illumination (green) provided from an optical fiber (orange).

A first stumbling block of the coaxial setup is related to particle image detectability. While typical volumetric experiments feature a negligible variation in object distance compared to the overall operating distance, such variation is significant for the CVV measurement domain. The deep illuminated volume realized by the coaxial system (dashed red line Fig. 10.2) requires a small imaging aperture for particles to be imaged in-focus,

which reduces the overall amount of light collected on the imager. In addition, the laser light intensity remains relatively uniform and focused for planar or tomographic PIV to achieve sufficient light scattering from micron sized tracer particles. Instead, in the coaxial configuration the laser light is expanded from its source point to illuminate the full camera field of view. The combination of the above effects produces adverse conditions in terms of particle image intensity variability, which need to be accounted for while designing the CVV system. The problem is addressed in the present study by introduction of tracers with a high scattering efficiency. The scattered light from helium filled soap bubbles as flow tracers (HFSB, Bosbach et al. 2009) has been reported to be 10^4–10^5 times more intense (for a bubble diameter in the sub-millimeter range) than that of micrometer droplets (Caridi and Sciacchitano 2017) enabling a significant increase of the measurement domain for tomographic PIV experiments. The suitability of helium-filled soap bubbles for wind tunnel measurements at relatively large scale was recently ascertained in a series of studies (Scarano et al. 2015; Schneiders et al. 2016; Caridi et al. 2016).

A second stumbling block stems from the very small tomographic aperture of the imaging system of the CVV. This leads to a poor positional accuracy of particle tracers along the depth direction (Elsinga et al. 2006; Fahringer et al. 2015; amongst others). The problem is dealt with by a substantial increase of the time interval along which the particle motion is followed. Registration of the particle position over multiple frames yields a longer trajectory and in turn increases the velocity dynamic range compared to double-pulse systems (Shake-the-Box, Schanz et al. 2016, amongst others). Therefore, the time-resolved measurement condition needed for CVV requires the use of high-speed CMOS cameras and diode-pumped solid-state lasers operating in the kilohertz range.

The work discusses first the fundamental properties of the CVV in terms of hardware configuration, illumination and imaging optics, followed by the data analysis procedure. The system performance is estimated in terms of measurement accuracy and spatial resolution of the time-averaged velocity field. Experiments with a prototype CVV that has been realized are shown later in Chapter 11.

10.1 Measurement range and resolvable flow scales

10.1.1 Measurement volume

Tomographic PIV is taken here as a term of comparison when evaluating the spatial dynamic range of the CVV technique. In tomographic PIV, the depth of the measurement volume is often controlled by cutting of the laser beam with knife edge filters. The measurement volume of the CVV (dashed red line in Fig. 10.2) results from the propagation of the laser beam expanding conically with a given angle φ. The cameras angle of view is chosen to approximately coincide with φ.

Measurement volume width and height

Assuming that the illumination covers the full field of view, both the width L_x and height L_y of the measurement volume are dependent on the sensor size ($W \times H$) and focal length f, of the lens:

$$L_x(z) = \frac{W}{M}, \tag{10.1}$$

where M is the optical magnification. In the imaging regime of CVV, the magnification cannot be considered constant as it varies widely within the measurement domain. The magnification is inversely proportional to the distance z from the imaging system:

$$M = \frac{d_i}{z} \approx \frac{f}{z}, \tag{10.2}$$

where d_i is the distance of the lens from the image plane. The former can be approximated by the focal length when $M \ll 1$.

Measurement volume depth

The depth of the measurement volume is limited by the laser pulse energy, and the camera sensitivity and its noise level. The laser light expands at an angle φ (Fig. 10.3) after a single spherical lens from the exit of the fiber optic laser guide. Given the conical propagation of illumination, the laser light intensity decays with the square of the distance z. The angle φ needs to be sufficiently large for the illumination to cover the field of view and can be approximated by,

(10.3) $\varphi \geq 2\,\mathrm{atan}\frac{L_x}{2z}$.

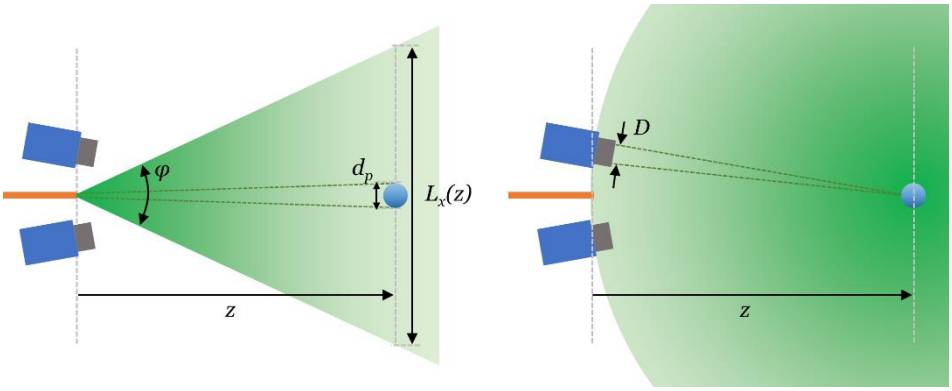

Fig. 10.3 Schematic illustration of laser light propagated from the optical fiber, interacting with a tracer particle (left) and collected back by the cameras (right). Arrangement of optical fiber (orange) in between the cameras (blue) for illustration purposes. Tracer particle not drawn to scale.

A particle of diameter d_p placed at distance z will scatter the light back towards the imagers collecting it through an aperture D. Considering the spherical propagation by an angle φ of a laser light pulse of energy I_0 from the fiber end (fiber diameter d_f), the expression of the collected light I_p reads as:

(10.4) $I_p = I_0 \frac{d_f^2}{z^2 tan^2\left(\frac{1}{2}\varphi\right)} \frac{Q\pi d_p^2 D^2}{z^2}$

where Q is the optical scattering efficiency of the soap bubble in backward direction. In the above equation the first ratio on the right-hand side term describes the light extinction due to propagation from the source to the tracer. The second term, models the amount of light scattered and collected back by the imagers, given their aperture.

An important conclusion is that the particle image intensity I_p decreases moving away along the measurement volume depth with the power four:

(10.5) $I_p \propto \frac{1}{z^4}$.

The above scaling is experimentally verified by imaging particles placed within a range of distances. The experiment is performed with the CVV system realized in Chapter 11. The position of the tracers is controlled by translating a single HFSB generator along the depth of the measurement volume. In Fig. 10.4 the integral of particle image intensity is shown. The numerical aperture $f_\#$ is varied from 4 to 11. The results expressed in logarithmic scale agree with fourth-power scaling (grey line). Also, premultiplying by $f_\#^2$ to account for the different aperture used in the experiments makes the data series collapse consistently with eq. (10.4).

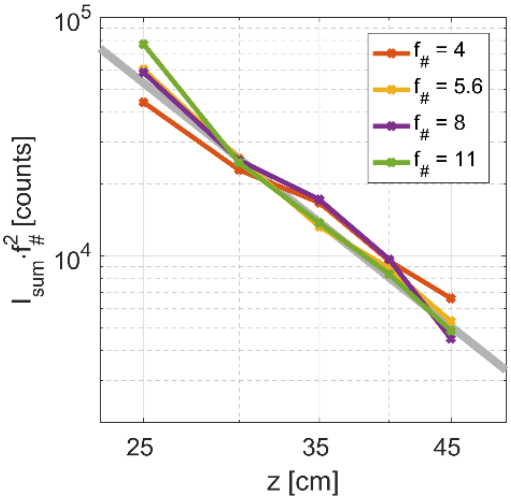

Fig. 10.4 Particle image integral intensity measured by the CVV system. The grey line indicates the theoretical slope of -4 on the log-log scale.

Given this fourth order relationship between particle image intensity and z, one can relate the achievable depth of measurement to the imager bit depth. The ratio between the volume depth, or maximum measurement distance, z_{max} and the closest position where particle images begin to produce intensity saturation z_{sat} equals:

$$\frac{z_{max}}{z_{sat}} = \left(\frac{2^b}{I_n}\right)^{\frac{1}{4}}, \tag{10.6}$$

where I_n is the minimum detectable particle image intensity and b the imager bit depth. The exponent is due to the fourth order relation between

particle image intensity and distance. For illustration, a 10-bit camera with a minimum level for detectability of 20 counts allows for a measurement volume depth of 50 cm. In these conditions, particles closer than 20 cm are imaged at saturated intensity.

Measurement volume size

Using the expression for the measurement volume width (eq. 1), the measurement volume of the CVV can be approximated by a truncated square pyramid with a height corresponding to the difference between maximum and minimum distance along depth. The CVV system (Chapter 11) features an angle of view of approximately φ =50 deg. Considering the closest measurement distance of z_{min} = 10 cm and a furthest z_{max} = 50 cm, the resulting measurement volume is approximately 30 liters. Moreover, given the compactness and fixed camera configuration of the CVV, the device is intended to be pointed in several directions and translated with the aid of a robotic arm (Jux et al. 2017).

10.1.2 Spatial resolution

As the CVV returns the time-averaged velocity field, the estimation of the velocity vector field is obtained by ensemble averaging particle velocity in interrogation bins or cells. Ample discussion of data processing techniques is given in Kähler et al. (2012a,b). Rules for ensemble averaging have been extended to 3D data recently by Agüera et al. (2016). Producing a statistically converged estimate of the velocity within a cubic element or bin requires that enough data samples are captured within a bin. If one assumes an instantaneous tracers concentration C and a minimum number of samples N_I to be collected inside a bin, the needed number of uncorrelated measurements N_t is inversely proportional to the bin (linear) size l_B:

$$l_B = \sqrt[3]{\frac{N_I}{N_t C}}. \quad (10.7)$$

The upper limit for the tracer particle seeding concentration C_{max} is dictated by the maximum particle image density often expressed as N_p in particles per pixel (ppp). Considering the latter:

$$(10.8)\quad N_p = C\frac{V}{N_{pix}} \quad \Rightarrow \quad C_{max} = N_{p,max}\frac{N_{pix}}{V}$$

where N_{pix} is the number of pixels of the imager. Tomographic reconstruction is reliably obtained up to $N_p = 0.05$ ppp (Elsinga et al. 2006, among others). A similar value has been demonstrated for the STB algorithm (Schanz et al. 2016) and this value is retained as upper bound for the CVV. This value dictates the maximum tracer particle concentration according to eq. (10.8). Considering z_{min} = 10 cm and z_{max} = 50 cm, eq. (10.8) yields a maximum concentration of approximately 1 particle/cm^3. The spatial resolution of the time-averaged velocity field is based on the above concentration, but it also depends upon the number of uncorrelated measurements following eq. (10.7). Increasing the number of measurements N_t allows reducing l_v with a consequent increase in spatial resolution.

10.2 Particle imaging and velocity estimation

10.2.1 Lens aperture and focus

The measurement volume of the CVV requires a significantly larger depth of field (DOF) than a typical tomographic PIV apparatus. To avoid that particles are imaged out-of-focus, the near and far limits of the DOF, D_N and D_F, should include the range between z_{min} and z_{max} respectively (Fig. 10.2). The limits D_N and D_F can be approximated by (Larmore 1965):

$$(10.9)\quad z_{min} \geq D_N = \frac{Hz_f}{H+z_f}$$

$$(10.10)\quad z_{max} \leq D_F = \frac{Hz_f}{H-z_f} \qquad \text{for } z_f < H,$$

where z_f is the focal plane and H is the hyperfocal distance. The latter, for the CVV, is equal to:

(10.11) $H = \frac{f^2}{f_\# d_\tau}$

where $f_\#$ is the numerical aperture of the objective, d_τ is the particle image size estimated by eq. (10.14). Solving the above equations for the minimum $f_\#$ yields:

(10.12) $z_f = \frac{2z_{min}z_{max}}{z_{min}+z_{max}}$

(10.13) $f_{\#,min} = \frac{1}{2}\frac{f^2}{d_\tau}\left(\frac{1}{z_{min}} - \frac{1}{z_{max}}\right)$

Therefore, the focal plane of the CVV should not be centered, but be closer to D_N than to D_F. The CVV realized in Chapter 11, for instance, is focused at z_f = 17 cm, when z_{min} = 10 cm and z_{max} = 60 cm. The minimum aperture setting, to ensure the full measurement volume is in focus, is $f_\#$ = 7. A higher aperture setting of 8 is desired, however, to achieve particles larger than 2 pixels (Sec. 10.2.2).

10.2.2 Particle image size and displacement

Considering that the optical magnification of CVV varies between 10^{-1} and 10^{-2} the particle image size is dominated by diffraction with a rather constant value along the entire measurement volume depth. In backward scattering mode, the distance between glare points vanishes below the diffraction limit. Therefore, the particle image size is well approximated by diffraction only and reads as:

(10.14) $d_\tau = 2.44\lambda f_\#(1 + M)$

The particle image displacement, is inversely proportional to distance according to

(10.15) $\Delta x_i = Mu\Delta t = u\Delta t\frac{f}{z}$

where Δt is the pulse separation time. Therefore, particles close to the camera appear travelling faster than particles further away. This is illustrated in Fig. 10.5 in case of the CVV realized in Chapter 11 and a

constant free-stream particle displacement of 4 mm. The working range of the CVV (Jux et al. 2016) is indicated in the figure on the horizontal axis.

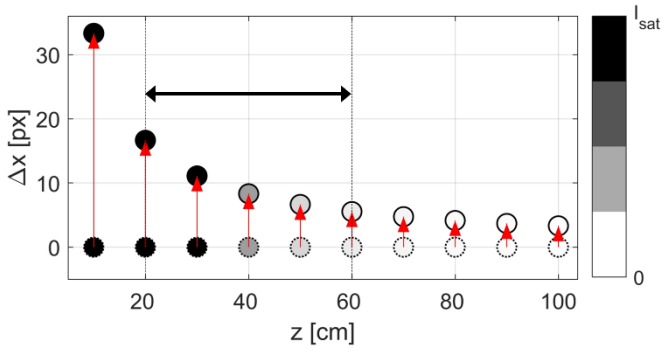

Fig. 10.5 Particle image displacement along the measurement volume depth in case of a constant free-stream particle displacement of 4 mm. The color indicates the particle intensity. The typical working range of a CVV is indicated by the black arrow.

10.3 Velocity resolution

10.3.1 Estimation of particle position

Measuring the position of a particle tracer is affected by an error ϵ_x proportional to the particle image size:

(10.16) $\epsilon_x = c_\tau d_\tau$

when d_τ is larger than approximately 1.5 times the pixel size (e.g. Raffel et al. 2007) and where the coefficient c_τ represents the uncertainty in locating the centroid of the particle (Adrian 1991; Adrian and Westerweel 2011). This coefficient typically falls in the range 0.1 to 0.2.

In case of 3D measurements, the relevant property is the reconstructed particle size, whereby the particle image is reprojected to physical space. The reconstructed particle size along the x- and y-axis depends almost entirely upon the particle image size:

(10.17) $d_x = d_y = \frac{d_\tau}{M}$.

Therefore, in case of 3D measurements:

(10.18) $\epsilon_x = \frac{c_\tau d_\tau}{M}$.

Particle reconstruction along z depends upon the system aperture β. In the case of tomographic PIV, the limited solid angle subtended by the camera typically causes the particles to be elongated two to three times (Fig. 10.6, Elsinga et al. 2006; Fahringer et al. 2015; amongst others).

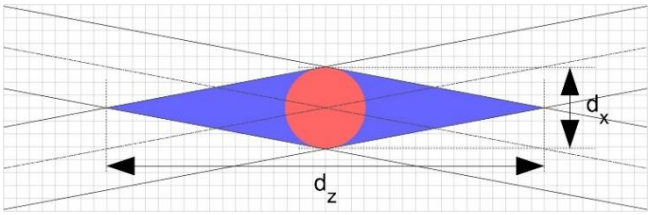

Fig. 10.6 Schematic of the reconstructed particle intensity.

For small aperture ($\beta \ll 1$ rad), the extent of the particle elongation is linearly dependent from β as follows:

(10.19) $\frac{d_z}{d_x} = \frac{2}{\beta}$.

It should be kept in mind that the angle β is not a constant as it decreases by increasing distance z,

(10.20) $\beta = \frac{\beta_0 z_0}{z}$,

with β_0 the local solid angle at chosen position z_0 (c.f. Fig. 10.2). For illustration, taking the CVV realized in Chapter 11 at z = 30 cm, a local value of β = 7 degrees corresponds to a particle elongation of factor 16. If a particle is imaged at a diffraction limited size of 2 pixels the region of high intensity in 3D space will be of the extent of $d_x = d_y$ = 0.7 mm and d_z = 12 mm. These equations are validated in Appendix C by means of tomographic reconstructions of particle images acquired by a prototype CVV.

Consequently, the particle positional uncertainty in the z-direction is significantly larger than in the other two directions:

(10.21) $\epsilon_z = \frac{2}{\beta}\epsilon_x$.

Assuming $c_\tau = 0.1$ for eq. (10.18), an instantaneous particle positional error $\epsilon_x = 0.1$ mm translates into $\epsilon_z = 1$ mm. As discussed in the remainder, this effect needs to be compensated by enlarging the particle displacement ΔX:

(10.22) $\frac{\Delta X}{\varepsilon_z} \gg 1$.

Extending overly the time separation in two-pulse systems increases the effect of temporal truncation of the tracer velocity estimation (Boillot and Prasad 1996). The latter effect is countered by sampling the particle position at multiple times and analyzing its trajectory by multi-framing techniques, as illustrated in Fig. 10.7 and discussed in detail in the next section.

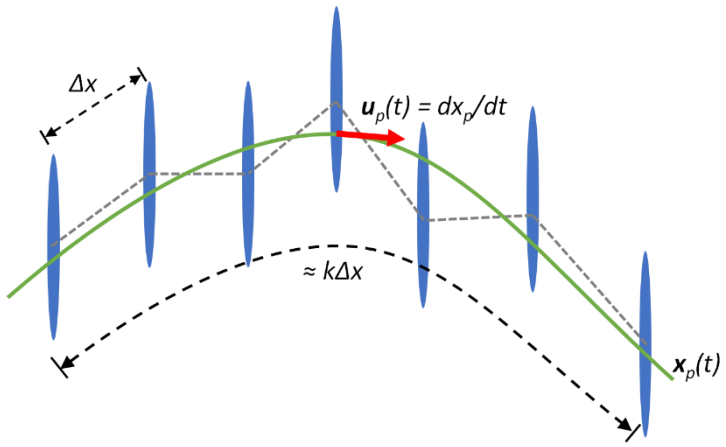

Fig. 10.7 Schematic of a particle trajectory evaluated along a discrete number of exposure and with particle elongation due to the low tomographic aperture. The grey dotted lines show the result from two-frame analysis and green line shows a second order polynomial fit over a track length of $k\Delta x$.

10.3.2 Uncertainty of instantaneous velocity vector estimation

For double pulse systems, the relative measurement uncertainty of the particle displacement estimation is approximated from superposition of the variances of the particle position estimation:

(10.23) $\epsilon_u = \frac{\epsilon_x\sqrt{2}}{\Delta x} = \frac{\epsilon_x\sqrt{2}}{u\Delta t}$,

where Δx is the particle displacement and Δt is the pulse-separation time.

Estimating the velocity from multiple frames allows for a reduction of the velocity measurement error (Cierpka et al. 2013; Lynch and Scarano 2013; Schanz et al. 2016; amongst others). The concept of track regularization is illustrated in Fig. 10.7, where a second order polynomial (i.e. Savitzky-Golai filter, Savitzky and Golay 1964) is fitted through discrete particle positions including the effect of the non-isotropic reconstruction. While multi-frame approaches exist for cross-correlation analysis (Lynch and Scarano 2013; Jeon et al. 2014), the analysis for the CVV is limited to volumetric Lagrangian particle tracking approaches (e.g. Novara et al. 2013; Schanz et al. 2016).

With multi-frame analysis of *k* frames, two effects contribute to the error reduction: the first is given by the longer overall time separation according to eq. (23) by a factor *k*. Secondly the error reduction with factor $\sqrt{k}$ is obtained when averaging of random error corresponding to the particle position estimation from each sample along the integral path length (Fig. 10.7). The combined effects yield a scaling of the error with $k^{-3/2}$ already retrieved for the analysis based on cross-correlation (Lynch and Scarano 2013). The resulting expression for the relative velocity uncertainty when using multi-frame analysis reads as:

(10.24) $\epsilon_u = \frac{c_\alpha \epsilon_x}{k\Delta x\sqrt{k}}$

where c_α is a coefficient dependent upon the particle track regularization technique that is used and Δx is the displacement between two subsequent exposures of the multi-frame recording. The above expression is valid under the hypothesis that the particle trajectory is fitted with a function that avoids truncation of the velocity variations along the trajectory. Typically, polynomials of order 2 to 3 have been used with multi-frame recordings of length *k* ranging from 5 to 15. In the mentioned range little to no effect of temporal truncation had been reported (e.g. Schanz et al. 2013; Novara et al. 2013).

A polynomial fitting procedure returns an analytical expression for the temporal evolution of the tracer position $\boldsymbol{x}_p(t)$:

(10.25) $\boldsymbol{x}_p(t) = \boldsymbol{a}_1 + \boldsymbol{a}_2 t + \boldsymbol{a}_3 t^2 \quad \rightarrow \quad \boldsymbol{u}_p(0) = \boldsymbol{a}_2$

In the above example the Taylor expansion is truncated to the second order. The particle velocity is subsequently obtained from the time derivative of the above expression. For a time-centered estimate, the velocity corresponds to the coefficient $\boldsymbol{a}_2$.

The work of Schneiders and Sciacchitano (2017) establishes that $c_\alpha \approx 3.5$ in eq. (24) for a second order polynomial, under the assumption that truncation errors (low-pass filtering) are negligible.

In conclusion, an operational criterion is proposed here for low-aperture systems ($\beta \ll 1$ rad). The criterion dictates the minimum number of exposures k to be included in the trajectory estimation that will return a velocity estimate with the component along depth of accuracy comparable to that of the in-plane components as obtained with a double-pulse system.

(10.26) $k \geq 3/\beta^{\frac{2}{3}}$

Considering for instance, an aperture $\beta = 0.1$ radians and a sequence of 10 frames, where the particle displacement between frames is 5 mm, the measurement uncertainty for u and v components is approximately 0.2% and approximately 4% for the w component.

10.3.3 Uncertainty of time-averaged velocity estimation

The discussion in the previous section pertains to the uncertainty of the instantaneous velocity measurements. When dealing with the estimation of time-averaged velocity, the uncertainty is typically dominated by the temporal velocity fluctuations due for instance to flow turbulence. The dependence of time-average estimation uncertainty upon the latter and the number of samples considered for ensemble averaging reads as follows:

$$(10.27)\ \epsilon_{\bar{u}} = \frac{\sqrt{\sigma_{\bar{u}}^2 + \epsilon_u^2}}{\sqrt{N_I}} \approx \frac{\sigma_{\bar{u}}}{\sqrt{N_I}}.$$

where $\sigma_{\bar{u}}$ is the turbulence intensity and N_I is the number of velocity measurements in the bin used for ensemble averaging (Sec. 10.1.2). The second approximate equality holds when $\sigma_{\bar{u}} \gg \epsilon_u$.

The uncertainty of the time-averaged velocity vector field therefore largely depends upon the number of velocity measurements in the ensemble averaging bin. A trade-off between measurement accuracy and spatial resolution emerges clearly from the above discussion, since increasing the number of samples N_I implies a larger size of the bin chosen for ensemble averaging.

10.4 Dynamic spatial and velocity range

Here, the ranges of resolvable velocity field variations and spatial scales are estimated considering the properties of the CVV measurement system. The smallest resolvable length scale in the velocity field stems from the interrogation bin size l_B (Sec. 10.1.2), whereas the largest resolvable scale is determined by the measurement volume size (Sec. 10.1.1). Given the compactness of the device, the latter can be expanded by moving the measurement region with the aid of a traversing mechanism or a robotic arm, as demonstrated in Jux et al. (2017).

Adrian (1997) defined the dynamic spatial range (DSR) as the ratio between the largest and smallest resolvable measurement scales for instantaneous measurements. Analogously, the DSR for time-averaged CVV measurements can be defined using the length scales derived above:

$$(10.28)\ \overline{\mathrm{DSR}} = \frac{L_x}{l_B},$$

where L_x is selected as a typical dimension of the measurement domain (Sec. 10.1.1). Assuming a measurement domain extent of 50 cm and a bin size of 1 cm³, the resulting $\overline{\mathrm{DSR}}$ is in the order of 50.

Similar to the above, the dynamic velocity range (DVR, Adrian 1997) can be defined for the time-averaged velocity measurements, as the

ratio between the highest value of measured velocity and the smallest resolvable variation. The latter depends upon the velocity measurement uncertainty as derived in Sec. 10.3.3:

(10.29) $\bar{u}_{min} \approx \frac{\sigma_{\bar{u}}}{\sqrt{N_I}}$.

The maximum resolvable velocity is dependent upon the maximum particle displacement that can be afforded with a particle tracking algorithm:

(10.30) $u_{max} = \frac{\Delta x_{max}}{\Delta t}$.

Accordingly, the dynamic velocity range for time-averaged measurements, $\overline{\mathrm{DVR}}$, obtained by the CVV equals:

(10.31) $\overline{\mathrm{DVR}} = \sqrt{N_I}\left(\frac{\Delta x_{max}}{\sigma_{\bar{u}} \Delta t}\right)$,

For a typical CVV measurement, where $u_{max} = u_\infty$ and the turbulence intensity is 10%, this yields $\overline{\mathrm{DVR}} = 100$ when considering ensemble averaging bins with $N_I = 100$. The most common way to increase $\overline{\mathrm{DVR}}$ is by collecting larger sequences of images, at detriment of the computation time. Additionally, the velocity dynamic range can be increased acquiring images with shorter time separation (i.e. higher acquisition frequency).

10.5 Conclusions

A coaxial volumetric velocimeter (CVV) is proposed based on the use of multiple imagers positioned close together and at a small solid angle. Illumination of tracer particles is provided through an optical fiber positioned in between the cameras. The CVV therefore requires optical access only from one measurement direction. In this configuration, the particle image intensity recorded on the imagers scatters with the 4th power of the particle distance from the measurement device. The theoretical background derived in the study shows that the CVV is only of practical use when tracer particles are used that scatter light several orders of magnitude more than traditional fog droplets. Presently, the use

of CVV is demonstrated making use of HFSB as tracers. In addition, the study shows that due to the small solid angle of the system there is an approximately 15-fold higher particle positional and velocity measurement error for the axial component than for the in-plane components. To compensate for reduced accuracy of the z-component of velocity, particles are imaged multiple times along their trajectories to produce a time-accurate reconstruction of their motion. The spatial resolution of the instantaneous velocity measurements depends upon the particle image density and the number of recordings. A spatial resolution on the below a centimeter is achieved currently only when employing an ensemble averaging approach over several thousand images.

In the next chapter, a prototype CVV is realized and used for multiple wind tunnel experiments to assess its performance in a real-world environment.

Chapter 11
CVV Wind Tunnel Measurements

A CVV is realized (Sec. 11.1) and first used for measurement of the canonical flow around a sphere (Sec. 11.2). After establishing that the time-averaged flow field can be measured within acceptable agreement to the potential flow solution, a more complex flow case is considered. With help of robotic manipulation of the CVV, the flow around a full-scale cyclist model is measured (Sec. 11.3). It is proposed to leverage the ability of the CVV to measure the near-surface flow for calculation of skin-friction lines. The chapter concludes with a discussion on the use of these skin-friction lines and the CVV in general for interpretation of the three-dimensional flow field.

11.1 Prototype CVV system

A CVV system is realized that combines four cameras and laser illumination within a box as depicted in Fig. 11.1. Four compact LaVision *MiniShaker S* CMOS imagers (831 × 631 pixels at 471 fps, 10 bits) are positioned as schematically illustrated in Fig. 11.1. The cameras optical axes intersect at a point located at $z_0 = 50$ cm from the sensor plane with a corresponding base angle $\beta_0 = 4.3$ degrees. The cameras are fitted with $f =$ 4 mm lenses, with numerical aperture set to $f_\# = 8$ ensuring in-focus particle images over the expected volume depth ($z_{max} \sim 0.5\ m$). The light source is a Quantronix *Darwin-Duo* Nd-YLF laser (2 × 25 mJ pulse energy at 1 kHz). The light is transmitted from the source to the CVV through an optical fiber with its end in between the cameras (Fig. 11.1). The laser light spreading angle of 65° is achieved by focusing the collimated laser light at the source with a spherical lens of 20 mm focal length. An additional micro-lens is installed at the end of the optical fiber to further increase the spreading angle.

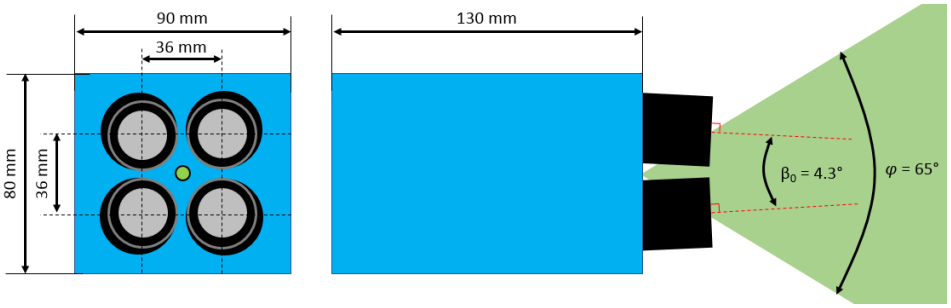

Fig. 11.1 Sketch of the front (left) and side (right) of the CVV.

As previously discussed, given its working principle, the CVV system is unsuited for volumetric measurements with standard micron sized tracer particles, as these would not scatter sufficient light. Therefore HFSB (Bosbach et al. 2009) with a diameter in the order of 300 μm are used as tracer particles.

11.2 Flow around a sphere

Experiments are performed in an open-jet low-speed wind tunnel with 60 × 60 cm² exit cross section at flow speed of 2.5 m/s. A sphere with a 10 cm diameter is placed 30 cm downstream of the exit (Fig. 11.2). The CVV system is positioned just outside of the jet-stream at 30 cm distance from the sphere. The optical magnification at the center of the sphere is approximately 0.01.

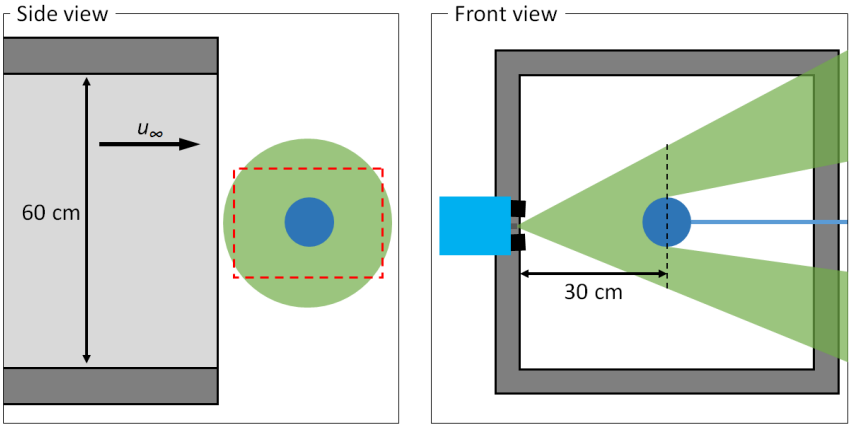

Fig. 11.2 Schematic of the measurement setup. The figures are drawn in a plane through the center of the sphere.

The expected measurement volume width and height at this distance are 30 cm and 22 cm, respectively (indicated by the dashed red line in Fig. 11.2-left). The measurement volume encompasses the inviscid laminar flow region ahead of the sphere, and a turbulent wake, including a separated flow region behind the sphere. Such measurement with planar or tomographic PIV requires at least two measurement directions due to the model shadow and optical blockage to the cameras.

Particle images are recorded at 471 Hz, corresponding to a 5 mm displacement in the free stream (corresponding to approximately 15 pixels particle image displacement at z = 30 cm). Measurements include 15 runs, totaling 25,000 image quadruplets. The particle image density is limited by HFSB seeding generation rate and equals approximately N_p = 0.015 ppp. The instantaneous particle images from the four CVV cameras are shown in Fig. 11.3. The figure shows the raw images for cameras 1, 2 and 3. Due to the small solid-angle of the imaging system, the differences between the four camera images is barely noticed by visual inspection. The time-series of images is pre-processed using a high-pass filter in the frequency domain (Sciacchitano and Scarano 2014) to reduce the reflections from the solid surface of the sphere (filter length of 7 recordings). The bottom-right figure shows the instantaneous particle image obtained by camera 4 after pre-processing. The particles peak intensity varies largely along the depth of the measurement volume (Sec. 10.1) and decays moving away from the viewing axis due to the Gaussian profile of laser light intensity. The measurement volume achieved is approximately 10 liters, based on z_{min} = 15 cm and z_{max} = 35 cm.

The center of the image is saturated where the light scattered by the surface of the sphere is reflected directly towards the imagers. As a result, no particle images can be detected in this region. Note that in the coaxial configuration, the illumination direction cannot be changed independently of the imagers viewing direction to reduce reflections. The effect of reflections can therefore not be reduced by changing illumination direction. Reflections could be reduced by use of paint or cameras with a larger full-well capacity. Alternatively, Jux et al. (2017) show how the CVV measurement results from multiple viewing directions can be

stitched together, providing an alternative strategy to mitigate surface reflections.

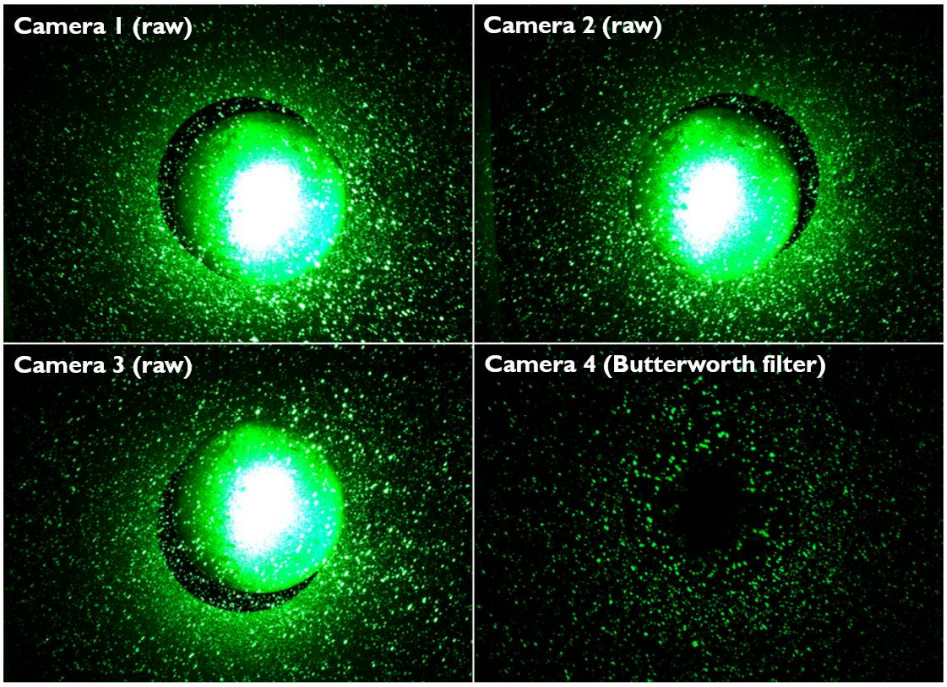

Fig. 11.3 Raw instantaneous particle images from cameras 1 to 3 and the pre-processed particle image from camera 4 (bottom-right).

The sequence of pre-processed images is analyzed using the algorithm Shake-the-Box (STB, Schanz et al. 2016) to estimate the particles velocity. Only tracks with a minimum length of 4-exposures are retained in the analysis. A 2nd order polynomial fit models the particle trajectory. Approximately 0.1 tracks/cm^3 are detected on average in every recording, which is less than the seeding concentration of 0.7 HFSB/cm^3 estimated from the particle image density and eq. (10.8).

For illustration, Fig. 11.4 shows a subset of tracked particles, colored by velocity magnitude. Particles at a distance larger than the sphere center plane are hidden for clarity of the visualization. The flow deceleration ahead of the stagnation point in front of the sphere is followed by a region where the flow accelerates beyond the free-stream value around the

sphere under the effect of the favorable pressure gradient. After the point of maximum cross section, the boundary layer separates generating a turbulent wake region downstream of the sphere. In the latter, erratic particle trajectories can be observed, corresponding to the chaotic motions in the turbulent separated flow regime.

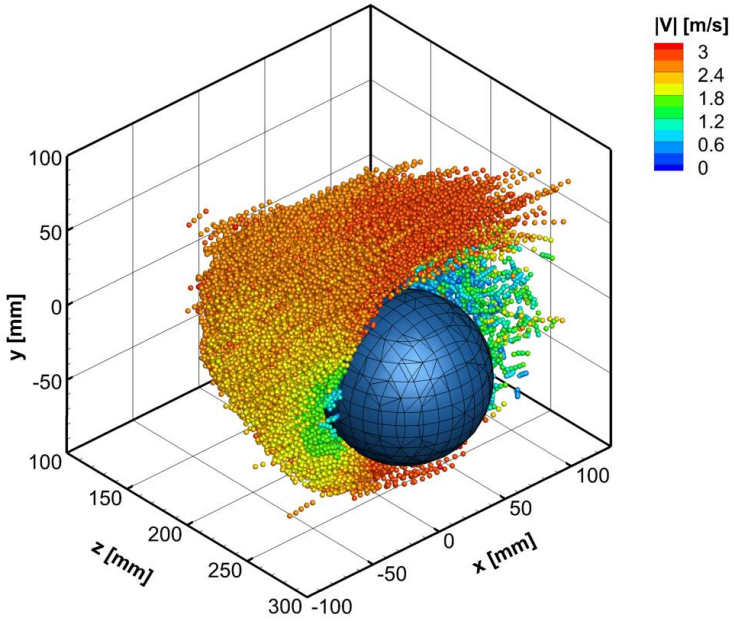

Fig. 11.4 Subset of the particle tracks. The volume is cropped for clarity of the visualization.

The time-averaged velocity field is obtained by ensemble averaging the scattered data over bins of 7.5 × 7.5 × 7.5 mm^3. The evaluation with 75% overlap results in vectors spaced by 1.9 mm. The dynamic spatial range for this measurement is estimated to $\overline{DSR}$ = 25. On average, there are N_I = 500 particles falling in every bin. Based on 10% intensity of the turbulent velocity fluctuations (wake region), the resulting $\overline{DVR}$ is in the order of 200.

The measured flow upstream of the sphere can be compared to the analytical solution from potential flow theory (e.g. Anderson 2010). The measured time-averaged flow field is shown in Fig. 11.5-left (color contours), along with the velocity from potential flow theory (dashed

contour lines). A generally good correspondence is observed within the angular range from the front stagnation point and moving approximately 45° along the surface of the sphere. Further than that point, the velocity field is affected by the separation in the rear of the sphere and the potential theory fails to adequately model the flow field. A detailed comparison is extracted along the stagnation streamline, where the velocity profile taken along y = 0 is considered (Fig. 11.5-right). The measured values correspond with good agreement to the theoretical reference up to x/R = -1.1. Any closer, the effect of the bin overlapping with the sphere yields an overestimation of velocity, similarly to the reported case of estimating the near wall velocity in boundary layers (Kähler et al. 2012b).

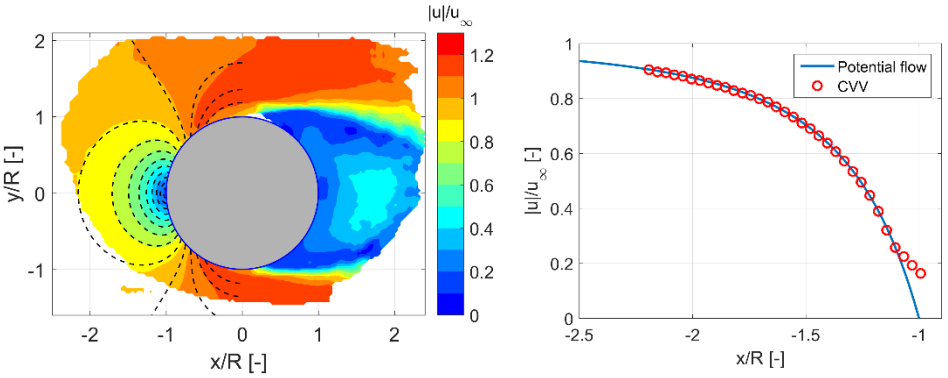

Fig. 11.5 Left: time-averaged velocity measurements of the flow around a sphere. Potential flow solution (dashed contours) superimposed on the CVV result. Right: streamwise profile of velocity along the stagnation streamline.

The level of velocity fluctuations measured by the CVV away from the sphere gives an indication of the uncertainty of instantaneous velocity measurements. For the streamwise component u'_{rms} = 0.02 m/s (approx. 1%), whereas along the depth w'_{rms} = 0.2 m/s (approx. 8%). These values are obtained considering trajectories evaluated along 7-frames with a 2nd order polynomial. From a parametric analysis, the value of u'_{rms} is found to be independent of the chosen track length and is therefore considered to correspond to the physical velocity fluctuations exhibited by the free stream of the open jet. The value for w'_{rms} is significantly higher and in

fair correspondence to the measurement error of the axial component predicted in Sec. 10.3. Considering that the time-averaged value is built in each bin with an ensemble of approximately 500 samples, the uncertainty of the mean value becomes 0.05% for the streamwise component and 0.4% for w.

11.3 Full-scale cyclist measurements

The previous section considered the relatively simple wind tunnel model of a sphere. In the present section, the capabilities of the CVV to measure the near-surface flow around the more complex model of a cyclist are investigated.

11.3.1 Experimental apparatus and setup

A full-scale 3d-printed model of *Giro d'Italia* winning cyclist Tom Dumoulin (van Tubergen et al. 2017) is used for the present wind tunnel measurements. The measurements on the cyclist model were performed by Jux et al. (2017) in an open jet wind tunnel facility with a 2.85 × 2.85 m^3 cross-section of the outlet. The wind tunnel speed of u_∞ = 14 m/s (Re = $5.5 \cdot 10^5$) corresponds to that practiced during time-trial competitions (see e.g. the review by Lukes et al. 2005). A photograph of the experimental setup (Fig. 11.6) shows the cyclist inside of the test section, downstream of the HFSB seeding rake. The relatively compact size of the CVV makes it suitable for manipulation by a robot arm, as also shown in Fig. 11.6. A full discussion of the robotic manipulation of the CVV for measurement of an extended measurement volume is given in Jux et al. (2017).

The present work considers three specific CVV measurements to illustrate the range of optical access, the data yield and the different types of utilization. The regions inspected (athlete's face, lower back and ankle-foot) are shown in Fig. 11.7-left. At the athlete's face, the measurement challenge lies in capturing the flow over a three-dimensional corrugated surface. At the back of the athlete, the flow is expected to exhibit unsteady separation with high levels of turbulence. Finally, the ankle-foot region is known to be the source of tip vortices emanating from this extremity. Capturing these vortices gives an indication of the small-scale velocity and vorticity scales that can be represented with the CVV.

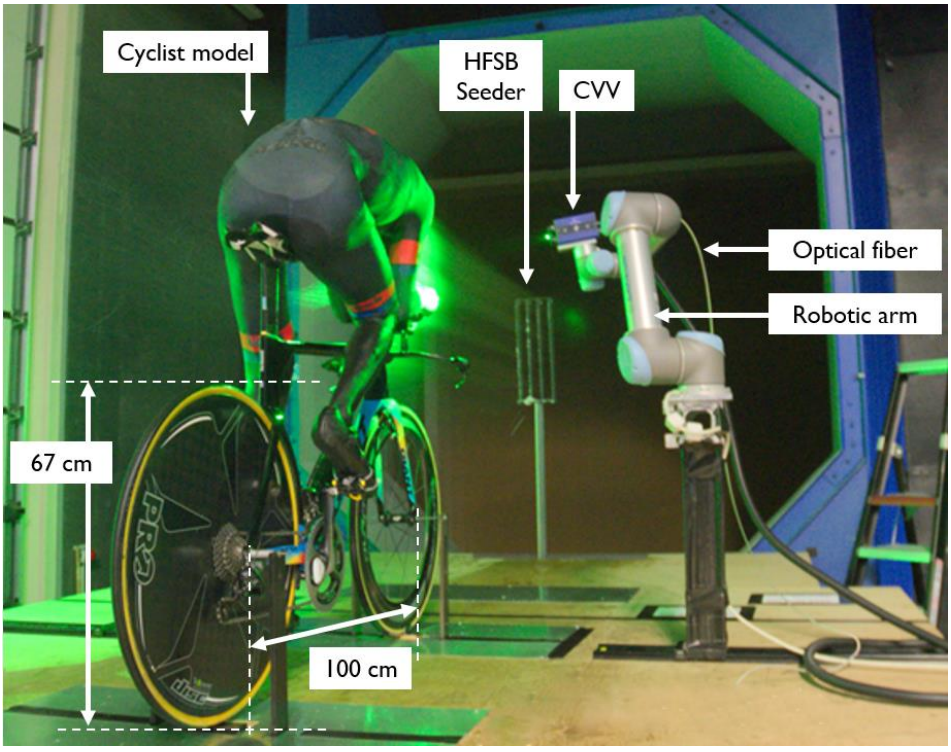

Fig. 11.6 Photograph of the robotic CVV setup (adapted from Jux et al. 2017).

The dashed red lines in Fig. 11.7-left show the approximate field of view employed for the measurements. The active area of the CVV imagers is cropped to 640 × 475 pixels to achieve a recording rate of 758 Hz that limits the particle image displacement within 18 mm (40 px at z = 30 cm) at a free-stream velocity of 14 m/s. From eq. (10.1), a measurement volume width of 23 cm is expected at z = 30 cm. Reducing the conical expansion angle yields an increased measurement volume depth of approximately 70 cm. Each sequence includes 5000 recordings.

Samples of particle image recordings are shown in Fig. 11.7-right. The particle image density is approximately N_p = 0.03 ppp. Using image pre-processing and particle motion analysis procedures like in the previous section, one tenth of the particles (1000 tracks per recording) are tracked successfully. The bin size for ensemble averaging is set to 20 × 20 × 20 mm^3 with 75% overlap (5 mm vector spacing). The criterion is

imposed that a minimum of 10 velocity measurements are used to estimate the time-average value in each bin. The choice of the bin size has been made in favor of spatial resolution rather than accuracy of the ensemble average estimate. Based on the volume depth, the $\overline{DSR}$ is estimated to 150. Assuming a turbulence intensity of 10% yields $\overline{DVR} = 30$.

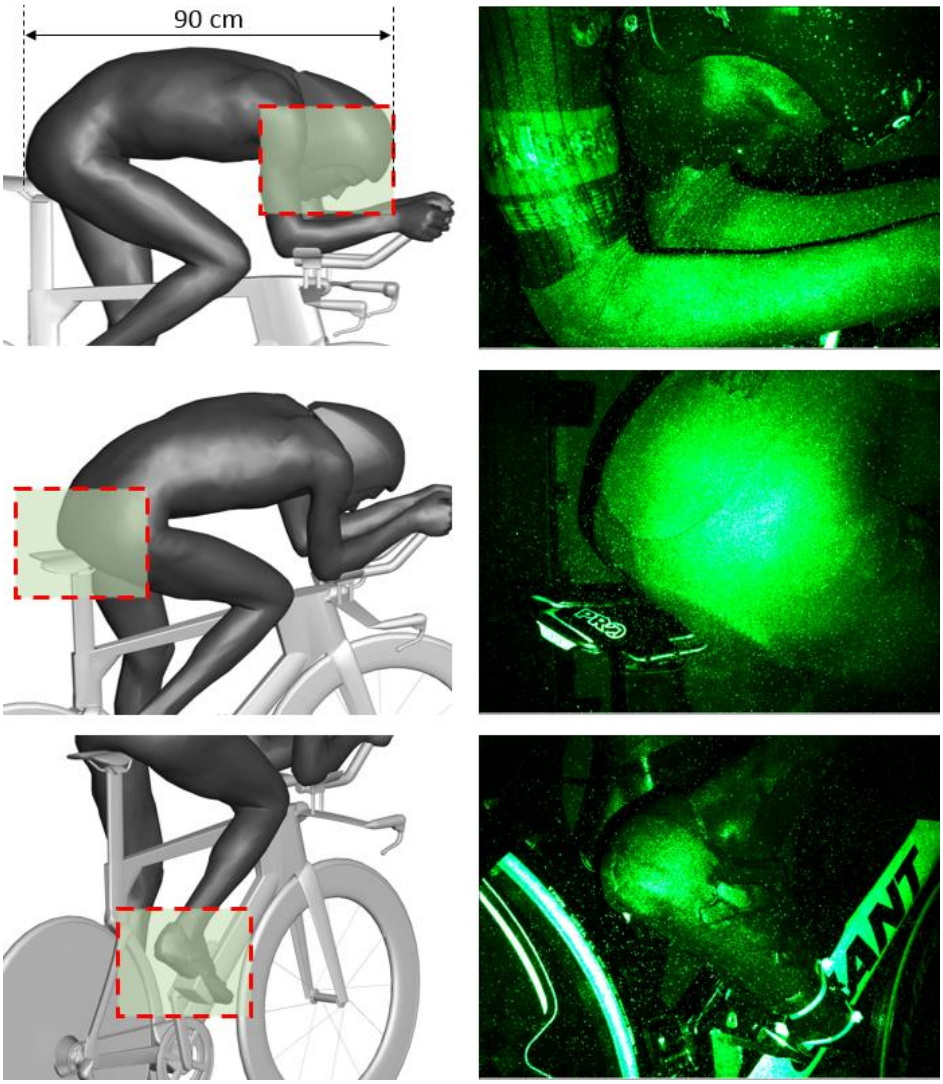

Fig. 11.7 Field of view relative to the cyclist model indicated by the dashed red box (left) and and example of a corresponding raw particle image (right). For clarity the particle images are colored green and saturated at 512 counts. From top to bottom the 'face', 'back' and 'foot' measurement cases are shown.

11.3.2 Near-surface streamlines

The flow near the face and arms of the cyclist exhibits stagnation on the biceps of right arm, which is positioned approximately perpendicular to the free-stream direction. The near-surface streamlines are computed from the CVV results at 5 mm (one vector-spacing) from the surface of the cyclist. The result is illustrated in Fig. 11.8, along with color contours of velocity magnitude distributed on the same surface.

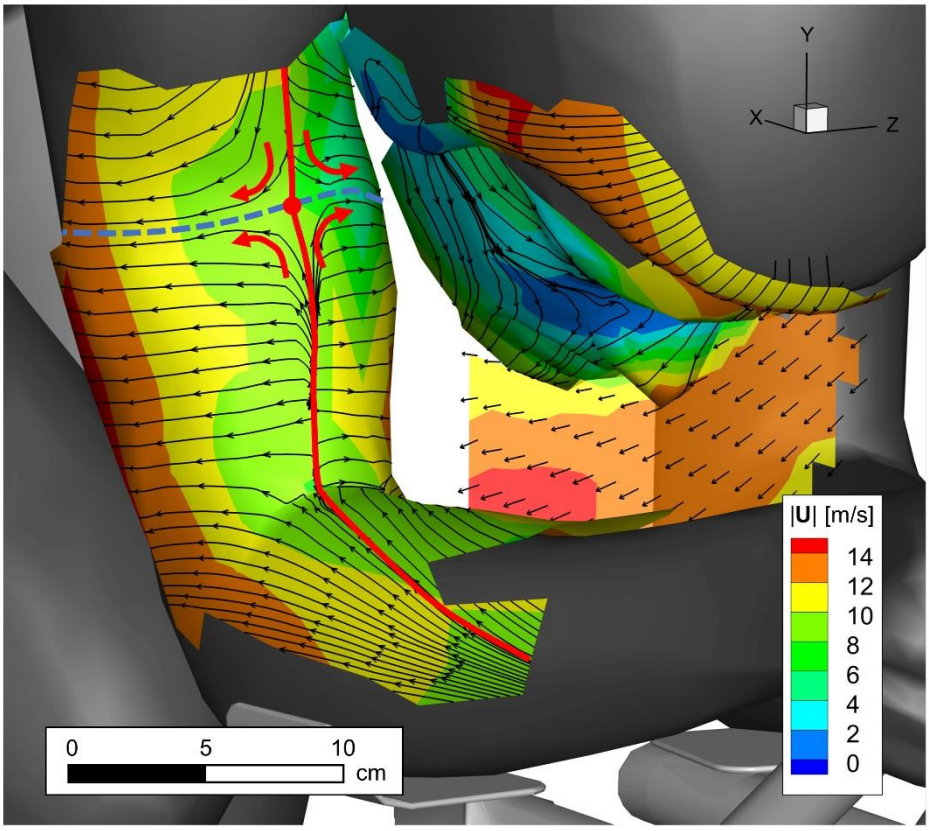

Fig. 11.8 Streamlines in the face and arm region evaluated at 5 mm from the body of the cyclist, plotted on color contours of velocity magnitude; the scale indicates the size of the measurement volume. The results come from a single CVV measurement location. Velocity vectors are sub-sampled by a factor 3.

The near surface streamlines on the forearm slightly diverge approaching the elbow, where a dividing stagnation line (red line) can be identified that starts on the side of the arm and curls up on top of the arm to continue over the top of the biceps. There is no indication of flow separation at the elbow as the direction of the velocity along the streamlines does not reverse. The separating streamline ends in a saddle point, where a secondary dividing stagnation line can be identified (dashed blue line) that goes through the saddle point.

The measurement domain also includes parts of the flow over the face of the cyclist. Here the more elaborate surface topology is accompanied by a more complex flow pattern. In general, the concave regions exhibit a lower velocity and the convex (protruding) regions see a local increase of the velocity. Inspection of the streamlines plotted near the face of the cyclist shows a dividing streamline on the cyclist's cheek. Above this streamline, near the eye of the cyclist, a region of reverse flow is observed. A slice of the velocity field plotted in the region between the face and the arms indicates the flow underneath the face accelerates as a result of the reduced cross section available.

Moving to the back of the cyclist (second field of view in Fig. 11.7), flow separation is expected on the relatively flat shaped lower back of the athlete. In Fig. 11.9 the near-surface streamlines confirm the above. The flow pattern is however not as intuitive, as a dividing separation line (red line) appears at an asymmetric position and runs downward along the cyclist back where it crosses at a saddle point and another separating streamline that is spiraling upward and ending up at approximately the Ilium. The spiraling pattern of this surface streamline suggests that the shear layer separating around this region is wrapped up into a tornado like vortex, rapidly tilting and developing along the stream-wise direction. This observation confirms the three-dimensional flow topology hypothesized in the study of Crouch et al. (2014).

The color contoured velocity magnitude indicates that the separated flow region is fairly limited to a fraction of the low-back region, with the caveat, however, that the velocity is sampled here at approximately 5 mm distance from the solid surface. A slice of the

velocity field downstream of the right upper leg indicates that the flow rapidly recovers the free-stream conditions after only a fraction of the leg cross-section diameter.

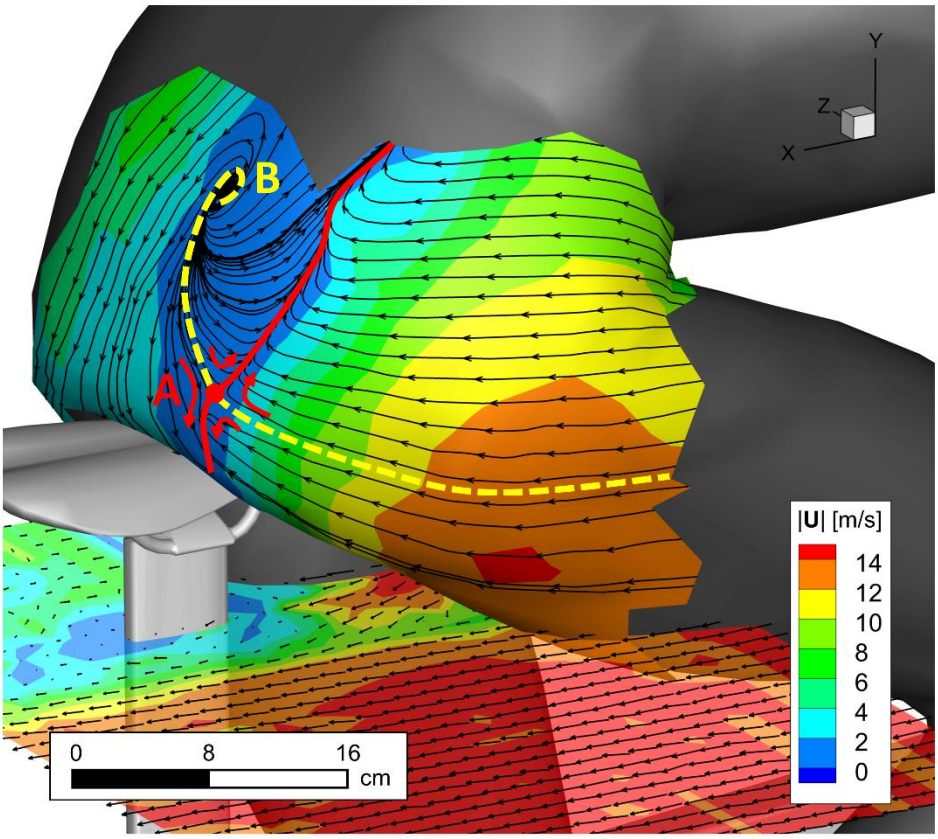

Fig. 11.9 Streamlines in the back region evaluated at 5 mm from the body of the cyclist, plotted on color contours of velocity magnitude; the scale indicates the size of the measurement volume. The results come from a single CVV measurement location. Velocity vectors sub-sampled by a factor 3.

11.3.3 Ankle-foot vortices

The field of view containing the right shoe of the cyclist (Fig. 11.7-bottom) is considered to visualize the vortical structures developing around in the shoe and ankle region. The green and red isosurfaces in Fig. 11.10 represent negative and positive streamwise vorticity, respectively. Elongated vortices (A, B and C) emanate from the sides of the shoe.

Vortices from each side have the same direction of rotation and merge into a single structure. A counter-rotating vortex (red) originates from the ankle and heel regions. The distance between the vortices B and C is approximately 30 mm, which is close to the spatial resolution limit of the current measurements, based on a bin size of 20 mm. Evaluating a-posteriori the $\overline{DSR}$ based on this length scale and the measurement volume width of 230 mm yields approximately $\overline{DSR}$ = 8.

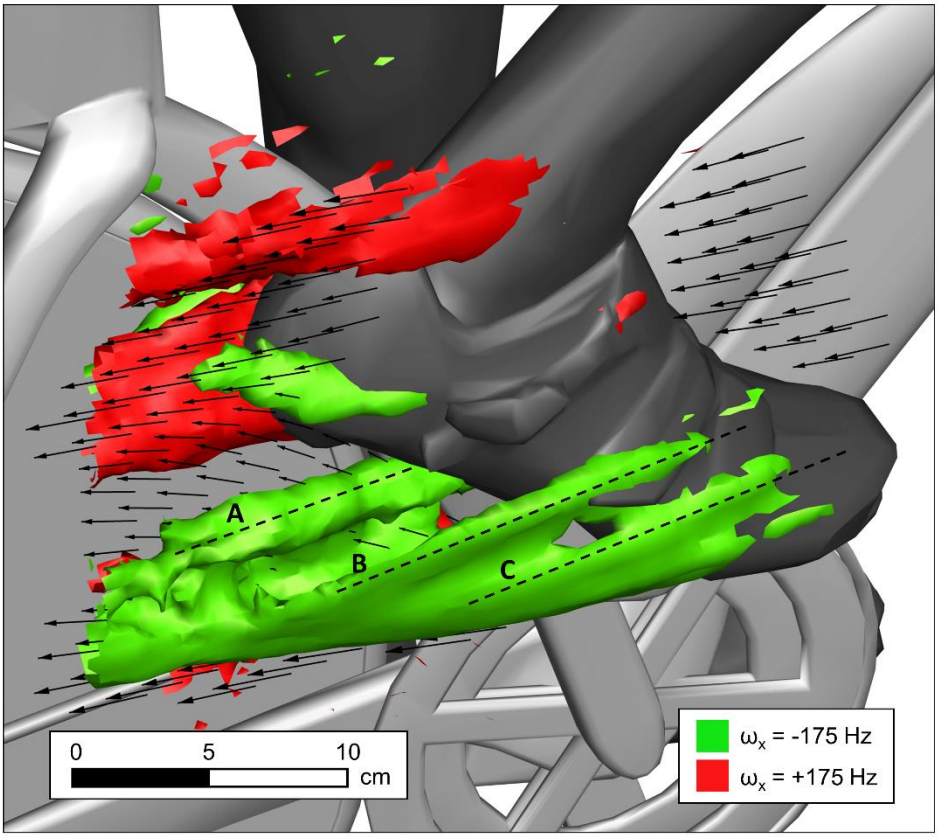

Fig. 11.10 Isosurface visualization of streamwise vorticity. An approximate scaling is included to indicate the size of the measurement volume. The results come from a single CVV measurement location. Velocity vectors sub-sampled by a factor 3.

11.3.4 Robotic manipulation

The robotic arm on which the CVV is mounted for the experiments (Fig. 11.6) allows for rapid change of field of view. For illustration: Jux et al. (2017) acquired more than 200 CVV measurements from both sides of the cyclist in a time-span of two days. The robot provides the user with information of the orientation of the CVV. Therefore, the measurement volumes can be rotated and translated into one common 'world' frame of reference around the cyclist. Subsequent bin-averaging is done on the full dataset to obtain the time-averaged flow field over the full cyclist. The scanning procedure is schematically illustrated in Fig. 11.11, which shows overlap is required between the conical measurement volumes to ensure full domain coverage.

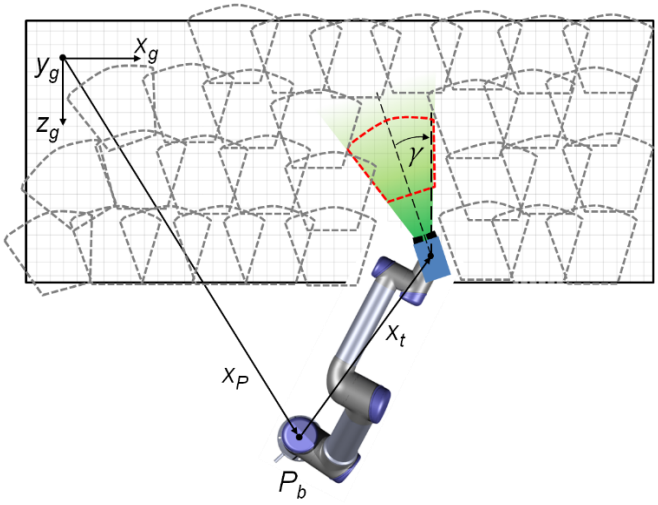

Fig. 11.11 Schematic of measurement volume scanning by robotic CVV. Figure reproduced from Jux et al. (2017).

A visualization of the resulting time-averaged flow field is given in Fig. 11.12. The figure shows a contour plot of streamwise velocity in the plane $z = 0$. The contours show the expected flow stagnation near the cyclist's head and flow acceleration over his back. An indication of the wake regions is given by the green isosurfaces of $u = 0.5u_\infty$. These show a large wake region emanating from the back of the cyclist, as expected from streamline analysis earlier in this chapter.

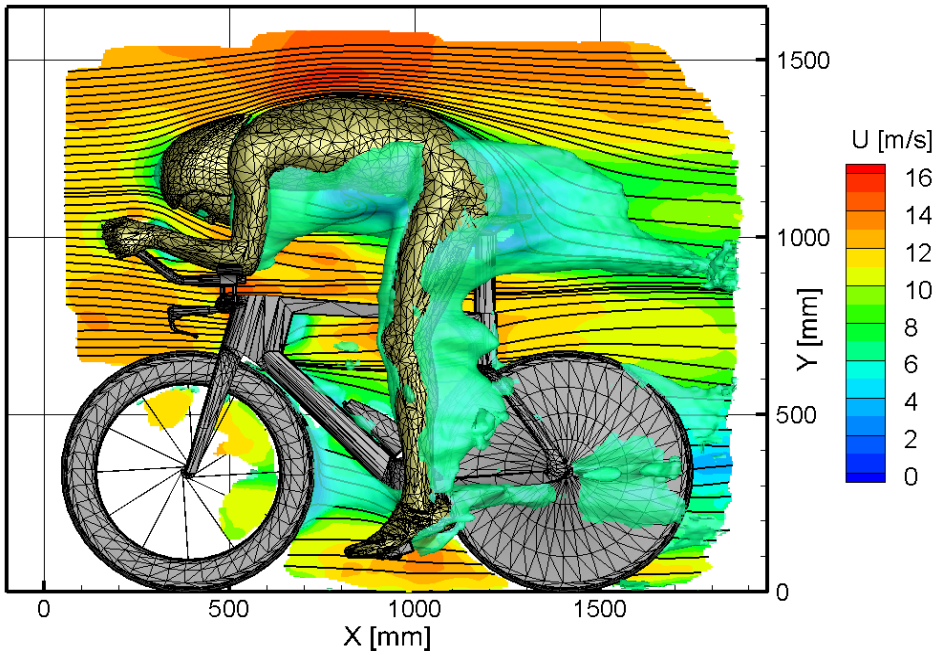

Fig. 11.12 Time-averaged flow field around the cyclist visualized by a contour of streamwise velocity in the center plane (green isosurface at $u = 7$ m/s). Figure reproduced from Jux et al. (2017).

The dynamic spatial range of the full measurement volume achieved after stitching of the 450 measurement volumes is 100, based on a volume width of 2000 mm and an ensemble averaging bin size of 20 mm.

11.4 Conclusions

A prototype CVV system has been employed for two wind tunnel experiments. The measured flow ahead of a sphere returns very good agreement with the potential flow theory. Measurements in three regions around a full-scale cyclist model show the capability of the CVV to access the near-wall velocity over a complex three-dimensional topology. Skin-friction lines can be inferred yielding the details of near-wall flow topology. The time-average vorticity field also illustrates the potential to represent the vortex skeleton developing around a complex three-dimensional body. The current levels of dynamic spatial and velocity range ($\overline{DSR}$ ~ 10, $\overline{DVR}$ ~ 30) lie below those typically achieved with planar

PIV measurements or with a conventional tomographic PIV system. Both $\overline{DSR}$ and $\overline{DVR}$ depend upon the number of tracers collected in the measurement bin. Therefore, experiments at higher resolution and accuracy require collecting larger data sets.

Epilogue

"Comunque vada sarà… successo"

—a good friend

Chapter 12
Conclusions and Recommendations

The primary conclusions and recommendations of both parts of this thesis are summarized in the following two sections.

12.1 Data augmentation using governing equations

The first part of this dissertation focused on the use of flow governing equations to leverage spatial resolution from PIV measurement to obtain information in the temporal domain. The reverse was also attempted, and high temporal resolution of particle tracking measurements was leveraged using the vorticity transport equation to increase spatial resolution. The first part was concluded with the proposal of an uncertainty quantification technique to aid future developments of such data assimilation techniques, but also as general uncertainty quantification technique for practical use.

12.1.1 Single-snapshot pressure

In an effort to allow volumetric pressure measurements in wind tunnels at flow speeds relevant for aircraft aerodynamics, a method is proposed that allows for approximation of the instantaneous volumetric flow pressure field from a single instantaneous tomographic PIV velocity snapshot. The work shows that it is possible to approximate the temporal velocity derivative and pressure by solution of the incompressible vorticity transport equation on a single velocity snapshot only. These quantities could otherwise only be measured by time-resolved measurements, which are unrealistic for high-speed air flows.

An extension of the work is envisaged for the future, where instead of only instantaneous pressure fields also pressure spectra are obtained. This could be possible by solving the governing equations not on a single-snapshot only, but by performing a short time-marching simulation. The

pressure spectral information that could be obtained is of relevance in the fields of aero-elasticity and aero-acoustics, since it provides information for estimation of unsteady loads and noise sources.

The present work has also touched upon limitations of the proposed technique. Use of the method should be cautioned when the contributions to fluctuating pressure from outside the measurement volume are significant. Indeed, the method leverages only data available from the measurements themselves. A more complete approach would consider a larger simulation domain in the numerical framework, which could, if one manages a cost-effective implementation, potentially also account for exterior effects. This was already successfully touched upon by padding of the measurement data with an empty buffer region, which could be improved by more accurate modelling of this region. Moreover, such an approach could potentially allow for extension of the pressure-from-PIV procedure to planar PIV measurements. The technique proposed in this dissertation is valid for volumetric measurements only, but if it would be made applicable to planar PIV measurements it would allow a significant increase in laboratories to perform pressure-from-PIV measurements using their existing planar PIV systems.

12.1.2 Particle trajectory data assimilation

In Chapter 5, the VIC+ technique for dense velocity interpolation of Lagrangian particle tracking measurements is proposed. The work shows that the measurement data ensemble that is used for an interpolation can be increased beyond just instantaneous velocity measurements. In addition to instantaneous velocity, also the temporal information available from the measurements in form of the velocity material derivative is used.

The validation of the method shows that this increased data ensemble allows for an increase in measurement fidelity: the VIC+ method is demonstrated to allow for measurement of vorticity and dissipation in a real-world experiment, where these quantities where previously damped by more than 40% with respect to reference values. The study is supported by quantification of the spatial response of VIC+

with a sine-wave lattice analysis. The results indicate a twofold increase of spatial resolution with respect to cross-correlation interrogation. The benefit of the increased measurement fidelity achieved by the VIC+ technique is twofold. Previously severely underestimated quantities can now be measured and seeding density requirements are lowered allowing for larger measurement volumes.

In a two-dimensional simulated assessment, it is shown that the VIC+ technique can be extended to leverage not only instantaneous information but measurements over an extended time-segment. Future work is envisaged to perform this assessment in three-dimensions. Here, it will be important to establish a cost-effective approach to this procedure, as the iterative procedure becomes significantly more expensive when a time-segment is considered.

In addition, despite the current work demonstrating significant measurement fidelity improvements, it has not been proven that the best possible solution is achieved. Closure parameters were proposed for the VIC+ technique, but future work is envisaged to establish whether these are the most optimal, or, most robust. Also, considering recent achievements in the field of compressed sensing, an alternative optimization based upon L1 minimization can potentially yield improved solutions when a sparse basis for the underlying flow field can be established.

Part 1 of this dissertation concludes with an uncertainty quantification approach for dense velocity interpolations. The work shows that Lagrangian particle tracking measurements themselves can be effectively used to quantify bias and random uncertainty in the interpolations, without requiring an independent reference measurement or simulation.

12.2 Large-scale volumetric flow measurements

The second part of this dissertation focused on development of a large-scale volumetric flow measurement technique, based upon the principles of tomographic PIV and Lagrangian particle tracking. The use of large HFSB tracer particles for large-scale volumetric pressure measurement is

first established. Subsequently, leveraging the good light scattering properties of the HFSB, the coaxial volumetric velocimeter was proposed to allow for volumetric measurements using a simplified measurement setup.

12.2.1 Large-volume pressure measurement

A technique is proposed for large-volume pressure measurement using HFSB tracer particles, Lagrangian particle tracking and ensemble bin-averaging. It is shown to allow for accurate time-averaged pressure measurements, simplifying wind tunnel models that otherwise needed to be instrumented with pressure transducers. Instantaneous pressure, however, is found to be affected by limited spatial resolution offered by the large-volume HFSB measurements. Future work is envisaged to couple this technique with the data assimilation techniques proposed in part 1 of this dissertation to achieve more accurate instantaneous pressure fields. The latter are of relevance to obtain pressure spectra and root mean squared pressure fluctuation levels, which can only be obtained through calculation of the instantaneous pressure fields.

12.2.2 Coaxial volumetric velocimeter

The coaxial volumetric velocimeter (CVV) is proposed. The CVV performs a volumetric measurement along one viewing direction and with a fixed camera and illuminations setting. Avoiding the need for mounting, calibration, focus, alignment and Scheimpflug settings, this significantly simplifies the established tomographic PIV measurement setup. The basic rules for imaging and expected measurement accuracy are derived in the work. These show that currently the CVV is possible only using the recent developments of large-scale PIV using HFSB tracer particles and Lagrangian particle tracking together with ensemble bin-averaging. Trajectory regularization is required to reduce measurement errors in the axial velocity component, which are on the order of 10 times higher than the errors in the other two components.

The CVV is demonstrated in the case of a real-world wind tunnel experiment considering the flow around a sphere where good

correspondence is found with the expected potential flow result upstream of the sphere. The analysis of three field of views in the more complex case of the flow around a cyclist at full scale shows the capability of the CVV to measure near-wall velocity. This allows the approximation of skin friction lines from the CVV measurements, also along concave and convex surfaces. A DSR on the order of 10 is achieved when considering a single CVV measurement volume. The use of robotic manipulation of the CVV is introduced and shown to allow for an increase in DSR to 100. The DVR in both cases is estimated on the order of 30.

However, even though the CVV has already been deployed in wind tunnel laboratories, the author recommends strongly future research to continue in its direction, as the full potential of the CVV has not yet been explored. The CVV currently only allows for time-averaged velocity measurements through ensemble bin-averaging. It has already been shown that this allows for extraction of vortical structures and skin-friction lines. Time-averaged pressure can also be calculated using the procedure for large-scale pressure from PIV discussed earlier in this dissertation. However, it could prove beneficial to include knowledge of the increased uncertainty in the depth component in the pressure solver. Similarly, this knowledge could be used to devise a smarter bin averaging procedure when a volume is viewed from multiple directions. Moreover, part 1 of this dissertation has shown the benefit of including governing equations in data analysis. This has not yet been leveraged to the fullest for the CVV. In particular, the author expects data assimilation procedures for time-averaged flow fields to be a particularly relevant research direction in this respect. This includes for example Reynolds averaged Navier-Stokes simulation of a full flow field, aided by CVV measurements.

A second recommendation relates to the maximum velocity at which the CVV can be used. Limited acquisition rates limit the maximum wind tunnel speed currently to approximately 15 m/s. A multi-pulse and multi-exposure strategy may provide a solution to this limitation, alternative to waiting for availability of faster compact and cost-effective high-speed cameras.

Finally, robotic manipulation of the CVV has already been demonstrated to allow for mapping of a large measurement volume. Efforts are still required to determine a strategy for aerodynamically transparent mapping of the flow, considering possible intrusiveness of the robotic arm and CVV system. This could problem be approached by development of a motion planning algorithm that is coupled with an aerodynamic model of the CVV.

References

Adrian RJ (1991) Particle-imaging techniques for experimental fluid mechanics. Annu. Rev. Fluid Mech., 23(1):261-304.

Adrian RJ (1997) Dynamic ranges of velocity and spatial resolution of particle image velocimetry. Measurement Science and Technology, 8(12):1393.

Adrian RJ, Meinhart CD, Tomkins CD (2000) Vortex organization in the outer region of the turbulent boundary layer. J Fluid Mech 422:1–54

Adrian RJ, Westerweel J (2011) Particle image velocimetry. Cambridge University Press. ISBN: 9780521440080

Agüera N, Cafiero G, Astarita T, Discetti S (2016) Ensemgle 3D PTV for high resolution turbulent statistics. Meas Sci Technol 27:124011

Agüí JC, Jiménez J (1987) On the performance of particle tracking. J Fluid Mech 185:447–468. doi:10.1017/S0022112087003252

Anderson C, Greengard C (1985) On vortex methods. SIAM journal on numerical analysis 22:413-440.

Anderson JD (2010) Fundamentals of Aerodynamics. McGraw-Hill Education. ISBN 0073398101.

Atkinson C, Coudert S, Foucaut JM, Stanislas M, Soria J (2011) The accuracy of tomographic particle image velocimetry for measurements of a turbulent boundary layer. Exp Fluids 50:1031–1056

Atkinson C, Coudert S, Foucaut JM, Stanislas M, Soria J (2011) The accuracy of tomographic particle image velocimetry for measurements of a turbulent boundary layer. Exp. Fluids. 50:1031–56

Azijli I (2016) Physics-Based Enrichment of Volumetric Velocity Measurements for Incompressible Flows. PhD Thesis. TU Delft

Bai Z, Wimalajeewa T, Berger Z, Wang G, Glauser M, Varshney PK (2015) Low-Dimensional Approach for Reconstruction of Airfoil Data via Compressive Sensing. AIAA Journal. 53(4):920-933.

Benedict LH, Gould RD (1996) Towards better uncertainty estimates for turbulence statistics. Exp. Fluids. 22:129–36.

Beresh SJ, Wagner JL, DeMauro EP, Henfling JF, Spillers RW, Farias PA (2016) Applications of Temporal Supersampling in Pulse-Burst PIV. In: 18th International Symposium on Applications of Laser and Imaging Techniques to Fluid Mechanics. Lisbon, Portugal. 4–7 July

Bernardini M, Pirozzoli S (2011) Wall pressure fluctuations beneath supersonic turbulent boundary layers. Phys Fluids 23:085102

Bertents G, van der Voort D, Bocenagra-Evans H, van de Water W (2015) Large-eddy estimate of the turbulent dissipation rate using PIV. Exp Fluids 56:89

Bitter M, Hara T, Hain R, Yorita D, Asai K, Kähler CJ (2012) Characterization of pressure dynamics in an axisymmetric separating/reattaching flow using fast-responding pressure-sensitive paint. Exp Fluids 53:1737–1749. doi:10.1007/s00348-012-1380-7

Blinde P, Michaelis D, van Oudheusden BW, Weiss P-E, de Kat R, Laskari A, Jeon YJ, David L, Schanz D, Huhn F, Gesemann S, Novara M, McPhaden C, Neeteson N, Rival D, Schneiders JFG, Schrijer F (2016) Comparative assessment of PIV-based pressure evaluation techniques applied to a transonic base flow. In: 18th international symposium on the application of laser techniques to fluid mechanics. Lisbon, Portugal, 4–7 July

Boillot A, Prasad AK (1996) Optimization procedure for pulse separation in cross-correlation PIV. Exp. Fluids 21:87-93

Bosbach J, Kühn M, Wagner C (2009) Large scale particle image velocimetry with helium filled soap bubbles. Exp Fluids 46:539–547

Bourgeois JA, Sattari P, Martinuzzi RJ (2011) Alternating half-loop shedding in the turbulent wake of a finite surface-mounted square cylinder with a thin boundary layer. Phys Fluids 23:095101. doi:10.1063/1.3623463

Candes E, Romberg J, Tao T (2006) Robust uncertainty principles: exact signal reconstruction from highly incomplete frequency information. IEEE Trans. Information Theory. 52(2):489-509. doi:10.1109/TIT.2005.862083

Caridi GCA, Ragni D, Sciacchitano A, Scarano F (2016) HFSB-seeding for large-scale tomographic PIV in wind tunnels. Exp Fluids 57:190. https://doi.org/10.1007/s00348-016-2277-7

Caridi GCA, Sciacchitano A (2017) Light scattering behaviour of Helium filled soap bubbles. In: Proceedings of the 12th Int. Symp. Particle Image Velocimetry. Busan. Republic of Korea

Casa LDC, Krueger PS (2013) Radial basis function interpolation of unstructured, three-dimensional, volumetric particle tracking velocimetry data. Meas Sci Technol 24:065304

Casey TA, Sakakibara J, Thoroddsen ST (2013) Scanning tomographic particle image velocimetry applied to a turbulent jet. Phys Fluids 25:025102

Charonko JJ, King CV, Smith BL, Vlachos PP (2010) Assessment of pressure field calculations from particle image velocimetry measurements. Meas Sci Technol 2010:105401

Charonko JJ, Vlachos PP (2013) Estimation of uncertainty bounds for individual particle image velocimetry measurements from cross-correlation peak ratio. Meas. Sci. Technol. 24:065301

Christiansen JP (1973) Numerical simulation of hydrodynamics by the method of point vortices. J Comput Phys 13:363–379

Cierpa C, Lütke B, Kähler CJ (2013) Higher order multi-frame particle tracking velocimetry. Exp. Fluids 54:1533

Claerbout J (2014) Geophysical image estimation by example. http://sepwww.stanford.edu/sep/prof/

Cottet G-H, Poncet P (2003) Advances in direct numerical simulations of 3D wall-bounded flows by Vortex-in-Cell methods. J Comput Phys 193:136–158

Crouch TN, Burton D, Brown NAT, Thompson MC, Sheridan J (2014) Flow topology in the wake of a cyclist and its effect on aerodynamic drag. Journal of Fluid Mechanics, 748:5-35.

Cuzol A, Memin E (2005) A stochastic filter for fluid motion tracking. In: 10th IEEE International Conference on Computer Vision, Beijing

Dalitz R, Petra S, Schnörr C (2017) Compressed Motion Sensing. In: Lauze F, Dong Y, Dahl A (eds) Scale Space and Variational Methods in Computer Vision. SSVM 2017. Lecture Notes in Computer Science, vol 10302. Springer, Cham

de Kat R, Ganapathisubramani B (2013) Pressure from particle image velocimetry for convective flows: a Taylor's hypothesis approach. Meas Sci Technol 24:024002

de Kat R, van Oudheusden BW (2012) Instantaneous planar pressure determination from PIV in turbulent flow. Exp Fluids 52:1089–1106. doi:10.1007/s00348-011-1237-5

de Silva CM, Philip J, Marusic I (2013) Minimization of divergence error in volumetric velocity measurements and implications for turbulence statistics. Exp Fluids 54:1557

Depardon S, Lasserre JJ, Boueilh JC, Brizzi LE, Borée . (2005) Skin friction pattern analysis using near-wall PIV. Experiments in Fluids, 39(5):805-818.

Dobriloff C, Nitsche W (2009) Surface pressure and wall shear stress measurements on a wall mounted cylinder. In: Nitsche W, Dobriloff C (eds) Imaging measurement methods, NNFM 106. Springer, Berlin, pp 197–206

Durst F, Melling A, Whitelaw JH (1976) Principles and practice of laser-Doppler anemometry. NASA STI/Recon Technical Report A, 76.

Ebbers T, Farnebäck G (2009) Improving computation of cardiovascular relative pressure fields from velocity MRI. J Magn Reson Imaging 30:54–61

Efron B (1979) Computers and the theory of statistics: thinking the unthinkable SIAM Rev. 21 460–80

Elsinga GE, Marusic I (2010) Evolution and lifetimes of flow topology in a turbulent boundary layer. Phys Fluids 22:015102

Elsinga GE, Poelma C, Schröder A, Geisler R, Scarano F, Westerweel J (2012) Tracking of vortices in a turbulent boundary layer. J Fluid Mech 697:273–295

Elsinga GE, Scarano F, Wieneke B, van Oudheusden BW (2006) Tomographic particle image velocimetry. Exp Fluids 41:933–947. doi:10.1007/s00348-006-0212-z

Elsinga GE, Westerweel J, Scarano F, Novara M (2011) On the velocity of ghost particles and the bias errors in Tomographic-PIV. Exp Fluids 50:825–838

Fahringer TW, Lynch KP, Thurow BS (2015) Volumetric particle image velocimetry with a single plenoptic camera. Meas. Sci. Technol. 26(11):115201.

Ganapathisubramani B, Lakshminarasimhan K, Clemens NT (2007) Determination of complete velocity gradient tensor by using cinematographic stereoscopic PIV in a turbulent jet. Exp Fluids 42:923–939

Gesemann S, Huhn F, Schanz D, Schröder A (2016) From noisy particle tracks to velocity, acceleration and pressure fields using B-splines and penalties. In: 18th Int. Symp. on Applications of Laser and Imaging Techniques to Fluid Mechanics. Lisbon, Portugal. 4–7 July

Ghaemi and Scarano (2013) Turbulent structure of high-amplitude pressure peaks within the turbulent boundary layer. J Fluid Mech 735:381–426

Ghaemi S, Ragni D, Scarano F (2012) PIV-based pressure fluctuations in the turbulent boundary layer. Exp Fluids 53:1823–1840

Ghaemi S, Scarano F (2010) Multi-pass light amplification for tomographic particle image velocimetry applications. Meas Sci Technol 21:127002. doi:10.1088/0957-0233/21/12/127002

Ghaemi S, Scarano F (2011) Counter-hairpin vortices in the turbulent wake of a sharp trailing edge. J Fluid Mech 689:317–356

Ghaemi S, Scarano F (2013) Turbulent structure of high-amplitude pressure peaks within the turbulent boundary layer. J Fluid Mech 735:381–426. doi:10.1017/jfm.2013.501

Giering R, Kaminski T (1998) Recipes for adjoint code construction. ACM Trans Math Softw 24(4):437–473

Gorry A (1990) General least-squares smoothing and differentiation by the convolution (Savitzky–Golay) method Anal. Chem. 62 570–3

Gregson J, Ihrke I, Thuerey N, Heidrich W (2014) From capture to simulation–connecting forward and inverse problems in fluids. In: Proceedings of ACM SIGGRAPH 2012

Gronskis A, Heitz D, Mémin E (2013) Inflow and initial conditions for direct numerical simulation based on adjoint data assimilation. J Comput Phys 242:480–497

Gurka R, Liberzon A, Hetsroni G (2006) POD of vorticity fields: A method for spatial characterization of coherent structures. Int. J. Heat Fluid Flow 27(3):416-423. doi:10.1016/j.ijheatfluidflow.2006.01.001

Hain R, Kähler CJ (2006) Single camera volumetric velocity measurements using optical aberrations. In: 12th International Symposium on Flow Visualization, Göttingen, Germany, Septermber 10-14

Hain R, Kähler CJ, Michaelis D (2008) Tomographic and time resolved PIV measurements on a finite cylinder on a flat plate. Exp Fluids 45:715–724. doi:10.1007/s00348-008-0553-x

Hayase T, Hayashi S (1997) State estimator of flow as an integrated computational method with the feedback of online experimental measurement. Journal of Fluids engineering 119:814-822

Heitz D, Mémin E, Schnörr C (2010) Variational fluid flow measurements from image sequences: synopsis and perspectives. Exp Fluids 48:369–393

Herman GT, Lent A (1976) Iterative reconstruction algorithms. Comput Biol Med 6:273–294

Herpin S, Stanislas M, Foucaut JM, Coudert S (2013) Influence of the Reynolds number on the vortical structures in the logarithmic region of turbulent boundary layers. J Fluid Mech 716:5–50

Hunt J, Wray A, Moin P (1988) Eddies, stream, and convergence zones in turbulent flows. Center for Turbulence Research Report CTR-S88 pp 193–208

Imaichi K, Ohmi K (1983) Numerical processing of flow-visualization pictures–measurement of two-dimensional vortex flow. J Fluid Mech 129:283–311

Jensen A, Pedersen GK (2004) Optimization of acceleration measurements using PIV. Meas Sci Technol 15:2275–2283

Jeon YJ, Chatellier L, David L (2014) Fluid trajectory evaluation based on an ensemble-averaged cross-correlation in time-resolved PIV. Exp Fluids 55:1766

Jeon YJ, Earl T, Braud P, Chatellier L, David L (2016) 3D pressure field around an inclined airfoil by tomographic TR-PIV and its comparison with direct pressure measurements. In: 18th international symposium on the application of laser techniques to fluid mechanics. Lisbon, Portugal, 4–7 July

Jodai Y, Elsinga GE (2016) Experimental observation of hairpin auto-generation events in a turbulent boundary layer. J Fluid Mech 795:611–633

Johnson KC, Thurow BS, Blois G, Christensen KT (2017) Volumetric Velocity Measurements in the Wake of a Hemispherical Roughness Element. AIAA Journal. 55:2158-2173.

Jux C, Sciacchitano A, Schneiders JFG, Scarano F (2017) Full-scale cyclist aerodynamics by co-axial volumetric velocimetry. 12th Int. Symp. Particle Image Velocimetry, Busan, Republic of Korea

Kähler CJ, Kompenhans J (2000) Fundamentals of multiple plane stereo particle image velocimetry. Exp Fluids 29:S70–S77

Kähler CJ, Scharnowski S, Cierpka C (2012a) On the resolution limit of digital particle image velocimetry. Exp Fluids 52:1629–1639. doi:10.1007/s00348-012-1280-x

Kähler CJ, Scharnowski S, Cierpka C (2012b) On the uncertainty of digital PIV and PTV near walls. Exp. Fluids 52:1641–56

Keane RD, Adrian RJ, Zhang Y (1995) Super-resolution particle image velocimetry. Meas Sci Technol 6:754

Kostas J, Soria J, Chong MS (2005) A comparison between snapshot POD analysis of PIV velocity and vorticity data. Exp. Fluids. 38(2):146-160. doi:10.1007/s00348-004-0873-4

Krogstad P-A, Kaspersen JH, Rimestad S (1998) Convection velocities in a turbulent boundary layer. Phys Fluids 10:949–957

Kühn M, Ehrenfried K, Bosbach J, Wagner C (2011) Large-scale tomographic particle image velocimetry using helium-filled soap bubbles. Exp Fluids 50:929–948. doi:10.1007/s00348-010-0947-4

Kurtulus DF, Scarano F, David L (2007) Unsteady aerodynamic forces estimation on a square cylinder by TR-PIV. Exp Fluids 42:185–196

Larmore L (1965) Introduction to Photographic Principles. 2nd ed. New York: Dover Publications, Inc.

Laskari A, de Kat R, Ganapathisubramani B (2016) Full-field pressure from snapshot and time-resolved volumetric PIV. Exp. Fluids 57(3): 44.

Lemke M, Sesterhenn J (2016) Adjoint-based pressure determination from PIV data in compressible flows—validation and assessment based on synthetic data. Eur J Mech-B/Fluids 58:29–38

Leonard A (1980) Vortex methods for flow simulation. Journal of Computational Physics 37:289-335

Leonard A (1985) Computing three-dimensional incompressible flows with vortex elements. Annual Review of Fluid Mechanics 17:523-559

Liu DC, Nocedal J (1989) On the limited memory method for large scale optimization. Math Program B 45:503–528

Liu X, Katz J (2006) Instantaneous pressure and material acceleration measurements using a four-exposure PIV system. Exp Fluids 41:227–240

Liu X, Katz J (2013) Vortex-corner interactions in a cavity shear layer elucidated by time-resolved measurements of the pressure field. J Fluid Mech 728:417–457

Lukes RA, Chin SB, Haake SJ (2005) The understanding and development of cycling aerodynamics. Sports engineering 8.2:59-74.

Lynch KP, Pröbsting S, Scarano F (2014). Temporal resolution of time-resolved tomographic PIV in turbulent boundary layers. In: 17th international symposium on the application of laser techniques to fluid mechanics. Lisbon, Portugal

Lynch KP, Scarano F (2013) A high-order time-accurate interrogation method for time-resolved PIV. Meas Sci Technol 24:035305

Lynch KP, Scarano F (2014) Material acceleration estimation by four-pulse tomo-PIV. Meas Sci Technol 25:084005

Lynch KP, Scarano F (2015) An efficient and accurate approach to MTE-MART for time-resolved tomographic PIV. Exp Fluids 56:66

Maas HG, Gruen A, Papantoniou D (1993) Particle tracking velocimetry in three-dimensional flows. Exp Fluids 15:133–146

Malik NA, Dracos T, Papantoniou DA (1993) Particle tracking velocimetry in three-dimensional flows. Exp Fluids 15:279–294

Marusic I, McKeon BJ, Monkewitz PA, Nagib HM, Smits AJ, Sreenivasan KR (2010) Wall-bounded turbulent flows at high Reynolds numbers: Recent advances and key issues. Phys Fluids 22(065103):1–24

Meng H, Pan G, Pu Y, Woodward SH (2004) Holographic particle image velocimetry: from film to digital recording. Meas. Sci. Technol. 15(4):673.

Michaelis D, Novara M, Scarano F and Wieneke B (2010) Comparison of volume reconstruction techniques at different particle densities. In: 15th International symposium on applications of laser techniques to fluid mechanics, Lisbon, Portugal

Neal DR, Sciacchitano A, Smith BL, Scarano F (2015) Collaborative framework for PIV uncertainty quantification: the experimental database. Meas. Sci. Technol. 26:074003

Neeteson NJ, Bhattacharya S, Rival DE, Michaelis D, Schanz D, Schröder A (2016) Pressure-field extraction from Lagrangian flow measurements: first experiences with 4D-PTV data. Exp Fluids 57: 102 doi:10.1007/s00348-016-2170-4

Neeteson NJ, Rival DE (2015) Pressure-field extraction on unstructured flow data using a Voronoi tessellation-based networking algorithm: a proof-of-principle study. Exp Fluids 56:44

Novara M, Batenburg KJ, Scarano F (2010) Motion tracking-enhanced MART for tomographic PIV. Meas Sci Technol 21:035401

Novara M, Scarano F (2013) A particle-tracking approach for accurate material derivative measurements with tomographic PIV. Exp Fluids 54:1584

Orlanski I (1976) A simple boundary condition for unbounded hyperbolic flows. J Comput Phys 21:251–269

Papadakis N, Mémin E (2008) Variational assimilation of fluid motion from image sequence. SIAM J Imaging Sci 1:343–363

Pattenden RJ, Turnock SR, Zhang X (2005) Measurements of the flow over a low-aspect-ratio cylinder mounted on a ground plane. Exp Fluids 39:10–21. doi:10.1007/s00348-005-0949-9

Patte-Rouland B, Lalizel G, Moreau J, Rouland E (2001) Flow analysis of an annular jet by particle image velocimetry and proper orthogonal decomposition. Meas. Sci. Technol. 12:1404

Pereira F, Gharib M, Dabiri D, Modarress D (2000) Defocusing digital particle image velocimetry: a 3-component 3-dimensional DPIV measurement technique. Application to bubbly flows. Exp. Fluids 29:S078-S084

Perret L, Braud P, Fourment C, David L, Delville J (2006) 3-Component acceleration field measurement by dual-time stereoscopic particle image velocimetry. Exp Fluids 40:813–824

Pothos S, Troolin D, Wing L, Ragan M (2009) V3V-Volumetric three-component velocimetry for 3D flow measurements main principle, theory and applications. Revista Termotehnica, 2, 2009.

Pröbsting S, Scarano F, Bernardini M, Pirozzoli S (2013) On the estimation of wall pressure coherence using time-resolved tomographic PIV. Exp Fluids 54:1567. doi:10.1007/s00348-013-1567-6

Raffel M, Richard H, Ehrenfried K, Van der Wall B, Burley C, Beaumier P, McAlister K, Pengel K (2004) Recording and evaluation methods of PIV investigations on a helicopter rotor model. Exp Fluids 36:146–156

Raffel M, Willert C, Wereley S, Kompenhans J (2007) Particle image velocimetry: a practical guide. Springer, New York

Ragni D, Ashok A, van Oudheusden BW, Scarano F (2009) Surface pressure and aerodynamic loads determination of a transonic airfoil based on particle image velocimetry. Meas Sci Technol 20:074005

Saikrishnan N, Marusic I, Longmire EK (2006) Assessment of dual plane PIV measurements in wall turbulence using DNS data. Exp Fluids 41:265–278

Savitzky A, Golay MJE (1964) Smoothing and differentiation of data by simplified least squares procedures. Anal. Chem. 36:1627–1639. doi:10.1021/ac60214a047

Scarano F (2013) Tomographic PIV: principles and practice. Meas Sci Technol 24:012001

Scarano F, Ghaemi S, Caridi GCA, Bosbach J, Dierksheide U, Sciacchitano A (2015) On the use of helium-filled soap bubbles for large-scale tomographic PIV in wind tunnel experiments. Exp Fluids 56:42. doi:10.1007/s00348-015-1909-7

Scarano F, Moore P (2012) An advection-based model to increase the temporal resolution of PIV time series. Exp Fluids 52:919–933

Scarano F, Poelma C (2009) Three-dimensional vorticity patterns of cylinder wakes. Exp Fluids 47:69–83

Scarano F, Poelma C (2009) Three-dimensional vorticity patterns of cylinder wakes. Exp. Fluids 47:69–83

Scarano F, Riethmuller ML (2000) Advances in iterative multigrid PIV image processing. Exp Fluids 29:S051–S060

Schanz D, Gesemann S, Schröder A (2016) Shake the box: lagrangian particle tracking at high particle image densities. Exp Fluids 57:70. doi:10.1007/s00348-016-2157-1

Schanz D, Schröder A, Gesemann S, Michaelis D, Wieneke B (2013) Shake-the-Box: a highly efficient and accurate tomographic particle tracking velocimetry (TOMO-PTV) method using prediction of particle position. In: 10th international symposium on particle image velocimetry—PIV13. Delft, The Netherlands, 1–3 July 2013.

Scharnowski S, Kähler CJ (2016) Estimation and optimization of loss-of-pair uncertainties based on PIV correlation functions. Exp. Fluids 57:23

Schiavazzi D, Coletti F, Iaccarino G, Eaton JK (2014) A matching pursuit approach to solenoidal filtering of three-dimensional velocity measurements. J Comput Phys 263:206–221

Schlatter P, Örlü R (2010) Assessment of direct numerical simulation data of turbulent boundary layers. J Fluid Mech 659:116–126

Schneiders JFG (2014) Time-Supersampling 3D-PIV Measurements by Vortex-in-Cell Simulation. MSc Thesis. TU Delft.

Schneiders JFG, Dwight RP, Scarano F (2014) Time-supersampling of 3D-PIV measurements with vortex-in-cell simulation. Exp Fluids 55:1692

Schneiders JFG, Dwight RP, Scarano F, (2015) Tomographic PIV noise reduction by simulating repeated measurements. In: 11th International Symposium on Particle Image Velocimetry, PIV15, Santa Barbara, CA, USA, September 14–16

Schneiders JFG, Pröbsting S, Dwight RP, van Oudheusden BW, Scarano F (2016a) Pressure estimation from single-snapshot tomographic PIV in a turbulent boundary layer. Exp Fluids 57:53

Schneiders JFG, Scarano F (2016) Dense velocity reconstruction from tomographic PTV with material derivatives. Exp Fluids 57:139. doi:10.1007/s00348-016-2225-6

Schneiders JFG, Scarano F, Elsinga GE (2017) Resolving vorticity and dissipation in a turbulent boundary layer by tomographic PTV and VIC+. Exp. Fluids. 58:27. doi:10.1007/s00348-017-2318-x

Schneiders JFG, Sciacchitano A (2017) Track benchmarking method for uncertainty quantification of particle tracking velocimetry interpolations. Meas. Sci. Technol. 28:065302.

Schrijer FFJ, Scarano F (2008) Effect of predictor–corrector filtering on the stability and spatial resolution of iterative PIV interrogation. Exp Fluids 45:927–941

Schröder A, Geisler R, Elsinga GE, Scarano F, Dierksheide U (2008) Investigation of a turbulent spot and a tripped turbulent boundary layer flow using time-resolved tomographic PIV. Exp Fluids 44:305–316

Schröder A, Geisler R, Staack K, Elsinga GE, Scarano F, Wieneke B, Henning A, Poelma C, Westerweel J (2011) Eulerian and Lagrangian views of a turbulent boundary layer flow using time-resolved tomographic PIV. Exp Fluids 44:305–316

Sciacchitano A, Dwight RP, Scarano F (2012) Navier–Stokes simulations in gappy PIV data. Exp. Fluids. 53(5):1421-1435.

Sciacchitano A, Lynch KP (2015) A posteriori uncertainty quantification for tomographic-PIV data. In: 11th international symposium particle image velocimetry, Santa Barbara, California, Sept 14–16

Sciacchitano A, Neal DR, Smith BL, Warner SO, Vlachos PP, Wieneke B, Scarano F (2015) Collaborative framework for PIV uncertainty quantification: comparative assessment of methods. Meas. Sci. Technol. 26(7):074004.

Sciacchitano A, Scarano F (2014) Elimination of PIV light reflections via a temporal high pass filter. Meas. Sci. Technol. 25:084009. doi:10.1088/0957-0233/25/8/084009

Sciacchitano A, Scarano F, Wieneke B (2012) Multi-frame pyramid correlation for time-resolved PIV. Exp Fluids 53:1087–1105

Sciacchitano A, Wieneke B (2016) PIV uncertainty propagation. Meas. Sci. Technol. 084006:27

Sciacchitano A, Wieneke B, Scarano F (2013) PIV uncertainty quantification by image matching. Meas. Sci. Technol. 24:045302

Sheng J, Meng H, Fox R (2000) A large eddy PIV method for turbulence dissipation rate estimation. Chem Eng Sci 55:4423–4434

Sitou A, Riethmuller ML (2001) Extension of PIV to super resolution using PTV. Meas Sci Technol 12:1398

Stanislas M, Perret L, Foucaut J-M (2008) Vortical structures in the turbulent boundary layer: a possible route to a universal representation. J Fluid Mech 602:327–382

Stuer H, Blaser S (2000) Interpolation of scattered 3D PTV data to a regular grid. Flow Turbul. Combust. 64:215–32

Sumner D (2013) Flow above the free end of a surface-mounted finite-height circular cylinder: a review. J Fluids Struct 43:41–63. doi:10.1016/j.jfluidstructs.2013.08.007

Suzuki T (2012) Reduced-order Kalman-filtered hybrid simulation combining particle tracking velocimetry and direct numerical simulation. J Fluid Mech 709:249–288

Suzuki T (2014) POD-based reduced-order hybrid simulation using the data- driven transfer function with time-resolved PTV feedback. Exp Fluids 55:1798

Talapatra S, Katz J (2012) Three-dimensional velocity measurements in a roughness sublayer using microscopic digital in-line holography and optical index matching. Meas. Sci. Technol. 24:024004. doi:10.1088/0957-0233/24/2/024004

Tanahashi M, Kang S-J, Miyamoto T, Shiokawa S, Miyauchi T (2004) Scaling law of fine scale eddies in turbulent channel flows up to Re τ = 800. Int J Heat Fluid Flow 25:331–340

Theunissen R, Scarano F, Riethmuller ML (2008) On improvement of PIV image interrogation near stationary interfaces. Exp Fluids 45:557–572

Timmins BH, Wilson BW, Smith BL, Vlachos PP (2012) A method for automatic estimation of instantaneous local uncertainty in particle image velocimetry measurements. Exp. Fluids. 53:1133–47

Tokgoz S, Elsinga GE, Delfos R, Westerweel J (2012) Spatial resolution and dissipation rate estimation in Taylor-Couette flow for tomographic PIV. Exp Fluids 53:561–583

Tropea C, Yarin A, Foss JF (2007) Springer handbook of experimental fluid mechanics. Springer, Berlin. ISBN 978-3-540-30299-5

Tsai RY (1987) A versatile camera calibration technique for high-accuracy 3D machine vision metrology using off-the-shelf TV cameras and lenses. IEEE J. Robot. Autom. RA-3:323–44

Tsinober A, Kit E, Dracos T (1992) Experimental investigation of the field of velocity gradients in turbulent flows. J Fluid Mech 242:169–192

van Gent P, Michaelis D, van Oudheusden BW, Weiss P-É, de Kat R, Laskari A, Jeon YJ, David L, Schanz D, Huhn F, Gesemann S, Novara M, McPhaden C, Neeteson N, Rival D, Schneiders JFG, Schrijer F (2017) Comparative assessment of pressure field reconstructions from particle image velocimetry measurements and Lagrangian particle tracking. Exp Fluids. doi:10.1007/s00348-017-2324-z

van Oudheusden BW (2013) PIV-based pressure measurement. Meas Sci Technol 24:032001. doi:10.1088/0957-0233/24/3/032001

van Tubergen J, Verlinden J, Stroober M, Baldewsing R (2017) Suited for performance: fast full-scale replication of athlete with FDM. In: Proceedings of the 1st Annual ACM Symposium on Computational Fabrication. Cambridge, Massachusetts, June 12-13.

Vedula P, Adrian R (2005) Optimal solenoidal interpolation of turbulent vector fields: Application to PTV and super-resolution PIV. Exp Fluids 39:213–221

Violato D, Moore P, Scarano F (2011) Lagrangian and Eulerian pressure field evaluation of rod-airfoil flow from time-resolved tomographic PIV. Exp Fluids 50:1057–1070

Violato D, Scarano F (2011) Three-dimensional evolution of flow structures in transitional circular and chevron jets. Phys Fluids 23:124104

Vlasenko A, Steele ECC, Nimmo-Smith WAM (2015) A physics-enabled flow restoration algorithm for sparse PIV and PTV measurements. Meas Sci Technol 2015:065301

Wang C, Gao Q, Wang H, Wei R, Li T, Wang J (2016) Divergence-free smoothing for volumetric PIV data. Exp. Fluids. 57:15. https://doi.org/10.1007/s00348-015-2097-1

Westerweel J, Elsinga G, Adrian J (2013) Particle Image Velocimetry for Complex and Turbulent Flows. Annu. Rev. Fluid Mech. 45:409-436.

Westerweel J, Scarano F (2005) Universal outlier detection for PIV data. Exp Fluids 39:1096–1100

Wieneke B (2013) Iterative reconstruction of volumetric particle distribution. Meas Sci Technol 24:024008. doi:10.1088/0957-0233/24/2/024008

Wieneke B (2015) PIV uncertainty quantification from correlation statistics. Meas. Sci. Technol. 26:074002

Willert CE, Gharib M (1991) Digital particle image velocimetry. Exp. Fluids 10:181–93

Willert CE, Gharib M (1992) Three-dimensional particle imaging with a single camera. Exp. Fluids, 12(6):353-358.

Wills JAB (1964) On convection velocities in turbulent shear flows. J Fluid Mech 20:417–432

Wilson BM, Smith BL (2013) Uncertainty on PIV mean and fluctuating velocity due to bias and random errors. Meas. Sci. Technol. 24:035302

Xue Z, Charonko JJ, Vlachos PP (2015) Particle image pattern mutual information and uncertainty estimation for particle image velocimetry. Meas. Sci. Technol. 26:074001

Yamagata T, Hayase T, Higuchi H (2008) Effect of Feedback Data Rate in PIV Measurement-Integrated Simulation. J. Fluid Sci. Technol. 3:477-487.

Yang Y, Robinson C, Heitz D, Memin E (2015) Enhanced ensemble-based 4DVar scheme for data assimilation. Comput Fluids 115:201–210. doi:10.1016/j.compfluid.2015.03.025

Yegavian R, Leclaire B, Champagnat F, Marquet O (2015) Performance assessment of PIV super-resolution with adjoint-based data assimilation. In: 11th International symposium on particle image velocimetry, Santa Barbara, USA, 14–16 September

Zhong JL, Weng JY, Huang TS (1991) Vector field interpolation in fluid flow. Digital signal processing. In: International conference on DSP, Florence, Italy

Zhou J, Adrian RJ, Balachandar SK en dall TM (1999) Mechanisms for generating coherent packets of hairpin vortices in channel flow. J Fluid Mech 387:353–39

Appendices

Appendix A
VIC+ Adjoint equations

This appendix outlines the adjoint procedure for efficient and exact calculation of the gradient $\partial J/\partial \boldsymbol{\xi}$ for the gradient-based VIC+ optimization procedure (Chapter 5). The equations are derived through the tangent-linear of the VIC+ code, as explained for general cases in Giering and Kaminski (1998). For a detailed discussion on how the adjoint code is derived, the reader is referred to the latter paper and here only the resulting equations are given. Following the naming convention of Giering and Kaminski (1998), adjoint variables are named corresponding to their counterparts in Sec. 5.2, but with the prefix δ^*.

The procedure follows in reverse order the steps to calculate the cost function at each iteration (Sec. 5.2.2), and thus starts with the adjoint counterpart of the cost function,

(A.1) $$\delta^* \boldsymbol{u}_{h,p} = 2\left(\boldsymbol{u}_{h,p} - \boldsymbol{u}_m\right),$$

(A.2) $$\delta^* \frac{D\boldsymbol{u}_{h,p}}{Dt} = 2\alpha^2 \left(\frac{D\boldsymbol{u}_{h,p}}{Dt} - \frac{D\boldsymbol{u}_m}{Dt}\right),$$

where the subscript '*h,p*' indicates the variables on the computational grid, interpolated to the PTV measurement locations. The adjoint of linear interpolation is applied to move from these scattered locations back to the grid. Linear interpolation can be written as a linear system, $\boldsymbol{u}_{h,p} = \mathbf{A}\boldsymbol{u}_h$, where $\mathbf{A}$ is the (sparse) matrix containing the weights for the linear interpolation. The corresponding adjoint becomes (see also e.g. Claerbout 2014),

(A.3) $$\delta^* \boldsymbol{u}_h = \mathbf{A}^{\mathrm{T}}\, \delta^* \boldsymbol{u}_{h,p},$$

(A.4) $$\delta^* \frac{D\boldsymbol{u}_h}{Dt} = \mathbf{A}^{\mathrm{T}}\, \delta^* \frac{D\boldsymbol{u}_{h,p}}{Dt},$$

where the superscript 'T' means the transpose. Velocity was calculated from vorticity using a Poisson equation (eq. 1). The Laplacian is self-adjoint, hence the existing Poisson solver can be used to solve,

(A.5) $\nabla^2 \delta^* \boldsymbol{R}_{\boldsymbol{\omega}} = \delta^* \boldsymbol{u}_h$,

where $\delta^* \boldsymbol{R}_{\boldsymbol{\omega}}$ is the adjoint variable corresponding to the right-hand side of the Poisson equation, $\boldsymbol{R}_{\boldsymbol{\omega}} = -\nabla \times \boldsymbol{\omega}_h$. The sub-script 'h' is dropped in the remainder of this appendix for clarity. Subsequently,

(A.6) $\delta^* \boldsymbol{\omega} = -\widetilde{\nabla} \times \delta^* \boldsymbol{R}_{\boldsymbol{\omega}}$,

where,

(A.7) $\widetilde{\nabla} = \left[\frac{\widetilde{\partial}}{\partial x}, \frac{\widetilde{\partial}}{\partial y}, \frac{\widetilde{\partial}}{\partial z}\right]$,

is the adjoint of the gradient operator. Finite differences are used for the spatial derivatives, hence the corresponding adjoint operators are the transpose of the finite difference matrices. The radial basis function evaluation (eq. 11) can also be written as a matrix multiplication, $\boldsymbol{\omega} = \boldsymbol{\Phi} \boldsymbol{w}$, where $\boldsymbol{\Phi}$ contains the value of the radial basis function (eq. 10) at each grid point and $\boldsymbol{w}$ is the vector with the weights. The corresponding adjoint equation equals,

(A.8) $\delta^* \boldsymbol{w}_1 = \boldsymbol{\Phi}^{\mathrm{T}} \delta^* \boldsymbol{\omega}$.

The velocity material derivative was calculated from eq. (2). The adjoint counterpart of this step is,

(A.9) $\delta^* \frac{\partial \boldsymbol{u}}{\partial t} = \delta^* \frac{D\boldsymbol{u}}{Dt}$,

(A.10) $\delta^* \boldsymbol{C} = \delta^* \frac{D\boldsymbol{u}}{Dt}$,

where $\delta^* \boldsymbol{C}$ is the adjoint variable corresponding to the convective part of the velocity material derivative. The adjoint variable $\delta^* \boldsymbol{u}_2$, is calculated from $\delta^* \boldsymbol{C}$ using,

(A.11) $\delta^* u_{i,2} = \frac{\partial u_j}{\partial x_i}\delta^* C_j + \widetilde{\frac{\partial}{\partial x_j}}\left(u_j \delta^* C_i\right)$,

written in Einstein notation for clarity. The tilde again indicates the adjoint counterpart of the spatial derivative, which equals the transpose of the finite difference matrix. Subsequently, $\delta^* \boldsymbol{w}_2$ is calculated from $\delta^* \boldsymbol{u}_2$,analogously to $\delta^* \boldsymbol{w}_1$ using equations (A.5) to (A.8).

Analogous to eq. (A.5) and (A.6), the adjoint counterpart of the temporal vorticity derivative is obtained from $\delta^* \frac{\partial \boldsymbol{u}}{\partial t}$,

(A.12) $\nabla^2 \delta^* \boldsymbol{R}_{\partial \boldsymbol{\omega}} = \delta^* \frac{\partial \boldsymbol{u}}{\partial t}$,

(A.13) $\delta^* \frac{\partial \boldsymbol{\omega}}{\partial t} = -\widetilde{\nabla} \times \delta^* \boldsymbol{R}_{\partial \boldsymbol{\omega}}$.

The temporal derivative of vorticity is calculated from the vorticity transport equation (eq. 4). The adjoint counterpart yields,

(A.14) $\delta^* \omega_{i,2} = \frac{\partial u_j}{\partial x_i}\delta^* \frac{\partial \omega_j}{\partial t} - \widetilde{\frac{\partial}{\partial x_j}}\left(u_j \delta^* \frac{\partial \omega_i}{\partial t}\right)$,

(A.15) $\delta^* u_{i,3} = \widetilde{\frac{\partial}{\partial x_j}}\left(\omega_j \delta^* \frac{\partial \omega_i}{\partial t}\right) - \frac{\partial \omega_j}{\partial x_i}\delta^* \frac{\partial \omega_j}{\partial t}$,

where again the Einstein notation is adopted for clarity. Subsequently, $\delta^* \boldsymbol{w_3}$ is calculated from $\delta^* \boldsymbol{\omega}_2$ using equation (A.8) and $\delta^* \boldsymbol{w_4}$ is calculated from $\delta^* \boldsymbol{u}_3$ using equations (A.5) to (A.8). The gradient $\partial J/\partial \boldsymbol{\xi_\omega}$ is then calculated by,

(A.16) $\frac{\partial J}{\partial \boldsymbol{\xi_u}} = \delta^* \boldsymbol{w}_1 + \delta^* \boldsymbol{w}_2 + \delta^* \boldsymbol{w}_3 + \delta^* \boldsymbol{w}_4$.

Analogously, the gradients $\partial J/\partial \boldsymbol{\xi_{BC,u}}$ and $\partial J/\partial \boldsymbol{\xi_{BC,\partial u}}$ for the boundary conditions are calculated.

Appendix B
VIC+ Pseudo code

```
% VIC+ Pseudo Code
% Schneiders and Scarano (2016)

% Initialize PTV measurements
x_ptv  = Tracer particle locations;
u_ptv  = Velocity measurements;
Du_ptv = Material derivative measurements;

% Definition of initial conditions
u_initial    = Velocity initial condition;
vort_initial = curl(u_initial);
dudt_initial = zeros(size(u_initial));

% Set initial optimization variables vector "xi"
xi_vort = Calculate RBF weights from "vort_initial";
xi_bcu  = Calculate RBF weights from the boundary values of "u_initial";
xi_bcdu = Calculate RBF weights from the boundary values of "dudt_initial";
xi(k=0) = [xi_vort, beta1*xi_bcu, beta2*xi_bcdu];

% Iterative optimization procedure
converged = FALSE;
while converged == FALSE
    % Calculate u and Du/Dt on the grid
    vort_h    = Evaluate vorticity on the grid from RBF coefficients in xi(k);
    u_h       = Solve Poisson equation for velocity: ∇²u_h = −∇ × ω_h with boundary conditions from xi(k);
    dvortdt_h = Solve ∂ω_h/∂t from vorticity transport: ∂ω_h/∂t = (ω_h · ∇)u_h − (u_h · ∇)ω_h;
    dudt_h    = Solve Poisson equation for ∂u_h/∂t: ∇²∂u_h/∂t = −∇ × ∂ω_h/∂t with boundary conditions from xi(k);
    conv_h    = Calculate the convective part of the material derivative: (u_h · ∇)u_h
    DuDt_h    = Calculate the material derivative: "dudt_h" + "conv_h";

    % Interpolate to particle locations
    u_h_ploc  = Interpolate "u_h" to "x_ptv" using linear interpolation;
    Du_h_ploc = Interpolate "DuDt_h" to "x_ptv" using linear interpolation;

    % Calculate the cost function (eq. 6)
    J_u  = sum((u_h_ploc - u_ptv)^2);
    J_Du = sum((Du_h_ploc - Du_ptv)^2);
                        J(k) = J_u + alpha^2 * J_Du;

    % Adjoint equations for calculateion of the gradient of the cost function (Appendix A)
    up_AD       = Equation (A.1): 2*(u_h_ploc  - u_ptv);
    uh_AD       = Calculate adjoint of the linear interpolation (eq. A.3);
    vort_AD_1   = Calculate δ*ω₁ from "uh_AD" with eq. (A.5) and (A.6);
    w_AD_1      = Calculate δ*w₁ from "vort_AD_1" with eq. (A.7);
    Dup_AD      = Equation (A.2): 2*alpha^2*(Du_h_ploc  - Du_ptv);
    Duh_AD      = Calculate adjoint of the linear interpolation (eq. A.4);
    uh_AD_2     = Calculate δ*u₂ from "Duh_AD" with eq. (A.9) and (A.10);
    w_AD_2      = Calculate δ*w₂ from "uh_AD_2" with eq. (A.5) to (A.7);
    dvortdt_AD  = Calculate δ*δω/δt from "Duh_AD" with eq. (A.8), (A.11) and (A.12);
    vort_AD_2   = Calculate δ*ω₂ from "dvortdt_AD" with eq. (A.13);
    uh_AD_3     = Calculate δ*u₃ from "dvortdt_AD" with eq. (A.14);
    w_AD_3      = Calculate δ*w₃ from "vort_AD_2" with eq. (A.7);
    w_AD_4      = Calculate δ*w₄ from "uh_AD_3" with eq. (A.5) to (A.7);

    % Gradient of cost function (Appendix A)
    dJdxi = w_AD_1 + w_AD_2 + w_AD_3 + w_AD_4;

    % Update the optimization variables using the L-BFGS algorithm
    p = Calculate the update direction of the optimization variables using L-BFGS and the gradient "dJdxi"
    s = Obtain stepsize using L-BFGS and "p"
    xi(k+1) = Update the optimization variables using: xi(k) + s * p;

    % Check for convergence
    if (k > 1) && (J(k+1) - J(k)) < threshold
              converged = TRUE;
    end

    k = k + 1;
end

% Output velocity field
vort_h = Evaluate vorticity on the grid from the RBF coefficients in xi(k);
u_h    = Solve Poisson equation for velocity: ∇²u_h = −∇ × ω_h with boundary conditions from xi(k);
```

Appendix C
Tomographic CVV reconstruction

In this appendix, the reconstructed particle size in case of CVV measurements is obtained in an experiment and compared to the analytical results obtained in Chapter 10. It was derived that the reconstructed particle size in case of tomographic reconstructions equals

$$d_x = d_y = \frac{d_\tau}{M} = \frac{d_\tau}{f} z \tag{C.1}$$

along the x and y-axis and

$$d_z = \frac{2}{\beta} d_x \tag{C.2}$$

along the z-axis. In the diffraction limited range, d_τ is approximately constant and the particle size along the x- and y-axis is proportional to z. However, along the z-axis the particle size becomes proportional to z^2, because of the particle elongation effect.

A free-stream flow measurement (u_∞ = 2.5 m/s) is performed using a CVV system (Chapter 11). The particle size in tomographic MLOS reconstructions is obtained by fitting of a Gaussian along each coordinate direction. The measured particle size of particles positioned along the z-axis is plotted in Fig. C.1. The predicted value of d_x (dashed black line) is obtained from eq. (C.1), where it is used that the diffraction limited particle size in the experiment is approximately 3 px. Similarly, the expected value of d_z (solid black line) is obtained from eq. (C.2). Despite an underestimation of the predictions, the experiment confirms the expected trend and most importantly the difference between in-plane and out-of-plane particle size up to z = 350 mm. For larger values of z, the measured out-of-plane particle size flattens, indicating a second order effect that is not accounted for in the analytical analysis, such as reduced particle image intensity.

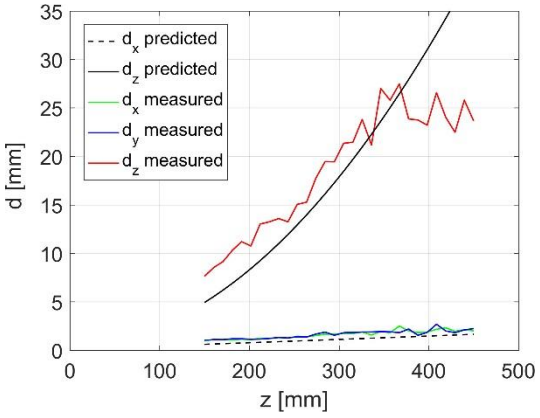

Fig. C.1 Measured reconstructed particle size in comparison to the analytical results (black lines).

Note that the elongated particle shape is only oriented along the z-axis for particles on the axial center-line of the CVV. As illustrated in Fig. C.2, off-center particles will be reconstructed as tilted ellipses in the tomographic reconstructions. This reduces the effective particle intersection, d^*, along the depth direction. However, the actual particle aspect ratio d_z/d_x remains approximately constant.

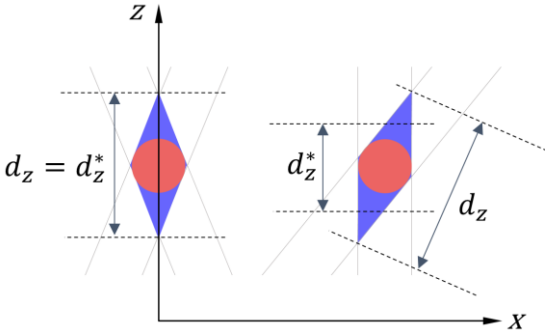

Fig. C.2 Off-center particles (right) appear elongated in tomographic reconstructions but are tilted in comparison to particles positioned on the measurement axis (left).

Approximating a reconstructed particle by an ellipse with semi-major and semi-minor axes equal to d_z and d_x, respectively, a particle that is displaced on the y-axis accordingly has a smaller effective intersection with the z-axis, d_z^*,

(C.3) $$d_z^*(x) = \left[d_x^{-2} \sin^2 \frac{|x|}{z} + d_z^{-2} \cos^2 \frac{|x|}{z}\right]^{-\frac{1}{2}}$$

and a marginally increased intersection with the y-axis,

(C.4) $$d_x^*(x) = \left[d_x^{-2} \cos^2 \frac{|x|}{z} + d_z^{-2} \sin^2 \frac{|x|}{z}\right]^{-\frac{1}{2}}.$$

These equations are also assessed using the experiment. The average effective particle cross sections with each coordinate axis along the line z = 300 mm and y = 0 mm is plotted in Fig. C.3. The expected peak value in d_z^* is found (red line) as predicted by eq. (C.3). Moreover, as expected from eq. (C.4), d_x^* remains relatively constant in comparison to d_z^*.

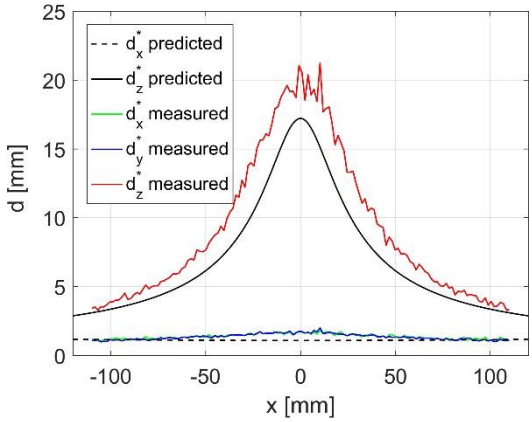

Fig. 16.1 Effective reconstructed particle size at z = 0.3 m and y = *0* in comparison to the analytical results (black lines).

This could affect positional uncertainties towards the domain edges when standard peak-finding algorithms are employed along the three coordinate directions.

Acknowledgements

These days I have the great pleasure of working with the programming department of LaVision GmbH. on implementation of VIC+ in their Davis software. Working here in Göttingen, being one month away from my defense, I can't help but somewhat sentimentally think back of all those great moments over the past years that fueled the research and lines of code that are now being transferred into a commercial software package.

It is now a bit more than 3.5 years ago that I completed my MSc project with prof. dr. *Fulvio Scarano*. Already during my MSc, I was impressed by the amount of dedication of Fulvio to both the research and development of students. It wasn't a tough decision to continue our collaboration for a PhD. Fulvio, looking at how positively an impressive list of former PhD colleagues have acknowledged you in their dissertation, it is hard to find new superlatives to use in my acknowledgements. I want to thank you a thousand times for the past years of great coaching. I am looking back with the greatest pleasure on our brainstorming talks and all the moments where we progressed our work together.

I would also like to thank *Bernd Wieneke*. As managing director of LaVision you were able to fund my PhD studies; as great scientist you were able to always ask the right questions that pushed my work in the right direction. Also at LaVision, I would like to thank *Dirk Michaelis* and *Uwe Dierksheide* for our discussions on PIV, Davis and HFSB, and for always welcoming me in Göttingen.

Early on in my PhD, *Bas van Oudheusden* allowed me to join the activities of the European NIOPLEX consortium. Together with *Ferry Schrijer*, *Paul van Gent* and the international members of the consortium we were able to move pressure-from-PIV forward. I thank you all for the work we managed together, and for the possibilities it has given me to interact with other research groups.

I would like to thank *Andreas Schröder* for our always very pleasant, sometimes late-night, discussions and collaborations, and in particular for co-organization of the CFD for PIV/LPT workshop series.

Also, I should not forget thanking the master students that jumped on board for a thesis or internship: *Thomas King*, *Piyush Singh*, *Constantin Jux*, *Stefano Meloni* and *Edoardo Saredi*, it was great to work with you all.

Thinking back of my PIV experiments, I must acknowledge the incredible efforts of *Giuseppe Caridi* and *Andrea Sciacchitano*, who always patiently helped me during my experimental campaigns.

Less visible from publications and work output, but not less important and likely even critical for successful completion of a PhD, I would like to thank our secretary *Colette Russo*. Also, *Peter Duyndam*, *Frits Donker Duyvis*, *Stefan Bernardy* and *Henk-Jan Siemer*, thank you for always supporting my wind tunnel experiments and making often unexpected last-minute changes possible. Thanks also to *Nico van Beek* for supporting and solving all my IT related problems and *Ruud van Rooij* for making sure finances went smooth.

To *Koen Groot* I also owe a great acknowledgement. We started our studies of Aerospace Engineering on the same day and have followed very similar path, to the point that I wrote large parts of this work sitting next to you in the PhD office. I have great respect for your ability to work on very abstract problems, and your ability to transform every night out into an unforgettable one. Together with *Darun Barazanchy*, *Gabriel Maher*, *Rijk de Rooij* and *Ruben Sevenois* we made great memories during our undergraduate studies. Later during the PhD this journey continued with *Kyle Lynch*, *Rogier Giepman* and *Wouter van der Velden*, and with some blue mountains cold Coors Light beers in Florida of course.

Given the amount of Italian colleagues at our laboratories, their hospitality and their access to sfogliatelle, it was easy to become friends with *Daniele Ragni*, *Serena de Simone*, *Giuseppe Caridi*, *Jacopo Serpieri*, *Greta Quaranta*, *Valeria Gentile*, *Francesco Avallone*, *Teresa Prezzemolo* and

many other of our now mutual friends. Our holidays and conferences, together with, *Theo Michelis, Egle Kalonaityte, Qingqing Ye, Cesar Bernal* and *Pablo Hernandez Clemente* will remain forever in my mind. Let's plan something again soon, *Daniele Ragni*: once the salary is paid we book Micronesia!

Besides colleagues I would like to thank *Yotam Raz* for always remaining a great friend since high school. Our wine journeys certainly have fueled good parts of this work. Similarly, *Kilian Treurniet*, I cannot wait for our next political debate, fueled by fury and friendship. Before I forget, *Yotam* and *Kilian*, are you available for curling training this Saturday? Also, *Miriam Piening*, thank you for our friendship throughout this journey.

Finally, I thank my parents and family. Without you nothing of this would've been possible.

Biographical Note

Jan Ferdinand Gerardus Schneiders was born on the 12th of July 1990 in Leidschendam, The Netherlands. Jan completed his pre-university education at the Gymnasium Haganum with honors in 2008, excelling in mathematics and physics, but also showing a broad interest in other topics such as web development, Latin and debating.

Following a summer break, Jan boarded the TU Delft faculty of Aerospace Engineering for his bachelor studies. Jan also immediately joined the Formula Zero hydrogen racing team and participated in extracurricular activities, such as in the editorial team of the Leonardo Times magazine and the media committee of the freshman opening week. Jan completed his bachelor *cum laude* with a grade point average that ranked him within the top 1% of all students.

In September 2011, Jan joined the Aerodynamics group in Delft for his master studies. During his master, Jan spent half a year in the United Kingdom to work for Roll-Royce on certification of the jet engine for the Airbus A350. Back in Delft, Jan got in touch with prof. dr. Fulvio Scarano for his thesis project. This marked the beginning of Jan's journey into data assimilation for the PIV measurement technique. Jan graduated *cum laude* with a 10 for his thesis and received the best graduate of TU Delft Aerospace Engineering award, on the basis of Jan's research and his exemplary achievements in his studies.

Jan secured funding for a PhD from the German company LaVision GmbH, which he started in March 2014 with his promotor prof. dr. Fulvio Scarano. On 14 December 2017, at 27 years of age, Jan is defending his PhD work, that has focused on the topics of data assimilation for PIV and development of a new velocimeter

The work of Jan has been awarded internationally multiple times. Most recently, Jan received the best paper award in Busan, South Korea, for his work on the coaxial volumetric velocimeter.

List of Publications

Journal Publications

10. **Schneiders JFG**, Scarano F, Jux C, Sciacchitano A "*Coaxial volumetric velocimetry*" under review
9. Jux C, Sciacchitano A, **Schneiders JFG**, Scarano F "*Robotic large scale volumetric PIV for cycling aerodynamics*" under review
8. **Schneiders JFG**, Avallone F, Pröbsting S, Ragni D, Scarano F "*Pressure spectra from single-snapshot tomographic PIV*" under review
7. **Schneiders JFG**, Sciacchitano A "*Track benchmarking method for uncertainty quantification of particle tracking velocimetry interpolations*" Meas. Sci. Technol. 28, 065302 (2017)
6. van Gent PL, Michaelis D, van Oudheusden BW, Weiss P-É, de Kat R, Laskari A, Jeon YJ, David L, Schanz D, Huhn F, Gesemann S, Novara M, McPhaden C, Neeteson NJ, Rival DE, **Schneiders JFG**, Schrijer FFJ "*Comparative assessment of pressure field reconstructions from particle image velocimetry measurements and Lagrangian particle tracking*" Exp. Fluids 58, 33 (2017)
5. **Schneiders JFG**, Scarano F, Elsinga GE "*Resolving vorticity and dissipation in a turbulent boundary layer by tomographic PTV and VIC+*" Exp. Fluids 58, 27 (2017)
4. **Schneiders JFG**, Caridi GCA, Sciacchitano A, Scarano F "*Large-scale volumetric pressure from tomographic PTV with HFSB tracers*" Exp. Fluids 57, 164 (2016)
3. **Schneiders JFG**, Scarano F "*Dense velocity reconstruction from tomographic PTV with material derivatives*", Exp. Fluids 57, 139 (2016)
2. **Schneiders JFG**, Pröbsting S, Dwight RP, van Oudheusden BW, Scarano F "*Pressure estimation from single-snapshot tomographic PIV in a turbulent boundary layer*" Exp. Fluids 57, 53 (2016)

1. **Schneiders JFG**, Dwight RP, Scarano F "*Time-supersampling of 3D-PIV measurements with vortex-in-cell simulation*" Exp. Fluids 55, 1629 (2014)

Selected Conference Publications

12. **Schneiders JFG**, Jux C, Sciacchitano A, Scarano F "*Coaxial volumetric velocimetry*" 12th Int. Symp. Particle Image Velocimetry, Busan, Republic of Korea (2017)
11. Jux C, Sciacchitano A, **Schneiders JFG**, Scarano F "*Full-scale cyclist aerodynamics by coaxial volumetric velocimetry*" 12th Int. Symp. Particle Image Velocimetry, Busan, Republic of Korea (2017)
10. **Schneiders JFG**, Avallone F, Pröbsting S, Ragni D, Scarano F "*Pressure spectra from single-snapshot tomographic PIV*" 12th Int. Symp. Particle Image Velocimetry, Busan, Republic of Korea (2017)
9. **Schneiders JFG**, Singh P, Scarano F "*Instantaneous flow reconstruction from particle trajectories with vortex-in-cell*" 18th Int. Symp. Appl. Laser. Techn. Fluid Mech., Lisbon, Portugal (2016)
8. **Schneiders JFG**, Scarano F, Elsinga GE "*On the resolved scales in a turbulent boudnary layer by tomographic PIV and PTV aided by VIC+*" 18th Int. Symp. Appl. Laser. Techn. Fluid Mech., Lisbon, Portugal (2016)
7. Blinde P, Michaelis D, Van Oudheusden BW, Weiss P-E, De Kat R, Laskari A, Jeon YJ, David L, Schanz D, Huhn F, Gesemann S, Novara M, Mcphaden C, Neeteson N, Rival D, **Schneiders JFG**, Schrijer F "*Comparative assessment of PIV-based pressure evaluation techniques applied to a transonic base flow*" 18th Int. Symp. Appl. Laser. Techn. Fluid Mech., Lisbon, Portugal (2016)
6. Pröbsting S, **Schneiders JFG**, Avallone F, Ragni D, Scarano F "*Trailing-edge noise diagnostics with low-repetition-rate PIV*" 22nd AIAA/CEAS Aeroacoustics Conference, 3023, Lyon, France (2016)
5. **Schneiders JFG**, Azijli I, Scarano F, Dwight RP "*Pouring time into space*" 11th Int. Symp. Particle Image Velocimetry, Santa Barbara, CA, USA (2015)

4. **Schneiders JFG**, Dwight RP, Scarano F "*Tomographic PIV noise reduction by simulating repeated measurements*" 11th Int. Symp. Particle Image Velocimetry, Santa Barbara, CA, USA (2015)
3. **Schneiders JFG**, Lynch KP, Dwight RP, van Oudheusden BW, Scarano F "*Instantaneous pressure from single-snapshot tomographic PIV by vortex-in-cell*" 17th Int. Symp. Appl. Laser. Techn. Fluid Mech., Lisbon, Portugal (2014)
2. Blinde PL, Lynch KP, van Oudheusden BW, **Schneiders JFG**, Schrijer F "*Assessment of instantaneous pressure determination in a transonic base flow based on four-pulse tomographic PIV*" 17th Int. Symp. Appl. Laser. Techn. Fluid Mech., Lisbon, Portugal (2014)
1. **Schneiders JFG**, Dwight RP, Scarano F "*Vortex-in-cell method for time-supersampling of PIV data*" 10th Int. Symp. Particle Image Velocimetry, Delft, The Netherlands (2013)